Towards Cooperatively Enhanced Resonant Dipole Forces in Optical Levitation, Harnessing Quantum Emitters in Diamonds

By

Reece P. Roberts

A thesis submitted to Macquarie University
for the degree of Doctor of Philosophy
Department of Physics and Astronomy
November 2019

MACQUARIE
University
SYDNEY·AUSTRALIA

Typeset in LaTeX 2_ε.

Except where acknowledged in the customary manner, the material presented in this thesis is, to the best of my knowledge, original and has not been submitted in whole or part for a degree in any university.

Reece P. Roberts

Acknowledgements

Over three years ago I started this project aimed to assert my control over very tiny specks of diamond. This thesis is only the report of the work that was completed. The work in this thesis does not express the determination needed to keep chasing shadows and false trails, or the time required to keep fumbling in the dark, both literally aligning photosensitive detectors, and figuratively searching for those answers to those questions that no one has answers to. Of course, looking back it is much easier to see the path you should have taken; the space you should have left to include the spectrometer in your experiment or to search for, find and read that paper that puts the missing pieces together. However arduous the journey has been, I would like to thank those who have helped me complete this work.

I would firstly like to thank my supervisor Gabriel Molina-Terriza who has helped me develop as a better physicist and inspire me to become a strong and independent researcher. I would also like to thank Thomas Volz for his expert advice and support. Special thanks goes to Mathieu Juan who has been a true mentor, who always makes time for any questions I may have. From guiding me to understand intricate theoretical details, to providing insight on the best way to build an experiment, his help has been invaluable throughout.

Getting through this PhD has required more than academic support; I have many, many people to thank for listening to and at times, having to tolerate me over the past three years. I cannot begin to express my gratitude and appreciation for their friendship. In particular I must thank Matt van Breugel, Thomas Guff, Tiffany Day, Christina Baldwin, Shane Vickers, Andrew Wood and Johannes Stark who have traveled the postgraduate life with me. Alex Stokes, Katie Cave, Josh Tubb and Rokiah Alford have all helped in this journey by keeping

my mind off my research and my body fit with our continuous obsession with rock climbing. For many memorable evenings out and in, I must also thank Robert Thew, Andrew Jones, Matt O'Neil and Ryan Spooner. A special mention must go to Glen Douglass who has taken a similar course in life as me and belongs in all three of the aforementioned friendship groups. Finally, I must thank my family who have always supported me in my life.

> 'Sometimes our light goes out but is blown into flame by another human being. Each of us owes deepest thanks to those who have rekindled this light.'
>
> –Albert Schweitzer

Abstract

Optical trapping offers a non-contact, non-destructive tool for manipulating and handling particles, from micron sized particles down to individual atoms with light. One can distinguish two different applications for optical trapping. The first relying on the ability to trap small particles (from tens of nm to tens of μm); the second, related to the confinement and cooling of atoms or collections of atoms. Until now there has been no system that combines the forces due to both dielectric particle trapping and atom trapping as they are usually contained in completely separate parameter regimes, even though both of these trapping applications arise from the same force. The force is the result of the interaction of the polarisability of the trapped object with the electric field of the trapping laser, which depends directly on the dipole strength trapped object. In the case of classical trapping, the force acts on an induced dipole caused by the electric field on the object, whereas in the case of atom trapping, the induced dipole arises from the optical transitions present in the electronic structure.

In this way, optically trapped nano-particles containing embedded optical defects brings about a new regime of trapping and cooling nano-particles. This new trapping regime will allow well established techniques from atom trapping to be applied to the more massive nano-particles. The result is an optical trap showing capabilities with improved trapping strengths and cooling mechanisms. The enhanced control will allow us to cool the centre of mass motion of nano-particles down to their quantum ground state, even in a room temperature environment, exciting for high precision sensing and macroscopic quantum experiments.

In this thesis I focus primarily on identifying and observing the trapping forces on the

optical defects inside of optically trapped nano-diamonds. I developed an experimental set-up and procedure to isolate, trap and reliably measure the trapping behaviour of nano-particles as a platform for investigating the atomic forces on optical defects in nano-diamonds.

I continue with a detailed analysis of the photo-physics of the Nitrogen Vacancy centre which is the most interesting and studied optical defect in diamond. I explore the implications of the intense trapping laser field, required for optical trapping, on the feasibility of observing defect related forces on NV centres in nano-diamonds. Due to the limitations of the Nitrogen Vacancy defect I explore the properties of Silicon Vacancy centres in diamond, highlighting the properties that an ideal particle would posses, with a particular emphasis on generating collective effects. I investigate the effects of the high intensity, near infra-red trapping laser field and show the exciting possibilities of cooling the centre of mass motion and the internal temperature of the nano-particle simultaneously.

Whilst I have not yet reached the goal of levitating a particle and observing the cooperatively enhanced resonant optical dipole forces on its internal embedded defects, I have undertaken a number of steps providing the ground work and foundations for ultimately observing and using these forces.

> 'I like it when somebody gets excited about something. It's nice.'
>
> – J.D. Salinger, The Catcher in the Rye

Contents

List of Figures

List of Tables

Organisation of Thesis

This thesis brings together three fields of physics: cold atom physics, opto-mechanics of levitated nano-particles and diamond material science; combining them into a unique system offering distinct advantages for inertial sensing. In **Chapter 1** I provide an introduction into the three distinct fields of physics that are involved in this thesis and how they can be combined within a single system. I begin with an introduction into optical forces and optical trapping with light, presenting a review on how this field developed from first observations in the 1970s, through to the 1997 Nobel prize in Physics 'for development of methods to cool and trap atoms with laser light'. At this point I digress into the field of diamond material science and its fascinating physical and optical properties and finally show how we can merge these two fields to provide potentially significant advantages in the field of quantum opto-mechanics.

Chapter 2 gives an extensive review of optical trapping forces. I introduce the two approaches to optical trapping: classical trapping and atom trapping. I provide an intuitive understanding of optical trapping before analysing the individual forces arising from a classical approach for optical trapping and then from a quantum approach for atom trapping. I then show a new optical trapping design we have developed using focused-Bessel beams, that enables us to enhance the frequency tuning of an optically levitation sensor. Finally I end the chapter by delving into a discussion on the optical cooling strategies for both atom trapping and classical trapping.

Chapter 3 contains the experimental work to measure and monitor the optical forces

of a nano-diamond containing NV centres. I begin with the analysis of combining the standard radiation pressure forces on a diamond nano-particle along with the internal atom like optical transitions embedded within the diamond matrix. I provide important details on the preliminary study that observed cooperatively enhance dipole forces on nano-diamonds in liquid trapping as a motivation for observing the same forces in an optically levitated system. I then focus on the process of developing a custom built optical trapping system and developing an imaging system to comprehensibly monitor the motion of particles within the optical trap. I show how the trapping stiffness of the system can be extracted by quantitative measurements of the trapped particles position and demonstrate that the sensitivity is sufficient to observe the expected optical forces. Finally, I focus on trapping Nitrogen Vacancy centres in nano-diamonds and the development of the protocols for quantitatively measuring the classical and atomic trapping components. I show that unfortunately the NV centre can not be simplified to an ideal two level system and further analysis of its internal structure is required before the resonant optical forces on the nano-diamond can be observed.

In **Chapter 4** I present the theoretical and experimental work to investigate the near infrared quenching mechanism on NV centres in nano-diamonds. I begin with the development of the confocal microscopy set-up designed to investigate the lack of fluorescence observed. I follow this by providing a more comprehensive analysis of the Nitrogen Vacancy centre and its internal photo-physics. Finally, I show that the quenching observed is provided by a dramatic increase in the charge state interconversion processes. Finally I discuss the implications of this result on generating optical forces on NV centres in an optically levitation regime.

As a result of the previous study into the NV centre, the Silicon Vacancy (SiV) centre was investigated as a colour centre in diamond that could potentially replace the NV centre with respect to observing the resonant radiation pressure forces on nano-diamonds. **Chapter 5** begins with the the description of the Silicon vacancy centre and discuss the nano-diamond samples I have available. I present a new optical levitation system for the SiV centres as well as introduce an acid treatment process to clean the nano-diamond samples. In addition, I present the preliminary measurements made to ensure that the trapping laser did not have an effect on the SiV centres as shown in the NV centre. These preliminary measurements

then motivate a deeper investigation into the photo-dynamics of the SiV centre, showing that the SiV centre exhibits an anti-stokes process with possibilities for optical refrigeration. I end this chapter with a discussion of the implications of our analysis of the SiV centres with respect to observing the resonantly enhanced optical dipole forces.

Chapter 6 contains the conclusions of this work and novel now directions that this work provides the foundations for.

> 'I may not have been sure about what really did interest me, but I was absolutely sure about what didn't.'
>
> – Albert Camus, The Stranger

'There are things known and there are things unknown,
and in between are the doors of perception.'
– Aldous Huxley

1 Introduction

1.1 Optical Trapping

In 1970, Arthur Ashkin of Bell Labratories calculated that a focused beam of light incident on a microsphere could exert a large force through radiation pressure or conservation of momentum off a reflecting surface [1]. This result motivated a simple experiment to examine such a force on a sample of transparent latex spheres suspended in water [2]. Surprisingly, not only did this experiment demonstrate forward motion due to laser radiation pressure, but also the existence of a transverse force that results in particle guiding, particle separation, and stable three-dimensional trapping [3].

Optical trapping of dielectric particles in an aqueous media has found the majority of its applications in biology. For *in vitro* applications, optical traps are used to study the properties of a variety of objects, such as polymers [4], DNA [5], single molecules [6] and

molecular motors [7]. For *in vivo* applications, optical traps are usually employed in a non-quantitative manner to manipulate the relative position of biological objects, such as sorting cells [8] and positioning fluorescent probes [9]. However more importantly, in Ashkin's seminal papers he also observed that one could levitate a dielectric particle in air with the laser radiation pressure acting on the induced dipole of the particle [10]. This is an important step towards removing the mechanical interactions between the environment and the motion of the particles that destroys any possibility of observing desirable quantum effects.

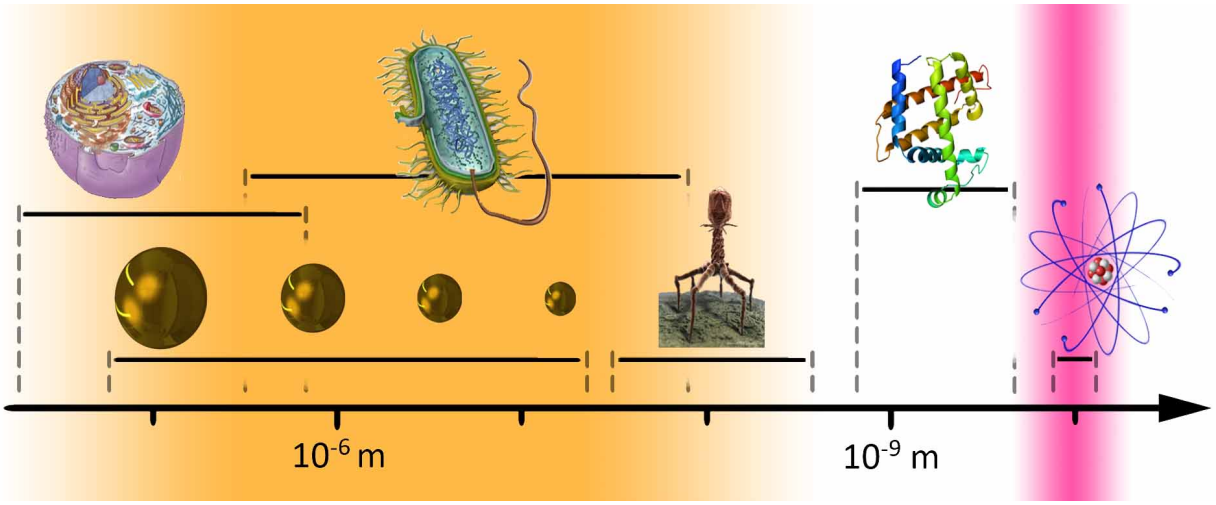

Figure 1.1: Typical size regimes of optical trapping with the dielectric trapping range shown in orange and the atom trapping range shown in pink. Typically optical forces on dielectrics are capable of manipulating organic and inorganic objects ranging from tens of microns down to tens of nanometres, whereas atom trapping is confined to trapping of single atoms.

Whilst optical levitation of dielectric materials did not gain much traction at the time, it was predicted in the early 70's that similar trapping forces were possible with atoms. The main difference between atom trapping and trapping of dielectric particles is the structure of the internal dipole. For atom trapping the force is acting on the dipole of an optical transition instead of acting on an induced dipole of the bulk material, generated by the incident electric field. The issue preventing the successful trapping of atoms was that the optical forces were tiny. The potential wells created were so shallow that the thermal energy of the atoms was sufficiently high enough for them to 'boil' out of the optical trap. Hence, in order to trap atoms they must first be pre-cooled so that they do not have sufficient kinetic energy to escape. It wasn't until 1986 when Steven Chu et al. demonstrated the

first working optical trap for neutral atoms [11], who along with Claude Cohen-Tannonudji and William D. Phillips were awarded the 1997 Nobel Prize, 'for development of methods to cool and trap atoms with laser light.' This work allowed the preparation of atoms in their quantum ground state. The methods they developed to cool the atoms to their ground state include Doppler cooling [12], optical molasses [13], velocity selective coherent population trapping [14] and Sisyphus cooling [15]. These techniques enabled further discoveries which resulted in applications such as producing one-component plasmas [16], producing Bose-Einstein condensations in a dilute gas [17], measuring quantum properties on single atoms [18], and increasing precision of atomic clocks [19].

Recently, optical levitation of dielectric particles has made a resurgence [20]. Levitated nano-particles are now being investigated for the development of macroscopic quantum experiments and for high-precision force and acceleration sensing [21–24]. It is important to note that there are two distinct temperatures related to levitated nano-particles: the internal temperature of the nano-particle matrix as well as the temperature related to the oscillatory centre of mass (CoM) motion of the nano-particle. The interesting temperature in this system is the temperature of the CoM motion which is typically decoupled from the internal temperature of the nano-particle itself due to their vastly different energy scales. The consequence is that the levitated nano-particles can be optically trapped and cooled, even if their internal temperature is at room temperature or hotter. The goal is to cool the CoM temperature from room temperature down to or towards the quantum ground state*. Once we reach this regime we aim to control and manipulate the CoM motion of the whole system enabling macroscopically distinct superposition states [25]. Additionally, the large mass of the solid nano-particle provides avenues for exceedingly accurate acceleration and force sensing [26, 27]. Currently, the major limitation for achieving a quantum ground state in these systems is the poor control over the CoM motion of the particle. Unfortunately, many of the regimes used for cooling atoms are not applicable for cooling the CoM motion

*Due to the equipartition theorem, when the particles are trapped at atmospheric conditions the CoM motional temperature must also be at room temperature due to the thermal coupling arising from the Brownian collisions between the particle and the air molecules. To cool the CoM temperature we must first decouple the Brownian collisions heating the particle by transitioning the particle into a vacuum environment. It is therefore fair to assume that whenever cooling of a particle is mentioned, it is occurring in a vacuum environment.

of nano-particles due to the lack of a resonant force provided by the atomic transitions. Current techniques that are being developed to cool the CoM motion include parametric feedback cooling [28–30] and cavity cooling [24, 31, 32]. Whilst these techniques are showing promise in cooling the nano-particles towards the ground state they will greatly benefit from a strong optically resonant force similar to the optically resonant force in atoms.

Our aim is to create this strong optically resonant force in an optically levitated dielectric particle. If we can dominate the optical forces with a strong optically resonant force, the particle will behave like a giant atom. In this way we will be able to open up many of the well established techniques used in atom trapping and apply them to the more massive dielectric nano-particle as shown in Figure (1.2). We propose to generate this strong resonant optical dipole force by utilising the interesting physical and optical properties of embedded optical defects contained within diamond.

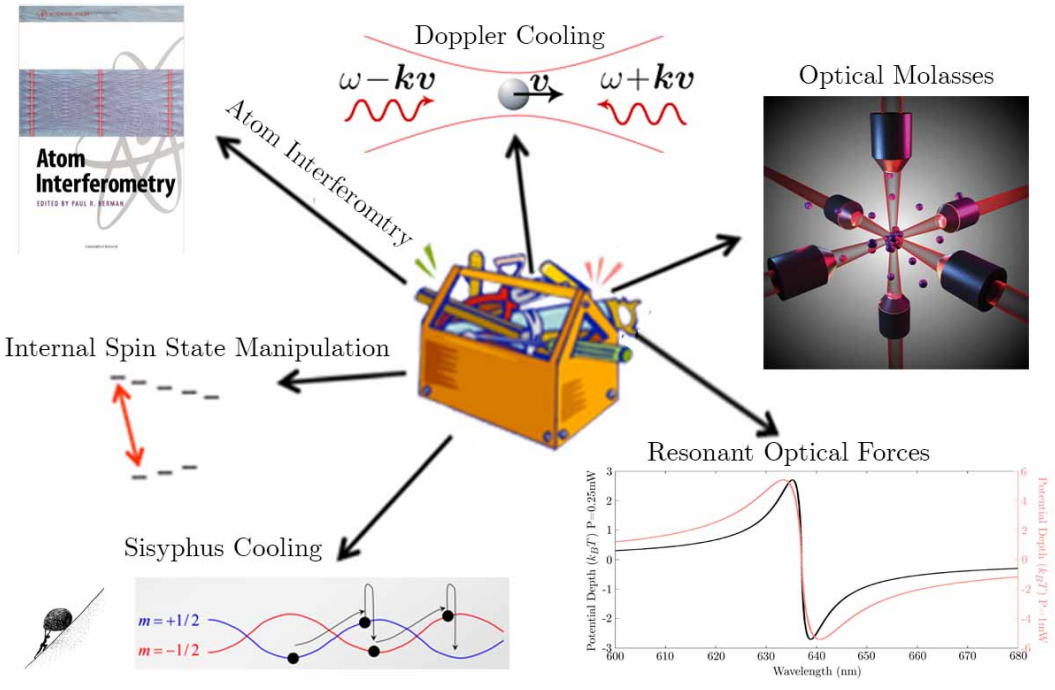

Figure 1.2: Atom trapping toolbox applicable to dielectric particles exhibiting a strong resonant optical dipole force. We aim to generate a strong resonant optical dipole force within a dilectric nano-particle to open up many of the well developed atom trapping techniques and apply them to the more massive dielectric object.

1.2 Diamond

Diamond has been known for thousands of years as both a prized gemstone and as an engraving tool, however the popularity of diamond grew rapidly in the 19^{th} century when techniques improved to cut and shape the material. In fact, the popularity of diamond was transformed by the marketing campaign of De Beers', who owned and still owns the majority of the world's diamond supplies. De Beers' marketing campaign focused on advertising the product rather than the brand and can be argued to be one of the greatest advertising campaigns, the result of which made diamonds a true icon in the eyes of the public. These diamonds are natural diamonds which are found in many different types and colours, each with different optical and physical properties. Natural diamonds contain many imperfections and defects that are desirable in jewellery and are responsible for producing their vibrant colours as shown in Figure (1.3).

Figure 1.3: Natural diamonds which are found in many different types and colours, each with different optical and physical properties. Unlike pure diamonds which are colourless, natural diamonds typically contain many impurities and defects that are desirable for jewelry and produce a vibrant range of coloured gems. Different diamond defect types and atomic inclusions have been identified and produce different coloured diamonds. For example, nitrogen defects tend to turn the diamonds a yellow or orange colour, whereas natural radiation from exposure to radioactive uranium from rocks near the earths surface can produce diamonds with a distinctive green hue.

Unlike diamonds found in nature, pure diamond is optically transparent from the near UV all the way through to the far infrared as seen by the negligible extinction coefficient (k) in Figure (1.4). In combination with its extreme mechanical, electrical and thermal properties, diamond based applications have proliferated into a diverse range of fields including mechanical machining, high-power high frequency electronics, high power non-linear optics, optical windows and many more [33]. Important for strong optical forces, diamond exhibits a relatively high refractive index (n) that varies slowly in its transparent window as shown in Figure (1.4).

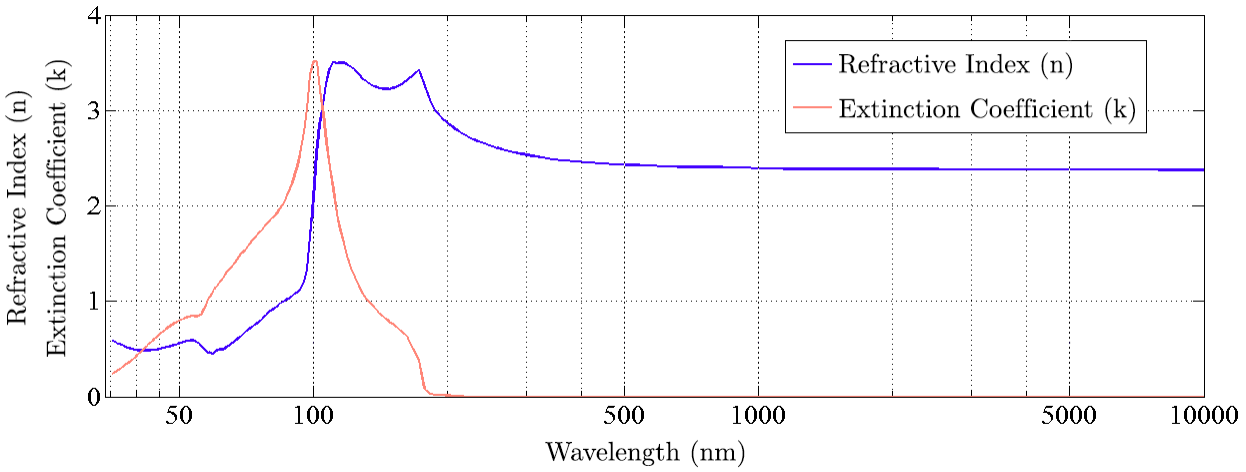

Figure 1.4: Dependence of the complex refractive index of diamond as a function of wavelength. It can be observed that the real part of the refractive index remains fairly constant at $\sim$ 2.44 from the visible to the far infrared, where the complex absorptive part goes to zero. In comparison water has a real part of the refractive index of $\sim$1.33 and fused quartz has a refractive index of $\sim$1.46 [34].

Recent advancements in diamond synthesis now provides us with dramatically improved diamond samples with specified properties of our choosing. These new techniques not only give the science community the possibility of tuning the characteristics of the diamond, but now diamonds can be grown with a wide variety of desirable defects. For instance, by choosing specific defects one can affect the diamonds hardness or change its electrical conductivity. More specifically, some of the defects in the crystal structure can produce a system with its own optically accessible energy level structure separate to that of the diamond matrix, which is called a colour centre or optical defect. Many atomic inclusion

impurities are known to form colour centres in diamond with a variety of different inclusion structures [35–38]. In fact, diamond has been found to contain over 500 optically active defects over the range of 170 nm to 10 µm [36].

Of all of the optical defects found in diamond, by far the most intensively studied is the Nitrogen Vacancy (NV) centre presented in Figure (1.5)[†]. The NV centre possesses interesting optical properties and has become prominent in at least three fields of research: high-resolution magnetometry, biomedicine, and quantum information technology. The internal energy structure of the NV centre is shown in Figure (1.5).

The most explored and useful property of the NV centre is its fluorescence, which can be easily detected from individual centres. The NV centre can exist in two separate charge states depending on the presence of an extra external electron. The neutral charge state (NV^0) emits fluorescence at a characteristic zero phonon line (ZPL) wavelength of 575nm whereas the negative charge state (NV^-) emits fluorescence at 637nm. It is only the NV^- centre however, that exhibits interesting spin optical properties that can be spin polarised and observed at room temperature. As a result, the NV^0 charge state is often neglected by exciting with a wavelength that favours the fluorescence of NV^-. It is typically only the NV^- centre that is referred to when mentioning the NV centre as a whole.

NV centres have found promising applications in detecting single spins and weak magnetic fields. The external magnetic fields acting on a single NV centre can measurably alter the fluorescence. The detection of the modified fluorescence of the NV can be used to probe the surrounding fields. This technique has even enabled the detection of electron spins and nuclear spins in ambient conditions [39, 40]. NV centres for high resolution magnetometry have been used in encouraging applications for the read out of single spin based magnetic memories and for high-resolution imaging techniques [41–44].

Recently, research into NV centres in diamond for biological and medical purposes has been quite active. Nano-diamonds containing fluorescent centres have several important properties in this field. They are bio-compatible and non-toxic due to their inert carbon

[†]There are in fact at least four other optical defects made up of nitrogen impurities and vacancies in the diamond crystal lattice, however it is the VN_1 crystalographic defect that is being referred to as the NV centre and more often than not it is only the negative charged state of the VN^1 defect that is referred to as the NV centre.

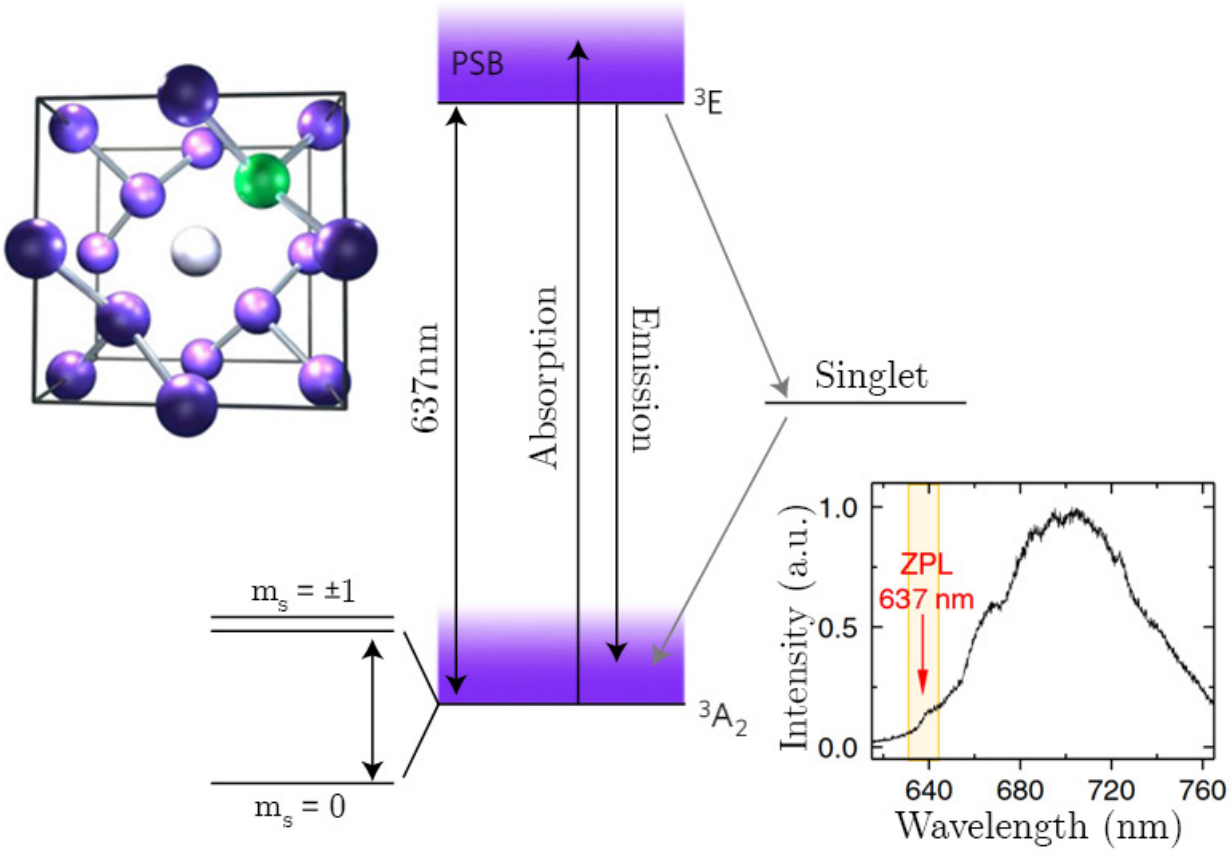

Figure 1.5: Physical and energy level structure of the NV centre with its associated fluorescence spectra. Top left is the unit cell structure of the NV centre in the diamond matrix. The carbon atoms are shown in purple, the lattice vacancy in white and substitutional nitrogen atom indicated in green connected together by the associated covalent bonds. In the centre of the image is the level scheme of the NV^- centre displaying the typical optical and non radiative transitions. Bottom right is an example of the NV^- centre room temperature fluorescence signal. The NV^- shows a strong stable zero phonon line (ZPL) around 637nm followed by wide a broad phonon side band (PSB) emitting fluorescence out past 765 nm. For a more detailed understanding of the NV centre, its charge states and its internal spin structure refer to Chapter 4.

structure. They can be excited by a laser through tissue and the resulting emission from the defect can also penetrate tissues. As a result, fluorescent nano-diamonds are being extensively used as new types of probes for bio-labelling and as drug delivery vehicles [45–48].

NV defects in diamond are also being investigated for their implementation of solid state quantum technologies. One avenue is to use NV centres in diamond as addressable and easy to manipulate quantum states (qubits), even in room temperature conditions [49]. There

are several properties that make NV centres an excellent candidate for use in quantum information. Firstly, a single emitter shows a large dipole transition moment between the ground and excited state providing a strong optical interaction strength. In addition, the spin state of the NV centre can be optically initialised, coherently manipulated and read out with optical and microwave excitation resulting in long coherence lifetimes even at room temperature [50–53].

As a consequence, levitating optical defects such as the NV centre is especially exciting as information can be encoded into the vibrations and spin structure within the diamonds, which can be extracted using the light they emit. This mechanism is aimed to be used in a ground state opto-mechanical system for studying macroscopic quantum mechanics and for creating hybrid quantum systems. Recently photo-luminescence from optically levitated nano-diamonds containing NV centres has been observed, showing a reduction in fluorescence for increased trapping laser powers [54–56]. The reduction or quenching of fluorescence has not previously been explained in this regime. In this thesis I investigate this quenching mechanism and examine the limitations this mechanism has on the feasibility of utilising levitated NV centres for quantum-opto-mechanical applications. Nevertheless our approach to using NV centres in this thesis differs to these approaches since we are not interested in their optical spin properties. Instead, we would like to use the NV centre as an ideal two level atom in order to apply an additional force on a levitated nano-diamond as a whole. Using the atomic structure of the colour centres in the diamond matrix allows us to observe resonant optical dipole forces that are both repulsive and attractive depending on the resonant detuning, analogous with the resonant dipole force in atom trapping. By dominating the force with the resonant optical dipole forces we aim to create an optically levitated nano-particle that behaves like a giant atom. In this regime we can apply a number of well developed cooling strategies that have been developed for atoms and apply them to the more massive levitated nano-particle. This will be a particularly exciting step since we would control a highly isolated massive mechanical oscillator that can be cooled towards its quantum ground state and manipulated through a strong resonant optical dipole force. As such, we will have developed a platform with all of the key ingredients for performing quantum opto-mechanical applications and protocols with unprecedented superposition sizes.

1.3 Quantum Opto-Mechanics

The motivations behind the huge interest in developing quantum opto-mechanical systems are varied. On a technological level, these systems are pushing the limits of high precision sensing for the detection of small forces, displacements, masses and accelerations which when packaged appropriately provide sought-after commercial applications. On a more fundamental level, quantum opto-mechanics focuses on manipulating and detecting of the mechanical motion in the quantum regime using light, thereby allowing for the generation non-classical states of the mechanical oscillator [57–59]. As such, these devices offer a promising approach for further scientific developments, such as for developing a hybrid quantum information processing system linking incompatible quantum systems together and preserving their quantum coherence. They also allow for more fundamental tests of quantum mechanics, such as probing quantum gravity and collapse theories in a parameter space of size and mass that remains challenging to access.

In any case, these systems rely on the generation of mechanical quantum coherence states. Generating these states requires three key ingredients: good coherence which requires good isolation, strong non-linearities, and efficient cooling mechanisms to bring the mechanical motion into its quantum ground state. Recent experimental achievements in this field include ground state cooling [59], producing light matter entangled states [60] and observation of single photon phonon correlations [61]. Many designs for quantum opto-mechancal experiments at many mass scales have been developed as shown in Figure (1.6). However, in all of these and many other systems, with the exception of cold atoms, the mechanical oscillator is physically clamped to a substrate or support resulting in an unavoidable coupling to a thermal reservoir. Fluctuations in the thermal reservoir place limitations on the opto-mechanical sensitivity and add decoherence, leading to a faster collapse of the targeted quantum states. In order to maintain a long quantum ground state lifetime it is thus ideal to minimise the effect of the thermal reservoir and as a result these systems require cryogenic cooling.

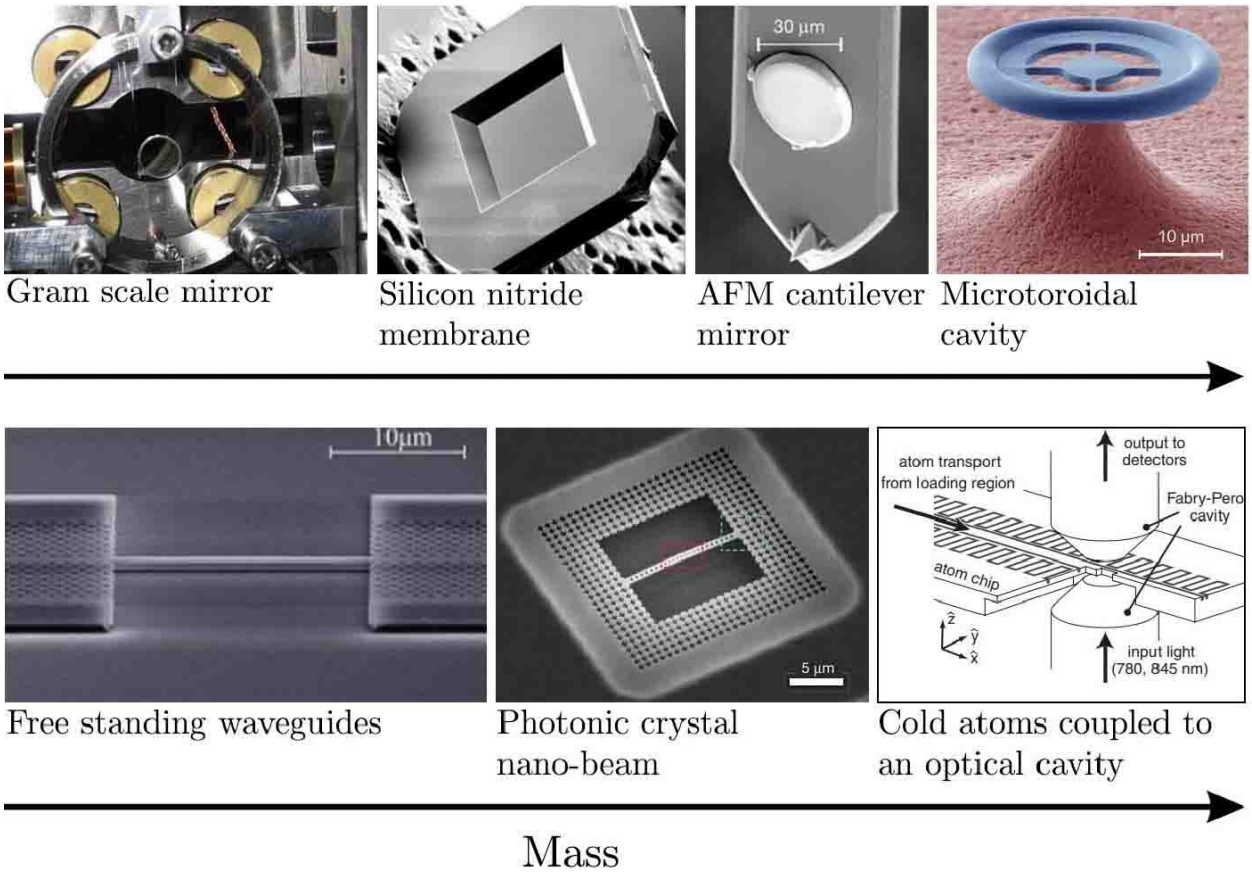

Figure 1.6: A variety of opto-mechanical experiments arranged according to mass [59, 62–67].

In this context, optical levitation completely eliminates the need for any material supports allowing for much higher thermal isolation as shown in Figure (1.7). In this regime the motion is extremely well isolated from the environment because not only is the object mechanically isolated by levitation in ultra-high vacuum, but the motion is also naturally decoupled from the internal thermal degrees of freedom due to their vastly different energy scales. With mechanical Q-factors of optically levitated systems reaching 10^{11} this is a clear advantage for maintaining quantum coherence of the mechanical resonator [68]. In this regime the limiting factor of thermalisation and decoherence is the momentum recoil of the scattered photons which is strongly dependent on trapping laser intensity [69]. Whilst optical levitation systems offer a clear advantage over current cryogenically cooled systems in maintaining any quantum coherence generated, cooling to and manipulating the quantum ground state is technologically challenging due to the weak interaction between the dielectric particle and the optical field.

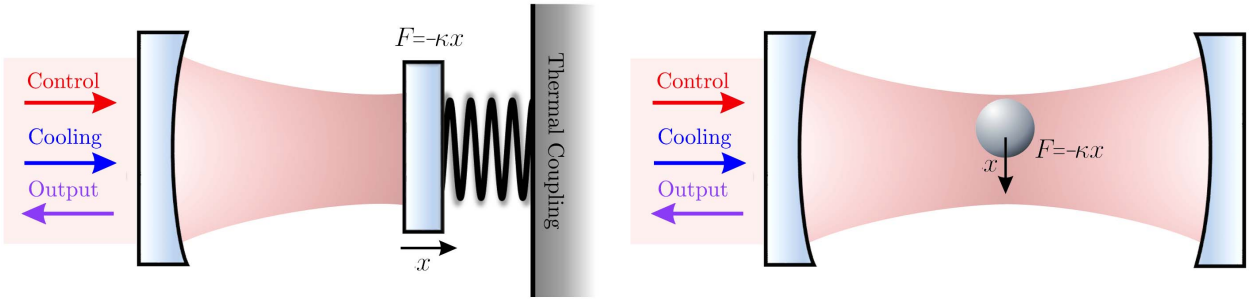

Figure 1.7: Comparing schematics of a generic opto-mechanical experiment with an opto-mechanical experiment based on levitated nano-particles. In typical opto-mechanical experiments the oscillator is physically connected to the environment and must be cryogenically cooled to remove heating from thermal coupling to the environment. In an experiment based on levitated particles there is no physical connection between the oscillator and the environment and the particle can be cooled towards the quantum ground state even in a room temperature environment. Indeed the particles internal temperature may be quite hot, however since it is decoupled from the centre of mass temperature of the particle, it will not affect the oscillatory quantum mechanical modes of the system.

Introducing optically resonant dipole forces from optical defects in levitated nano-diamonds as shown in Figure (1.8) is expected to enhance the control we have over the particle and benefit all of the quantum opto-mechanical applications. These resonant optical forces will enable us to use a multitude of cooling and state generation techniques borrowed from atom trapping and apply them to the more massive nano-particle. In addition, the increased forces on the NV centres will allow trapping of nano-diamonds with significantly lower trapping powers which will reduce many detrimental effects such as the heating of the nano-diamond itself and reducing shot noise heating once in the ground state. This approach can be further extended by including other optical defects into the diamond lattice in order to create new and unprecedented hybrid quantum systems.

> 'All you really need to know for the moment is that the universe is a lot more complicated than you might think, even if you start from a position of thinking it's pretty damn complicated in the first place.'
>
> – Douglas Adams, Hitchhiker's Guide to the Galaxy, Mostly Harmless

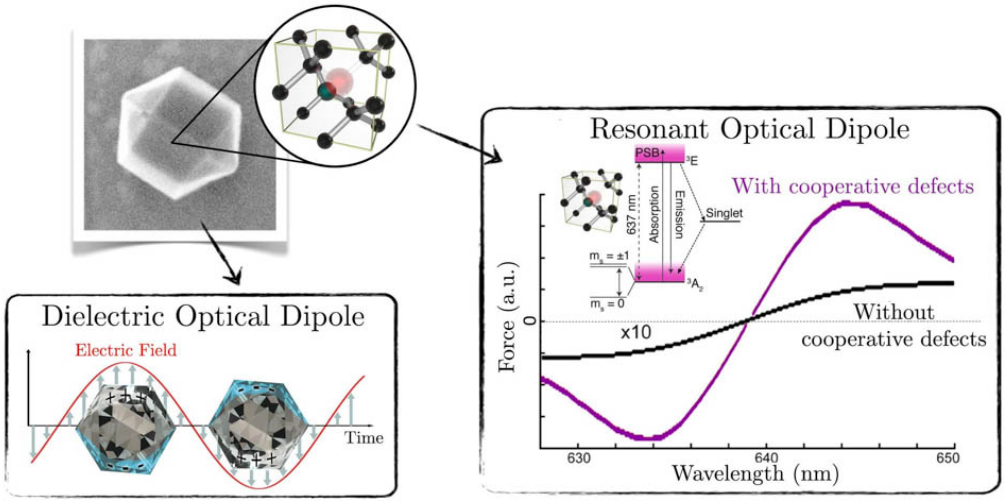

Figure 1.8: Optical levitation with optically enhanced resonant dipole forces. The optical dipole force in a focused gaussian beam trap is dependant only on the incident beam power and the polarisability of the object. My aim is to levitate a dielectric particle with embedded optical defects, thus not only will the particle experience a force due to the delectric optical dipole force but it will also experience a resonant dipole force on the collection of embedded optical defects. This force will provide both an attractive and repulsive force conditional on the detuning of the trapping laser field.

'Alice: How long is forever?

White Rabbit: Sometimes, just one second.'

–Lewis Carol

2

Optical Trapping

The idea that sparked off this project was to generate wavelength dependent resonant optical dipole forces in a dielectric particle such that it behaves like a giant atom. The concept was to use well developed techniques from cold atom physics on a collection of embedded optical transitions within a dielectric nano-particle in order to cool the massive dielectric particle toward the ground state. This chapter provides a comprehensive review of the origin of optical trapping forces, for both atoms and dielectric particles. In particular, I show a comparison between the two optical trapping regimes and emphasise the resonant mechanisms in atom trapping that allow for enhanced manipulation techniques, providing cooling to the quantum ground state.

I begin this chapter by exploring the general concept of optical trapping in order to provide an intuitive understanding of the underlying mechanisms for all types of optical trapping. I present the general expression of the radiative forces that are valid for both

atoms and dielectric particles, showing that the forces are dependent on both the beam profile and the polarisability of the trapped object. I describe how manipulating the trapping beam profile can enhance the sensing capabilities of the levitated nano-particle and present a technique using focused Bessel Gaussian beams to achieve this. I then focus on describing the gradient and scattering forces that result from the polarisability of dielectric particles and then similarly, for atoms.

I then discuss the various techniques for laser cooling for both atoms and dielectric particles. For atom trapping I show how most of the cooling strategies arise from the resonance of the polarisability with a particular emphasis on Doppler cooling. Finally, I discuss the current cooling strategies for a dielectric particle and the possibility of harnessing optical transitions in such objects to enable Doppler cooling of the more massive dielectric objects.

2.1 General Description

Optical traps are capable of controlling and manipulating particles using incident light fields. Optical trapping requires a balance between two forces: the scattering force and the gradient force. The scattering force pushes the particle along the propagation direction of the light, whereas the gradient force pulls the particles along the gradient of the light field, usually towards the region of highest field intensity. Generally to produce a stably trapped particle, the gradient force must overcome the scattering force and the particle will be trapped in the focus of the light field [70]. In most implementations, to obtain gradient fields strong enough to enable consistent trapping and overcome the scattering force, a Gaussian laser beam is tightly focused down to a diffraction limited spot in order to create rapid beam divergence. Optical traps of this kind are known as a single beam trap or optical tweezer [71].

For optical trapping and manipulation in aqueous media, near infra-red lasers such as Nd:YAG ($\lambda = 1064\,\mathrm{nm}$) and Nd:YLF ($\lambda = 1047\,\mathrm{nm}$) are the most commonly used. These lasers are chosen for three reasons. Firstly, the wavelength is short enough to avoid absorption in water which peaks at $3\,\mu\mathrm{m}$. Secondly, optical tweezers are often used for biological applications where many organic tissues have a transparency window in the near infrared

region. Finally, laser systems of these types are readily available with extremely high power and stability.

In addition the index of refraction of the particle to be trapped plays an important role in the dynamics of the optically trapped particle. When the refractive index of the particle is a higher refractive index than the surrounding medium, the particle is drawn towards the region of highest intensity. Conversely, if the particles index is lower than the surrounding medium, the reverse occurs and the particle will be pushed away from the highest intensity regions.

2.2 Ray Optics Regime

Trapping was initially performed on particles much larger than the wavelength of light. In this regime, optical traps can be qualitatively understood in terms of geometrical ray optics which can provide an intuitive understanding of how the particle will behave in a tightly focused beam. Figure (2.1) shows the force vectors arising from a Gaussian light beam incident on a particle with a refractive index (n_p) higher than the surrounding medium (n_m).

In Figure (2.1a) the focused laser beam refracts off the boundary of the spherical particle. Due to conservation of momentum, the total refraction off the particle imparts a momentum shift $\Delta\rho$ and hence a force on the particle. Since the particle is sitting in the centre of the Gaussian beam, symmetry cancels the transverse components and the net force on the particle is backwards towards the focus. In Figure (2.1b) if the particle is displaced transversally on the beam axis then the rays entering the particle have uneven amplitudes. In this case the forces due to refraction are uneven and there is a net restoring force towards the centre of the trap. The scattering forces on the particle are caused by momentum transfer due to the reflection components of the rays entering and exiting the particle that are absent in Figure (2.1). When the particle is placed symmetrically in the beam, the scattering force pushes the particle only in the direction of propagation, whereas if the particle is displaced transversally on the beam axis then the scattering force has a component in the direction away from the beam centre. It is clear that to optically trap the particles we want to maximise the gradient force and minimise the scattering forces.

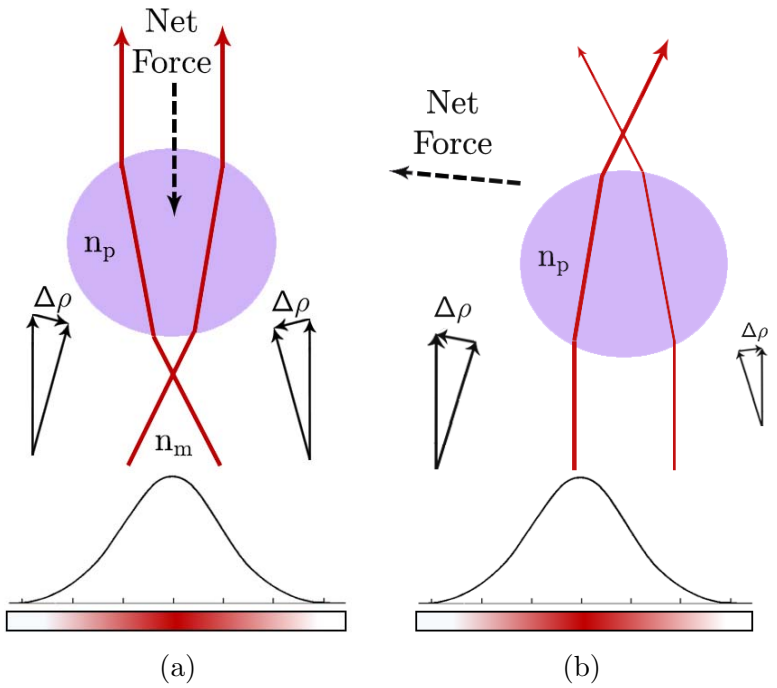

Figure 2.1: Forces on a particle due to a Gaussian light beam. **(a)** The focused laser beam refracts off the boundary of the spherical particle. The total refraction off the particle imparts a momentum shift ΔP and hence a force on the particle. Due to the particle sitting in the centre of the Gaussian beam symmetry cancels the transverse components and the net force on the particle is backwards towards the focus. **(b)** If the particle is displaced transversally on the beam axis then the rays entering the particle have uneven amplitudes. In this case the forces due to refraction are uneven and hence there is a net restoring force towards the the highest intensity region. In this geometry there is a slight component in the direction of propagation since the incident beam is collimated. The combination of a displaced particle and a focused beam will provide a net force, due to refraction towards the centre of the trap. The scattering forces on the particle are caused by momentum transfer due to the reflection components of the rays entering and exiting the particle that are absent in this figure.

In order to calculate the forces on the trapped object the trapping beam can be split up into a number N of representative rays with powers P and incident angles θ. By considering the forces due to the Fresnel reflections and transmissions of each ray, the total force can be calculated using a summation of the forces due to each ray.

$$F_{scat} = \sum_{i}^{N} \frac{n_m \cdot P_i}{c} \left(1 + R_i \cos(2\theta_{R_i}) - \frac{T_i^2(\cos(2\theta_{R_i} - 2\theta_{T_i}) + R_i \cos(2\theta_{R_i}))}{1 + R_i^2 + 2R_i \cos(2\theta_{T_i})} \right) \tag{2.1}$$

$$F_{grad} = \sum_{i}^{N} \frac{n_m \cdot P_i}{c} \left(1 + R_i \sin(2\theta_{R_i}) - \frac{T_i^2(sin(2\theta_{R_i} - 2\theta_{T_i}) + R_i \cos(2\theta_{R_i}))}{1 + R_i^2 + 2R_i \cos(2\theta_{T_i})} \right), \tag{2.2}$$

where R and T are the Fresnel reflection and transmission coefficients of the surface at the reflection and transmission angles θ_R and θ_T of the incident rays. The forces are polarisation dependent as the Fresnel coefficients are different for rays polarised perpendicularly or parallel to the plane of incidence. This regime gives an understanding of particle trapping, however it is only valid where the particle radius a is much larger than the wavelength ($a \gg \lambda$). Moreover for most optical traps, and those considered in this thesis, the particles are much smaller than the wavelength; hence, to accurately calculate the forces on the particles we must consider the induced dipole regime.

2.3 Rayleigh Regime

In this section I begin with a brief description of how a laser beam both induces a dipole in an object and how the interaction of this induced dipole with the incident field can generate a trapping force. Following this, I will more formally explain the theory of the forces on both atoms and dielectric nano-particles.

For an object in a focused laser beam, the electrons react to the electric field due to the Lorentz force, $F = qE$, where the force F is equal to the charge q multiplied by the strength of the electric field E. This displaces the electron cloud within the object by a small distance creating an oscillating induced dipole. The relative tendency for any object to have its charges displaced by an external electric field is given by its polarisability α.

This induced dipole will now experience a scattering force in the direction of light propagation as well as a gradient force if it is subject to a non uniform electric field. The gradient force arises due to one charge of the dipole experiencing a stronger electric field and therefore stronger force than the other separated charge. Since a dipole will move to the maximum of an electric field gradient, the object will be pushed along the gradient of the electric field towards the centre of the tightly focused laser beam. You can also see the effects of the gradient force in terms of energy. For a dipole in an external electric field, the induced dipole is anti-aligned with the incident field. Thus, the coupling energy between the induced dipole and the field is negative, and therefore the induced dipole will want to move towards the highest field region where the coupling energy is minimised.

From this description we can observe that the forces on an object in an optical trap are reliant on two main properties, the gradient of the electric field created by the focused laser beam profile and the strength of the induced dipole within the trapped object given by its polarisability. The following sections provide a rigorous derivation of both radiation pressure forces, gradient and scattering, that arise from these two considerations. I begin with the general expression of the radiative forces that is valid for both atoms and dielectric particles. I follow this with an extended discussion on manipulating the optical trapping profile in order to provide interesting potential well geometries. Subsequently, I discuss the features of the polarisability of dielectric particles and then atoms, highlighting the differences between the two. I finally conclude with a discussion on the laser cooling strategies that are applicable in each regime.

2.3.1 General Expression of the Radiative Forces

To derive the motion of an object within an optical trap we must look at the radiation forces on the induced dipole. This description is independent on whether the dipole arises from an atomic transition or from a dielectric medium, relying only on the polarisability of the object. The time averaged optical force $\boldsymbol{F}$ acting on the expectation value of the dipole moment of the object $\langle \hat{\boldsymbol{D}}_\epsilon \rangle$ at position $\boldsymbol{r}_0$ in an electric field $\boldsymbol{E}$ is then [72],

$$\boldsymbol{F} = \overline{\langle \hat{\boldsymbol{D}}_\epsilon \rangle \nabla \boldsymbol{E}(\boldsymbol{r}, t)_{\boldsymbol{r_0}}}. \tag{2.3}$$

The object undergoes forced oscillations at the frequency ω of the field, and hence we can write,

$$\langle \hat{\boldsymbol{D}}_\epsilon \rangle = \epsilon_0 \alpha \boldsymbol{E}(\boldsymbol{r}, t) \tag{2.4}$$

where α is the polarisability of the object. The polarisability is a complex number,

$$\alpha = \alpha' + i\alpha'' \tag{2.5}$$

which depends on the wavelength and the field amplitude, and has the dimensions of length cubed.

We now assume that the internal state of the object reaches a steady state at a point $\boldsymbol{r}_0$ under the effect of the field,

$$\boldsymbol{E}(\boldsymbol{r},t) = \mathcal{E}(\boldsymbol{r},t) + \mathcal{E}^*(\boldsymbol{r},t), \tag{2.6}$$

where the electric field vector is given by,

$$\mathcal{E}(\boldsymbol{r},t) = \hat{\boldsymbol{x}}\frac{E_0(\boldsymbol{r})}{2}e^{i\phi(\boldsymbol{r})}e^{-i\omega t}, \tag{2.7}$$

where $\hat{\boldsymbol{x}}$ is the unit vector in the polarisation direction, E_0 is the electric field strength, ω is the trapping frequency and $\phi(\boldsymbol{r})$ is the phase at position $\boldsymbol{r}$.

And now substituting Equation (2.4) into (2.3), we obtain four force terms,

$$\begin{aligned}\boldsymbol{F}(\boldsymbol{r}) = {} & \epsilon_0\alpha\overline{\mathcal{E}\nabla\mathcal{E}_{\boldsymbol{r}_0}} + \epsilon_0\alpha^*\overline{\mathcal{E}^*\nabla\mathcal{E}^*_{\boldsymbol{r}_0}} \\ & + \epsilon_0\alpha\overline{\mathcal{E}\nabla\mathcal{E}^*_{\boldsymbol{r}_0}} + \epsilon_0\alpha^*\overline{\mathcal{E}^*\nabla\mathcal{E}_{\boldsymbol{r}_0}}.\end{aligned} \tag{2.8}$$

The two first terms oscillate at 2ω and give rise to no effects when averaged over time. The two remaining terms do not oscillate at all and thus give rise to a force [72].

$$\boldsymbol{F}(\boldsymbol{r}) = \epsilon_0\alpha'\nabla\frac{|E_0(\boldsymbol{r})|^2}{4} - \epsilon_0\alpha''\frac{E_0^2(\boldsymbol{r})}{2}\nabla\phi(\boldsymbol{r}). \tag{2.9}$$

The radiative force thus comprises two contributions. The first of these relates to the real part α' of the polarisability and depends on the gradient field of the electromagnetic wave. This corresponds to the dipole force, also known as the gradient force. The other contribution relates to the imaginary part α'' of the polarisability and depends on the gradient of the phase of the wave. This force corresponds to the resonant scattering force or resonance radiation pressure force which is related to the absorption of the photons.

2.3.2 Gradient Force

The first term in Equation (2.9), called the gradient force is given by,

$$\boldsymbol{F}_{grad}(\boldsymbol{r}) = \epsilon_0 \alpha' \nabla \frac{|E_0(\boldsymbol{r})|^2}{4}, \tag{2.10}$$

which depends only on the real part of the polarisability α' and the gradient of the electric field amplitude squared $|E_0(\boldsymbol{r})|^2$.

To relate the gradient force as a function of the beam intensity we must use the time dependent Poynting vector $\boldsymbol{S}(\boldsymbol{r}, t)$, which describes the instantaneous energy flux crossing a unit area per unit time and is given by,

$$\boldsymbol{S}(\boldsymbol{r}, t) \equiv \mathcal{E}(\boldsymbol{r}, t) \times \boldsymbol{H}(\boldsymbol{r}, t), \tag{2.11}$$

where the associated magnetic field vector under this approximation is given by,

$$\boldsymbol{H}(\boldsymbol{r}, t) = \hat{\boldsymbol{z}} \times \frac{\mathcal{E}(\boldsymbol{r}, t)}{Z_0} \simeq \hat{\boldsymbol{y}} n_m \epsilon_0 c E_0(\boldsymbol{r}, t) = \hat{\boldsymbol{y}} H(\boldsymbol{r}, t), \tag{2.12}$$

with, $Z_0 = \sqrt{\mu_m/\epsilon_m} \simeq 1/(n_m \epsilon_0 c)$ is the intrinsic impedance of the medium, $c = 1/\sqrt{\epsilon_0 \mu_0}$ is the speed of light and ϵ_0 and μ_0 are the vacuum permittivity and permeability, respectively.

The beam intensity $I(\boldsymbol{r})$, defined as the time-averaged version of the Poynting vector is then given by,

$$\begin{aligned} I(\boldsymbol{r}) &\equiv \overline{\langle \boldsymbol{S}(\boldsymbol{r}, t) \rangle} \\ &= \frac{n_m \epsilon_0 c}{2} |E_0(\boldsymbol{r})|^2. \end{aligned} \tag{2.13}$$

Now by combining Equation (2.13) with Equation (2.10) we can see how this force is dependent on the gradient of the intensity of the trapping beam,

$$\boldsymbol{F}_{grad}(\boldsymbol{r}) = \frac{\alpha'}{n_m c} \nabla \frac{I(\boldsymbol{r})}{2}. \tag{2.14}$$

Since this force depends on the gradient of the beam intensity, the beam profile is thus very

important to determine the optical trapping behaviour. As an example, we will consider the conventional beam profile used in optical tweezers and the profile predominately but not exclusively used in this thesis, the Gaussian beam profile as shown in Figure (2.2).

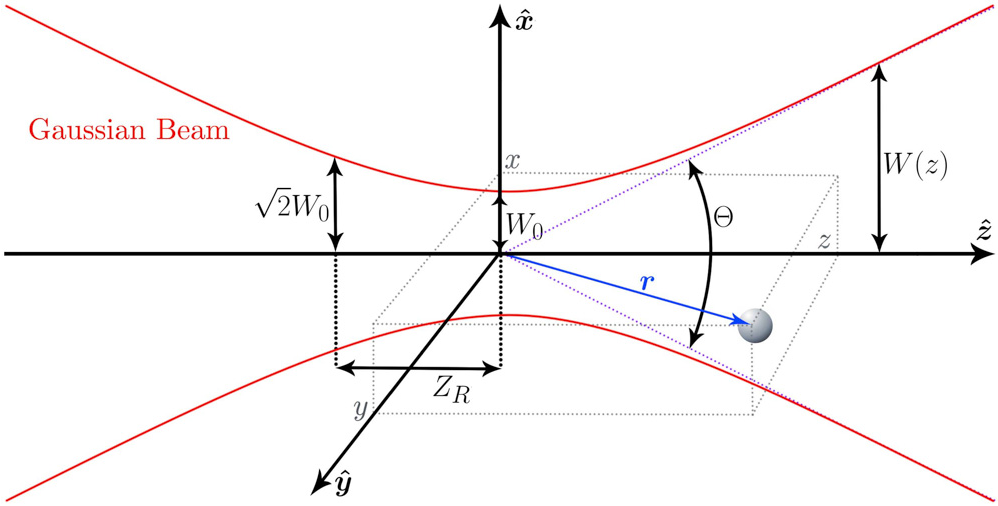

Figure 2.2: Geometry of a particle of radius a at a position $\boldsymbol{r} = (x, y, z)$ in a Gaussian beam with a beam waist W_0, Rayleigh range Z_R and total angular divergence Θ.

Using a paraxial Gaussian beam description with linear polarisation, the electric-field vector at the position $\boldsymbol{r}$ in terms of complex amplitude $\mathcal{E}(\boldsymbol{r}, t)$ is given by [73]

$$\begin{aligned}\mathcal{E}(\boldsymbol{r},t) &= \hat{\boldsymbol{x}}\frac{1}{2}\sqrt{\frac{4P}{\pi W_0^2 n_m \epsilon_0 c}}\frac{ikW_0^2}{ikW_0^2+2z}\exp\left[-\frac{(kW_0)^2(x^2+y^2)}{(kW_0^2)^2+(2z)^2}\right]e^{-ikz} \\ &\quad \times \exp\left[-i\frac{2kz(x^2+y^2)}{(kW_0^2)^2+(2z)^2}\right]e^{-i\omega t} \\ &= \hat{\boldsymbol{x}}\frac{E_0(\boldsymbol{r})}{2}e^{i\phi(\boldsymbol{r})}e^{-i\omega t}. \end{aligned} \tag{2.15}$$

where $\hat{\boldsymbol{x}}$ is the unit vector in the polarisation direction, P is the beam power given by $P = \pi W_0^2 n_m \epsilon_0 c E_0^2/4$, W_0 is the beam width, ω is the trapping frequency and k is the wave number in the medium given by $k = n_m\omega/c$. It follows that the Gaussian beam intensity is then given by,

$$I(\boldsymbol{r}) = \left(\frac{2P}{\pi W_0^2}\right)\frac{1}{1+(2\tilde{z})^2}\exp\left[-\frac{2(\tilde{x}^2+\tilde{y}^2)}{1+(2\tilde{z})^2}\right]. \tag{2.16}$$

where, $\tilde{x}$, $\tilde{y}$ and $\tilde{z}$ are the normalised spacial co-ordinates given by,

$$(\tilde{x}, \tilde{y}, \tilde{z}) = (x/W_0, y/W_0, z/kW_0^2). \tag{2.17}$$

Now substituting Equation (2.16) into Equation (2.14) and differentiating, the gradient force can be expressed in terms of each of its three components*,

$$\boldsymbol{F}_{grad,x}(\boldsymbol{r}) = -\hat{\boldsymbol{x}}\alpha' \frac{4\tilde{x}/W_0}{1+(2\tilde{z})^2}\left(\frac{P}{\pi W_0^2}\right)\frac{1}{1+(2\tilde{z})^2}\exp\left[-\frac{2(\tilde{x}^2+\tilde{y}^2)}{1+(2\tilde{z})^2}\right] \tag{2.18}$$

$$\boldsymbol{F}_{grad,y}(\boldsymbol{r}) = -\hat{\boldsymbol{y}}\alpha' \frac{4\tilde{y}/W_0}{1+(2\tilde{z})^2}\left(\frac{P}{\pi W_0^2}\right)\frac{1}{1+(2\tilde{z})^2}\exp\left[-\frac{2(\tilde{x}^2+\tilde{y}^2)}{1+(2\tilde{z})^2}\right] \tag{2.19}$$

$$\begin{aligned}\boldsymbol{F}_{grad,z}(\boldsymbol{r}) = &-\hat{\boldsymbol{z}}\alpha' \frac{8\tilde{z}/(kW_0^2)}{1+(2\tilde{z})^2}\left[1-\frac{2(\tilde{x}^2+\tilde{y}^2)}{1+(2\tilde{z})^2}\right]\left(\frac{2P}{\pi W_0^2}\right)\\ &\times\frac{1}{1+(2\tilde{z})^2}\exp\left[-\frac{2(\tilde{x}^2+\tilde{y}^2)}{1+(2\tilde{z})^2}\right].\end{aligned} \tag{2.20}$$

The gradient force consists of three components acting as restoring forces directed towards the centre of the focused laser beam for all objects with positive real polarisablities. Additionally it can be observed that this restoring force increases linearly with beam power, which in fact, can be generalised for all beam shapes.

It should be noted that due to the paraxial approximation of Maxwell's equations being used in the description of the Gaussian beam, this derivation does not rigorously describe a highly focused beam where $s = \frac{\lambda}{2\pi W_0} \gg 0$. In this case, the equations do not account for the mixed field components of the electric and magnetic fields that are formed in tightly focused beams [74]. Barton and Alaxander [75] compared this derivation with a derivation that contained fifth-order corrections to the Gaussian beam description. According to their analysis the paraxial approximation solution contains average errors of $\sim 0.8\%$ for $s = 0.02$ and $\sim 4.4\%$ for $s = 0.1$. Consequently errors of these magnitudes are to be expected depending on the value of s. However, it should be noted that this description is used only in this section in order to obtain a stronger qualitative description of the resonant radiation forces in optical traps.

*Hidden by representing the force using normalised notation is the scaling of the force with beam waist. The scaling of the force with the beam waist is $\boldsymbol{F} \propto W_0^{-4}$ in the $\hat{\boldsymbol{x}}$ and $\hat{\boldsymbol{y}}$ coordinates but $\boldsymbol{F} \propto W_0^{-6}$ in the $\hat{\boldsymbol{z}}$ coordinate.

Trapping Frequency

For displacements small enough the trapping forces acting upon a particle sitting in the focus of an optical trap, can be approximated as a simple harmonic oscillator $F = -\kappa x$. The spring constant κ also known as the trap stiffness is then a direct measure of the optical restoring forces acting on the particle: a property that can be easily measured experimentally. The easiest method to determine the trap stiffness is to measure the variance in the Brownian motion of the trapped particle. The energy J, stored in the spring is equal to half the spring constant κ times the variance in motion $\langle x^2 \rangle$,

$$J = \frac{1}{2}\kappa\langle x^2 \rangle. \tag{2.21}$$

By the equipartition theorem, the energy in the Brownian motion of the trapped particle is equal to $\frac{1}{2}k_BT$. By setting these two energies equal and solving for the stiffness yields:

$$\kappa = \frac{k_BT}{\langle x^2 \rangle}. \tag{2.22}$$

Calculation of the variance in the position is straightforward, however it requires an accurately calibrated position detector. A more useful method of measuring the trapping stiffness involves measuring the frequency spectrum of the Brownian noise exhibited by the particle. The mass of the particle is so small that inertial forces are much weaker than those of hydrodynamic drag. In this case, the motion of the object is that of a massless, damped oscillator driven by Brownian motion,

$$\beta\dot{x}(t) + \kappa x(t) = F(t), \tag{2.23}$$

where, $\beta = 6\pi\nu a$ is the drag coefficient of the particle, ν is the dynamic viscosity of the surrounding fluid, a is the radius of the particle and $F(t)$ is the force arising from Brownian noise. The frequency spectrum of the Brownian noise source, $\tilde{F}(f)$, is modelled as a Wiener process which has zero mean and is essentially constant in amplitude,

$$|\tilde{F}(f)|^2 = 4\beta k_BT. \tag{2.24}$$

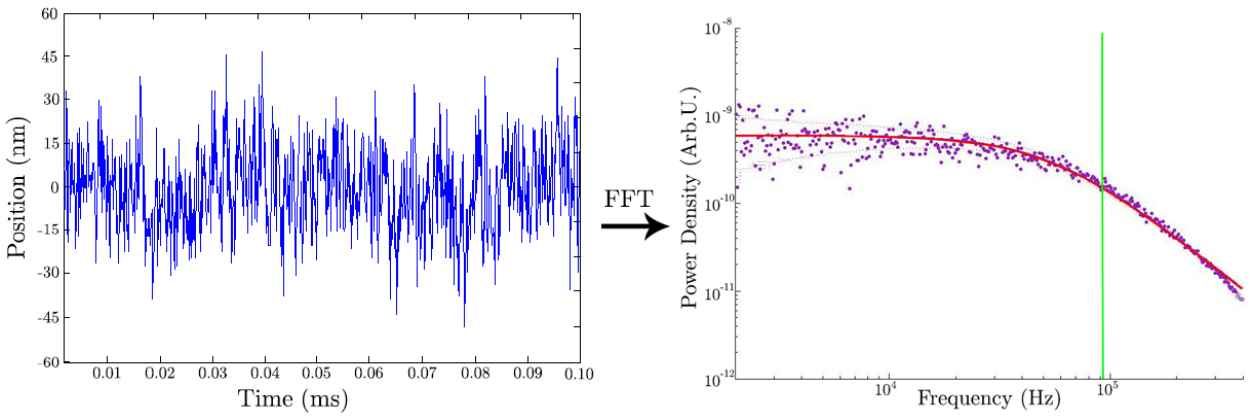

Figure 2.3: Measurement of the position and characteristic trap frequency of a particle trapped in the over-damped regime. By performing a fast Fourier transform (FFT) on the position signal of the particle we obtain the power spectrum of the particle. In the over-damped regime the power spectrum is given by the Lorentzian function in Equation (2.26) shown in red. From the Lorentzian function we can extract the corner frequency of the particle shown in green which is a measure of the trapping stiffness using Equation (2.27) A more comprehensive discussion on how the corner frequency measurments are obtained can be found in Section (3.4.2).

The Fourier transform of Equation (2.23) is then,

$$2\pi\beta\left(\frac{\kappa}{2\pi\beta} - if\right)\tilde{x}(f) = \tilde{F}(f), \tag{2.25}$$

and the power spectrum is then given by,

$$|\tilde{x}(f)|^2 = \frac{k_B T}{\pi^2\beta\left[\left(\frac{\kappa}{2\pi\beta}\right)^2 + f^2\right]}. \tag{2.26}$$

Equation (2.26) is that of a Lorentzian with a corner frequency $f_c = \kappa/2\pi\beta$. Therefore the stiffness of the optical trap can be extracted from the measurement of the corner frequency by,

$$\kappa = 2\pi\beta f_c. \tag{2.27}$$

In an over damped optical trapping experiment we do not have access directly to the trapping stiffness κ. By measuring the displacement of the particle and applying a Fourier transform we obtain the power spectrum of the oscillation. By fitting the Lorentzian describing the

power spectrum shown in Equation (2.26) to the Fourier transform, we obtain the corner frequency f_c, which can then be related to the trap stiffness κ by using Equation (2.27) as shown in Figure (2.3).

2.3.3 Radiation Pressure Force

The radiation pressure force[†] is related to the absorption of photons by the object and is given by,

$$\boldsymbol{F}_{scat}(\boldsymbol{r}) = \epsilon_0 \alpha'' \frac{E_0^2(\boldsymbol{r})}{2} \nabla \phi(\boldsymbol{r}), \tag{2.28}$$

which depends only on the complex part of the polarisability α'' and the gradient of the phase of the electromagnetic phase $\phi(\boldsymbol{r})$. Taking the example of a travelling plane wave,

$$\mathcal{E}(\boldsymbol{r}, t) = \frac{E_0}{2} e^{i\boldsymbol{k}\cdot\boldsymbol{r}} e^{-i\omega t}, \tag{2.29}$$

with constant amplitude E_0 and wave-vector $\boldsymbol{k}$, where $|\boldsymbol{k}| = k = \omega/c$, the scattering force is given by,

$$\boldsymbol{F}_{scat} = \epsilon_0 \alpha'' \frac{E_0^2}{2} \nabla(\boldsymbol{k}\cdot\boldsymbol{r}) = \epsilon_0 \alpha'' \frac{E_0^2}{2} \boldsymbol{k} = \frac{\alpha''}{n_m c} \frac{I(\boldsymbol{r})}{2} \boldsymbol{k}. \tag{2.30}$$

The force lies along the direction of propagation $\boldsymbol{k}$ of the wave, increasing linearly with the imaginary part of polarisability and laser intensity.

In a weakly focused Gaussian beam where the local field acting on the object can be approximated as plane waves, the scattering force is obtained by substituting Equation (2.16) into Equation (2.30):

$$\boldsymbol{F}_{scat} = \frac{\alpha''}{n_m c} \left(\frac{P}{\pi W_0^2} \right) \frac{1}{1 + (2\tilde{z})^2} \exp\left[-\frac{2(\tilde{x}^2 + \tilde{y}^2)}{1 + (2\tilde{z})^2} \right] \boldsymbol{k}. \tag{2.31}$$

Unfortunately, obtaining an accurate description of the scattering force in optical traps is difficult since the trapping beam is a tightly focused beam and the Gaussian beam phase profile is much more complicated than a plane wave. To model the scattering forces of

[†]The radiation pressure force is often simply called the scattering force, however for trapping of dielectric particles one needs to distinguish between a scattering force arising from absorption of photons and one that arises from Rayleigh scattering.

the beam near the focal region beyond the paraxial limit, an approach using Mie theory is necessary [76].

We have seen in the previous sections that there are now two main properties that strongly influence the forces within the optical trap. The first is the optical trapping profile and the second is the polarisability of the trapped particle. In this thesis we are mainly concerned with tailoring the polarisability of a dielectric particle to include the resonant properties that are observed in atoms; however for sensing applications, it is interesting to first begin a discussion on manipulation of the optical trapping profile.

2.4 Manipulation of Optical Trapping Profile

At the outset of this project we were interested in potential applications of optical levitation. Optically levitated nano-particles have the unique property that they are strongly isolated from any interaction with their environment: except for air particles and the trapping laser beams. Air particles act as a noise source as they randomly hit the levitated particle, as well as damping the motion of the harmonic oscillator. However, by trapping the particle inside a vacuum chamber and evacuating the air from the chamber, we can remove the detrimental effects of collisions between the particle and air molecules. In this way, the levitated particle is completely isolated from its environment, interacting only with the optical field and gravity. By having very good isolation from the environment and no collisions with air molecules, this kind of system presents very narrow motional resonances with frequencies typically in the kHz regime. Thus, if the particles motion can be coupled to an external force with the same frequency as the one provided by the optical trap, the motion of the particle will be amplified, producing an enhanced signal. As such, this kind of system has all the characteristics of a selective mechanical transducer.

The unique feature of optically levitated particles in vacuum compared with other standard acoustic sensors, such as Micro-electro-mechanical systems (MEMS), is that the mechanical motion of the levitated particle is almost perfectly decoupled from the environment as well as its internal temperature. The result is the possibility to cool its internal noise to the quantum regime without the need of using cryogenic fridges. The idea is to use the

optical trap to modulate the motion of the particle and bring to a stop, or as close to a stop as quantum mechanics allows. These features make a mechanical transducer or gravimeter based on optically levitated particles a potentially disruptive emerging technology, ensuring high gain and low intrinsic noise, whilst having the possibility of further enhanced measurements by using quantum sensing techniques.

Apart from the challenges of cooling the particle towards its ground state, which is an ultimate goal throughout this thesis, controlling the trapping frequency of the transducer is an also integral component to successful sensors. In traditional MEMS technologies it is difficult to tune the mechanical frequency of the oscillator, whereas for optically trapped particles the oscillator frequency can easily be tuned with laser intensity. The only issue is that to get to low frequencies you need to dramatically reduce the intensity, inevitably losing the particle if only a single focused Gaussian beam is used. As a result, I investigated tailoring the optical trapping potential to push towards lowering trapping frequencies down towards 0 Hz. Whilst the optical sensor can be used for frequency dependent acoustic sensing, as we bring the trapping frequency towards 0 Hz the transducer becomes highly sensitive to any continuous external force. For example in this regime, the sensor can be optimized as a gravimeter where the noise sensitivity is limited only by shot noise of the trapping lasers.

To reduce the trapping frequencies towards 0 Hz, I wanted an optical profile that has a strong gradient transversally to maintain the particle in the trap and have a weak gradient in the axial direction for low frequency mechanical resonances and hence measurement. In order to tailor the optical trapping profile we investigated the use of Bessel beams. A Bessel beam, is a beam whose amplitude is described by a Bessel function of the first kind as shown in Figure (2.4). A true Bessel beam has an optical profile with strong confinement in the radial direction and is non diffractive in the axial direction. The beam is also a self-healing beam, meaning that the beam can be partially obstructed at one point, but will reform at a point further down the beam axis.

Due to the non-diffractive nature of Bessel beams, when used for optically trapping they provide a strong gradient force in the radial direction and zero force in the axial direction. As a result, the trapped particle is free to move in only a single dimension, ideal for sensitive measurements of weak forces in this direction. However, ideal Bessel beams are not physical

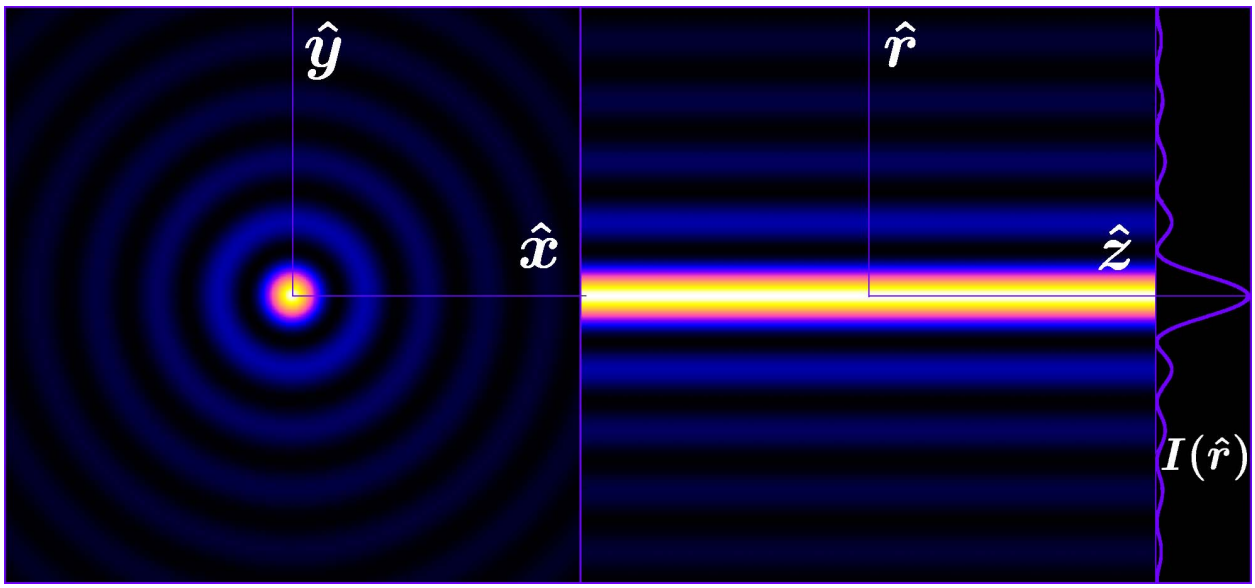

Figure 2.4: Bessel beam intensity profiles. Left panel is the radial intensity profile of a Bessel beam that remains unchanged over the entire propagation distance of the beam. The middle panel is the axial intensity profile of the beam showing the diffraction free propagation of the Bessel beam. The right panel is the intensity plot of the radial axis given by the zeroth order Bessel function.

as they must posses infinite energy across the beam. Instead, we can generate truncated Bessel beams or quasi-Bessel beams which are approximations of the Bessel beam, having the same properties as a Bessel beam over only a finite region. Quasi-Bessel beams can be generated with spatial light modulators (SLM), however SLM's can only be used at low power. To create Gaussian-Bessel beams with higher intensities we can use diffractive optics by illuminating a conical prism called an axicon with a Gaussian beam as shown in Figure (2.5).

The inherent structure of the Bessel beam consists of a central core and many concentric rings where the total power of the beam is equally distributed amongst the core and the outer rings, ($P_{core} = \frac{P_{total}}{N_{rings}}$) [77–79]. Producing a quasi-Bessel beam with a longer Bessel zone requires a wider beam and therefore a larger number of rings than a shorter Bessel beam. This relationship therefore presents a trade-off between central core intensity and Bessel beam length. In optical trapping we need sufficient power within the central core to maintain a stable trap, thereby setting a limit on the length of the Bessel zone.

Trapping particles in a long Bessel beam is technically challenging for two reasons. Firstly,

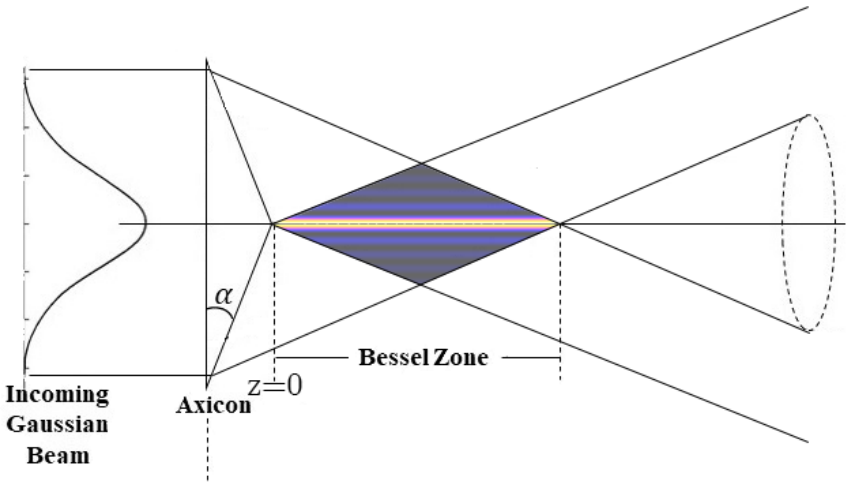

Figure 2.5: Generating a quasi-Bessel beam using an axicon. From left to right through axis z a collimated Gaussian beam incident on the axicon with axicon angle α generates a quasi-Bessel beam within the shaded region. Since the axicon is simply diffracting the incident Gaussian beam it is compatible with high intensity input powers.

since we have a slowly varying gradient in the axial direction the scattering force dominates over the gradient force thereby pushing the particle out of the trap. The second issue is that the beam power is distributed among a large number of rings and thus the central core intensity required for trapping is dramatically reduced. To solve the first challenge we require the use of two counter propagating Bessel beams to balance and cancel out the scattering forces. Removing the scattering forces on the particle leaves only the weak gradient force, providing the desired lower trapping frequencies. Introducing a second counter propagating beam creates a new challenge and that is to optimise the alignment of the two central cores in order to perfectly cancel out the scattering forces and hold the particle. If the two beams are not aligned along the entire Bessel beam propagation length the particle will not be confined within the optical trap. Due to the challenge of aligning the two counter propagating Bessel beams we anticipate the need of a single Gaussian beam optical trap to initially trap the nano-particles as shown in Figure (2.6). By initially trapping the particles in the single beam trap we can then align the quasi-Bessel beams and balance the counter propagating scattering forces. We can then slowly reduce the power of the single beam trap until the nano-particle is trapped by only the counter propagating quasi-Bessel beams. Without the single beam trap I anticipate the Beam alignment and balancing of scattering forces within

the quasi-Bessel beams to be practically infeasible.

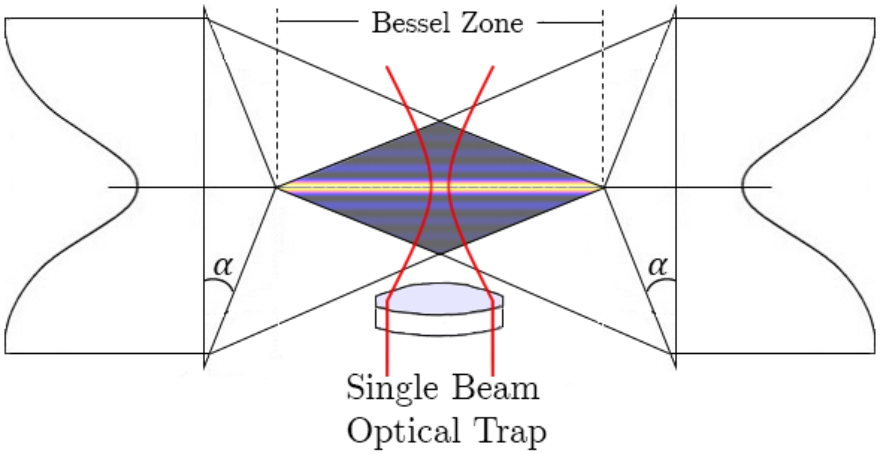

Figure 2.6: Experimental optical trapping design using counter propagating quasi-Bessel beams. The two counter propagating Bessel beams will generate a strong gradient of the intensity in the radial direction and slowly varying gradient in the axial direction. The two beams are essential to cancel out the scattering forces from each beam. An additional single beam optical trap is needed to initially trap the levitated nano-particle and align the counter propagating Bessel beams.

Unfortunately, the introduction of the single beam trap introduces geometrical constraints on the allowable separation of the two axicons generating the counter propagating Bessel beams. To efficiently cancel out the scattering forces the length of the generated Bessel zone needs to closely match the separation of the axicons. The minimum allowable Bessel length is then also fixed by the minimum allowable axicon separation. Looking at our current levitation experiments we can determine an allowable axicon separation distance. The smallest footprint lens I can currently optically levitate particles with is an $f = 3.1$ mm, 0.7 NA aspheric lens (C330TMD-B, Thorlabs). Using this lens for initially optical trapping the particles permits the separation distance between the two axicons to be approximately 14 mm[‡].

To determine a rough estimate of the input laser powers required to levitate particles in this experimental design we can compare the Bessel beam properties to the properties of our single beam Gaussian trap described in detail in Chapter 3. Our single beam optical trap

[‡]This approximation includes accounting for space needed for the optical mounts and ensuring that the single beam optical trap does not clip the quasi-Bessel beams. Interestingly, a long working distance lens does not offer significant improvement on the allowable space as these lenses require a larger physical footprint in order to create the required k-vectors.

can optically trap 100 nm nano-diamond particles with 50 mW and 170 nm silica particles with 25 mW of input laser power. The focal spot size of the trap is $W_0 \approx 1\,\mu m$ at 1064 nm. In order for the Bessel beam to trap in the axial direction it must have a similar gradient profile. From the geometry of the Bessel beam as seen in Figure (2.5) the number of rings N at the centre is given by,

$$N \approx \frac{Z_{max}}{2\Delta r}, \tag{2.32}$$

where, Δr is the spacing between Bessel rings, which is fixed for a given axicon angle, and Z_{max} is the length of the Bessel zone [80]. Now using an axicon producing a $Z_{max} = 11.2$ mm Bessel zone will have its maximum central core intensity displaced 7 mm from the axicon tip, ideal for two counter propagating beams with a 14 mm axicon separation[§]. In combination with a Bessel beam producing a central core diameter of $W_0 = 1\,\mu m$ obtained by setting $W_0 = 0.72\Delta r$, we must have a total of $N \approx 4000$ rings[♦]. Due to each ring containing identical laser power, the power in the central core is then,

$$P_{core} = \frac{P_{total}}{N}. \tag{2.33}$$

Thus a Bessel beam with these parameters requires at least $P_{total} = 200$ W and $P_{total} = 100$ W of input laser power to optically trap the 100 nm nano-diamond and 170 nm silica particles respectively in the radial direction. Currently these power constraints make this platform infeasible in its current design.

In order to reduce the required laser power and allow tunability of the optical trapping potential we propose to use a combination of a lens and an axicon with a displacement d between the two elements as shown in Figure (2.7). The initial idea prompting the investigation of this geometry was that the Bessel beam profile will be modulated by the focused Gaussian beam reducing the total number of rings, thereby increasing the intensity in the central core whilst only mildly reducing the axial Bessel zone. In actuality, the lens focuses the Bessel rings into a tighter Bessel zone where the radial pattern varies much faster as

[§]This value was calculated from the theory presented in Section (2.4.1)

[♦]Whilst the separation of each subsequent ring of the Bessel function is Δr the central core has a slightly different width, where the central core beam width ($\frac{1}{e^2}$) is given by $r_0 = 0.72\Delta r$.

shown in Figure (2.8). As a result, we found that we can theoretically produce Bessel zones with much stronger beam gradients or conversely similar beam gradients displaced further from the tip of the axicon.

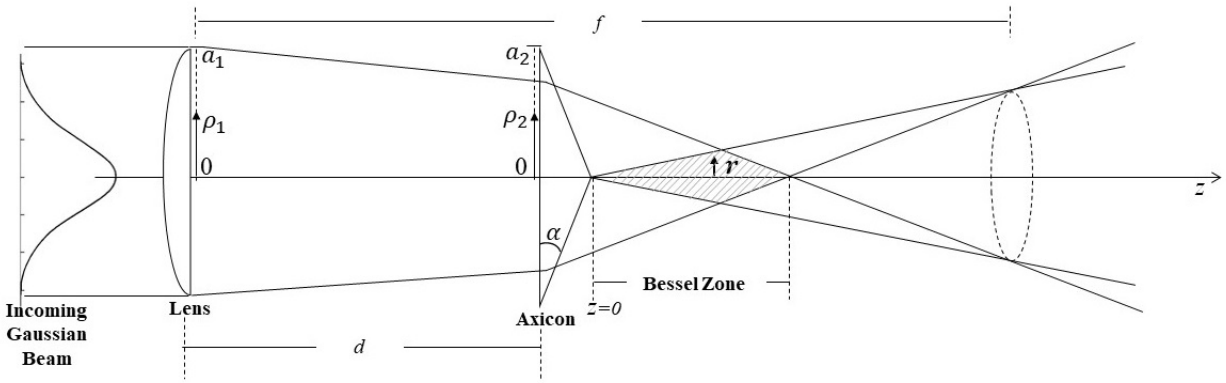

Figure 2.7: Generating a focused quasi-Bessel beam using a lens-axicon system. From left to right through axis z a collimated Gaussian beam incident on the lens with aperture radius a_1 and focal length f. The beam is then propagated through the lens, adding the phase factor, by distance d and integrated over ρ_1. Then, we have a cylindrically symmetric intensity profile at distance d (axicon plane with radius aperture a_2 and apex angle α) from the lens and at a distance ρ_2 from the optical axis. Finally, we have a cylindrically symmetric intensity profile from the tip of the axicon along the axial distance and at distance r from the optical axis.

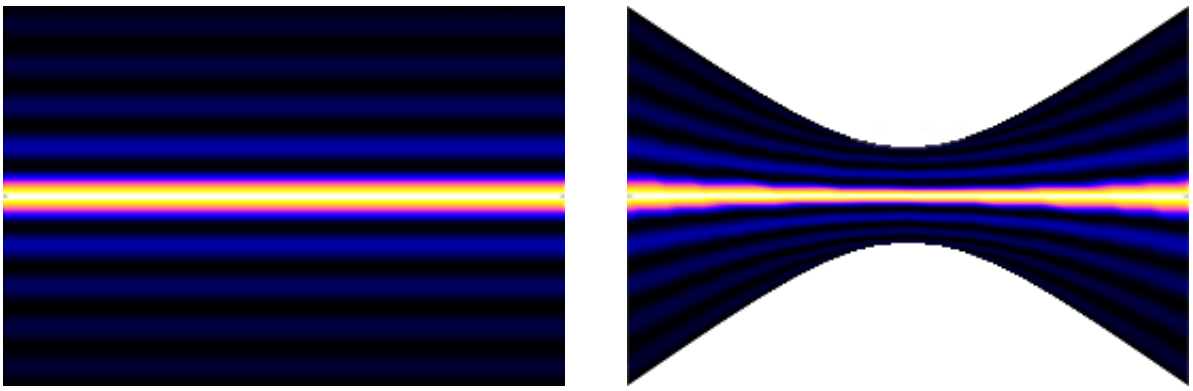

(a) (b)

Figure 2.8: Conceptual intensity pattern of the focused quasi-Bessel beam. **(a)** Axial intensity profile of a Bessel beam showing the diffraction free propagation. **(b)** Conceptual behaviour of the axial intensity profile of a focused-quasi-Bessel beam showing the focusing of the Bessel pattern and reduction of central core radius providing an increase in the gradient of the intensity useful for optical trapping.

Upon our initial investigation we noticed that the lens-axicon system has previously been proposed for generating optical Bottle beams in the far field [81]; however, studies of the focal region of a lens-axicon system, useful for optical trapping, concentrate on the appearance of spherical aberrations destroying the Bessel like properties [82].

We show that it is possible to engineer tightly confined focal regions with various tight focal spot sizes, with increased central core intensities by separating the spherical lens and the axicon by a distance d. The lens-axicon separation allows for the use of longer focal length lenses playing a crucial role in reducing the effects of spherical aberrations. We also show that when short focal length lenses are still required to generate the focused Bessel-Gaussian field, we can eliminate the effects of spherical aberrations and still have an agreement between theory and experiment by using parabolic lenses instead of spherical lenses.

In order to further appreciate the desirable properties of focused Bessel Gaussian beam, it is useful to formally describe the beam profile by calculating the diffraction propagation of a Gaussian beam through both optical elements.

2.4.1 Theory

Through a circular aperture with radial coordinate ρ and phase retardation $\phi(\rho)$, the Kirchhoff-Fresnel (K-F) integral in cylindrical co-ordinates calculates the diffraction propagation of a monochromatic wave at position (r, z) with initial electric field profile $A(\rho)$ [83]:

$$u(r,z) = e^{\frac{ikr^2}{2z}} \frac{k}{z} \int_0^a A(\rho) e^{-ik\phi(\rho)} e^{-ik\frac{\rho^2}{2z}} J_0\left(\frac{kr\rho}{z}\right) \rho d\rho, \tag{2.34}$$

where $k{=}\frac{2\pi}{\lambda}$ is the wavenumber with wavelength λ, a is the aperture size and J_0 is the zeroth order Bessel function. The geometry and parameters of the optical system are also represented in Figure (2.7).

The analytical solution for the lens-axicon combination with separation d and Gaussian input involves two K-F integrals. The first K-F integral evaluates over the radius of the lens a_1, the electric field diffraction from the lens plane with radial coordinate ρ_1 to the axicon plane with radial coordinate ρ_2 with a separation d, such that,

$$u_1(\rho_2, d) = e^{\frac{ik\rho_2^2}{2d}} \frac{k}{d} \int_0^{a_1} A(\rho_1) e^{-ik\phi_{lens}(\rho_1)} e^{-ik\frac{\rho_1^2}{2d}} J_0\left(\frac{k\rho_2\rho_1}{d}\right) \rho_1 d\rho_1, \tag{2.35}$$

with Gaussian input, $A(\rho_1) = \sqrt{I_0} e^{-(\frac{\rho_1}{W})^2}$, and parabolic lens phase retardation, $\phi_{lens}(\rho_1) = (n_{lens} - 1)\left(R\left[1 - \sqrt{(1 - (\frac{\rho_1^2}{R^2})}\right]\right)$ [84], where I_0 is the input beam intensity with beam diameter W, n_{lens} is the refractive index of the lens and R is the radius of curvature of the plano-convex lens [85].

The second K-F integral then evaluates the electric field diffraction from the axicon plane to the Bessel zone with coordinate (r, z) such that,

$$u_2(r, z) = e^{\frac{ikr^2}{2z}} \frac{k}{z} \int_0^{a_2} u_1(\rho_2, d) e^{-ik\phi_{axicon}(\rho_2)} e^{-ik\frac{\rho_2^2}{2z}} J_0\left(\frac{kr\rho_2}{z}\right) \rho_2 d\rho_2, \tag{2.36}$$

with axicon phase retardation given by $\phi_{axicon}(\rho_2) = (n_{axicon} - 1)\alpha\rho_2$ where a_2 is the radius of the axicon, n_{axicon} is the refractive index of the axicon and α is the apex angle of the axicon.

Unfortunately, this double integral is computationally expensive for $d > 0$ due to the rapidly varying phase factor which requires sampling of ρ_2 of the order of λ. In order to calculate the focused Bessel beam profile, we replaced the first K-F integral with Gaussian beam optics using the thin lens approximation with a focal length f, assuming that the axicon tip is placed far from the focus of the lens, ($f - d \gg z_R = \frac{\lambda f^2}{\pi W}$). In this way we can replace u_1 in Equation (2.36) with,

$$u_1(\rho_2, d) = \sqrt{I_0}\left(\frac{f}{f - d}\right) e^{-\frac{\rho_2^2}{W^2\left(\frac{f-d}{f}\right)^2}} e^{-ik\frac{\rho_2^2}{2(f-d)}}. \tag{2.37}$$

Contrary to the exact analytical solution using two K-F integrals, the Gaussian approximation, assuming thin lenses, will not include spherical aberrations. Note that in the instance where d=0 (a lens-axicon doublet), both phase terms can be included in a single K-F integral which can then be numerically solved including spherical aberrations [82]. Spherical aberrations are more significant for shorter focal length lenses in lens-axicon doublets, which is also true for lens-axicon systems separated by d.

2.4.2 Simulation

Now we proceed to integrate Equation (2.36), substituting in the thin lens approximation for the input electric field given in Equation (2.37) in order to analyse the effect of focusing a quasi-Bessel beam. We show the effect of tuning the separation d between the lens and the axicon on the peak intensity, the peak position and the Bessel zone length.

Figure (2.9) shows the simulation of the axial beam profile for an axicon only. The radial axes ρ is normalized to the first ring radius of no light $r_0(\alpha)$, where α is the angle of the axicon as depicted in Figure (2.7). Figure (2.9b) shows the evolution of the size of r_0 with respect to α. The first ring radius of no light r_0 is typically of the order of micrometers. Hence, Figure (2.9a) gives the idea of a radially symmetric shape of the intense central core and the surrounding concentric rings throughout the Bessel zone. Again I point out that the total beam power is equally distributed between the core and the outer rings since the intensity in each ring drops away at the rate of $\frac{1}{\rho^2}$ [77–79]. Thus, the central core contains the total power of the beam divided by the number of rings.

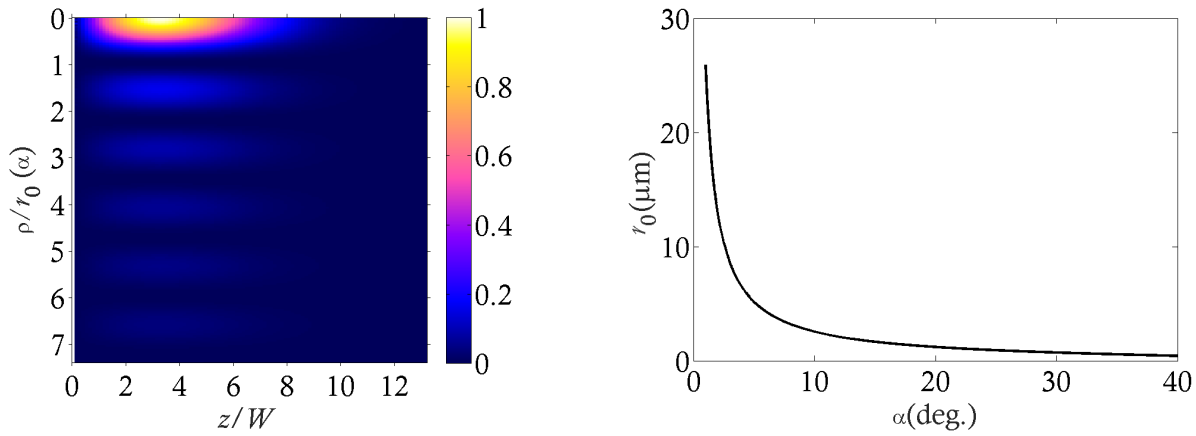

(a) (b)

Figure 2.9: Normalised numerical calculations of a quasi-Bessel beam. **(a)** Numerical calculation of the beam profile normalized to the incident beam radius on the axicon W as a function of the radial coordinate ρ normalized to the first ring of no light $r_0(\alpha)$, where α is the angle of the axicon. Intensity distribution normalized at its maximum intensity. **(b)** Evolution of the size of r_0 with respect α for a collimated Gaussian beam, which is independent of beam size.

Considering the geometric structure of the lens-axicon system (Figure 2.7), significant changes appear in the beam shape compared to the Bessel-Gaussian beam generated by an axicon alone. Figure (2.10) shows the numerical simulations of a lens-axicon system for different distances d between the lens and the axicon. The profiles shown are for a 30 mm-5° lens-axicon combination, where the first value is the focal length of the lens and the second is the apex angle of the axicon. This notation is maintained throughout this section. Firstly, the presence of a lens focuses the Bessel beam structure such that the radial width of the core and the concentric ring radii are no longer constant. The width of the central core and the concentric ring radii narrow down, tilting towards the focus of the lens as we move along the axial direction. Consequently, the central core spot size reduces significantly. Secondly, due to the focusing, the effective incident beam diameter reduces through the propagation of the axicon. Therefore, the total number of concentric rings decreases thereby increasing the intensity in the central core.

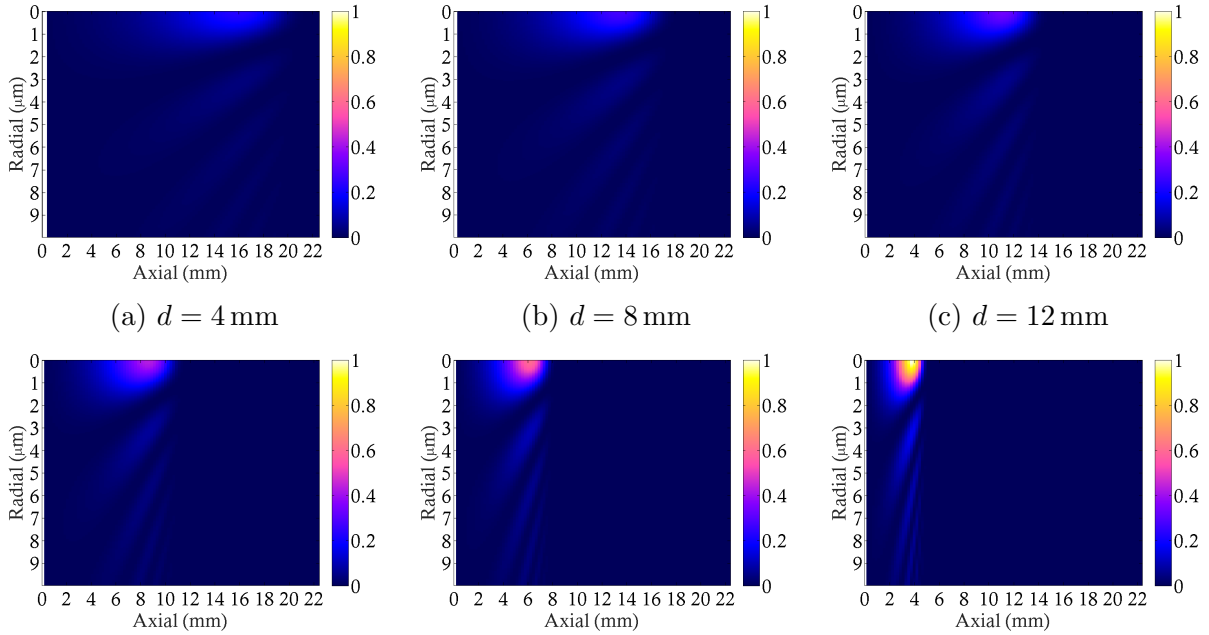

(a) $d = 4\,\text{mm}$ (b) $d = 8\,\text{mm}$ (c) $d = 12\,\text{mm}$

(d) $d = 16\,\text{mm}$ (e) $d = 20\,\text{mm}$ (f) $d = 24\,\text{mm}$

Figure 2.10: Numerical calculation of the beam profile using a 30 mm-5° lens-axicon combination with six different distances d. **(a)** 4 mm, **(b)** 8 mm, **(c)** 12 mm, **(d)** 16 mm, **(e)** 20 mm and **(f)** 24 mm. All intensity distributions are normalized to the maximum of **(f)**.

In Figure (2.11) we present a plot of the intensities of the focused-quasi-Bessel beams calculated for the 30 mm-5° combination including a comparison with a quasi-Bessel beam from only a single 20° axicon. Figure (2.11a) shows the intensity of the focused-quasi-Bessel beams in the axial direction and Figure (2.11b) shows the intensity distributions of the focused-quasi-Bessel beams in the radial direction evaluated at the peak intensity. As the lens-axicon separation distance is increased, the focal point of the lens moves closer to the tip of the axicon resulting in less rings and a higher central core intensity at the cost of a reduced effective Bessel zone. Interestingly, the size of the central core at peak intensity remains unchanged for any lens-axicon combination as exemplified in Figure (2.11b). Figure (2.11c) and (2.11d) shows a comparison between the focused-quasi-Bessel beams and the quasi-Bessel beams generated by a single 20° axicon. Only the largest and smallest lens-axicon separations are compared: $d = 24\,\text{mm}$ (yellow) and $d = 4\,\text{mm}$ (red). For comparison with these beam profiles, the beam widths incident on the 20° axicon are equivalent to the beam widths incident on the 5° axicon after propagating the distance d from the lens to the axicon for the corresponding lens-axicon combinations. The dashed black curve corresponds to $d = 24\,\text{mm}$ (yellow) and the solid black curve corresponds to $d = 4\,\text{mm}$ (red).

The result of the lens acting on the quasi-Bessel beam is that we produce a smaller Bessel zone with higher peak intensities. Whilst this can be achieved by simply illuminating a sharper angled axicon with a smaller beam profile, Figures (2.11c) and (2.11d) highlight that the peak intensity is higher for the focused-quasi-Bessel beams than for the 20° axicon alone. For optical trapping, since the optical potential depth is proportional to the maximum beam intensity♣, we observe that the lens-axicon combination provides a stronger optical trapping potential further from the axicon tip than is possible with an axicon alone. The displacement from the axicon tip is particularly advantageous for our experimental design in Figure (2.6) when the minimum distance between two axicons is constrained.

♣The optical potential depth is proportional to the maximum beam intensity for any continuously integrable beam profile, which can be observed in Equation (2.44)

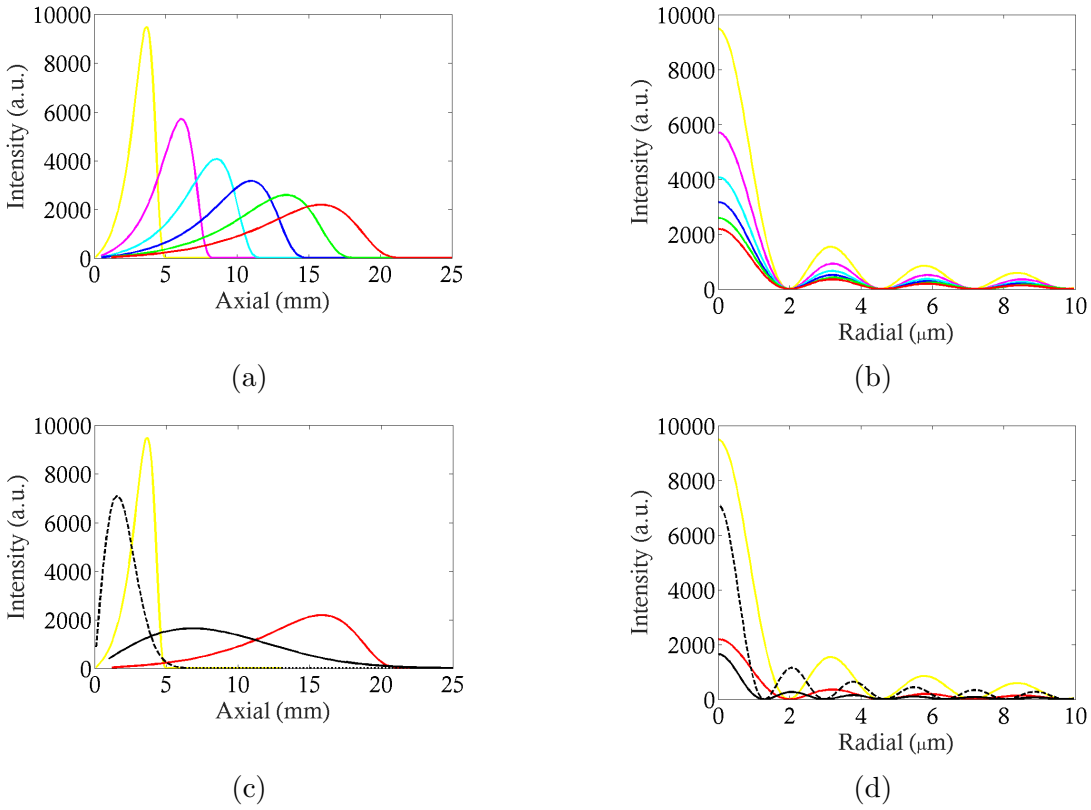

Figure 2.11: Numerical calculation of the intensity for 30 mm-5° lens-axicon combinations with six different values of d: 4 mm (red), 8 mm (green), 12 mm (blue), 16 mm (cyan), 20 mm (magenta) and 24 mm (yellow). **(a)** On-axis the core intensity profile. **(b)** Radial intensity distribution at the peak intensity. **(c)** and **(d)**, comparison of the focused quasi-Bessel beams with quasi-Bessel beams generated using only a 20° axicon. Solid black has the equivalent beam radius on the axicon as the red curve and the dashed black curve has the equivalent beam radius on the axicon as the yellow curve.

2.4.3 Results and Analysis

An experimental implementation to confirm the theory I developed was constructed predominantly by Md Iftekher Chowdhury and can be observed in detail in reference [86]. All experimental values are obtained using high dynamic range (HDR) imaging of the Bessel profile for varying axial positions. A summary of the experimental results are presented. It was initially found that for a shallow 5° axicon and longer 50 mm focal length lens, we obtained good agreement between the simulation and experiment as shown in Figure (2.12); however, for the shorter 30 mm focal length lens, the expected numerical intensity distribution simulations differed drastically from the experimental profile as shown in Figure (2.13).

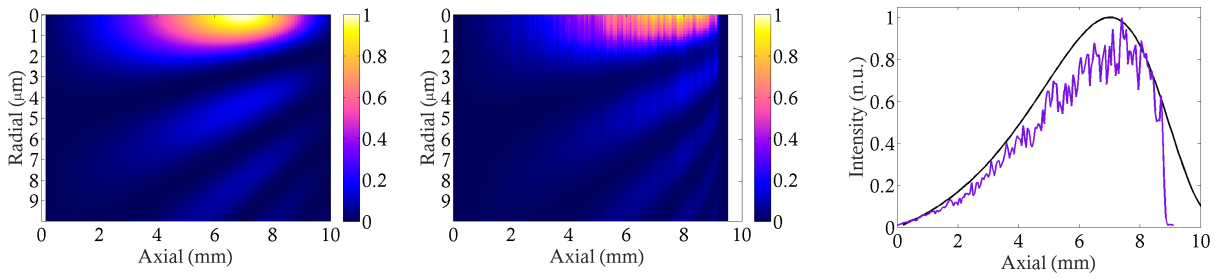

(a) 50 mm-5° Simulation (b) 50 mm-5° Experiment (c) 50 mm-5° Comparison

Figure 2.12: Simulation **(a)** and experiment **(b)** of a normalized intensity beam profile generated with a 50 mm-5° lens-axicon combination separated by $d = 35$mm. **(c)** Comparison of the simulation (black) with the experimental data (purple) for the intensity distribution of the central core. All plots normalized to their peak intensities.

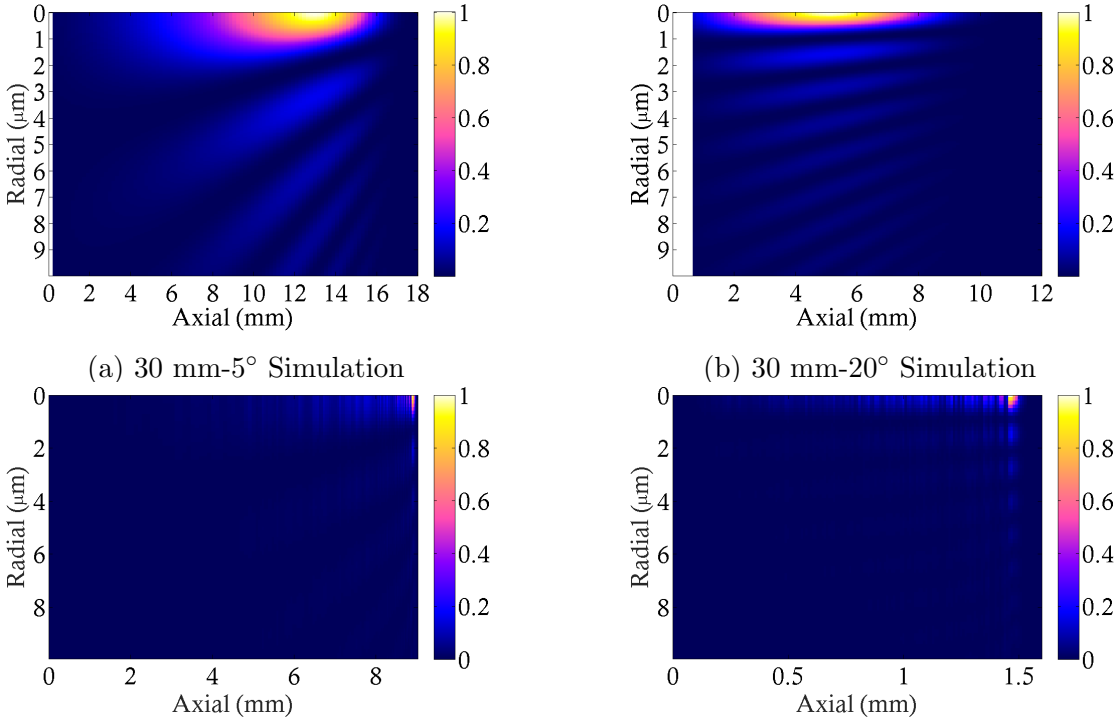

(a) 30 mm-5° Simulation (b) 30 mm-20° Simulation

(c) 30 mm-5° Experiment (d) 30 mm-20° Experiment

Figure 2.13: Simulation (top row) and experiment (bottom row) of the intensity beam profile generated with a 30 mm-5° lens-axicon (left column) and 30 mm-20° lens-axicon (right column) with the lens-axicon separation $d = 8$ mm for all plots. All plots normalized to their own peak intensity.

Since the beam profile is strongly dependant on the rapidly varying phase of the incident beam we attributed the altered beam profiles to spherical aberrations induced by the spherical lenses. To investigate and reduce the effects of spherical aberrations we implemented an aspheric lens with a focal length of 32 mm to replace the 30 mm spherical lens. Figure (2.14a) and Figure (2.14b) show the simulation and experimental result for the axial beam profiles generated by a 32 mm-20° aspheric lens-axicon combination with a lens-axicon separation distance of $d = 22.15\,\text{mm}$. Similarly, Figure (2.14d) and Figure (2.14e) show the 32 mm-5° aspheric lens-axicon combination with a lens-axicon separation distance of $d = 17.65\,\text{mm}$. Figures (2.14c) and(2.14f) show a comparison of the theoretical and experimental axial intensity data for the 32 mm-20° and 32 mm-5° aspheric lens-axicon combination respectively.

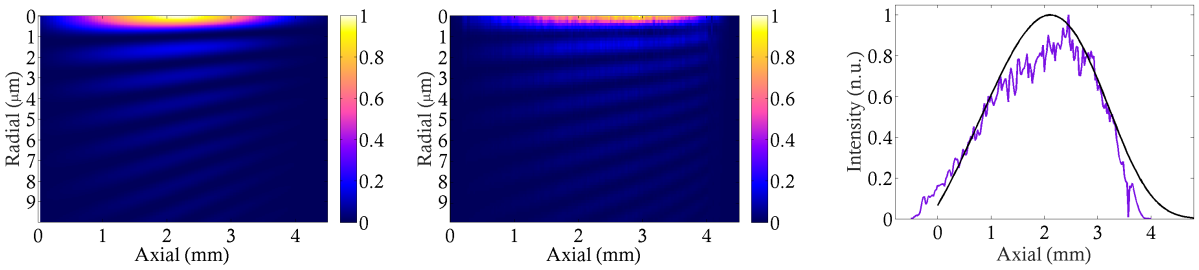

(a) 32 mm-5° Simulation (b) 32 mm-5° Experiment (c) 32 mm-5° Comparison

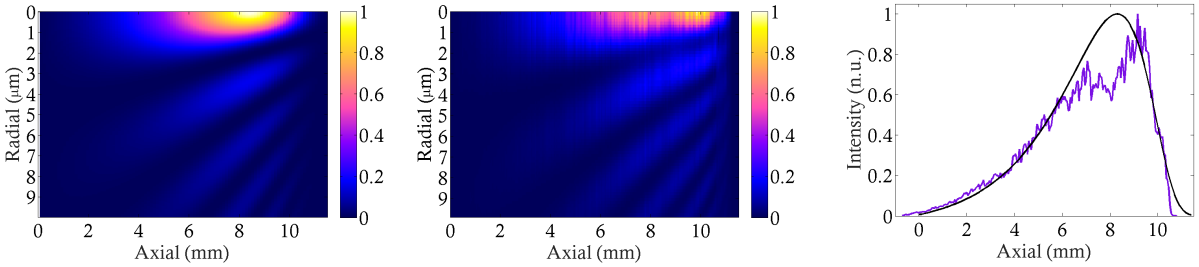

(d) 32 mm-20° Simulation (e) 32 mm-20° Experiment (f) 32 mm-20° Comparison

Figure 2.14: Simulation **(a)** and experiment **(b)** of a normalised intensity beam profile generated with a 32 mm-20° aspheric lens-axicon combination separated by $d = 22.15\,\text{mm}$. **(c)** Comparison of the simulation (black) with the experimental data (purple) for the intensity distribution of the central core. Simulation **(d)** and experiment **(e)** of a normalized intensity beam profile generated with a 32 mm-5° aspheric lens-axicon combination separated by $d = 17.65\,\text{mm}$. **(f)** Comparison of the simulation (black) with the experimental data (purple) for the axial intensity distribution. All plots normalized to their own peak intensity.

From Figure (2.14) we obtain a good agreement between theory and experiment showing that spherical aberrations are indeed detrimental to the generation of focused-Bessel beams but can be removed using aspheric lenses. We attribute the remaining spherical aberrations in the data to the spherical imaging lens in the set-up [86].

2.4.4 Experiment Outlook

By using an aspheric lens-axicon system we have shown that we can increase the central core intensity and maintain a long propagation distance further from the axicon tip than by using an axicon by itself. Using a suitable choice of axicon and lens, we can tune the Bessel-Gaussian beam to meet the specific needs of the Bessel-Gaussian beams. To give an example of a desired use of focused-quasi-Bessel beams, I return to the idea of the experiment for force sensing using two counter propagating Bessel beams as shown in Figure (2.6).

In Figure (2.15) I have compared four differing numerically simulated quasi-Bessel beam profiles designed for optical trapping. Two of the profiles, black and blue are generated using a single 25° axicon and beam widths of 1.2 mm and 5 mm respectively, providing a central core FWHM of 950 nm and Bessel propagation length of 2.5 mm and 7.3 mm respectively. The third Bessel profile (red) is generated with a 32 mm-20° lens-axicon combination with a separation of $d = 22$ mm. The result is a Bessel beam similar to the black curve with closely matching propagation length (2.5 mm) and central core FWHM (950 nm). This beam design produces a Bessel zone with much higher axial symmetry such that the intensity profiles of the two counter propagating are better matched, providing a more optimal balancing of the scattering forces.

Unfortunately in our particular experimental implementation, we foresee the need of a single beam optical trap which sets a minimum separation between the axicons of approximately 14 mm. Whilst in principle there is nothing preventing the implementation and trapping of particles with only the counter propagating Bessel beams, aligning the beams and balancing the scattering forces will be practically infeasible without the initial single beam trap. As a result, we investigated the potential of generating a focused-quasi-Bessel

beam displaced axially from the axicon tip. The final green beam profile is therefore generated with a 20 mm-5° lens-axicon combination separated by $d = 10\,\text{mm}$ producing a 2.5 mm long Bessel beam profile displaced from the tip of the axicon by 7 mm. This displacement from the axicon tip now allows for the axicons to be separated by approximately 14 mm providing an overlapping 2.5 mm Bessel zone at the centre. This combination now allows for the additional space required for the single beam optical trapping lens.

We calculated previously that a Bessel beam profile with the same properties as the blue curve will require a beam intensity of 100 W to radially trap the 170 nm silica particles♥. By comparing directly the maximum beam intensity of the axicon only blue curve with the lens-axicon system green curve we observe a 4.06 times increase in the maximum of the field intensity which is directly proportional to the optical potential depth as shown in Equation (2.46). I now estimate that it will require a more reasonable 24.6 W of input laser power to optically trap silica particles in a focused-quasi-Bessel beam with an axial propagation length of 2.5 mm displaced by 7 mm from the axicon tip. Using this new lens-axicon system we can now separate the axicon tips by 14 mm allowing for the additional space required for the single beam optical trap. The importance of this result is that the lens-axicon system now provides us with a previously unattainable experimental design for optical trapping, ideal for sensing of weak forces.

In this section I have covered only the shape of the optical trapping beam. The second mechanism to increase the optical trapping strength on the object relies on the polarisability of the particle. In the following sections we look at the polarisability of trapped objects and how resonances in the polarisability can lead to enhanced cooling and manipulation strategies.

♥By using larger silica particles the gradient force will increase with radius cubed thereby further reducing the required laser power. It it true that the scattering force will increase at a much faster rate, scaling with the radius to the sixth power. In our design however, since the scattering force is cancelled out by the counter propagating beams, the drastic rise in scattering force will not be a significant issue and trapping of larger particles will be more suitable, allowing for reduced beam intensities.

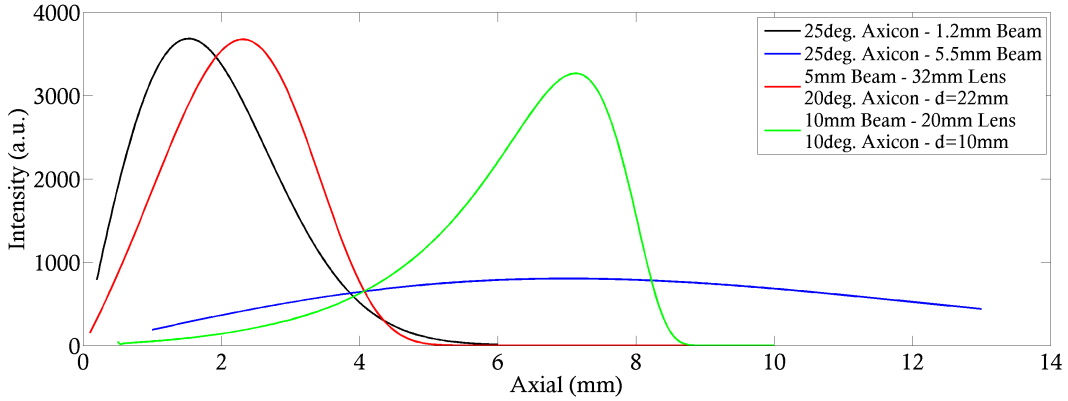

(a)

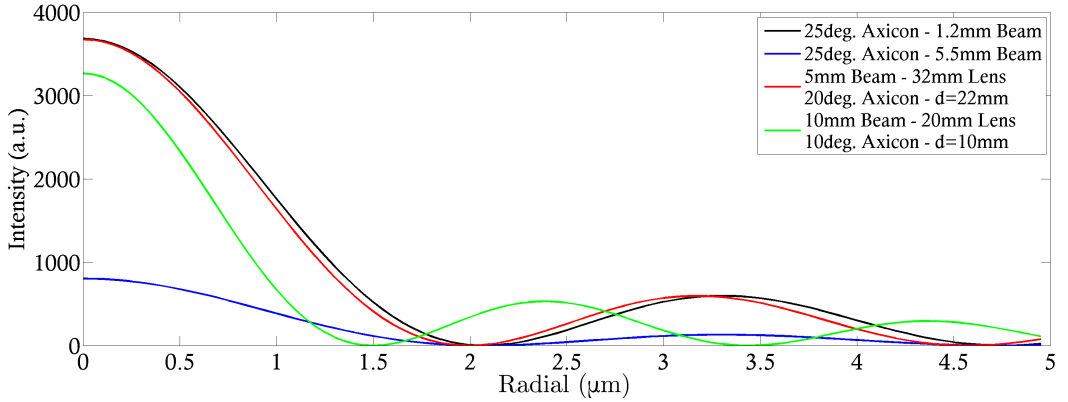

(b)

Figure 2.15: Numerical simulations of four quasi-Bessel beams for experimental implementation. Black and Blue are calculated without a lens for a 25° axicon with beam widths of 1.2 mm and 5.5 mm respectively producing beams with a central core radius of 950 nm and Bessel propagation lengths of 2.5 mm and 11.2 mm respectively. The red curve is generated with a 5 mm beam, incident on a 32 mm lens and 20° axicon separated by 22 mm. The resulting Bessel beam has a Bessel zone that is 2.5 mm in length and central core radius of 950 nm. The final green Bessel beam is generated with a 10 mm beam, incident on a 20 mm lens and 10° axicon separated by 10 mm. The resulting Bessel beam has a central core radius of 700nm and Bessel propagation zone that is 2.5 mm but axially displaced with the maximum intensity 7 mm from the axicon tip. Figure **(a)** shows the beam intensity from the axicon tip in the axial direction. Figure **(b)** shows the radial beam intensity at the position of maximum axial intensity.

2.5 Polarisability

For optical trapping, once the beam geometry has been set, the most important property is then the complex polarisability of the trapped object. The polarisability is a measure

of an objects ability to have its charge distribution displaced under the influence of an external electric field. It is therefore a measure of the ability to form instantaneous dipoles. Whilst the optical force on the instantaneous dipole is identical for all objects, the complex polarisability of an object creating the instantaneous dipole changes depending on the nature of the object. In this thesis I focus on two particular objects: atoms and dielectric particles. For atoms, it is the resonances from the atomic transitions that provide additional degrees of freedom to the optical traps, thereby providing additional cooling mechanisms. In order to further investigate the radiative forces we must now consider the polarisability of dielectric particles and then contrast it with the polarisability of atomic transistions, highlighting the resonant properties that that make these objects ideal for optical manipulation and control that resulted in many famous quantum optics applications.

2.5.1 Dielectric Polarisability

For dielectric Rayleigh particles, where the radius of the particle is much smaller than the wavelength ($a \ll \lambda$), the amplitude of the illuminating light is constant over the extent of the particle, and the electrostatic approximation can be used to calculate the polarisabilities [87]. The complex polarisability of a small particle is,

$$\alpha = 3V \frac{\hat{\epsilon} - \epsilon_m}{\hat{\epsilon} + 2\epsilon_m}, \tag{2.38}$$

where $\hat{\epsilon} = \epsilon_1(\lambda) + i\epsilon_2(\lambda)$ and $\epsilon_m = n_m^2$ are the dielectric constants of the particle and the surrounding medium respectively and $V = \frac{4}{3}\pi a^3$ is the volume of the particle with radius a [87]. In most situations the trapped object is a dielectric particle with negligible absorption such that the refractive index is real ($\hat{\epsilon} = n_p^2$) and thus the polarisability can be written as

$$\alpha = 4\pi n_m^2 a^3 \left(\frac{m^2 - 1}{m^2 + 2} \right), \tag{2.39}$$

where n_p and n_m are the refractive indexes of the particle and medium respectively and $m = n_p/n_m$ is the relative refractive index of the particle♠. Since the polarisability is now

♠It is important to note that although the refractive index can be complex, this equation is only valid for a real refractive index. Interestingly however, in the Rayleigh regime the light interaction pictures for

real, it may be interpreted that there will be no scattering force on the dielectric particle due to Equation (2.28) now having no contribution; however, one must be careful when calculating the total scattering forces on a dielectric nano-particle as we must consider both the absorptive scattering force as well as the scattering force from photons that are deflected or re-emitted from the particle. The absorptive scattering force arises from the photons that are absorbed by the particle and not re-emitted, whereas the remaining scattering force arises from the fact that as the electric field of the incident laser beam oscillates harmonically in time, the induced dipole oscillates synchronously with it, radiating secondary scattered waves in all directions. If we use the complex dielectric constants and evaluate both the real and imaginary parts of the polarisability in Equation 2.38 we indeed obtain the complete scattering force. However, it is typical in the field of optical trapping and levitation to neglect the absorption of the particle and calculate the polarisability from the refractive index as in Equation (2.39). In this case the scattering force is calculated using Rayleigh scattering and momentum transfer as described in Section (2.5.1).

Gradient Force

By substituting the real part of Equation (2.39) into Equation (2.14) the gradient force on a transparent dielectric particle is given by,

$$\boldsymbol{F}_{grad} = \mathbb{R}\left[\frac{2\pi n_m a^3}{c}\left(\frac{m^2-1}{m^2+2}\right)\right]\nabla I(\boldsymbol{r}). \tag{2.40}$$

The gradient force in a Gaussian beam can now be expressed in terms of each of its three components by substituting in the beam intensity from Equation (2.16):

$$\begin{aligned}\boldsymbol{F}_{grad,x}(\boldsymbol{r}) =& \hat{\boldsymbol{x}}\frac{2\pi n_m a^3}{c}\left(\frac{m^2-1}{m^2+2}\right)\frac{4\tilde{x}/W_0}{1+(2\tilde{z})^2} \\ &\times\left(\frac{P}{\pi W_0^2}\right)\frac{1}{1+(2\tilde{z})^2}\exp\left[-\frac{2(\tilde{x}^2+\tilde{y}^2)}{1+(2\tilde{z})^2}\right]\end{aligned} \tag{2.41}$$

metals and dielectrics are similar and thus Equation (2.39) can be used for calculating the gradient force for metal nano-particles with the appropriate correction to the volume due to attenuation of the incident light field [88].

$$\begin{aligned}\boldsymbol{F}_{grad,y}(\boldsymbol{r}) =& \hat{\boldsymbol{y}}\frac{2\pi n_m a^3}{c}\left(\frac{m^2-1}{m^2+2}\right)\frac{4\tilde{y}/W_0}{1+(2\tilde{z})^2} \\ &\times\left(\frac{P}{\pi W_0^2}\right)\frac{1}{1+(2\tilde{z})^2}\exp\left[-\frac{2(\tilde{x}^2+\tilde{y}^2)}{1+(2\tilde{z})^2}\right] \qquad (2.42)\\ \boldsymbol{F}_{grad,z}(\boldsymbol{r}) =& \hat{\boldsymbol{z}}\frac{2\pi n_m a^3}{c}\left(\frac{m^2-1}{m^2+2}\right)\frac{8\tilde{z}/(kW_0^2)}{1+(2\tilde{z})^2} \\ &\times\left[1-\frac{2(\tilde{x}^2+\tilde{y}^2)}{1+(2\tilde{z})^2}\right]\left(\frac{2P}{\pi W_0^2}\right)\frac{1}{1+(2\tilde{z})^2}\exp\left[-\frac{2(\tilde{x}^2+\tilde{y}^2)}{1+(2\tilde{z})^2}\right]. \qquad (2.43)\end{aligned}$$

Typically we think of the gradient force producing a restoring force towards the centre of the trap, but this is valid only when the refractive index of the particle is larger than the refractive index of the medium ($n_p > n_m$). This is strictly true in optical levitation regimes where the surrounding medium is a vacuum or gaseous medium where the refractive index is $n_m \simeq 1$, however in liquid, the particle may have a lower refractive index than the medium and be pushed away from the region of highest intensity. In this case, the particle can be trapped in a local minima of intensity. The gradient force on the particle increases for larger differences in refractive index and is zero when the refractive indexes match. Additionally, the gradient force on the particle increases with the third power of the radius of the particle. Whilst it may initially appear that in order to produce a stronger optical trap, one can use larger particles, this reasoning is not strictly true as you also need to consider the increase in the scattering force that may push the particle out of the optical trap. In comparison to what we will see with the forces on an optical transition, the forces on a dielectric particle varies slowly with wavelength. In the Rayleigh regime this dependence on wavelength appears only from the refractive index of the particle $n_p(\lambda)$**.

Another feature of the gradient force is that by integrating Equation (2.40) we see that the dipole force can be derived from a potential:

**For larger dielectric particles, there may also be an additional wavelength dependence due to Mie resonances that will be strongly dependent or particle size and shape.

$$\begin{aligned}\boldsymbol{F}_{grad}(\boldsymbol{r}) &= -\nabla U_{grad}(\boldsymbol{r}) \\ &= -\frac{\alpha'}{2n_m c} I(\boldsymbol{r}).\end{aligned} \tag{2.44}$$

In the situation above where we consider a Gaussian beam, the potential is given by,

$$U_{grad}(\boldsymbol{r}) = -\frac{2\pi n_m a^3}{c}\left(\frac{m^2-1}{m^2+2}\right)\left(\frac{2P}{\pi W_0^2}\right)\frac{1}{1+(2\tilde{z})^2}\exp\left[-\frac{2(\tilde{x}^2+\tilde{y}^2)}{1+(2\tilde{z})^2}\right]. \tag{2.45}$$

In order to achieve a stable, optically trapped particle, the depth of this potential well, which has a maximum at $(\tilde{x}, \tilde{y}, \tilde{z}) = (0, 0, 0)$, should be much larger than the average kinetic energy of the particle (typically generated by Brownian motion[††]). For a focused Gaussian beam trap this is satisfied when,

$$\Delta U_{grad} = \frac{2\pi n_m a^3}{c}\left(\frac{m^2-1}{m^2+2}\right)\left(\frac{2P}{\pi W_0^2}\right) \gg k_B T. \tag{2.46}$$

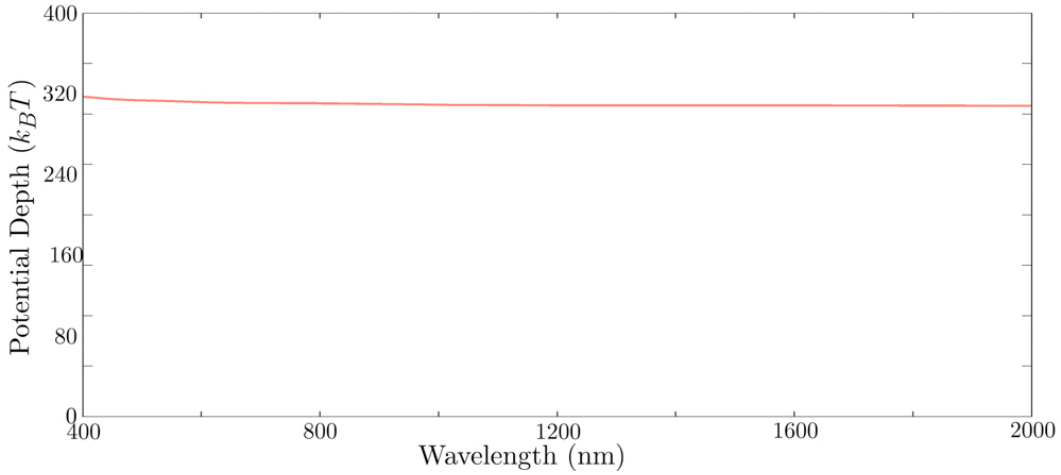

Figure 2.16: Optical potential depth of a single 100 nm nano-diamond in a 100 mW Gaussian beam focused to a beam waist of 1 µm. The particle depth is expressed in multiples of average kinetic energy (k_BT at $T = 300$K). The optical potential depths dependence on wavelength arises only from the change in refractive index as shown in Figure (1.4) [34].

[††]In vacuum, it does not need to be as large because the variance of average kinetic energy is not nearly as large.

Fortunately for dielectric particles, it is possible to produce optical traps with trap potentials deeper than k_BT even at room temperature. Figure (2.16) gives an example of the optical potential depth of an optically trapped nano-diamond and its wavelength dependence. It should be noted that not only does the restoring gradient forces need to overcome Brownian motion[‡‡] but also overcome the scattering forces pushing the particle out of the trap.

Scattering Force

From Equation (2.30) we saw that scattering force is related to the complex part of the polarisabiliy α'' such that,

$$\boldsymbol{F}_{abs} = \frac{\alpha''}{n_m c}\frac{\boldsymbol{I}(\boldsymbol{r})}{2}\boldsymbol{k}. \tag{2.47}$$

By substituting the imaginary part of Equation (2.38) into Equation (2.30) we obtain the force on the particle in a plane wave due to absorption given by,

$$\boldsymbol{F}_{abs} = \mathbb{I}m\left[4\pi n_m a^3 \frac{\hat{\epsilon}-\epsilon_m}{\hat{\epsilon}+2\epsilon_m}\right]\frac{\boldsymbol{I}(\boldsymbol{r})}{2}\boldsymbol{k}. \tag{2.48}$$

This equation is valid for both metallic and dielectric particles, however in order to determine absorptive scattering forces acting on the particle we must be careful in correctly determining the imaginary parts of the polarisability. It is important to note that one can not use the typical polarisability using the refractive index for dielectric particles as shown in Equation (2.39) since,

$$\mathbb{I}m\left[4\pi n_m a^3 \frac{\hat{\epsilon}-\epsilon_m}{\hat{\epsilon}+2\epsilon_m}\right] \neq \mathbb{I}m\left[4\pi n_m a^3 \frac{m^2-1}{m^2+2}\right]. \tag{2.49}$$

In a classical framework, Equation (2.48) only accounts for the scattering force due to absorption of photons that are not re-emitted. The total scattering force must also include the scattering forces that arise from the fact that as the electric field of the incident laser beam oscillates harmonically in time, the induced dipole oscillates synchronously with it

[‡‡]The typical bound for Brownian motion to obtain stable trapping, proposed by A. Ashkin, is for the potential depth to be greater than $10k_BT$.

thereby radiating secondary scattered waves in all directions. The total scattering force acting on the particle can then be written as,

$$\boldsymbol{F} = \boldsymbol{F}_{abs} + \boldsymbol{F}_{scat} = \left(k\mathbb{I}m\left[\alpha\right] + \frac{k^4}{6\pi}\frac{n_m}{c}\left|\alpha\right|^2 \right) \frac{\boldsymbol{I}(\boldsymbol{r})}{2}\frac{\boldsymbol{k}}{k}. \tag{2.50}$$

For dielectric particles in the Rayleigh regime where the absorption of the particle is negligible, the scattering force due to isotropic Rayleigh scattering dominates over the scattering due to absorption. The typical way to derive the scattering force for dielectric particles is using photon momentum transfer. The momentum of a single photon of energy $\boldsymbol{J}$ is given by,

$$\boldsymbol{p} = \hbar\boldsymbol{k} = \frac{\boldsymbol{J}n_m}{c}. \tag{2.51}$$

A beam of incident photons can be scattered by a particle resulting in two impulses. The force on the particle is equal to the difference between the momentum of the input beam and the scattered field from the particle. The scattered field, since the particle is in the Rayleigh regime, is isotropic in all directions; hence, the impulse arising from the scattered light has no preferable direction and results in no net force. The change in momentum, or force, of a particle can be calculated by considering the photon flux impinging on an object under the conservation of momentum:

$$\begin{aligned} \boldsymbol{F}_{scat} &= \hat{\boldsymbol{z}}\frac{n_m\sigma}{c}\langle\mathbf{S}\rangle_T \\ &= \hat{\boldsymbol{z}}\left(\frac{n_m}{c}\right)\sigma\boldsymbol{I}(\boldsymbol{r}), \end{aligned} \tag{2.52}$$

where n_m is the refractive index of the particle, $\langle\mathbf{S}\rangle_T$ is the time averaged Poynting vector, c is the speed of light and σ is the scattering cross section for the radiation pressure of the particle. In the case of a small dielectric particle in the Rayleigh regime where the light scatters isotropically, the scattering cross section σ is given by [89],

$$\sigma = \frac{k^4}{6\pi}\left|\alpha\right|^2. \tag{2.53}$$

Now substituting Equations (2.16) and (2.53) into Equation (2.52), the scattering force

is given in terms of the intensity distribution in a weakly focused Gaussian beam:

$$\hat{\boldsymbol{F}}_{scat}(\hat{\boldsymbol{r}}) = \hat{\boldsymbol{z}}\frac{8}{3}\pi\left(\frac{n_m^3}{c}\right)\left(\frac{2\pi}{\lambda}\right)^4 a^6\left(\frac{m^2-1}{m^2+2}\right)^2 \times\left(\frac{2P}{\pi W_0^2}\right)\frac{1}{1+(2\tilde{z})^2}\exp\left[-\frac{2(\tilde{x}^2+\tilde{y}^2)}{1+(2\tilde{z})^2}\right]. \tag{2.54}$$

We can see here that the scattering force increases with the radius to the sixth power compared to the gradient force which scales with the third power. So whilst both forces will increase with the size of the particle, the scattering force increases much faster and will start to dominate as the particle size increases. The implication is that smaller particles are more likely to be trapped and larger particles are pushed out of the trap. A comparison of the gradient force and scattering force for our 100 nm nano-diamonds trapped in a 100 mW Gaussian beam focused to a beam waist of 1 µW is shown in Figure (2.17), highlighting the lack of dependence on trapping laser wavelength.

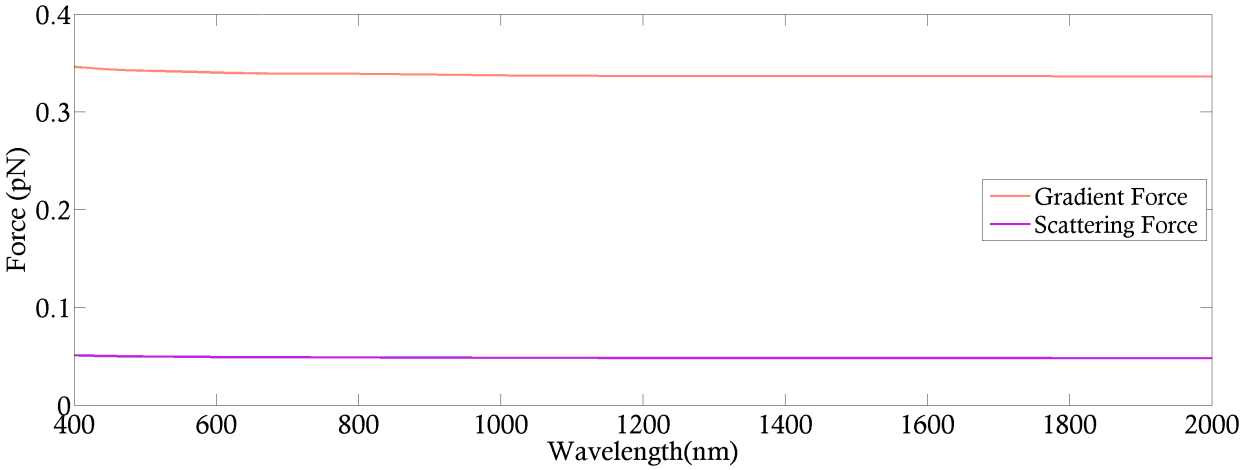

Figure 2.17: Optical forces on a single spherical 100 nm nano-diamond in a 100 mW Gaussian beam focused to a beam waist of 1 µm evaluated at $z = \frac{2kW_0^2}{\sqrt{3}}$ where the gradient force is at a maximum. Optical scattering forces arising from absorption of photons, such as from surface impurities, are neglected. These forces are calculated from the refractive index profile of the diamond taken from Figure (1.4).

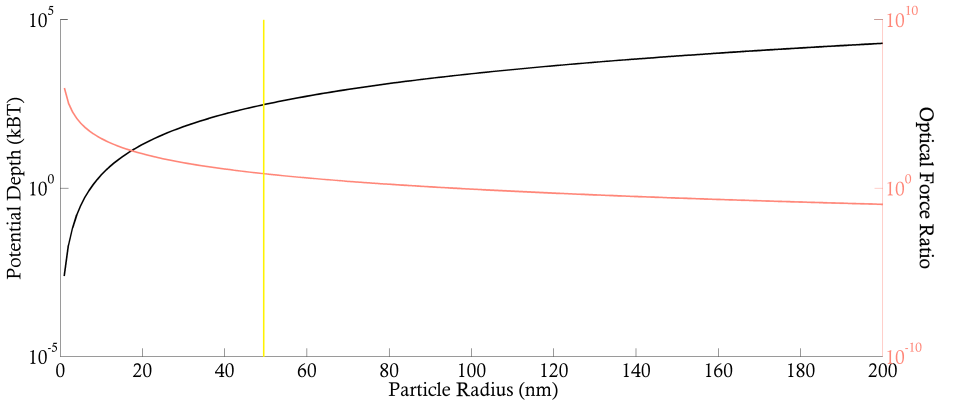

(a)

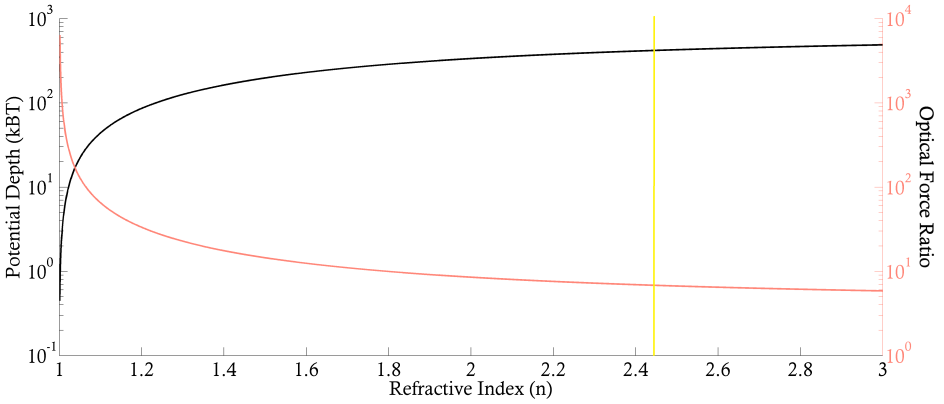

(b)

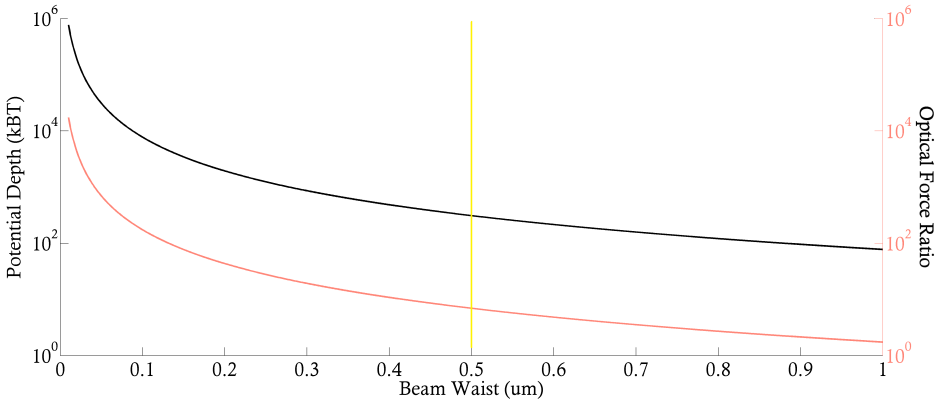

(c)

Figure 2.18: Dependence of the optical forces and potential depth on the physical properties of the optically trapped particle. The potential depth is expressed in multiples of average kinetic energy at room temperature, (k_BT at $T = 300$K), and the ratio between the axial gradient force and scattering forces evaluated at $z = \frac{2kW_0^2}{\sqrt{3}}$ where the gradient force is at a maximum is shown. Unless otherwise stated the values are calculated for a single 100 nm nano-diamond ($a = 50$ nm) in a 100 mW 1064 nm Gaussian beam focused to a beam radius of 0.5 µm, indicated by the yellow line in each plot. Figure **(a)** shows the dependence on particle radius, figure **(b)** the dependence on refractive index of the trapped object and finally figure **(c)** shows the dependence on the Gaussian beam waist.

Figure (2.18) provides a deeper understanding of the optical trapping forces dependence on different properties of the trapping system. For each of the properties, **(a)** particle radius, **(b)** refractive index and **(c)** beam waist, the axial optical force ratio $\left(\frac{F_{grad}}{F_{scat}}\right)$ and the optical potential depth is shown. The optical potential depth is expressed in multiples of average kinetic energy at room temperature, (k_BT at $T = 300$K), and the optical forces are calculated at the point $z = \frac{2kW_0^2}{\sqrt{3}}$, where the gradient force is at a maximum. Unless otherwise stated the values are calculated for a single 100 nm nano-diamond ($a = 50$ nm) in a 100 mW, 1064 nm Gaussian beam focused to a beam radius of 0.5 µm, indicated by the yellow line in each plot. Figure (2.18a) shows that as the radius of the particle is increased, the gradient force also increases generating a deeper potential well; however, since the scattering force scales much faster than the gradient force, the scattering force quickly dominates and the particle can no longer be trapped. Similarly in Figure (2.18b), a larger refractive index generates a deeper potential well, but simultaneously leads to the scattering force overcoming the gradient force, pushing the particle out of the trap. It is only the beam waist in Figure (2.18c), where, by decreasing the beam waist, there is a clear gain in both the optical potential depth and optical force ratio simultaneously, highlighting the constant need for strong focusing.

2.5.2 Atomic Polarisability

In order to better understand why the trapping and cooling of dielectric particles has not had the same success in quantum applications as the trapping and cooling of atoms, it is ideal now to look at the properties of trapping atoms that make them an ideal trapping candidate.

In order to determine the forces on an optical transition inside of an optical trap we must consider its complex polarisability. In comparison to the forces on a dielectric particle, the forces show a resonance behaviour around the transition frequency ω_0. The polarisability of a two-level atom with zero velocity is given as,

$$\alpha = \frac{d^2}{\epsilon_0 \hbar} \frac{(\omega_0 - \omega) + i\Gamma/2}{(\omega_0 - \omega)^2 + \frac{1}{2}\left(\frac{dE_0}{\hbar}\right)^2 + \frac{\Gamma^2}{4}}, \tag{2.55}$$

where, d is the dipole moment of the transition, Γ is the transition linewidth, ω_0 is the

transition frequency, ω is the trapping laser frequency and E_0 is the electric field strength. We can rewrite this as a linear polarisability term with a saturation term $(1+s)^{-1}$ which tends to zero at high intensities:

$$\alpha = \frac{d^2}{\epsilon_0 \hbar} \frac{(\omega_0 - \omega) + i\Gamma/2}{(\omega_0 - \omega)^2 + \frac{\Gamma^2}{4}} \frac{1}{1+s}, \tag{2.56}$$

where the saturation parameter s is given by,

$$s = \frac{1}{2}\left(\frac{dE_0}{\hbar}\right)^2 \frac{1}{(\omega_0 - \omega)^2 + \frac{\Gamma^2}{4}} = \frac{I}{I_{sat}} \frac{1}{1 + 4\left(\frac{\omega - \omega_0}{\Gamma}\right)^2}, \tag{2.57}$$

with,

$$I_{sat} = \frac{2I}{\Gamma^2}\left(\frac{dE_0}{\hbar}\right)^2. \tag{2.58}$$

We can see from Equation (2.55) that the polarisability of the two-level atom shows resonant behaviour around the transition frequency ω_0. Note also that if the velocity $\boldsymbol{v}$ of the atom is non-zero, the Doppler effect should be taken into account in the polarisability, by replacing ω by $\omega - \boldsymbol{k} \cdot \boldsymbol{v}$. This non zero velocity plays a very important role in Doppler cooling of atoms as described in Section (2.5.3).

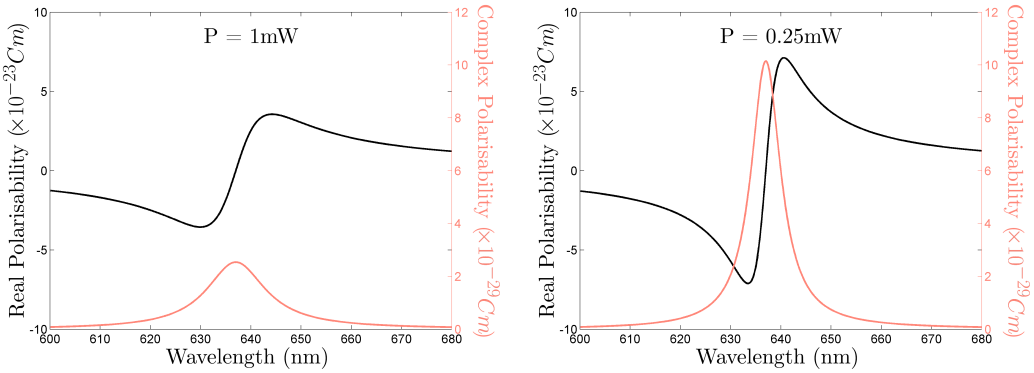

(a) (b)

Figure 2.19: Power broadened polarisability of a 637 nm two level transition, with a $2\pi \times$ 20MHz transition linewidth at the centre of an optical trap with **(a)** 1 mW and **(b)** 0.25 mW of power at the focal spot of a 0.85 NA objective. The resonance of the transition for typical dielectric trapping intensities is power broadened. The resonance width is then given by $\sqrt{\Gamma^2 + \left(\frac{dE_0}{\hbar}\right)^2}$ rather than Γ as observed from Equation (2.55).

Gradient Force

By substituting the real part of Equation (2.56) into Equation (2.14) the gradient force on a atom is then given by,

$$\boldsymbol{F}_{grad} = \frac{d^2}{\epsilon_0 \hbar} \frac{\omega - \omega_0}{(\omega - \omega_0)^2 + \frac{\Gamma^2}{4}} \frac{1}{1+s} \frac{\nabla |E_0(\boldsymbol{r}, t)|^2}{2}. \tag{2.59}$$

Now a simpler expression can be obtained by recalling that the Rabi angular frequency Ω_1 is equal to $-dE_0/\hbar$ such that,

$$\boldsymbol{F}_{grad} = \frac{\hbar(\omega - \omega_0)}{2} \frac{\nabla(\Omega_1^2/2)}{(\omega - \omega_0)^2 + \frac{\Gamma^2}{4}} \frac{1}{1+s} \tag{2.60}$$

We can see now that the dipole force varies directly with the gradient of the light intensity. There is also interesting behaviour about the atomic transition ω_0. For a blue detuning ($\omega > \omega_0$) the atoms are repelled from regions of high intensity, whereas for red detuning ($\omega < \omega_0$) the atoms are attracted towards such regions.

By integrating Equation (2.60) we see that the dipole force derives from a potential:

$$\boldsymbol{F}_{grad} = -\nabla U_{grad}(\boldsymbol{r}), \tag{2.61}$$

with,

$$\begin{aligned} U_{grad}(\boldsymbol{r}) &= -\frac{\hbar(\omega - \omega_0)}{2} \ln \left[1 + \frac{\Omega_1^2(\boldsymbol{r})/2}{(\omega_0 - \omega)^2 + \frac{\Gamma^2}{4}} \right] \\ &= -\frac{\hbar(\omega - \omega_0)}{2} \ln \left[1 + s(\boldsymbol{r}) \right] \\ &= -\frac{\hbar(\omega - \omega_0)}{2} \ln \left[1 + \frac{I(\boldsymbol{r})}{I_{sat}} \frac{1}{1 + 4\left(\frac{\omega - \omega_0}{\Gamma}\right)^2} \right]. \end{aligned} \tag{2.62}$$

where the choice of integration constant gives a zero potential outside the laser beam. This potential now suggests that it may be possible to trap atoms at the focal point of a laser beam if the frequency is red detuned ($\omega < \omega_0$). The potential has a minimum in both the x

and y dimensions of typical width ω_0, and also has a minimum in the z direction of typical width $z_R = \pi\omega_0^2/\lambda$, where z_R is the Rayleigh length. The atoms will only be trapped within the potential well provided that their kinetic energy is less than the depth of well. For a given laser frequency the trap depth is given when the saturation parameter s has a maximum which coincides with the maximum of the field such that,

$$\Delta U = \frac{\hbar(\omega_0 - \omega)}{2} \ln\left[1 + s_{max}\right]. \tag{2.63}$$

For a Gaussian beam trap as described in Section (2.3.2) we can substitute the relation for the electric field amplitude given by substituting Equation (2.16) into Equation (2.63) giving,

$$U_q = \frac{\hbar(\omega - \omega_0)}{2} \ln\left(1 + \frac{d^2}{\hbar^2} \frac{2P}{\pi W_0^2 n_m \epsilon_0 c} \frac{1}{(\omega - \omega_0)^2 + \frac{\Gamma^2}{4}}\right). \tag{2.64}$$

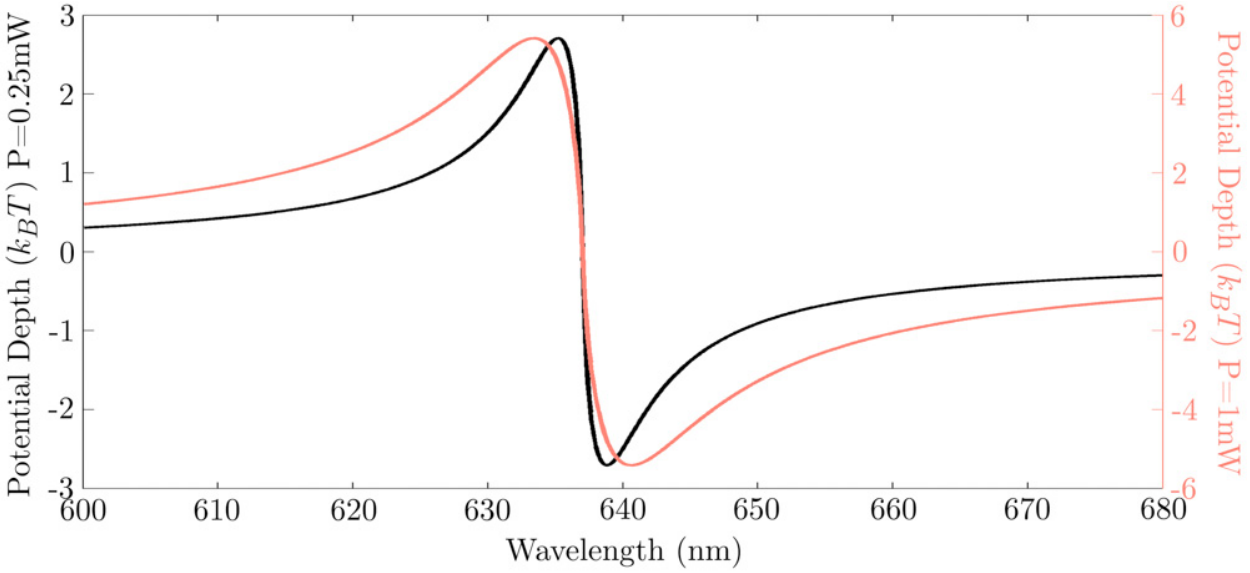

Figure 2.20: Optical potential depth for a single 637 nm transition, with $2\pi \times 20\,\text{MHz}$ transition linewidth at the centre of an optical trap with 0.25 mW and 1 mW of power at the focal spot of a 0.85 NA objective. The particle depth is expressed in fraction of average kinetic energy (k_BT at $T = 1\text{K}$). The resonance of the transition for typical dielectric trapping intensities is power broadened, where the resonance width is then given by $\sqrt{\Gamma^2 + \Omega_1^2}$.

It is important to note that whilst the trap depth always increases with the incident laser power, the increase in trapping power also leads to power broadening of the resonant transition as shown in Figure (2.20). For intensities below saturation the resonance width is given by the transition linewidth Γ, whereas for very large intensities the resonance width is given by $\sqrt{\Gamma^2 + \Omega_1^2}$. In practice, it is difficult to produce potential wells able to trap atoms with temperatures above a few milli-Kelvins; hence, the atoms have to be cooled first, before they can be trapped.

In addition to trapping, the dipole force also plays an important role for controlling and manipulating the trapped atoms. It is used to reflect atoms (atom mirrors), to focus them (atom lenses) and to diffract them (atom diffraction gratings).

Resonant Radiation Pressure Force

In order to determine the resonant radiation pressure forces on an atomic transition we need to consider the spontaneously scattered photons that interact with the atomic transition. By substituting the complex part of Equation (2.56) into Equation (2.30) the resonant radiation pressure force or scattering force is given by,

$$\boldsymbol{F}_{scat} = \hbar \boldsymbol{k} \frac{\Gamma}{2} \frac{\Omega_1^2/2}{(\omega - \omega_0)^2 + \frac{\Omega_1^2}{2} + \frac{\Gamma^2}{4}}, \tag{2.65}$$

where again we have used the fact that the Rabi angular frequency Ω_1 is equal to $-dE_0/\hbar$. This can be simplified by using the saturation parameter s such that,

$$\boldsymbol{F}_{scat} = \hbar \boldsymbol{k} \frac{\Gamma}{2} \frac{s}{1+s}, \tag{2.66}$$

where we recall that the saturation parameter is again given by,

$$s = \frac{I}{I_{sat}} \frac{1}{1 + 4\left(\frac{\omega - \omega_0}{\Gamma}\right)^2}, \tag{2.67}$$

with,

$$I_{sat} = \frac{2}{\Gamma^2} \frac{\Omega_1^2}{I}. \tag{2.68}$$

In writing the force in this form we can observe that for small values of the saturation parameter ($s \ll 1$), the radiation pressure is proportional to the the light intensity. However as the laser power is increased the force saturates such that the maximum scattering force is,

$$\boldsymbol{F}_{scat}^{max} = \hbar \boldsymbol{k} \frac{\Gamma}{2}. \tag{2.69}$$

We can now see that the scattering force has a strong resonant behaviour around the transition frequency ω_0 with a width on the order of the width Γ of the atomic line. Typically the atoms used in atom traps have extremely narrow linewidths and require specialised narrow lasers to address the transition with the appropriate detuning.

Interestingly, we have arrived at Equation (2.66) using a completely classical model of light, nevertheless, the momentum of a photon $\hbar \boldsymbol{k}$ appears in this equation even though the concept of a photon doesn't exist in this model. If one were to take care in tracking the emission and absorption rates using the optical Bloch equations, it can be proved that it is still valid to interpret this force as the result of momentum exchanges between laser photons and atoms. Additionally, we have not considered the absorption and stimulated emission of photons that one would expect from a quantum mechanical description of light. However, this effect contributes no force since the total momentum transfer is zero in this case, since,

$$\Delta \boldsymbol{P}_{sti} = -\Delta \boldsymbol{P}_{abs} = \hbar \boldsymbol{k}. \tag{2.70}$$

Now since both the gradient force and the resonant radiation pressure force will be acting on the atom simultaneously, it is worthwhile to identify the regimes that favour one force over the other. As has been shown earlier, in most practical trapping beams we require a high gradient field in order to trap. As such, we consider the case where the light intensity varies significantly on the scale of the wavelength, such that $|\nabla|$ is of the order of $\boldsymbol{k}$. In this case,

$$\frac{\boldsymbol{F}_{scat}}{\boldsymbol{F}_{grad}} \approx \frac{\Gamma}{|\omega - \omega_0|}. \tag{2.71}$$

For low detuning ($|\omega - \omega_0| \ll \Gamma$) the resonance radiation force dominates, whereas for high detuning ($|\omega - \omega_0| \gg \Gamma$) the gradient force dominates. Nevertheless too large a detuning

and the dipole force decreases as it is not resonant with the transition. As a result the optimal detuning of the laser to produce the strongest gradient force is given by,

$$(\omega - \omega_0) \approx \sqrt{\frac{\Omega_1^2}{2} + \frac{\Gamma^2}{4}}. \tag{2.72}$$

For atom trapping, the case of closed two-level atoms is important because radiative forces have a strong effect only if they are allowed to act continuously. If the two level system is not closed, the spontaneous emission, or non-radiative pathways will bring the atom into a different energy level where the radiative forces will be negligible because the detuning is very large and thus, the atom is practically transparent to the laser field. In an optical trap this is problematic as the atom will no longer experience a force holding it within the optical trap. In optical trapping of dielectric particles containing optical defects this condition is relaxed since the forces on the dielectric polarisability and remaining ensemble optical defects can still hold the entire object within the optical trap.

It should be emphasised here that when comparing the effects of the two optical forces, that the gradient force $\boldsymbol{F}_{grad}$ can be derived from a potential, whereas the scattering force $\boldsymbol{F}_{scat}$ does not. The consequence of this being that the gradient force is a conservative force and the scattering force is dissipative. Thus the gradient force alone can not take energy away from the motion of the atom and therefore the atom will have an oscillatory behaviour whilst trapped in this regime[§§]. Alternatively, since the scattering force is dissipative it can indeed cool or heat the motion of the atom within the harmonic gradient force potential. As a result, it is the manipulation of the scattering forces on the atom that are predominantly used to slow the motion of the atoms.

'Priority is like temperature.
Everything has a temperature,
but some are hotter than others.'

– Unknown

[§§]The exception is if there is an external control modulating the strength of the gradient force, thereby cooling the motion of the particle, as is done in feedback cooling.

2.5.3 Laser Cooling

Temperature is simply a measure of the average kinetic energy of the random motions within a system. In classical statistical mechanics, the equipartition theorem relates the temperature of a system to its average energies. The equipartition theorem states that systems in thermal equilibrium have the same average energy associated with each independent degree of freedom of their motion. For an atom in a fixed optical trapping potential, the temperature is a measure of the average kinetic energy of the gas molecules. As a result, to cool the temperature of a gas towards the quantum regime, the velocities of the ensemble of atoms needs to be reduced.

In comparison, a levitated nano-particle has two temperatures that need to be considered. The obvious temperature is the internal temperature of the nano-particle itself; however, the temperature we are interested in for quantum opto-mechanical applications is the temperature related to the oscillatory motion of the nano-particle as a whole and is called the centre-of-mass (CoM) temperature[◆◆]. The internal temperature of the nano-particle arises from vibrations in the crystal lattice and provides a net zero oscillation to the entire particle. In addition, since the mechanical frequency of the CoM motion is very different from the phonon vibration frequencies, in a vacuum environment the two temperatures are completely decoupled and the internal temperature of the nano-particle can typically be neglected on the dynamics of the opto-mechanical system. Whilst this temperature does not directly impact the opto-mechanical system, large changes in internal temperature can modify the physical and optical properties of the nano-particle and can even vaporise them from the trap. For the optically levitated particle in a fixed potential, the CoM temperature is related to the average kinetic energy of the nano-particle. As a result, in order to cool down the nano-particles CoM temperature the nano-particle motion needs to be minimised.

In the following sections, I will first cover Doppler cooling for atoms, relying on the resonances of atomic transitions, before investigating the current strategies for cooling dielectric particles. Chapter 3 will provide the feasibility study of using Nitrogen Vacancy centres to create an optically trapped dielectric particle that acts like a giant atom.

[◆◆]There is also a particle motion associated with rotations and libations that have not been considered in this thesis.

Doppler Cooling

Doppler cooling is the predominant cooling strategy that can be used to trap and slow the motion of atoms, thereby forming the foundation for a number of experiments that includes generating Bose-Einstein condensates and producing accurate atomic clocks: achieving accuracy better than 1 part in 10^{15}. I introduce Doppler cooling in detail since it is the ideal passive cooling technique to apply to a massive dielectric particle that exhibits strong resonant dipole forces in order to bring the motion of the particle down towards its quantum ground state. In light of this, it is worthwhile to describe this technique and mention the implications of applying this technique on a more massive object.

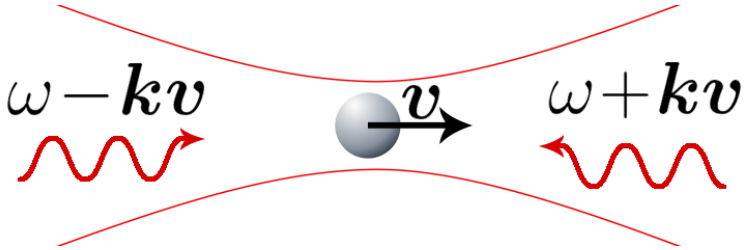

Figure 2.21: Doppler cooling shift in one dimension. The atom interacts with two counter-propagating waves with the same frequency $\omega < \omega_0$. In the reference frame of the the moving atom, the wave that opposes its motion is closer to resonance than the one in the direction of motion and the scattering force of the opposing wave dominates, slowing down the atom.

First we consider an atom with velocity $\boldsymbol{v}$, placed in two counter propagating laser waves of the same frequency ω, slightly below the atomic frequency ω_0 as shown in Figure (2.21). We denote the detuning from resonance by,

$$\delta = \omega - \omega_0 < 0. \tag{2.73}$$

The two counter propagating waves both produce a scattering force on the atom in opposing directions. For a stationary particle the components of each wave cancel, however for a moving atom with velocity along the laser axes $\boldsymbol{v}$, the atom 'sees' the two laser frequencies are now shifted by the Doppler shift $\pm\boldsymbol{kv}$. For a small saturation parameter ($s \ll 1$) and averaging over a half wavelength, coherences between the two waves can be neglected [90]. Thus the radiation pressure force $\boldsymbol{F_1}$ and $\boldsymbol{F_2}$ arising from each wave can be evaluated separately

and the total force on the atom is then given by,

$$\boldsymbol{F_{doppler}} = \boldsymbol{F_1} + \boldsymbol{F_2}. \tag{2.74}$$

The radiation pressure force for the wave in the positive $\boldsymbol{k}$ direction in the small intensity regime ($\Omega_1 \ll \Gamma$) is then,

$$\boldsymbol{F_1} = \hbar \boldsymbol{k} \frac{\Gamma}{2} s_1, \tag{2.75}$$

where,

$$s_1 = \frac{\Omega_1^2/2}{(\delta - \boldsymbol{kv})^2 + \frac{\Gamma^2}{2}} = \frac{s_0}{1 + 4\left(\frac{\delta - \boldsymbol{kv}}{\Gamma}\right)^2}, \tag{2.76}$$

with,

$$s_0 = \frac{2\Omega_1^2}{\Gamma^2} = \frac{I}{I_{sat}}. \tag{2.77}$$

Similarly the radiation pressure force for the wave in the negative $-\boldsymbol{k}$ direction in the small intensity regime ($\Omega_1 \ll \Gamma$) is,

$$\boldsymbol{F_2} = -\hbar \boldsymbol{k} \frac{\Gamma}{2} s_2, \tag{2.78}$$

where,

$$s_2 = \frac{\Omega_1^2/2}{(\delta + \boldsymbol{kv})^2 + \frac{\Gamma^2}{2}} = \frac{s_0}{1 + 4\left(\frac{\delta + \boldsymbol{kv}}{\Gamma}\right)^2}, \tag{2.79}$$

with the same s_0 defined previously.

The sum of the two forces is now,

$$\boldsymbol{F_{doppler}} = \hbar \boldsymbol{k} \frac{\Gamma}{2} \frac{I}{I_{sat}} \left(\frac{1}{1 + 4\left(\frac{\delta - \boldsymbol{kv}}{\Gamma}\right)^2} - \frac{1}{1 + 4\left(\frac{\delta + \boldsymbol{kv}}{\Gamma}\right)^2} \right). \tag{2.80}$$

For a negative laser detuning, the force on the atom is always in the direction opposite the motion. Figure (2.22) shows this dependence for a negative detuning ($\delta = -\Gamma/2$). We can see that for positive velocities, the atom experiences a negative force opposed to the motion. Similarly, for negative velocities the atom experiences a positive force further slowing down the motion. This can be interpreted by noting that as the atom moves towards a laser field, the Doppler shift ($\boldsymbol{kv}$) brings the atom closer to resonance increasing the scattering force and opposing the motion. A force opposing the velocity can be considered

as a friction force, damping the motion of the atoms. Since this friction force only acts in one direction, six Doppler beams are needed to cool the cloud of atoms, which can ultimately reach temperatures below one milli-Kelvin. This technique is also known as optical molasses, since the dissipative optical force resembles the viscous drag on an object moving through molasses.

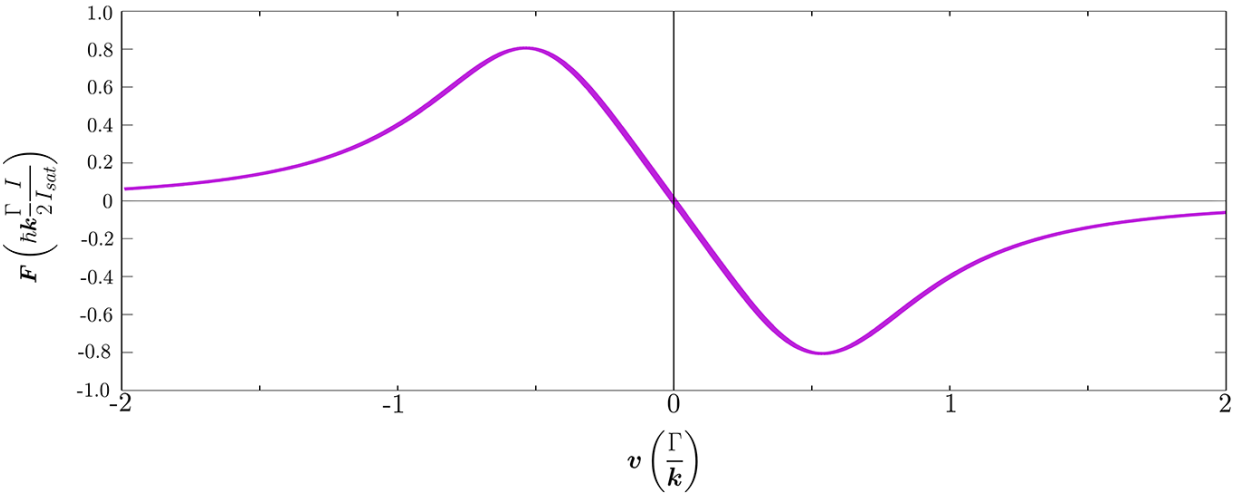

Figure 2.22: Doppler cooling force in normalised units. The resulting force arising from two counter propagating beams interacting with an atom with velocity $\boldsymbol{v}$ and detuning to the transition frequency by $\delta = -\frac{\Gamma}{2}$. The total radiative force on the atom always opposes the velocity of the atom resulting in a frictional force that damps the motion of the atom.

In order to obtain the minimum temperature reached by Doppler cooling, one must calculate the heating rate that opposes the effects of Doppler cooling. The heating rate arises due to fluctuations in the radiation pressure force arising from the statistical nature photon interactions imparting momentum on the trapped object. Assuming we are far from saturation ($s \ll 1$), this calculation predicts that the lowest temperature reached by Doppler cooling is given by [91],

$$k_B T = \frac{\hbar\Gamma}{8}\frac{1 + 4\delta^2/\Gamma^2}{-\delta/\Gamma}, \tag{2.81}$$

which is dependent on the detuning δ and the transition linewidth Γ, and surprisingly not on the intensity of the lasers forming the molasses. The minimum temperature that can be

achieved is when $\delta = -\frac{\Gamma}{2}$ and is then given by,

$$T_{Dop}^{min} = \frac{\hbar\Gamma}{2k_B}, \tag{2.82}$$

which is know as the Doppler limit.

Whilst this temperature limit appears to be much larger for optical defects than for atoms due to their much larger transition linewidths, there are numerous techniques developed in order to cool the particle past this theoretical limit. In fact, when the Doppler limit was investigated in detail for atoms [92, 93], it was shown that in certain circumstances the temperature of the atoms reached temperatures one or two orders of magnitude below the Doppler limit. This particular phenomenon was christened the Sisyphus effect and could cool the atoms further down towards the second temperature limit, called the recoil limit. In fact there are a large number of cooling mechanisms to bring the temperature down past the Doppler limit towards the recoil limit which rely on the internal energy structure given by the atom and its associated resonances. The recoil temperature however, arises for all of the radiative cooling techniques since each cooling photon is quantized and thus imparts a quantised recoil velocity,

$$V_R = \frac{\hbar k}{m} \tag{2.83}$$

where m is the mass of the atom. The lowest limit for radiative cooling called the recoil temperature and is then given by,

$$\begin{aligned} T_R &= \frac{mV_R^2}{k_B} \\ &= \frac{\hbar^2 k^2}{k_B m}, \end{aligned} \tag{2.84}$$

which interestingly does not depend on the transition linewidth and becomes colder for increased mass, as is the case with levitated nano-diamonds containing optical defects.

I have covered the main trapping and cooling strategies of atom trapping and the underlying concepts behind them, showing that the resonant energy structure within the atoms enables a wealth of cooling techniques. This section provides the foundation for investigating

and comparing the known forces and possible resonant forces on larger dielectric particles with an embedded internal structure. For completeness, I should mention that there are even more cooling strategies to bring the temperature of the atoms down even further into the sub-recoil temperature. I have only touched the surface of the complete array of cooling techniques for atoms as I believe it to be beyond the scope of this thesis, however further details can be found in the following review articles [94, 95].

'One must imagine Sisyphus happy.'

– Albert Camus, Myth of Sisyphus

Dielectric Cooling

There are two current approaches to cooling the CoM motion of levitated nano-particles, feedback cooling [28–30] and cavity cooling [24, 31, 32]. In feedback cooling, the particle position has to be measured accurately in order to operate a feedback loop. Measurement uncertainty in the position limits the lowest attainable temperature which is fundamentally limited by the standard quantum limit [29, 69]. The standard quantum limit is reached when the measured position uncertainty of the particle equals the momentum uncertainty due to photon recoil. For scattered light composed of a mean number of photons N, the uncertainty in the measurement due to shot noise is,

$$\Delta N = \sqrt{N}, \tag{2.85}$$

giving a nano-particle momentum uncertainty of,

$$\Delta p = \sqrt{N}\hbar k. \tag{2.86}$$

From the Heisenburg uncertainty principle, $\Delta x \Delta p = \frac{\hbar}{2}$, such that the minimum possible position uncertainty is,

$$\Delta x = \frac{1}{2k\sqrt{N}}. \tag{2.87}$$

Now we can see that the position measurement improves as the number of photons N increases. We can not however continue to increase N, since the large photon numbers lead to a large momentum spreads as seen from Equation (2.86). The increase in momentum spread due to large photon numbers is called recoil heating and causes an increase in the uncertainty of the oscillator energy, thereby allowing for an increase in the probability of exciting the quantum mechanical state of the mechanical oscillator.

The total uncertainty in the oscillator energy depends on the uncertainty of both Δx and Δp and is given by [29],

$$\begin{aligned}\Delta E &= \frac{1}{2}\left(m\Omega_0^2\Delta x^2 + \frac{\Delta p^2}{m}\right) \\ &= \frac{1}{2}\left(\frac{m\Omega_0^2}{4k^2N} + \frac{N\hbar^2k^2}{m}\right)\end{aligned} \tag{2.88}$$

The first term is related to the measurement uncertainty due to the random arrival of photons and the second part is the recoil heating arising from the measurement back-action due to momentum transfer. The lowest noise, known as the standard quantum limit occurs when the back-action equals the measurement uncertainty, giving $N = N_{SQL} = \frac{m\Omega_0}{2\hbar k^2}$.

Minimising this energy uncertainty reduces the probability of exciting the quantum mechanical state of the oscillator, which are separated in energy by $\hbar\Omega_0$, where Ω_0 is the CoM angular frequency defined by the particle mass and trap stiffness as $\Omega_0 = \sqrt{\frac{\kappa}{m}}$.

This discussion highlights the trade-off between measurement accuracy and recoil heating due to photon scattering. Whilst most photons do not interfere with the centre of mass state of the mechanical oscillator, the higher powers required to perform continuous position measurements limits the quantum state coherence time.

Cavity cooling is a passive cooling technique and therefore eliminates the need for continuous measurement acquisition allowing for the particles to be cooled to even lower temperatures with reduced trapping powers. Cavity cooling relies on the coupling between the cavity mode and Rayleigh scattering off the particle, shifting the cavity frequency along the cavity axis. In passive cooling strategies of this kind the temperature is reduced as the heating mechanisms are removed. In perfect vacuum, a cooling strategy of this kind is expected to

reach colder temperatures than a feedback mechanism, however due to the geometry of the system, the cooling can not be achieved in all three spatial dimension and the particle can boil out of the trap in the transverse dimensions as the vacuum is reduced.

Whilst these techniques are showing promise in cooling the nano-particles CoM motion towards the quantum ground state, they have not yet achieved this goal. In particular, proposals have been made to combine both the passive cavity cooling and feedback cooling strategies to achieve ground state cooling, however they will still greatly benefit from a strong non-linear coupling such as the case in atoms. Additionally, once the nano-particles are cooled to the ground state a number of the quantum opto-mechanical applications rely on a strong non-linear coupling to be feasible, which these strategies do not provide.

Besides controlling the CoM temperature, critical in quantum opto-mechanical applications, the nano-particles internal temperature must also be managed. Whilst the CoM temperature and the internal temperature are naturally decoupled due to greatly different energy scales, the internal temperature can directly influence the physical properties of the nano-particle and any embedded defects. Additionally, ensuring that the nano-particle does not melt or vaporise in the optical trap is important [96]. When the nano-particle is trapped in air, it can convectively cool to the surrounding gas medium, however in vacuum, unless laser cooling is used [97], the dominant way to reduce the temperature of the nano-particle is through radiative pathways. Whilst the transparency of diamond is ideal to avoid absorption of the trapping laser, the high transparency is maintained through to the far infrared preventing efficient radiative emission of thermal phonons. As a result, it has been observed that the nano-diamonds are heating and subsequently lost from the trap either through graphitisation or sublimation [98]. The heating in nano-particles in general is through absorption or inelastic Raman scattering of the trapping laser. In addition, any optical defects in the crystal lattice absorb photons of higher energy and emit lower energy photons where the difference in photon energy is dumped into thermal energy in the crystal. Multi-phonon excitation processes are often present in these optical defects that can thus produce a heating effect even when the trapping laser wavelength is lower in energy than the optical transition. These problems appear to be strongly sample dependent and I suspect this is due to some samples having more optical defects or attached amorphous carbon than

others. These heating mechanisms can lead to the nano-diamonds being incinerated once an efficient cooling mechanism is missing for high enough vacuum. Thus, the vast array of quantum opto-mechanical applications would not be feasible. In addition, the additional heat can alter the optical defect properties since they are strongly temperature dependent. For example, the width of the resonance of optical defects broadens with increased temperature. Ensuring the crystal is as cold as possible is therefore advantageous in improving the optical transitions required for cooling of the CoM temperature of the particle. As a result, improved sample preparation and control over the nano-diamonds internal temperature is essential for optically levitated nano-diamonds. In chapter 5, I will discuss the possibility of using the internal optical defects to passively cool the nano-diamond whilst simultaneously cooling the CoM motion of the nano-diamond.

'A subtle thought that is in error may yet give rise to fruitful inquiry that can establish truths of great value.'

– Isaac Asimov

3

Investigating the Dipole Force on Nitrogen Vacancy Centres in Nano-Diamonds

3.1 Introduction

The aim of this section is to explore the possibility of levitating a dielectric particle containing atomic tranisitions that interact with the incident light field producing a resonantly enhance optical dipole force. In this way, the massive* levitated object will behave like an atom and the vast toolbox of cooling techniques that have been developed for atoms can be used on the nano-scale object. Whilst detuning dependent forces have been studied for micro and nano-particles exhibiting plasmonic resonances or Mie resonances, they are typically several tens of nanometres wide [99]. To engineer sharp Mie resonances [100], large particles are needed

*Massive in relation to the mass of a single atom.

with either near field coupling or complex propagating beams to efficiently excite them [101, 102]. In comparison, I propose to use optical defects in diamond which provide spectrally sharp resonances, even at room temperature. Since both the dipole from the NV atomic transition and from the dielectric nano-particle can be manipulated by the same incident optical field, we propose that forces on both induced dipoles can be achieved simultaneously. One challenge with using optical defects in comparison to atoms, with respect to generating resonant optical forces, arises due to the coupling between the optical defects and their environment. This coupling leads to an increased dephasing of the artificial atoms within the nano-particle, reducing the strength of the induced dipole and hence optical forces. Alternatively, since we can have many identical optical defects within the same nano-particle, the defects can behave cooperatively, drastically increasing the induced dipole strength and therefore optical forces.

Nitrogen Vacancy (NV) centres were the initial candidate for observing theses forces since they have attracted significant attention over the past decade and there are readily available nano-diamond samples with high concentrations of NV centres exhibiting low strain and low amorphous carbon impurities. The NV centre consists of a Nitrogen atom and an adjacent vacancy site within a diamond crystal generating an array of interesting optical properties when it is in the negatively charged state NV^- (See Figure 3.1). The NV^- centre displays outstanding spin optical properties that persist even at room temperature making it suitable as a solid state spin qubit and nano-scale magnetic sensor. In this thesis I am mainly interested in the transisiton optical properties of the NV centre rather than the spin optical properties that the NV possesses. The NV^- shows a strong stable zero phonon line (ZPL) around 637 nm followed by a wide broad phonon side band (PSB) emitting fluorescence out to approximately 800 nm at room temperature. Due to their strong stable fluorescence, NV^- centres have also been used extensively as bio-labels for high resolution, real time and low disruption imaging of living cells [9].

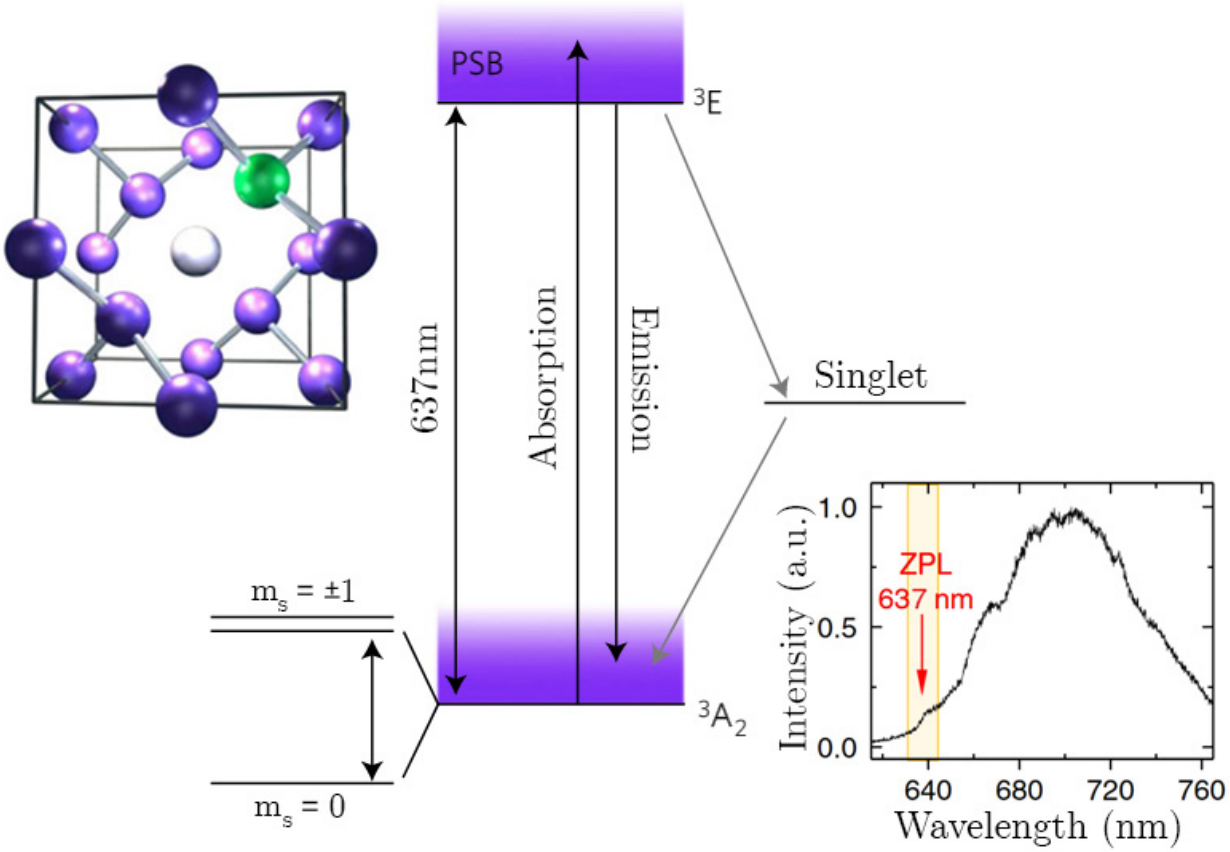

Figure 3.1: Physical and energy level structure of the NV centre with its associated fluorescence spectra. Top left is the unit cell structure of the NV centre in the diamond matrix. The carbon atoms are shown in purple, the lattice vacancy in white and substitutional nitrogen atom indicated in green, connected together by the associated covalent bonds. In the centre of the image is the energy level scheme of the NV^- centre displaying the typical optical and non radiative transitions. Bottom right is an example of the NV^- centre room temperature fluorescence signal. The NV^- shows a strong stable zero phonon line (ZPL) around 637 nm followed by wide a broad phonon side band (PSB) emitting fluorescence out past 780 nm. For a more detailed understanding of the NV centre, its charge states and its internal spin structure refer to Chapter 4.

3.2 Previous Work and Motivation

Initially, a proof of principle experiment was performed to observe the atomic dipole forces on NV centres in liquid trapping [103]. I will review this experiment as it sets the foundations of the work in this thesis. This experiment observed enhanced dipole forces in the same nano-diamond sample that we use to observe the resonant optical forces in levitation. It

also provides an introduction to a number of interesting properties of the nano-diamonds including the unexpected observation of cooperativity.

In this experimental platform, a Gaussian standing wave trap was formed by focusing a Gaussian beam on a silver coated mirror. The standing wave pattern creates a stronger trap along the direction of propagation compared with a standard single beam Gaussian trap. In addition, the scattering force can be neglected since the scattering force arising from incident and reflected beams will cancel out. The mirror forms the top of a static microfluidic chamber that contains the nano-diamonds suspended in deionised water (See Figure 3.2).

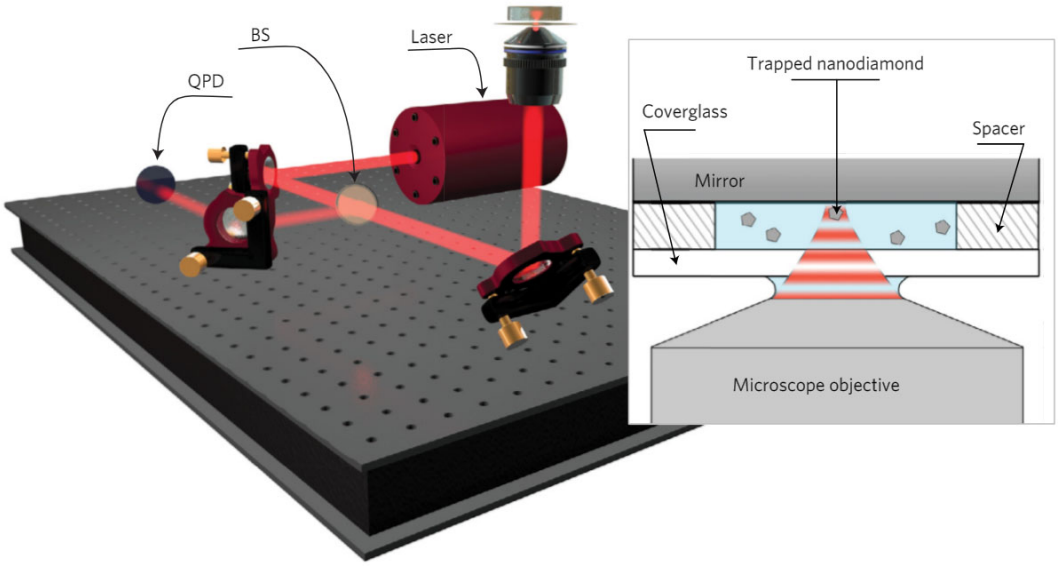

Figure 3.2: Experimental set-up for observing cooperatively enhanced dipole forces from Nitrogen Vacancy centres in trapped nano-diamonds. The trapping laser is focused through a high numerical aperture objective into a microfluidic chamber producing a strong optical trap. The microfluidic chamber (right panel) consists of a cover-glass (145 µm thick), a spacer (140 µm thick) and a mirror on the top that results in a standing wave, improving the trapping efficiency and minimizing the scattering force. [103]

The investigated nano-diamonds were initially characterised using a home built combined confocal/AFM microscope set-up [104]. The samples with a high concentration of NV centres show a ZPL centred at 639.1 $\pm$ 0.7 nm with an average spectral width of 2.1 $\pm$ 0.6 nm (See Figure 3.3a and 3.3b). The shifting and broadening of the NV^- centres' ZPL is attributed to imperfections in the surrounding lattice which includes strain, nearby charge traps or foreign

atoms within the nano-diamonds. Additionally, the size distribution of the nano-diamonds was determined using dynamic light scattering, resulting in an average size of $(100 \pm 23\,\text{nm})$. The expected number of NV centres per nano-diamond is $\langle NV \rangle \approx 9500$ [105].

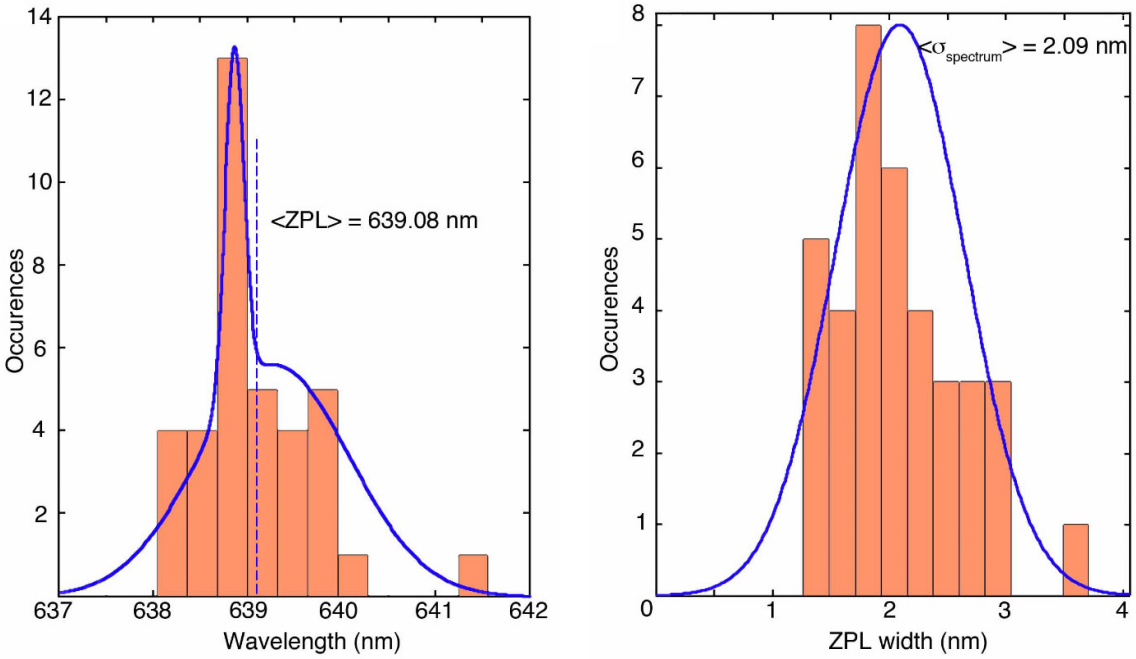

(a) (b)

Figure 3.3: Optical properties of nano-diamonds containing many NV centres extracted from photo-luminescence spectra obtained on 40 different nano-diamonds. **(a)** Position of the ZPL. The distribution consists of two clearly distinct populations which was approximated by two normal distributions. The overall average ZPL position is $\langle ZPL \rangle = 639.08\,\text{nm}$ **(b)** Spectral width of the ZPL peak. The distribution was fitted by a normal distribution (blue), giving an average value of $\sigma = 2.09\,\text{nm}$ [104].

In order to observe the forces on the nano-diamonds the trapping stiffness κ was measured. The trapping stiffness κ is obtained by recording the position of the particle using a quadrant photodiode (QPD) and by extracting the corner frequency (See Chapter 3.4.2 for comprehensive details on this method). Due to the stiffness' dependence on the size of the nano-diamond, which can not easily be measured in the trap, the trapping stiffness of a particular wavelength was always compared to a reference trapping wavelength of 639.13 nm. Since the atom like forces are dependent on the detuning of the trapping laser from the optical transition, it is expected that using a reference laser centred on the transition will

give no atom like forces. This comparison thus gives us a relative trap stiffness ratio, $\frac{\kappa(\lambda)}{\kappa(\lambda_{ref})}$, which is independent of the nano-diamond size.

To characterise the contribution due to the NV centres on the trap stiffness, the stiffness ratio was measured on a number of different nano-diamonds, for a given set of wavelengths, for two different nano-diamond samples: one with low concentration of NV centres and the second with a high concentration of NV centres. The low concentration sample serves as a reference as we do not expect the resonant forces to have a measurable effect on this sample. The resulting trap stiffness ratios as a function of laser wavelength for each sample of nano-diamonds with low and high concentration are displayed in Figures (3.4a) and (3.4b) respectively.

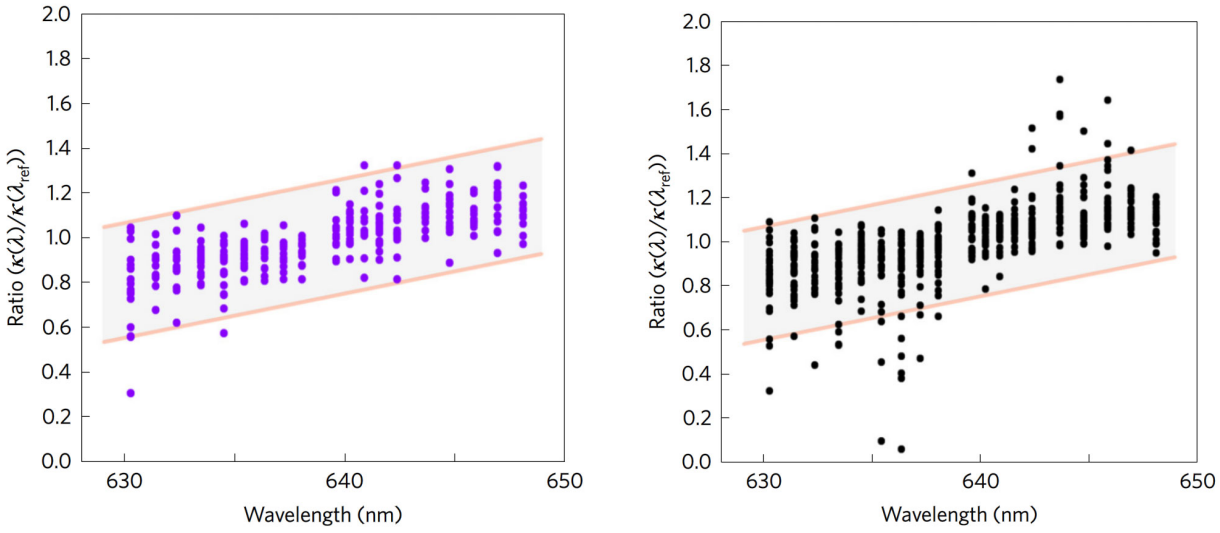

(a) Low NV concentration

(b) High NV concentration

Figure 3.4: Measured relative trap stiffness of trapped nano-diamonds in water for observing cooperatively enhanced dipole forces in NV centres with trap powers ranging from 4 mW to 6 mW. **(a)** Relative trap stiffness $\frac{\kappa(\lambda)}{\kappa(\lambda_{ref})}$ for nano-diamonds containing few NVs. The symmetric spread in the measured trap stiffness for a given wavelength is due to experimental noise. **(b)** Relative trap stiffness for nano-diamonds containing a high concentration of NV centres. The data scattering in this case is strongly asymmetric with stiffness ratios much lower than 1 for wavelengths below λ_{ref} and higher than 1 for wavelengths above λ_{ref}. The shaded areas are guides to the eye using three times the average standard deviation from the low-density NV sample with an overall linear trend. [103]

The monotonic trend in both samples is attributed to chromatic aberrations from the microscope objective that are aggravated by the standing wave pattern[†]. The large symmetric spread in the measured trap stiffness of the low density sample is due to experimental noise. Whilst the high density sample has both of these effects appearing, the data also exhibits a number of nano-diamonds that show significant deviations from the mean, displaying stiffness ratios much lower than 1 for wavelengths below λ_{ref} and higher than 1 for wavelengths above λ_{ref}. The extreme values are attributed to nano-diamonds with a large number of NV centres leading to a significant contribution of the atomic forces from the NVs to the trap stiffness. However, upon analysis it was found that the NV centres acting independently could not account for the trends observed or explain such dramatic deviations for a number of the nano-diamonds. To account for the trends observed, it was proposed that if there were cooperative effects between NV centres in the nano-diamonds, this effect would have a significant impact on the dipole forces by modifying both the spontaneous decay rate $\tau = \frac{1}{\Gamma}$ and the steady state population. The cooperative effect that could drastically increase the total dipole force and explain the observed trend is, superradiance.

Superradiance is a cooperative phenomenon which occurs when N collective emitters couple collectively to a mode of the electromagnetic field as a single, enhanced dipole. This gives rise to a burst of photon emission, with a peak emission rate proportional to N^2, rather than N for independent emission. The principle condition required for superradiance to arise is indistinguishability of emitters with respect to the field mode [106]. The two properties necessary to satisfy this criteria are spatial indistinguishability and spectral indistinguishability. Spatial indistinguishability occurs when the emitters are confined to a volume much smaller than the wavelength of the electronic transition, $V \ll \lambda$, which is satisfied for the case of NV centres in nano-diamonds. Spectral indistinguishability on the other hand is harder to satisfy in solid state emmiters due to the large inhomogeneous broadening and unavoidable dephasing. If the spectral separation of two emitters is much larger than the linewidth $\Delta\lambda \gg \Gamma$, then the two emitters are spectrally distinguishable and act independently. In contrast, if the spectral separation is within the linewidth the photons

[†]It appears that due to the non perfectness of the imaging system the microscope objective was in focus for 650 nm, rather than 639 nm: confirmed by an optical tweezer computational model [103].

emitters begin to become indistinguishable. The closer and better the overlap the stronger the spectral indistinguishably becomes.

The most observable feature of superradiance is the accelerated optical emission, scaling faster than linearly with the number of emitters. The nano-diamond sample was thus investigated for superradiance by measuring the decay curves of 100 separate nano-diamonds with high concentrations of NV centres. The nano-diamonds were then compared against a Dicke model of NV centre superradiance [107]. Figure (3.5a) shows a subset of NV decay curves representative of nano-diamonds of different size and brightness. The red curve is the decay curve for a single NV centre used for reference. The faster diamonds were not well fit by exponentials, but rather required a superradiant model [107].

The specific details of the model can be found in the supplementary material of reference [107]. Within each nano-diamond the spectral indistinguishability of each of the NV centres cannot be guaranteed. As a result the model breaks down the superradiance into D spectral domains of N cooperative NV centres. Within each domain the collective state is described using Dicke States [106]. Whilst the exact interpretation of breaking the superradiance into individual domains is not clear, this superradiance model accounts for the extreme variance observed between nano-diamonds and accurately fits the time resolve fast fluorescence measured in Figures (3.5b to 3.5e). What is clear is that there are many mechanisms involved that influence the spectral indistinguishability, including dipole-dipole interactions and dephasing, differing significantly due to crystal strain and distance between emitters. As a result the superradiance measured depends strongly on the nano-diamond and can range from domains of $D = 1$, where they are all acting independently, to $D = 50$ where the nano-diamond is strongly superradiant. It is important to realise here that the expected average number of NV centres in the nano-diamonds are $\langle NV \rangle = 9500$, and we are still in a regime far from purely superradiant.

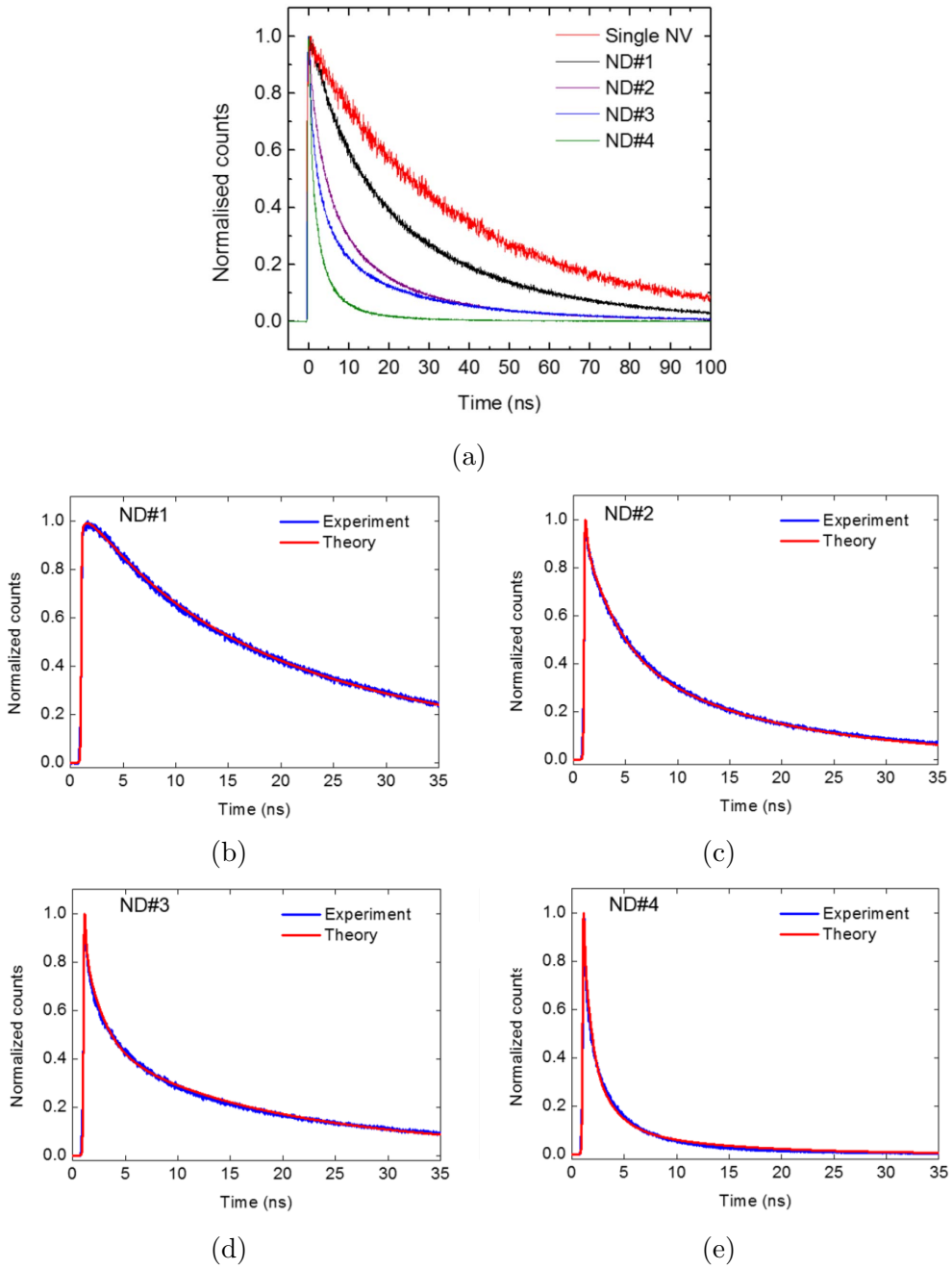

Figure 3.5: Superradiance from nano-diamonds with containing NV centres. **(a)**, Measured normalised fluorescence decay curves for five different NDs, with lifetimes ranging from the usual few tens of nanoseconds for a single NV centre in a ND (red trace), to lifetimes around 1ns for high NV density nano-diamonds (green trace, ND # 4). **(b-e)**, Fluorescence decay curves (blue) and corresponding fits (red) for four different high NV concentration nano-diamonds. Note that the curves are normalized to their respective maximum. The different nano-diamonds exhibit increasingly faster photo-emission with corresponding lifetimes of $(25, 3.6, 2.2, 1.1)$ns for NDs 1–4 respectively. The shorter lifetimes correspond to larger collective domain sizes of $D = (2, 7, 10, 50)$, respectively. [107]

Nevertheless, the skewness of the measured ratios in Figure (3.4) and the reason only a small number of the nano-diamonds exhibited a significant and strong resonant force arising from the NV centres can be attributed to the observation of superradiance in this nano-diamond sample. Whilst these measurements indicate that there are resonant forces acting on a bulk object we are far from dominating the motion of the particle with the atomic forces and being able to apply the powerful quantum technologies developed for atom trapping and cooling, in this more massive regime. Ideally, we aim to engineer or selectively trap strongly superradiant NV centres in nano-diamonds in order to continuously probe their resonant properties.

3.2.1 Optically Levitated NV centres

Moving to optical levitation is the clear next step for observing atomic dipole forces in nano-diamonds for a number of reasons. Firstly, levitation is one step closer to an under-damped trapping regime, which is essential for any optical cooling strategy to work. Secondly, in the water trapping experiment a single nano-diamond could not be held indefinitely since there was a significant probability that a second nano-diamond may randomly float into the optical trap. In this case the trapping trace must be discarded and a new single nano-diamond must be found. The consequence is that the trapping ratio can not be measured across the entire wavelength range and statistics on many nano-diamonds are essential. In optical levitation the trapped nano-diamond can be held indefinitely once the chamber has been purged of all additional nano-diamonds that are floating near the trap. In this case, it is possible to measure the trapping forces on a single nano-diamond as we tune the trapping laser across the transition of interest. Ideally, we would trap a nano-diamond that contains many NV centres with strong superradiance, such that the dipole force on the ensemble of NV centres is stronger than the dipole force on the bulk nano-diamond. In addition, we are not just interested in the 637 nm dipole transition of the NV centres, but also the 1042 nm singlet state transition of the NV centre, as well as the ZPL transitions of both the Silicon Vacancy (SiV) centre and Germanium Vacancy (GeV) centre shown in Figure (3.6). Silicon Vacancy and Germanium vacancy centres will be covered in Chapter 5, however at the outset, we

considered the NV centre as the optimal candidate due to the availability of a clean[‡], highly concentrated nano-diamond sample with previous evidence that cooperative dipole forces can be observed.

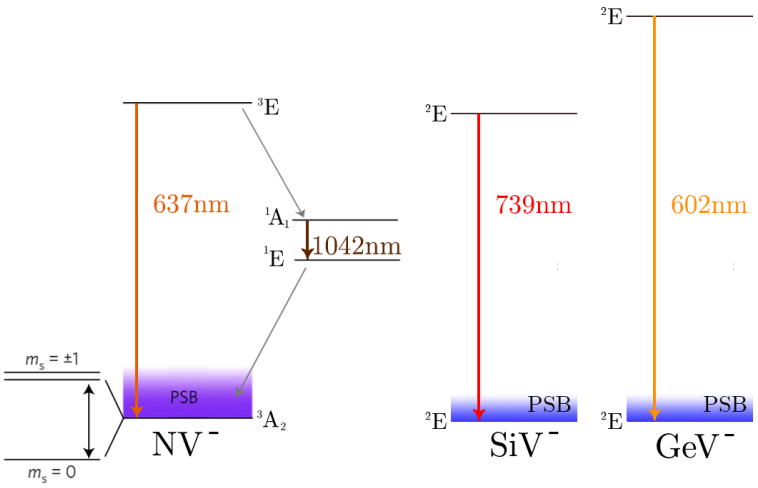

Figure 3.6: Transition diagram of optical defect in diamond. On the left is the level scheme of the NV$^-$ centre displaying the relevant optical and non radiative transitions. The NV$^-$ centres have a strong optical transition around 637 nm. From the excited state the defect can decay non-radiatively into the excited $^1A_1$ singlet state. The middle diagram is the level scheme of the SiV centre displaying the relevant optical and non radiative transitions. The SiV centres have a strong optical transition around 739 nm with a smaller PSB. On the right is the level scheme of the GeV centre displaying the relevant optical and non radiative transitions. The GeV centres have a strong optical transition around 602 nm. [108]

Whilst the experiment is designed to be customisable for investigating different optical resonances, we initially decided to concentrate on the 1042 nm singlet transition for a number of reasons. Firstly, it had been observed that under strong 637 nm laser irradiation, such as is required for levitation, the NV$^-$ centre fluorescence is quenched due to ionisation into the NV^0 state which will drastically reduce the expected resonant dipole force [109]. Additionally, the 1042 nm transition in the NV centre is expected to have a 10× stronger dipole moment than the 637 nm transition, as well as having a much sharper transition linewidth of 1 GHz rather than 100 MHz as for the 637 nm transition [110]. This transition is also not expected to have nearly as strong a phonon side band, which reduces the expected force by an estimated 96% for the 637 nm ZPL since there is only a 4% probability that the emitted photon is

[‡]The nano-diamonds are clean in regards to surface impurities such as graphitic and amorphous carbon that drastically increased absorption leading to much larger scattering forces and heating rates.

emitted within the ZPL. Unfortunately, the quantum yield of the 1042 nm transition is tiny, on the order of 10^{-4}–10^{-5}, which will also cause a large reduction in the optical dipole force. Our running hypothesis at the time was that the reduction in fluorescence from the NV centre under 1064 nm light was due to electron storage in this 1042 nm transition which would result in a drastically increased optical dipole force. Importantly, for the measurement of this force, the 1042 nm transition will have zero electron population unless the NV^- centre has first been excited. Only when the NV^- centre is excited will an electron population transition into the singlet states, enabling the field to interact with this transition, leading to the creation of an induced dipole and thus optical force. As a result the atomic trapping force can be conditionally switched on and off with a low power excitation beam ideal for experimental observation. The cooperative effects of this state however, are completely speculative so the possibility of this transition to show a significant atomic force was unknown[§]. Regardless of whether or not the forces on the 1042 nm transition could be observed or not, the optical levitation platform was designed in such a way that changing optical transitions and therefore tunable trapping laser wavelengths is a simple process and the 637 nm optical forces could be investigated instead.

3.3 Experiment Overview

In this section I present the experimental apparatus, procedures and technological solutions that I have developed in order to build an experimental platform to analyse the optical forces on optically trapped nano-particles. Specifically, I focus on developing a custom-built optical levitation system and developing an imaging system to comprehensively monitor the motion of the particles within the trap. I aim to accurately measure the trapping forces in real time to provide an ideal platform for investigating and characterising the forces on atomic defects within trapped nano-particles. Finally, I will focus on trapping the Nitrogen Vacancy centres in nano-diamonds and develop the protocols for quantitatively measuring the classical and atomic trapping components.

[§]In fact, the following experiment was started before the liquid trapping measurements were completely understood and explained by a cooperative process. In hindsight, this transition was not the optimal transition.

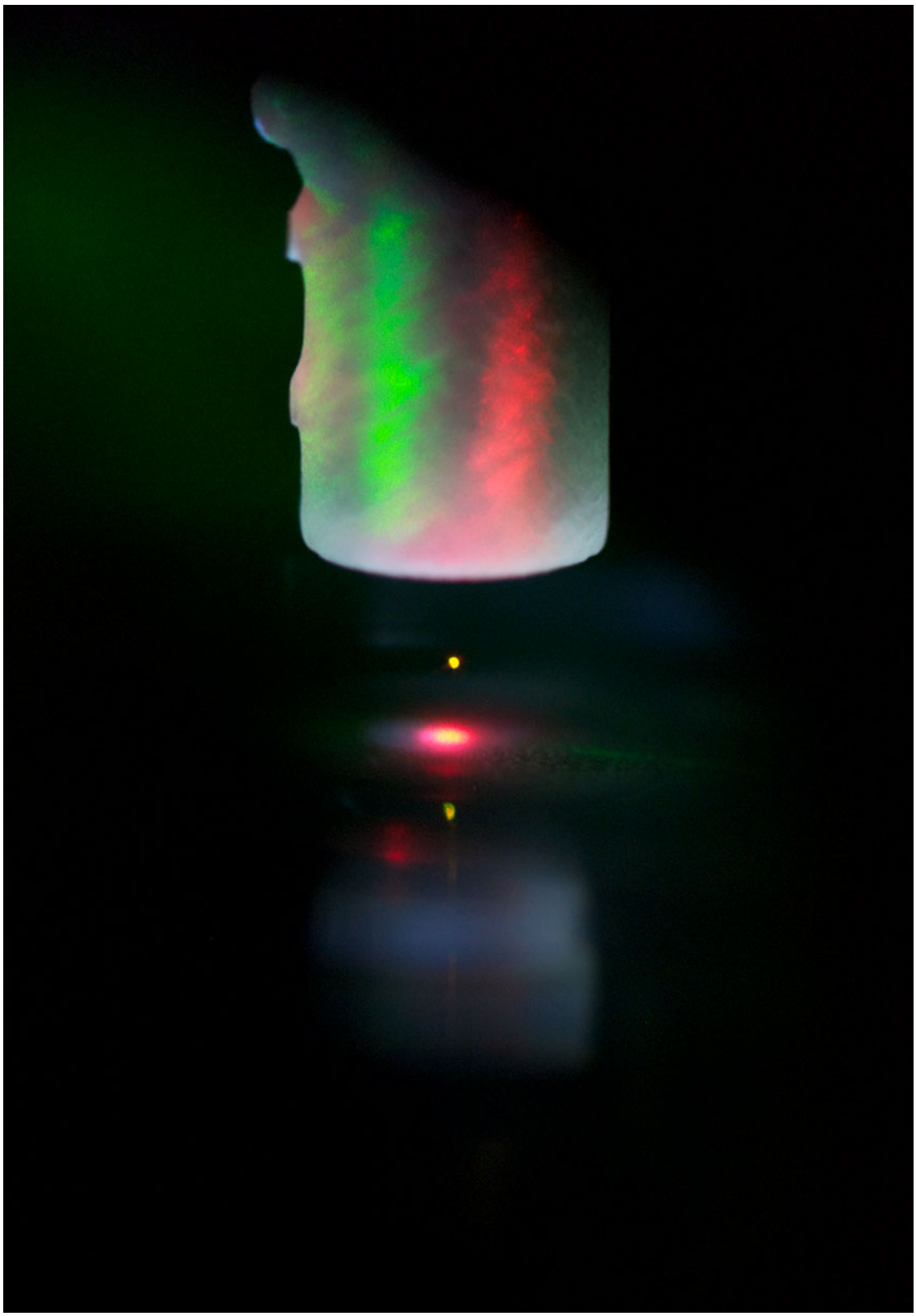

Figure 3.7: Photo of a levitated nano-diamond trapped in our optical levitation platform in air. The bright yellow spot is the diffraction limited scattering of the 100 nm nano-diamond. Above the nano-diamonds is the injection nozzle for nebulizing nano-diamonds into the trapping chamber. Below the nano-diamond is the trapping microscope objective covered by a microscope objective slide.

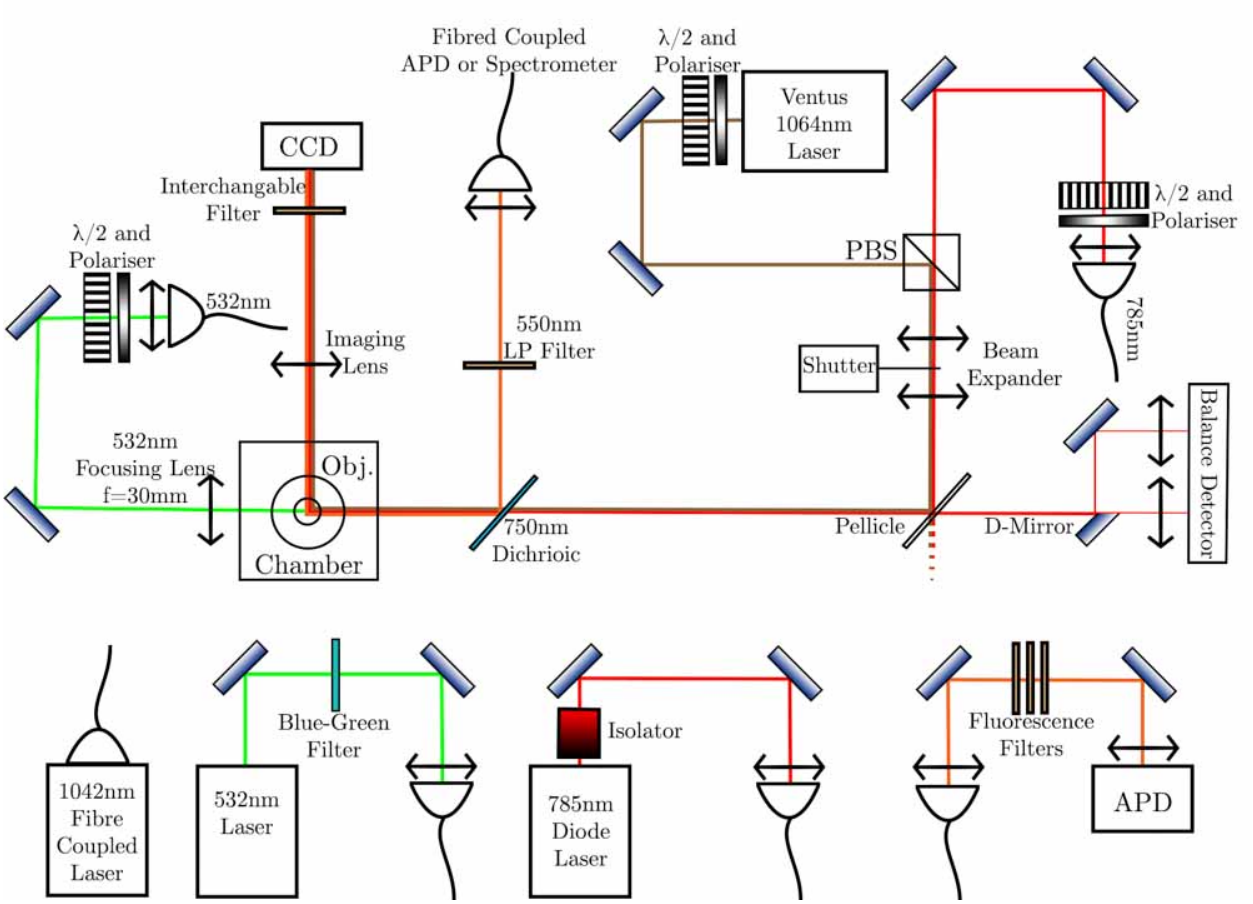

Figure 3.8: Schematic representation of the optical trapping optics providing a platform for measuring the forces on an optically levitated nano-particle. A nano-particle is trapped at the focus of the objective lens enclosed within a custom built chamber. The 785 nm and 1064 nm trapping laser are polarisation controlled and combined on the polarising beam splitter (PBS). The trapping lasers are then expanded to match the back aperture of the objective before being reflected off the pellicle beam splitter into to the microscope objective. The scattered signal from the trapped nano-particle is back reflected through the pellicle beam splitter and measured using a balance detector. A green laser is also focused onto the nano-particle for fluorescence excitation of NV centres. The fluorescence signal is collected by the microscope objective and reflected off a 750 nm longpass dichroic mirror and coupled into a multimode fibre. The fluorescence signal can then be connected to either a fibre coupled spectrometer or avalanche photo diode (APD) for detection. Fianlly, a CCD imaging camera is aligned to image the initial trapping of particles in the trapping chamber using a single $f = 75\,\mathrm{mm}$ imaging system.

The optical elements of the optical levitation platform can be observed in Figure (3.8). Two optical trapping lasers can be used independently by cross polarising the two NIR lasers and combining them with a polarisation beam splitter (PBS). The Ventus 1064 nm

laser is the main trapping laser, with the second laser being either a 785 nm diode laser or a 1042 nm tunable laser. The output of the Ventus 1064 nm trapping laser is incident on a half wave plate and polariser to control the power whilst simultaneously maintaining horizontal polarisation. The power of the 785 nm diode laser or 1042 nm tunable laser is controlled through the combination of a fibre paddle polarisation controller and a half waveplate and polariser, which also ensures that the polarisation on the PBS is vertically polarised. The output coupler for this path was chosen so that either the 785 nm or 1042 nm laser output will have a beam size that approximately matches the 2.4 mm diameter output of the Ventus 1064 nm laser. The trapping lasers are now combined through the PBS to be collinear and are then expanded using a beam expander to tailor the beam size of the lasers to fill the microscope objective in order to optimise the trapping potential at the focus.

A custom built shutter was aligned with the focal point of the beam expander in order to allow for transiently blocking all of the trapping laser power incident on the levitated particle. The trapping beams are then reflected by a pellicle beam splitter, transmitting through a 750 nm dichroic mirror before reflecting vertically into the microscope objective, enabling the trapping of a levitated nano-particle at the focal spot. The scattered light from the nano-particle is collected by the microscope objective and back propagated through the pellicle beam splitter and is imaged using a balanced detector set-up as described in Section (3.4.2) for position measurements. Imaging of the optical trapping chamber and visualising the behaviour of the particles is done using a CCD camera and a single one lens (100 mm) imaging system with a 2× magnification.

For excitation of Nitrogen Vacancy centres in optically levitated nano-diamonds a 532 nm laser is input coupled into a single mode optical fibre. The output of the 532 nm fibre is then collimated before being focused on the optically levitated nano-particle using a 30 mm lens. The emitted fluorescence of the nano-diamonds is collected and collimated through the trapping objective before being reflected by the 750 nm dichroic mirror, spectrally separating it from the trapping laser wavelengths. A 550 nm long pass filter blocks the excitation laser allowing for the 550 nm to 750 nm fluorescence to be fibre coupled using a lens into a multimode fibre providing a confocal microscopy collection arrangement. A 400 nm to 600 nm blue-green bandpass filter is used on the laser output of the 532 nm laser in order to remove

trace amounts of unwanted pump laser at approximately 700 nm. If the filter is removed, the trace pump laser light is also focused on the levitated nano-diamond and is subsequently efficiently detected by the confocal fluorescence detection. Using the blue green filter completely removes this small unwanted signal, however this unwanted wavelength matches the emission of the NV centres and thus by removing the blue-green filter we can precisely align the confocal fluorescence detection path. The florescence counts can be analysed through either a fibre coupled spectrometer or counted using an avalanche photodiode (APD). For collection in the APD path the multi-mode fibre is collimated and refocused onto the APD sensor. Within this beam path additional filters are used to enable the changing of the detection window and to further reduce the unwanted signal from the trapping and excitation lasers.

In order to produce strong optical potential fields that are capable of optically levitating nano-particles it is essential that the trapping laser profile fills the back entrance objective entrance of the objective. The Ventus 1064 nm laser and the fibre coupled tunable 1042 nm laser have exceptional TEM00 Gaussian spatial profiles and do not require any beam preparation in this regard. The 785 nm diode laser however, produces a far from Gaussian profile that cannot be used in free space for optical trapping. As a result the 785 nm diode laser is fibre coupled into a single mode fibre using a lens with two additional cylindrical lenses to optimise the fibre coupling. An optical isolator is also mounted on the input path to ensure that no back reflected laser power through the optical set-up can interfere with the power and spectral stability of the laser diode. The optical fibre acts as a spacial filter such that the output of the fibre is only a TEM00 Gaussian profile that can now be used for optical levitation.

3.3.1 Optical Sources

Compared to traditional optical trapping and levitation, we use a large number of optical sources. This is due to the wavelength dependency of the internal defects. We need specific wavelengths that can either strongly or weakly interact with the internal defects as well as diamond matrix. The main laser to optically trap individual particles in air is a continuous

wave 1064 nm Nd:YAG laser (Ventus 1064, Laser Quantum). Continuous wave 1064 nm Nd:YAG lasers are commonly used for optical trapping because lasers of this type are commercially available at relatively low costs with high power, high stability and excellent beam profiles. However, there are two disadvantages that make trapping with this wavelength less than ideal. Firstly, microscope objectives are usually designed for the visible spectrum and typically have low transmission values in this wavelength range: rarely stated by the manufacturer. Secondly, the detection of a levitated nano-particle relies on the balanced signal of two photodetectors. The standard photodetectors are silicon based, which have a poor response to the infrared spectrum. The combination of these two effects produces a weaker position measurement efficiency which will correspond to a reduction in the sensitivity of the optical forces we are trying to measure. Additionally, it had been observed previously that a 1064 nm trapping laser suppresses or quenches the observed fluorescence of NV centres within a levitated nano-diamond [54]. When we initially began this experiment we partially attributed the quenching to the possibility of population cycling within the 1042 nm singlet states♦.

As a result, I implemented the 785 nm diode laser into the set-up to optically trap nano-particles. This wavelength should provide a better photodetector response as well as an increased transmission through the microscope objective, allowing for higher sensitivity force measurements with lower incident powers. In addition, it was anticipated that the 785 nm laser would not interfere with the internal dynamics of the NV centres♣. Unfortunately, the 785 nm diode laser has poor beam shape and needs to be fibre coupled in order to clean the beam profile and generate a nice Gaussian TEM00 beam profile which is required for optical trapping.

The third trapping laser is a tunable CW Toptica Photonics 1000 nm to 1090 nm fibre coupled laser. This laser was chosen so that it had the capability to trap the nano-diamonds and tune the wavelength across the 1042 nm singlet transition of the NV centre to observe

♦In Chapter 4 I will show that this fluorescence quenching is dominated by a charge state interconversion process leading to increased channels for non radiative decay.

♣As explained in Chapter 4 there does not appear to be an easily accessible wavelength to use for trapping of NV centres without interfering with the defect. Potentially working in the deep infrared will be possible since these photons may not have enough energy to efficiently ionise and recombine the defects charge state.

both the attractive and repulsive forces acting on the singlet transition of the optically levitated NV centres in nano-diamonds.

The final laser that is incident onto the nano-particles is a CW solid state 532 nm laser. This laser was implemented into the set-up in order to excite the NV centres in the levitated nano-diamonds in order to modulate the atomic dipole forces from the 1042 nm singlet state. Additionally, it provides a fluorescence signal providing a measurement of the NV centres internal electron dynamics. However, since the laser is focused onto the nano-particle it will also experience an unwanted additional optical trapping force. To minimise the impact of these optical forces on our measurements, we used a low NA lens and an excitation orientation such that the axial direction was aligned with the detection path to minimise the addition trap strength along this direction.

3.3.2 Microscope Objective

Once the optical source has been chosen, the microscope objective is the most important element for an optical trap in order to produce a strong gradient of the intensity. The choice of objective directly determines the efficiency of the trap. The efficiency of the trap is given by the trap stiffness versus the laser input power, which is a function of both the NA and the transmittance of the objective. A necessary condition to trap the particles is to produce a gradient force sufficiently large enough to overcome the scattering force that will push the particle out of the trap. Typically, it takes a high NA objective to produce a strong enough gradient profile to overcome the scattering force. The vast majority of objective lenses are complex multi lens constructions, designed specifically for imaging purposes using visible light, not for focusing high intensity infrared laser beams. Therefore the optical properties of different objectives in the infrared can vary widely. Unfortunately, manufacturers rarely supply information regarding transmission characteristics in the infrared.

When microscope objectives absorb the laser power the trapping system is negatively impacted in three ways. Firstly, the power in the trap focus is diminished compared to the available power at the back entrance of the objective. Secondly, the signal on the position detector is also reduced but more so, as the necessary signal is back reflected through the

objective further reducing the intensity. The last impact from an absorbing objective is that less power can be used before damage is caused to the objective. Unfortunately, microscope objectives do not give a damage threshold for maximum intensity through the objective, and they are too valuable for us to experimentally determine this value. In summary the more the objective absorbs, the more care is needed with the input laser power, both in damaging the objective and receiving a sufficient trapping signal.

The best trapping objective I used to optically levitate the nano-particles was a 100× 0.85 NA IR Olympus Objective. I directly measured the transmission of the objective at a variety of wavelengths from 785 nm to 1064 nm and observed the transmission of the objective to be consistently $\approx 85\%$.

Once the objective is chosen, tailoring the trapping laser beam size to fit the back entrance aperture is essential. Typically, the back aperture of an objective is a few mm in diameter and in order to provide the strongest focus and full use of the numerical aperture the incident laser field has to fill or overfill the back aperture. In 'Principles of Optics' by Lukas Novotny and Bert Hecht, the influence of the filling factor f_0 of the back-aperture of an objective lens on the intensity profile of the focus is analysed. The filling factor of the back-aperture is defined as the ratio of beam waist with the back-aperture radius. The intensity profile at the focus is calculated for a Gaussian beam using a rigorous angular spectrum representation that takes into account the vector nature of the fields and as a result, includes the polarisation effects that produces an elongated field confinement in the direction of polarization. The tightest focal spot occurs at the limit $f_0 \to \infty$, which corresponds to an infinitely overfilled back-aperture which is identical to the solution with a plane wave incident on the lens. Figure (3.9) from 'Principles of Nano-Optics' by Lukas Novotny and Bert Hecht demonstrates the effect of the filling factor f_0 on the confinement of the electric field intensity $|\mathbf{E}|^2$ [111].

It is clearly evident from this analysis that the filling factor is important for the quality of the confinement of the electric field intensity and therefore strength of the optical trapping potential. For example, in the case where the beam waist matches the back-aperture of the objective ($f_0 = 1$), then the maximum intensity at the focus is reduced by a factor of 2.53. This highlights that the lack of intensity in the largest k-vectors drastically reduces

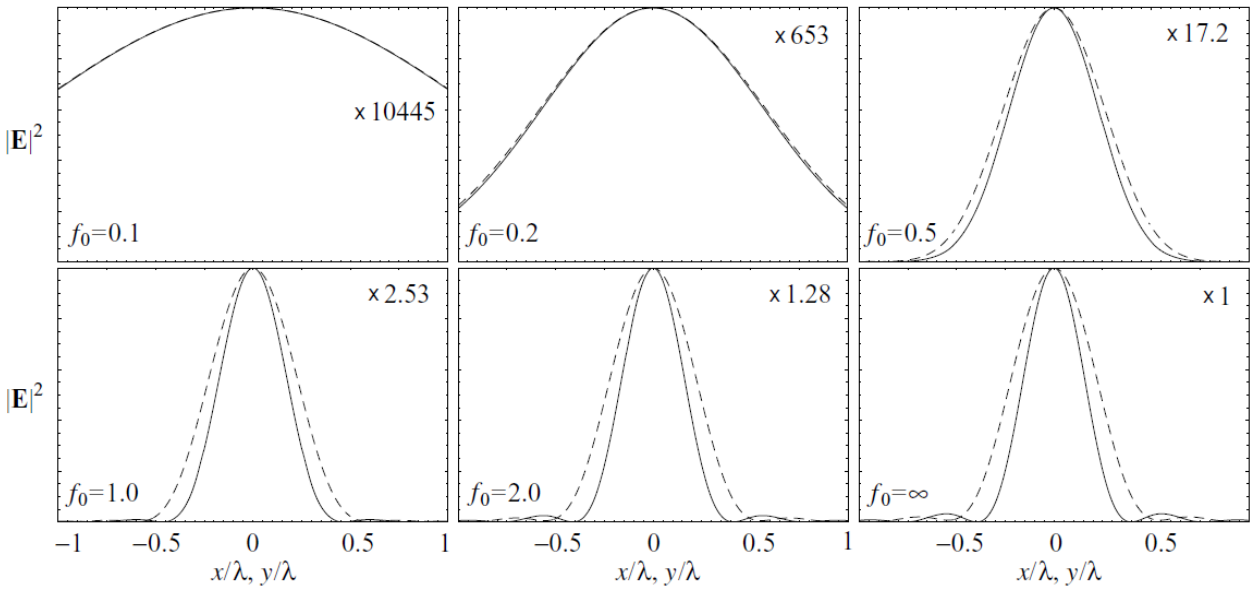

Figure 3.9: Influence of the filling factor f_0 on the back-aperture confinement of the focus. A lens with NA= 1.4 is assumed and the index of refraction is 1.518. The electric field intensity $|\mathbf{E}|^2$ is plotted at the focal plane for different filling factors. The dashed curves have been evaluated along the x-direction (plane of polarization) and the solid curves along the y-direction. All curves have been scaled to equal amplitude with the scaling factor indicated in the figures [111].

the spatial confinement at the focus. It is therefore necessary to ensure that the back-aperture of the objective is sufficiently filled to optimise the trapping strength. The obvious drawback by overfilling the objective is the loss of incident laser power that is not transmitted. Depending on the incident laser, if there is not sufficient laser power, what you may gain in field confinement might be lost in the reduction of having lower field intensity.

3.3.3 Trapping Chamber

The design of the trapping chamber has little influence on the levitated nano-particle once it has been trapped, however it is vital in initially loading the particle into the optical trap. The optical trapping dipole force is a conservative force. This means that this force will not dissipate any of its kinetic energy. In the absence of any damping, the particle would simply cross the beam. For a nano-particle to become stably trapped at the focus of an optical trap, the particle must move across the focus with a sufficiently small velocity such that the damping of the surrounding air will be able to slow the particle down to below the potential

depth of the optical trap.

The first method to load particles into an optical levitation trap used a piezoelectric transducer (PZT) [3]. By applying an alternating current to the PZT it will generate vibrations that provides enough momentum to the particle such that it can break the Van der Waals forces between the attached particles and the substrate, thereby launching the particles into the air. By carefully controlling the amplitude of the driving current, the particles are on average launched vertically, such that the peak of their trajectory coincides with the centre of the optical trap. This will provide a chance that there will be a particle that crosses the focus with sufficiently small velocity and become trapped. For this technique to work however the particle must have enough momentum to overcome the Van der Waals forces and therefore does not work for smaller nano-particles where the masses do not provide the necessary momentum.

In order to deliver and load smaller particles into an optical trap, we can use nano-particles dispersed in a volatile aerosol generated by a commercial OMRON MicroAIR U22 nebulizer. The nebulizer consists of a porous membrane driven by a piezo that vibrates at the top of a liquid reservoir, pressuring out a mist of very fine micron sized droplets into the air ($\approx 4\,\mu m$). By suspending the nano-particles in a volatile liquid, the micro-droplets emitted from the nebulizer evaporate quickly leaving only a cloud of nano-particles suspended in air. The nano-particles suspended in air then randomly pass through the laser focus and are trapped by chance when the velocity of the nano-particle is sufficiently small.

This method produces two main problems which need to be monitored and acknowledged when designing the optical trapping chamber. The first issue is that it is essential to minimise the air flow around the optical trap. If there is a constant air flow pushing the nano-particles in the chamber, the chance of a particle having a small enough velocity when passing through the focus is dramatically reduced. As a result, designing the trapping chamber to be completely enclosed enhances the chance that a particle will be optically trapped.

A second issue is that this method is not well suited to trap a specific particle within a sample, as a large spray of particles are needed. Unfortunately, this also means that there is a large number of particles deposited on the surfaces of the injection chamber. If the optical elements are exposed, they will be covered in a film of deposited nano-particles and

the optical properties of the elements will be significantly degraded. For example, if the microscope objective is coated with nano-diamonds, the transmitted beam may no longer be Gaussian, which will significantly affect the focus and thus optical potential. Therefore it is essential to protect any exposed optical elements. In order to do this, we designed a trapping chamber with replaceable optical windows. We used coverslip glass as optical windows to protect all of the lenses which are inexpensive to replace. Our trapping objective is corrected to work through a coverslip and this way, we not only protect the objective, but are also in the best possible condition for focusing. In our design the aerosol is sprayed down into the chamber onto the microscope objective. Due to this geometry a large number of particles are deposited onto the cover-slip placed on top of the objective. After repeated sprays, depending on the concentration of the sample, this coverslip needs to be replaced as it can significantly scatter the incoming trapping laser, resulting in a degraded optical potential that will not trap nano-particles.

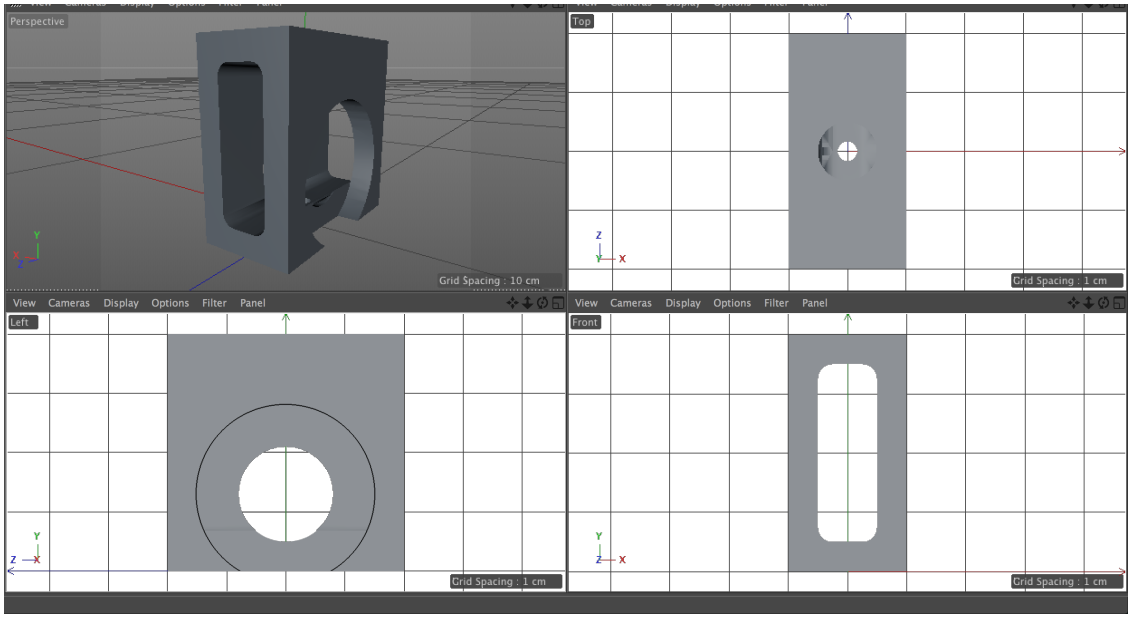

Figure 3.10: Schematic diagram of the trapping chamber. The trapping chamber has larger spherical openings for the microscope objective and condenser lenses. There is a small hole on the bottom of the chamber threaded with a M4 hole with a slightly large hole on top for injection of nebulized particles. The two rectangular openings are for imaging the trapped object with a CCD camera. The trapping chamber is made from steel so that glass coverslips can be attached to the surfaces of the chamber using magnets to both enclose the chamber, prevent air flow and protecting optical surfaces.

Considering these constraints, we designed the trapping chamber that was made of steel as shown in Figure (3.10). The larger circular opening is sized so that the microscope objective can be placed close to the centre of the chamber. The smaller circular opening is designed for a $\frac{1}{4}$ inch condenser lens for measuring the position in forward scattering if necessary. Glass coverslips are placed on the inner faces of the chamber with magnets to protect the optical elements. The rectangular opening on the front face is for imaging with a CCD camera and is also protected with a glass coverslip placed on the outer face of the chamber. The glass coverslips also have the advantage of limiting the air flow within the chamber. The bottom of the chamber is threaded with an M4 hole so that it can be fixed to a standard Thorlabs post for installation in the experiment. The final hole on the top face of the chamber is for delivering of particle with a nebulizer.

3.4 Detection

Observing the particles motion within the optical trap is essential for optical trapping. This system uses two distinct detection schemes to observe the nano-particles in the trap. The first is a standard CCD camera to observe the nano particles motion as they enter the trapping chamber and to determine when a particle has been optically trapped at the focus of the trapping laser. The second detection schemes involves a balanced photodetector, necessary for high speed sensitive measurements of the nano-diamonds position within the optical trap. This is essential for a quantitative analysis of the optical forces acting on the nano-particle.

3.4.1 CCD Camera

The first imaging system is a video based imaging system using a CCD camera (LU165M, Lumenera). The CCD camera's primary role is to monitor the injection of the nano-particles into the optical trap and determine if there is a particle trapped at the focus. The CCD camera also allows us to observe a number of detrimental effects reducing the quality of the optical trap, such as unclean optical elements and airflow issues.

The CCD camera scheme does not use the microscope objective but uses a simple 100 mm

one lens imaging system providing a 2× magnification that is aligned such that the image plane of the CCD coincides with the focus of the optical trap. When particles are injected into the trapping chamber and cross the laser beams, the scattered light from each individual nano-particle can be observed on the CCD camera. Only nano-particles that cross the focus of the optical trap with sufficiently small vibrational energy can be stably trapped by the optical trap. It is therefore essential to ensure that within the trapping chamber, in which the nano-particles are injected, that the airflow is reduced. If there is airflow within the chamber the nano-particles will consistently drift across the focus and fail to be slowed and held within the trap. The airflow in the chamber can be observed on the CCD camera as a constant drift of the particles in one direction. To reduce the airflow all sides of the trapping chamber are closed to further insulate the nano-diamonds from this effect. The result is that the injected nano-particles will slowly drift within the optical trapping chamber under the Brownian force and a small contribution from gravity. Once one of these particles crosses the optical focus of the chamber, it can be optically trapped, observed on the CCD camera as a stable bright diffraction limited spot. To ensure additional particles do not get trapped once the first particle has been trapped, we can apply a small airflow to the trapping chamber that is sufficient to vent the untrapped particles, whilst still maintaining the optically trapped particle. The trapped particle can now be held within the optical trap indefinitely.

For a CCD camera of this type it is possible to process the signal acquired from the camera in order to track the position of the particle within the optical trap with sub pixel accuracy, using several centroid fitting algorithms [112–114]. Video tracking of trapped objects has been implemented in real time [115, 116], however this technique is limited by the frame rate of the camera and hence, trapping frequencies near or above the frame rate of the CCD cannot be measured. Video tracking is common in water trapping for example since the trapping frequencies are much smaller. In air, we expect frequencies in the kHz range which will require an expensive high-speed camera. To obtain a high frequency position measurement, a quadrant photodiode (QPD) or high bandwidth balanced detector (BD) is required.

3.4.2 Balanced Detector

A balanced detector (BD) is a device that precisely measures a small difference in the intensity of two beams. A balanced detector consists of two photodetectors that measures the power of two incident beams and internal circuitry produces a voltage which is proportional to the difference in their intensities. The intuitive approach to how a balanced detector measures the position of a particle is shown in Figure (3.11)

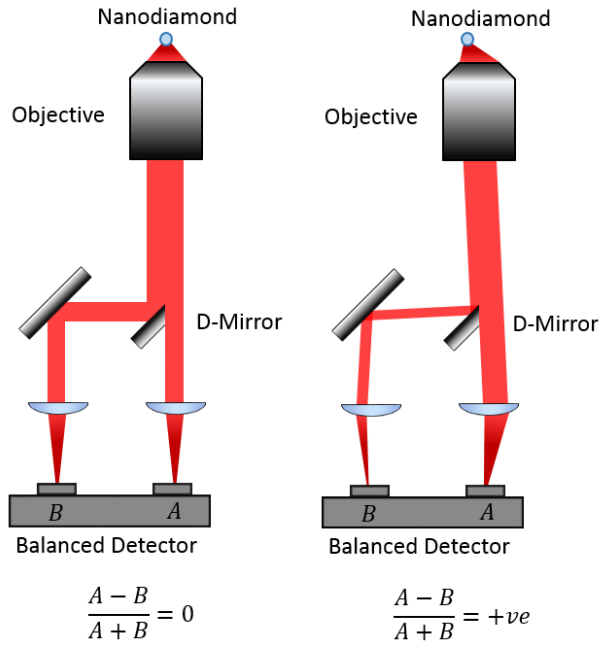

Figure 3.11: Schematic showing how the position of the nano-diamond affects the balanced detector (BD) signal. When a particle is on axis with the objective axis the scattered light is collimated back along this same axis. D-shape mirror is used to divide this beam in two equal part such that the differential power in the balanced detector is 0. When the particle is displaced off axis, the scattered light after the objective is no longer propagating along the microscope axis and the D-shape mirror is not dividing the beam in 2 equal parts, resulting in a non-zero equal signal on the two photodetectors. The internal electronics amplifies the difference in signal which is then proportional to the particles radial position.

When the particle is in the centre of the trap, the re-collimated back reflected signal is symmetric and centred on the centre of the back aperture of the objective. In this case a D-mirror splits the beam exactly in half so that the differential signal is zero. When the particle oscillates to one side of the trap the scattered signal from the particle is deflected to one side and the D-mirror splits the intensity unevenly resulting in a voltage signal on the

balanced detector. This signal increases the further the particle moves from the centre of the trap. If the particle is moved to the other side of the trap a negative voltage is recorded on the balanced detector. An example of a voltage signal of a optically levitated nano-diamond is shown in Figure (3.12).

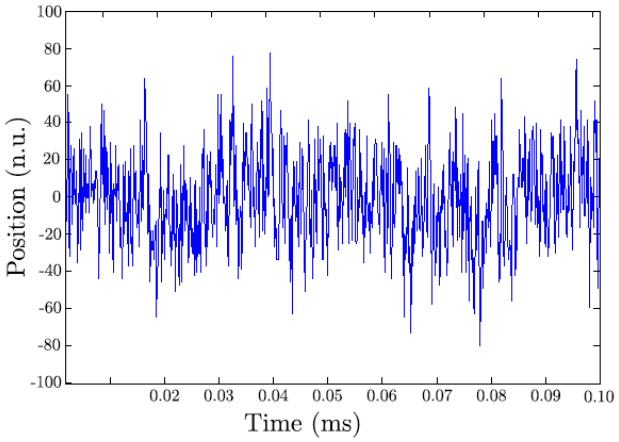

Figure 3.12: Position measurement of a levitated particle as a function of time at atmospheric pressure. The position axis is normalised to the smallest measurement increment of the detection signal.

The corner frequency as described in Section (2.3.2) can be evaluated from the position measurements using a MatLab package designed for precise calibration of optical tweezers, tweezercalib 2.0 [117]. Figure (3.13) is an example of a power spectrum density produced by the tweezercalib 2.0 Matlab program. The program fits a Lorentzian profile to the data to produce a value of the corner frequency of the trapped nano-diamond which then provides a value of the trapping stiffness through Equation (2.27).

Interestingly, from the corner frequency measurement we can determine the average variance in motion of the levitating nano-diamond by substituting Equation (2.27) into Equation (2.22) such that,

$$\langle x^2 \rangle = \frac{k_B T}{2\pi\beta f_c}, \tag{3.1}$$

where, $\beta = 6\pi\nu a$ is the drag coefficient of the diamond, ν is the dynamic viscosity of the surrounding air, a is the radius of the diamond. For the nano-diamond in Figure (3.13), using the typical value of the dynamic viscosity for air in ambient conditions $\nu = 1.846 \times 10^{-5}\mathrm{kg\,m^{-1}\,s}$ and a particle radius of $a = 500\,\mathrm{nm}$, the average root mean squared variance

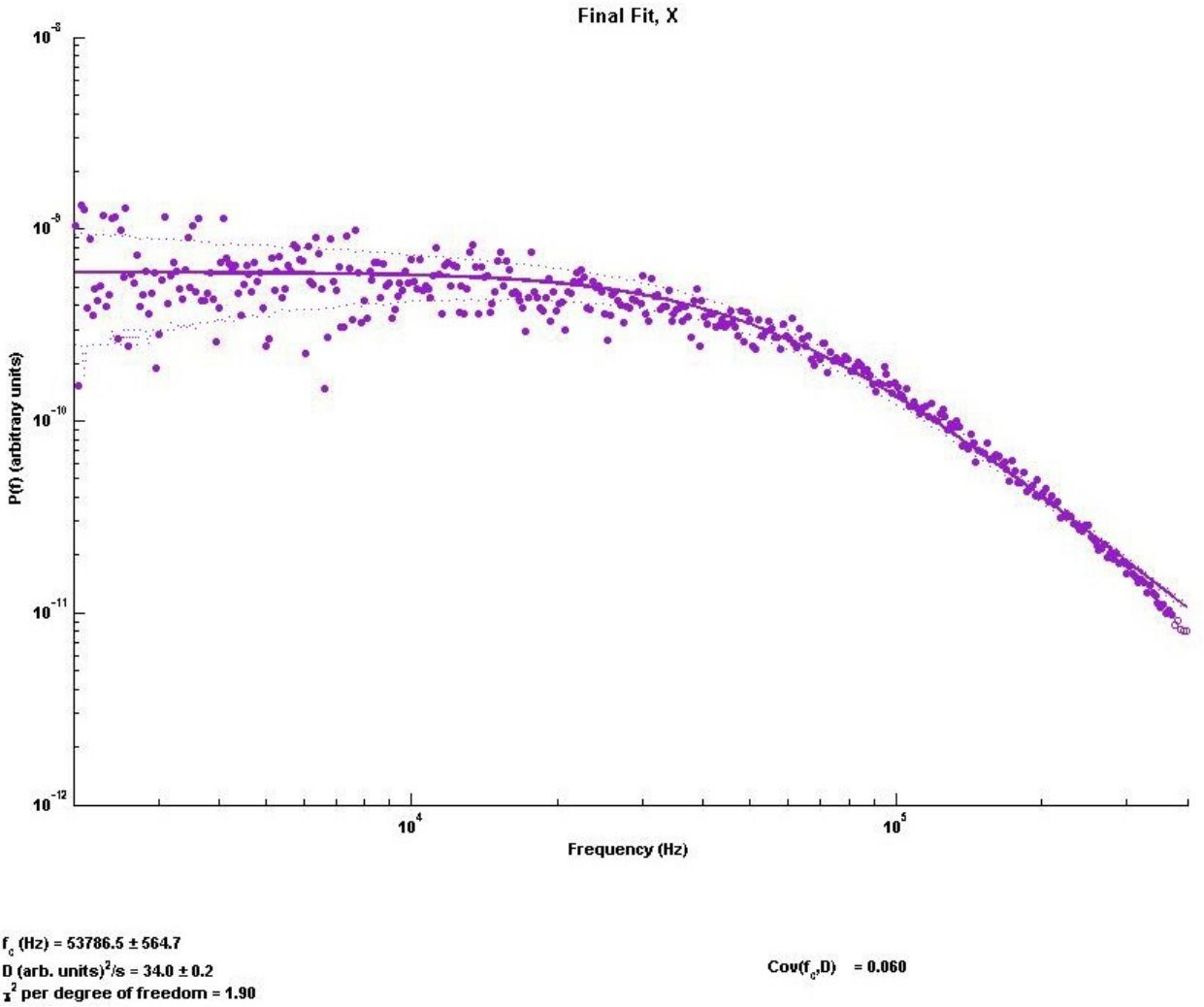

Figure 3.13: Power spectrum density plot of a trapped nano-particle in the optical trap. This is the raw image output of the MatLab program, Tweerzercalib 2.0, used to plot and fit a Lorentzian curve to the data (Solid line). The corner frequency of this trace is given as $f_c = 53800 \pm 600$Hz.

in position is $\sqrt{\langle x^2 \rangle} \approx 16\,\text{nm}$. Using this measurement we can then calibrate our raw position measurement data by normalising by the root mean squared (RMS) value from the data to this value of 16 nm as shown in Figure (3.14). For this nano-diamond the position detection resolution is then given by the smallest detectable position change on the calibrated trace. For this nano-diamond the balanced detector provides a measurement resolution of approximately 1 nm, far better than the Rayleigh criteria. The detector resolution is limited by the sensitivity of the balanced detector but more importantly by the intensity of the scattered signal from the levitated nano-particle.

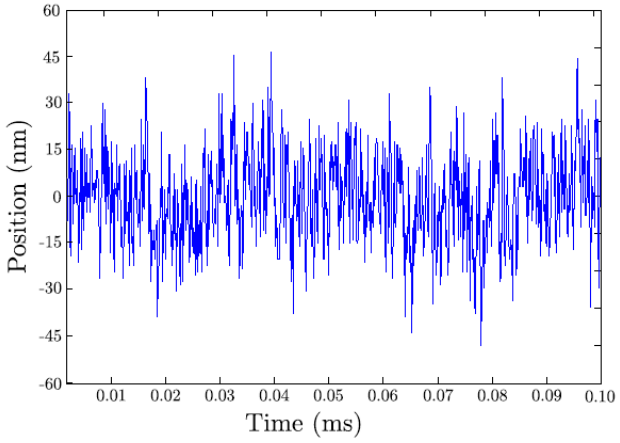

Figure 3.14: Calibrated position measurement of a levitated particle as a function of time.

All of the above measurements using the tweezercalib 2.0 software are performed in post processing after acquiring the raw data with an oscilloscope. In order to observe the power-spectrum and corner frequency in real time I implemented a field-programmable gate array (FPGA) with Labview.

3.4.3 Data Processing

In order to move to continuous data acquisition and processing of the corner frequency it was essential to reduce the processing load on the computer. I integrated the data collection and Fourier transform processes with an FPGA module as shown in Figure (3.15) in order to control and observe the experiment in real time as shown in Figure (3.16).

The FPGA card I used is a PCIe-7851R with an on-board clock of 40MHz. This card would allow for a maximum bandwidth of 20MHz, however the acquisition logic, mainly limited by the analogue to digital converter bandwidth, required 56 clock ticks to acquire all the incoming signals which included not only the balanced detector signal but two extra PD signals to track input laser powers as well as an APD counter for fluorescence detection.

Our maximum sampling rate was then $\frac{40\,\mathrm{MHz}}{56} = 714\,\mathrm{kHz}$ which provides us with a Nyquist frequency of 357 kHz, which is the maximum frequency of oscillation of the particle that can be measured with this system. We are working with trapping frequencies typically lower than 150 kHz and this system provides us with sufficient bandwidth to track the particles motion at higher frequencies in order to fit the corner frequency.

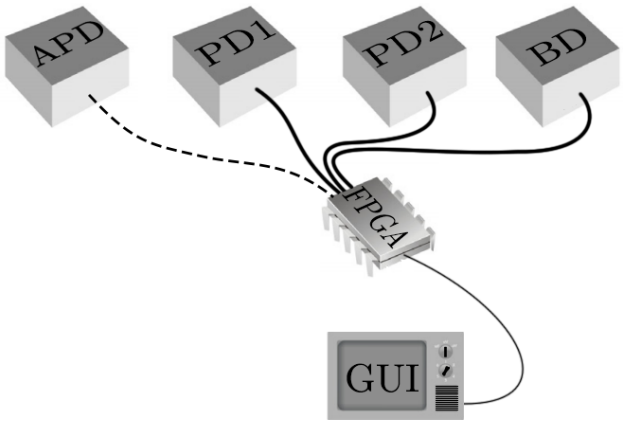

Figure 3.15: Continuous data acquisition scheme using a field programmable gate array (FPGA). Three analog inputs and a digital input are connected to the FPGA that accepts high bandwidth signals. The main role of the FPGA is to peform a 4096 point by point fast Fourier transform (FFT) on the input position singal from the balanced detector and pass the final binned transformation to the computer at a much lower bandwidth than the raw input data. A Labview program integrated with a Matlab kernel is then able to process the FFT and fit the corner frequency measurement in real time with a controllable graphical user interface (GUI).

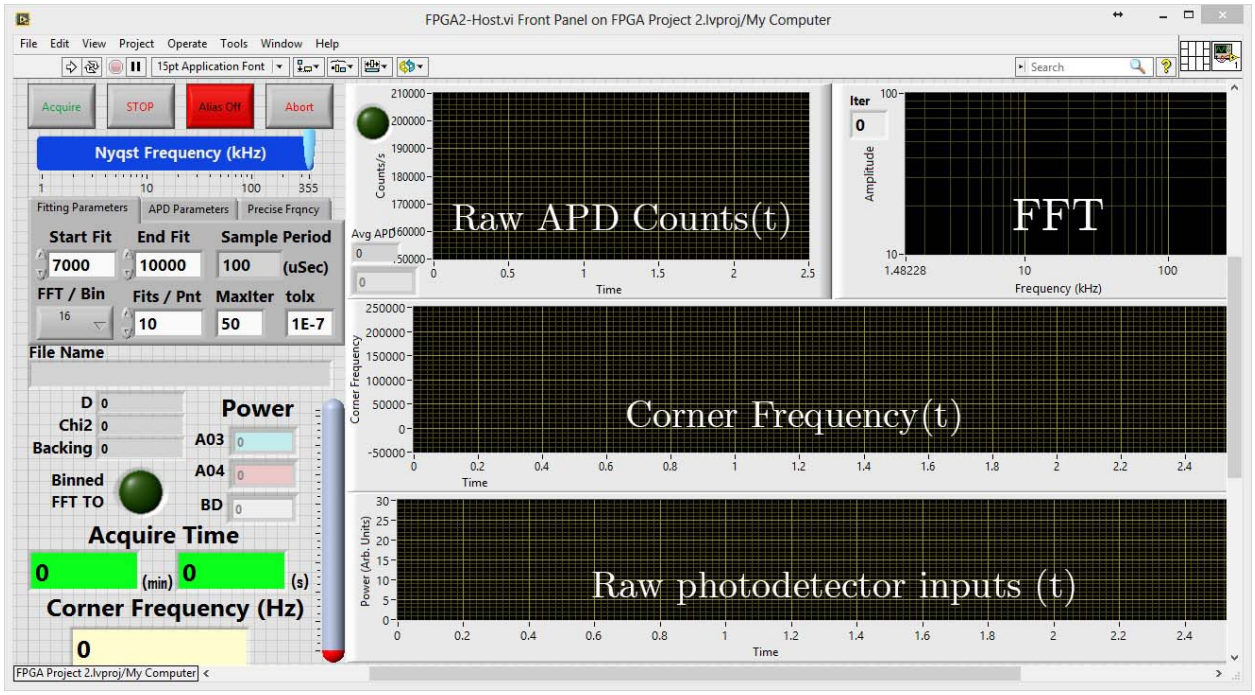

Figure 3.16: Labview front-end GUI for the data-acquisiton and fitting of the position detection signal which includes real time tracking of the the APD counter, corner frequency and laser powers.

To observe a power spectrum and fit of the corner frequency, the FPGA performs a point by point FFT on 4096 measurements of the particles position, which were then fitted using a combination of Labview and embedded Matlab code. We could then track the trapping frequency at a rate of $714\,\mathrm{kHz}/4069 = 174\,\mathrm{Hz}$ providing us with a real-time measurement of the trapping frequency.

The benefit of the FPGA system is that not only can we now observe real-time tracking of the particles trapping frequency, but it also sets the foundations for exerting feedback control on the particle in order to cool its CoM motional temperature. However, in order to cool the particles motion, the particle needs to be brought into the under-damped regime with a vacuum chamber such that the coherence time of the oscillation is longer than the feedback time of the electronics. It is also possible to obtain FPGA systems with GHz clock speeds, further increasing the feedback control. These ultra-fast signals however, would require a full rethinking of the electronic system as we would start to become sensitive to signal delays and signal reshaping in the system.

3.5 Levitation of NV Centres

So far I have shown the optical levitation platform for investigating optical defects. In this section, I investigate specifically the nano-diamond samples containing NV centres and the sensitivity with which I can measure changes in trapping strength.

3.5.1 Nano-Diamond Solution

In order to obtain the strongest atomic forces on the nano-diamond we desired nano-diamonds with a high concentration of NV centres. Prior to the optical levitation experiment the fluorescent nano-diamond solution was characterised by means of a lab-built confocal scanning fluorescence microscope (Olympus 100× oil immersion objective Up-lanFLN, NA 1.3) excited with a 532 nm CW diode-pumped solid-state laser (Coherent Scientific Compass 315) and combined with a commercial atomic force microscope (NT-MDT Ntegra) [104]. The measured average diameter of the nano-diamonds is $100.5 \pm 23.3\,\mathrm{nm}$, determined by atomic

force microscopy and confirmed by dynamic light scattering analysis (Malvern Instruments Zetasizer NanoZS). The nano-diamonds also have an estimated concentration of $\approx 10^4$ NV centres per nano-diamond [103].

In order to prepare nano-diamond samples for optical trapping the raw nano-diamond water solution is sonicated for 30 mins in an ultrasonic bath to break possible clusters that could have formed. The solution is then diluted in ethanol at various concentrations on the order of 1 part in a million to one part in a billion. The ideal nano-diamond dilution depends on the size of the trapping chamber, airflow conditions and the quality of the optical trap. To inject the nano-diamonds into the trap the diluted nano-diamond sample is placed in a commercial OMRON MicroAIR U22 nebulizer and nebulised into the trapping chamber. The nano-diamonds float in the chamber and it can take several minutes before a nano-diamond is trapped at the focus of the optical trap.

3.5.2 Force Sensing Protocol

Developing a protocol for trapping and measuring the forces on the nano-diamonds within the optical trap is essential for producing accurate data that is consistent between measurement sets. In order to measure the forces on the NV centres themselves, we must be able to easily compare against a reference force. By investigating the 1042 nm state we are able to switch on and off the resonance forces since there will be no available electron population in the singlet state unless the NV centres are excited with the 532 nm laser. To ensure each levitated nano-diamond behaves as expected in the trap we made a measurement of the corner frequency as a function of trapping laser strength. Since the trapping force is linear with power the corner frequency which is proportional to the trap stiffness should increase linearly with trapping power as shown in Figure (3.17).

The continuous acquisition code provides an error in the fitting of the corner frequency, this provides a single measurement uncertainty of approximately 2% for this nano-diamond. We can improve this uncertainty by measuring at a constant power and averaging over N samples, which reduces the noise by $\sqrt{N}$.

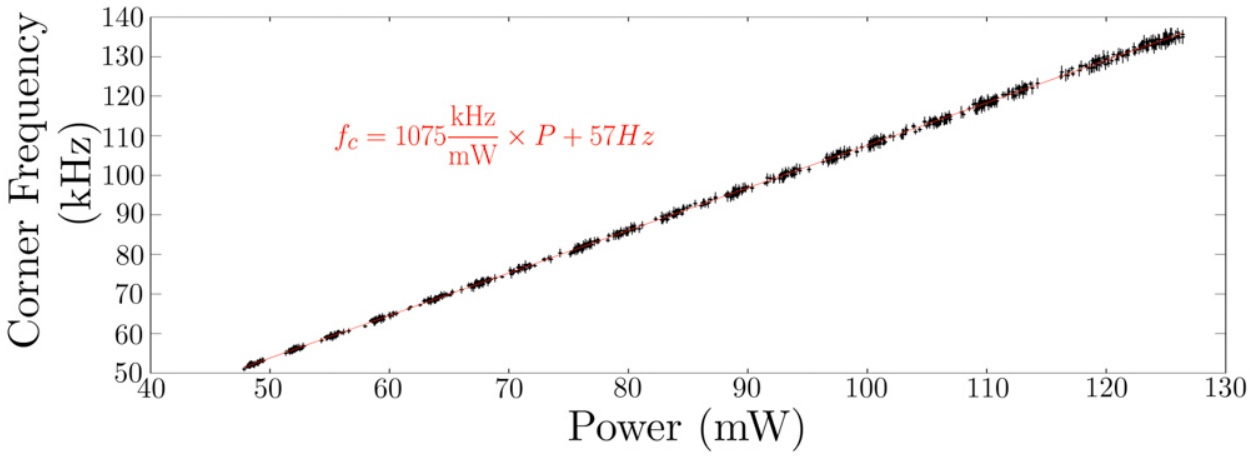

Figure 3.17: Corner frequency measurement of a levitated nano-diamond as a function incident laser power on the microscope objective. Each data point is one measurement made by the FPGA and Labview program with measurement errors of aprroximatly 2% per measuremnt. It is clear that the experimental platform is accuratly measuring the corner frequency in a wide frequency space as it is directly proportional to the incident laser power as expected from Equation (2.23).

I observed that the trapping stiffness remained constant over a period of a few minutes. However over longer periods the corner frequency was subject to slow drift which we attributed to thermal movement in the mirrors, changing the optical alignment and hence beam focal profile. To observe the optical dipole forces on the nano-diamond, I settled on an 80 second measurement. The nano-diamond was kept under constant power for the first and last 20 seconds in order to extract the classical trapping frequency of the nano-diamond as a reference $\kappa_{ref} = \kappa_{Diamond}$. The two reference traces were used to ensure that the trapping frequency measurement stayed consistent for the duration of the experiment and negligible drift occurred during the measurement. By adding the 532 nm excitation beam to the middle 40 seconds the singlet transition becomes populated and the trapping strength now has components from both the the force on the diamond and on the NV centres themselves. The trapping stiffness is then given by $\kappa_{tot} = \kappa_{Diamond} + \kappa_{NV}$. Now by taking the difference in corner frequency between the two measurements, we have just the trapping force from the NV centres alone $\kappa_{tot} - \kappa_{ref} = \kappa_{NV}$. An example corner frequency measurement of using this protocol with 50 mW of 1064 nm and 2 mW of 532 nm laser power is shown in Figure (3.18).

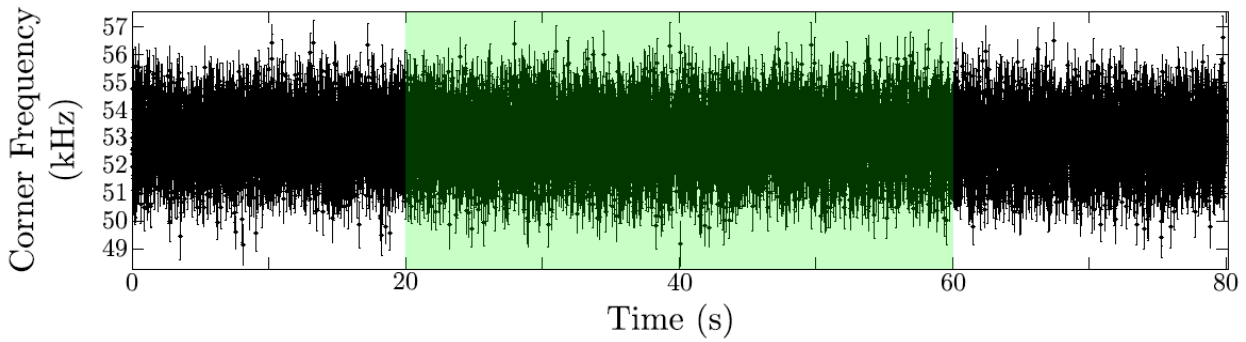

Figure 3.18: Continuous 80 second corner frequency measurement for detection of enhanced dipole forces in levitated nano-diamonds containing NV centres. The nano-diamond was trapped with 50 mW of 1064 nm laser power for the duration of the measurement. For the middle 40 seconds 2 mW of 532nm green excitation laser was incident on the nano-diamond exciting the NV centres to enable the resonant dipole forces. Each of the 13920 data points is one measurement made by the FPGA and Labview program with an errors of aprroximatly 2% per measurement.

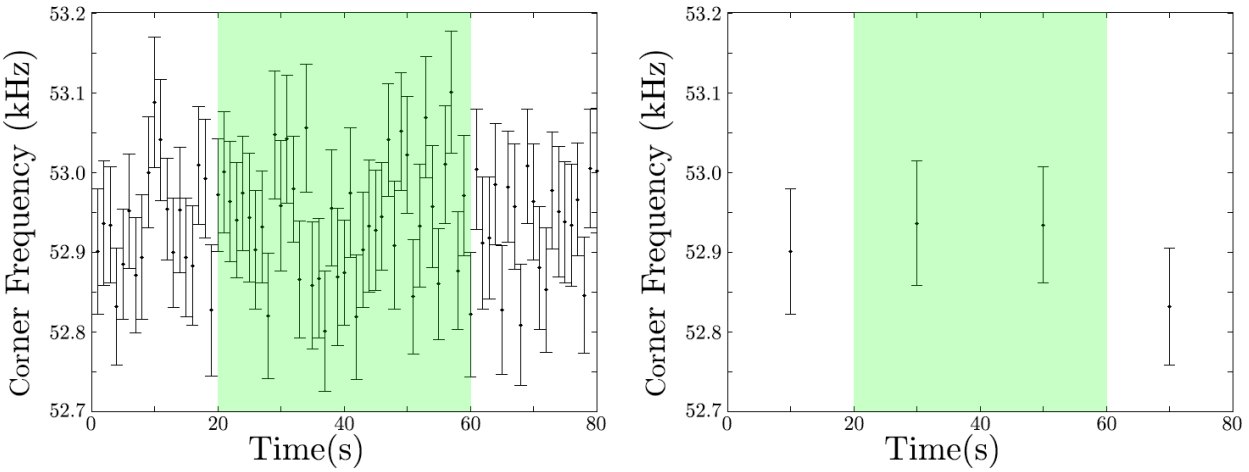

Figure 3.19: Analysis of 80 s corner frequency measurement for detection of enhanced dipole forces in levitated nano-diamonds containing NV centres. The nano-diamond was trapped with 50 mW of 1064 nm laser power for the duration of the measurement. For the middle 40 seconds 2 mW of 532nm green excitation laser was incident on the nano-diamond exciting the NV centres to enable the resonant dipole forces. To improve the measurement uncertainty we averaged over **(a)** 1 second intervals and **(b)** 20 second intervals. From **(b)** we obtain a value of the trapping frequencies $\kappa_{ref} = 52866 \pm 54$ Hz and $\kappa_{tot} = 52935 \pm 54$ Hz providing a trapping frequency due to the NV centres of $\kappa_{NV} = 69 \pm 107$ Hz.

In conjunction with the FPGA card this 80 second measurement protocol provides 13920 measurements of the corner frequency since the card can measure the trapping frequency

at a rate of 174 Hz. By averaging the measurements to one second intervals or 20 second intervals we can drastically reduce the error in the measurement as shown in Figure (3.19).

From this particular measurement we obtain a value of the trapping frequencies $\kappa_{ref} = 52866 \pm 54\,\text{Hz}$ and $\kappa_{tot} = 52935 \pm 54\,\text{Hz}$ providing a trapping frequency due to the NV centres of $\kappa_{NV} = 69 \pm 107\,\text{Hz}$. The force due to the NV centres in this measurement is below the measurement sensitivity and we therefore cannot confirm the presence of an additional optical trapping force as observed in the water trapping experiments. Interestingly, the measurement given above used the conditions where we expected the strongest atomic force component and the measured force is still less than our measurement uncertainty of approximately 0.2%. This measurement scheme was repeated for a range of powers of the 1064 nm laser and tunable 1042 nm laser and no observable force was observed across a significant number of nano-diamonds.

3.5.3 Complications

To understand why we're not observing an increase in trapping force we investigated a number of possibilities. We thought that it may be possible we are selectively trapping nano-diamonds with only a low number of NV centres, whereas highly fluorescing nano-diamonds had high scattering and were pushed out of the optical trap. To verify that we were trapping nano-diamonds containing a significant number of NV centres, we added a fluorescence detection pathway to the system. The fluorescence signal was collected by the objective and reflected by a 750nm dichroic mirror incident on a 50 µm core multimode fibre. The output of the multimode fibre was coupled into the APD through an array of filters to ensure that only the window from 550 nm to 750 nm was collected. The three filter stack included a Semrock 532/1064 notch filter (NF03-532/1064E-25), a Thorlabs 550 nm longpass filer (FELH0550) and a Thorlabs 750 nm shortpass filter (FESH0750). The filter stack was characterised by a Cary 5000 UV-Vis-NIR spectrometer showing the black transmission window shown in Figure (3.20).

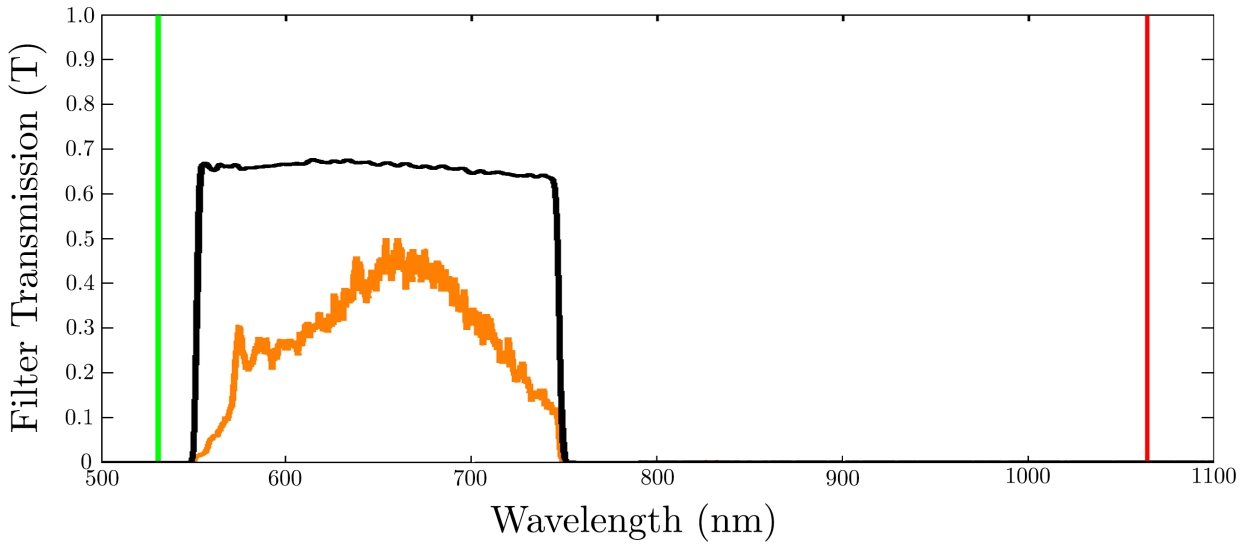

Figure 3.20: Transmission (black) of the filter stack for detection of NV centre fluorescence. The green and red lines indicate the excitation and trapping laser frequencies respectively, that are filtered out of the fluorescence spectra. The orange trace is a fluorescence spectra of the same nano-diamond sample measured through the same filter stack on a similar confocal microscopy set-up without the intense trapping laser.

The fluorescence pathway could be easily aligned by illuminating the levitated particle without the blue-green filter on the 532 nm laser and efficiently coupling a weak scattered light signal from the nano-diamonds on the APD. By illuminating the levitated nano-diamonds using 1 mW of 532 nm through the 30 mm lens, a back of the envelope calculation shown in Figure (A.1) suggests that even with a quenching strength of 99% we should still be able to observe a fluorescence signal.

However, for all trapped nano-diamonds and 532 nm excitation powers no fluorescence signal could be detected. It became clear that either the trapping laser was selecting nano-diamonds with little to no NV centres or that it was strongly interacting with the NV centre themselves. It became apparent that to understand the dynamics of the levitated nano-diamonds containing optical centres, we have to further understand the properties of the nano-diamonds and the optical defects it contains by probing them with the trapping laser on a cover-slip where the laser can be turned on and off without losing the particle.

‘Climb through your problems.
Failure is a huge part of success.’

– Ashima Shirashi

'There's a fine line between fishing and just standing on the shore like an idiot.'

– Steven Wright

4

Photo-Dynamics of Nitrogen Vacancy Centres in Nano-Diamonds

The most widely studied colour centre in diamond, the Nitrogen Vacancy (NV) centre, is a point defect consisting of a nitrogen-vacancy lattice pair embedded along the $\langle 111 \rangle$ axis of a diamond [118]. The NV centre has two stable charge states, the neutral charge state (NV^0) and the negatively charged state (NV^-), with photo-induced interconversion between these two states [119]. There also exists a third, almost entirely neglected positivly charge state (NV^+) that is optically dark and accessible through control of the surface charge acceptor rate [120, 121]. Of the three charge states, the NV^- charge state is the most prominent and has been intensively studied for a wide range of applications in both Physics and Biology due to its high stability and interesting spin-optical properties [122]. Biologists have used them extensively for biolabelling and imaging of internal biological structures [9, 123]. Meanwhile,

physicists have been investigating their use for nanoscale sensing and quantum technology applications [42, 124–128]. By exploiting the defects' internal spin state, room temperature quantum effects can be observed in the NV centre providing a platform to study a wide variety of quantum manipulation protocols [51]. However, these desirable effects rely solely on the properties arising from the NV^- charge state and in most applications the excitation wavelength is chosen to be from 510 nm to 540 nm, in order to maximise the NV^- charge state polarisation [109]. By using a single optimised excitation wavelength the impact of the neutral charge state NV^0 is often neglected, despite the optimal charge state polarisation being limited at $\approx 75\%$ [109]. While the spin-optical properties of NV^- centres are extremely robust [129], this is dependent on the ability to maintain the NV^- charge state polarisation. It has been observed however, that once a second probe laser is used in an experiment the fluorescence of the NV centre can be dramatically quenched [123, 130–133]. It was expected that there would be a reduction in fluorescence in our optical levitation experiment, but not sufficiently strong enough to completely prevent any observation of fluorescence counts. For extending the capabilities of the NV centre in platforms and systems that require additional laser wavelengths it is therefore essential to understand the quenching processes.

Probing the quenching mechanism in the optical levitation platform was not possible; even at our lowest trapping powers required to hold the nano-diamonds in the trap, I could not observe any fluorescence. Thus, to observe the quenching mechanism I had to build a new inverted confocal microscope to probe nano-diamonds immobilised on a coverslip.

In this chapter I clarify some of the mechanisms which lead to the quenching of the NV centre fluorescence. I find that in nano-diamonds this quenching is driven by a continuous charge state transfer between NV^0 and NV^- providing increased channels for non radiative decay from the excited states. In addition, I show that the ionisation from the NV^- to NV^0 charge state strongly depends on the spin state of the NV^-. Having a better understanding of this mechanism is essential for any application that requires a spin manipulation protocol. I experimentally observe the charge state interconversion process by probing the NV with a near infra-red (NIR) laser. The NIR source is a continuous-wave laser of a few tens of milli-watts, which allows us to avoid many of the mechanisms that rely on transient mechanisms or high intensity fields [123, 130–132]. By then collecting the fluorescence of both charge

states I finally show that the impact of the NV^0 charge state and the electron acceptor/donor density can not be neglected in a steady state regime.

4.1 Fluorescence Quenching Platform

The platform for investigating the quenching of NV centre fluorescence on a cover-slip is shown in Figure (4.1).

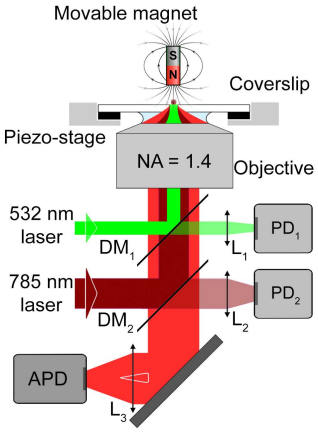

Figure 4.1: Schematic of the experimental set-up where the nano-diamond, deposited on a coverslip, is positioned using a piezo-stage. The two incident lasers (532 nm and 785 nm) are combined using two dichroic mirrors (DM_1 and DM_2) and focused by the 100× 1.4 NA Olympus oil objective. The small portion of the incident power that is transmitted through the dichroic mirrors is used to monitor the power of each lasers using photodiodes (PD). The emission from the nano-diamond is collected by the same objective and sent through the dichroic mirrors and a filter to an avalanche photodiode (APD).

The combination of the dichroic mirrors before the objective allows for superposition of the NIR laser mode with the 532 nm excitation laser on the 100× 1.4 NA Olympus oil objective lens so the foci are overlapping in the sample plane. I included the possibility of swapping the 785 nm laser out for either the 1064 nm or 1042 nm laser by changing optical fibres. Due to the inefficiency of the dichroic mirrors, the weak transmitted laser power was used to track the beam intensity on the photo-detectors in order to obtain a continuous reading of the input laser powers. The fluorescence is back-collected through the same objective and sent to either a fibred spectrometer or a fibre-coupled avalanche photodiode (APD), collecting all wavelengths from 550 nm to 750 nm. The input laser powers and

detection signals were controlled using Labview such that the fluorescence data could be systematically collected. A permanent neodymium magnet is placed on a moveable arm above the sample plane so that a large non zero magnetic field could be brought in close proximity to the nano-diamond. The effect of the magnet is to mix the internal spin state of the NV^- which can be observed through a reduction in fluorescence signal [134].

In the experiment, 100 nm diameter nano-diamonds were dispersed on a glass coverslip placed on the sample plane of the custom built scanning microscope. These were the same nano-diamonds used in the levitation experiment which contain a large density of NV centres providing high brightness useful for biological applications and sensing [105]. I first examined the spectral response of excited NV centres under 785 nm NIR illumination in a spectral window from 550 nm to 750 nm, showing both the NV^0 and NV^- emission. I excited the NV with a fixed power of 0.75 mW of 532 nm and acquired fluorescence spectra for varying powers of incident NIR, see Figure (4.2). Both the fluorescence of NV^0 and NV^- can be observed

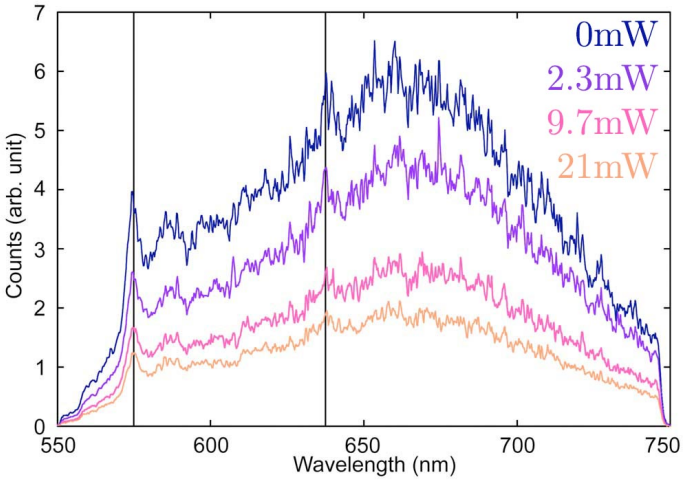

Figure 4.2: Quenching spectra of the NV centres. Spectra recorded for 0.75 mW of 532 nm for four different 785 nm powers: 0 mW, 2.3 mW, 9.7 mW and 21 mW. The lines indicate the ZPL transitions of the NV^0 (575 nm) and NV^- (637 nm) charge states.

to be decreasing with increased NIR power. This overall quenching of the fluorescence as a function of the incident power of 785 nm is confirmed by the APD measurements. I could not observe any significant differences on the relative ratio of NV^0 to NV^- emissions due to the difficulty to distinguish the fluorescence from the two charge states at room temperature, however the fact that the whole spectrum is affected by the NIR laser in the same way,

indicates that the quenching of fluorescence cannot be explained by simply a change in the charge polarisation of the NV centre. This measurement was similar for both the 785 nm and 1064 nm lasers. However due to extra processes that occur under 1064 nm illumination I concentrated only on the quenching due to the 785 nm laser. This is explained further in Section (4.9).

4.2 Quenching Data

In order to investigate the photo-dynamics of the NV centres in more detail, I used the APD to observe the fluorescence for varied excitation and quenching powers on five different nano-diamonds. This allows us to explore a large parameter space for model fitting. For each of the five measured nano-diamonds I retrieved first the saturation curve of the NV centres. The power dependence of the fluorescence under 785 nm illumination was then measured for five powers of the 532 nm excitation laser. The measurements were then repeated with a neodymium magnet placed $\simeq 0.5$ mm above the sample plane of the confocal microscope in order to mix the spin state of the NV^- charge state. This allowed us to study the impact of the spin state of NV^- on the fluorescence quenching. For each nano-diamond I observe similar behaviour. Figure (4.3) shows one of the nano-diamonds characterised as an example.

It is clear from this measurement that in our optical levitation platform, the trapping lasers were indeed providing a strong quenching mechanism preventing us from observing florescence. Indeed it confirms that the lack of observed fluorescence in the levitation experiment was not solely thermal or due to selective trapping of low NV concentration nano-diamonds. Current explanations of the quenching mechanism in levitated nano-diamonds indicate a stimulated emission (STED) like process or even the inclusion of a new 'D' state into the NV centre physics [133, 135]. However, these quenching mechanisms only considered the NV^- centre, whereas I observe that both the NV^0 and NV^- fluorescence is quenched. Additionally, I am interested in the impact on the internal spin dynamics, which I am probing by mixing the spin state with a magnet. In any case it is essential to explore the Nitrogen Vacancy centre in more detail and investigate the possible quenching mechanisms and their implications on the possibility of observing atomic dipole forces on NV centres within optically levitated nano-diamonds.

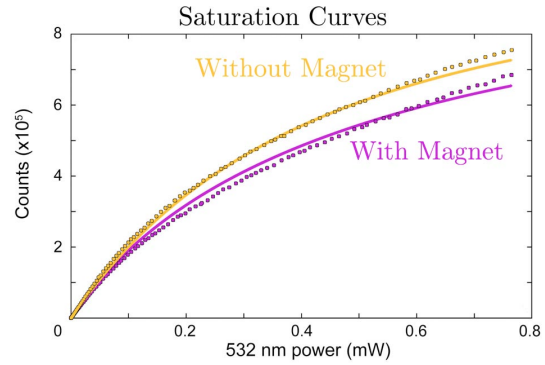

(a)

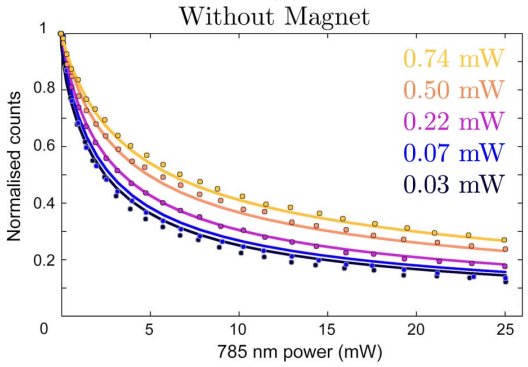

(b)

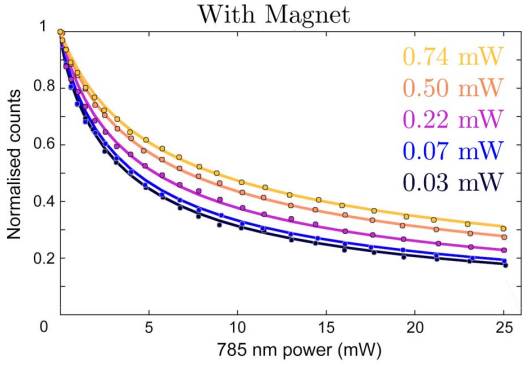

(c)

Figure 4.3: Experimental quenching data of NV centres. (**a**) Saturation curve for a given nano-diamond without and with a magnet in close proximity in light and dark colours respectively. The open symbols are the experimental measurement while the curve show the result from the best model obtained by fitting both of the saturation curves along with all of the quenching data. (**b**) fluorescence quenching for a given nano-diamond as function of the incident near-infrared power. The different curves are obtained for different green powers: 0.03 mW, 0.07 mW, 0.22 mW, 0.5 mW and 0.74 mW in this order from dark to light coloured curves. Interestingly, a stronger green laser excitation reduces the fluorescence quenching. (**c**) same as **(b)**, with a magnet in close proximity to the nano-diamond. Interestingly, for high near-infrared laser powers the the quenching induced by the magnet is minimal indicating that the quenching laser is also depolarising the system.

4.3 The Nitrogen Vacancy Centre

The nitrogen-vacancy (NV) centre is an extrinsic diamond crystallographic defect incorporated in the tetrahedral structure diamond where two adjacent carbon atoms are removed. One carbon is replaced by a nitrogen atom and the other is left vacant (vacancy). The defect has a trigonal symmetry of point group C_{3v} where the C_3 principle axis is along the NV pair in the crystallographic $\langle 111 \rangle$ direction as shown in Figure (4.4a)*.

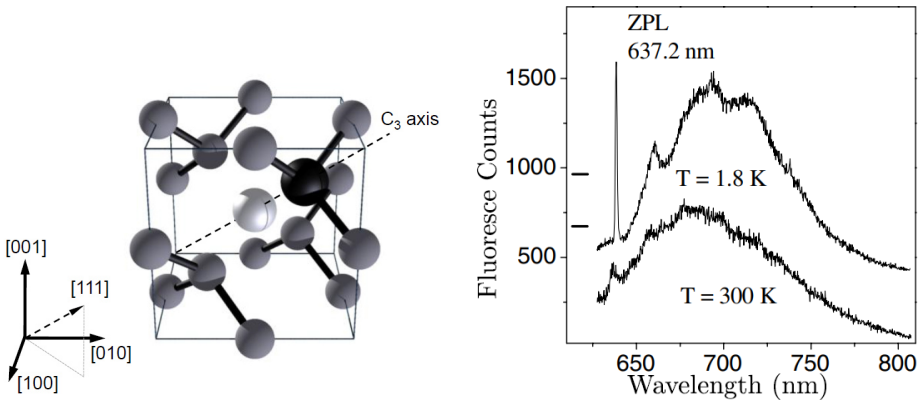

(a) (b)

Figure 4.4: NV structure in the diamond lattice and photo-luminescence spectrum. (**a**) The NV centre has a principal axis of symmetry in the crystallographic $\langle 111 \rangle$ direction. The nitrogen atom is shown in black, carbon atoms are in grey, and the vacancy in white with no bonds (black sticks) [35]. (**b**) Fluorescence emission spectra of single NV centres at room temperature and liquid helium temperatures. The excitation wavelength for this spectrum was 514 nm [51].

The nitrogen atom being in group V of the periodic table atom has five valence electrons. In the NV defect, three of the valence electrons are shared with the three nearest neighbour carbon atoms, and the last two occupy the dangling bond towards the vacancy. In this situation the vacancy now has five unsatisfied active bonding electrons, two from the nitrogen and one each from the dangling bonds of the three adjacent carbon atoms [137]. The NV centre in this configuration with five free electrons is denoted as the neutral charge state NV^0, however, if the defect acquires an additional sixth electron from elsewhere in the lattice, then the optical properties are completely changed and the NV centre becomes the

*It is this group symmetry that gives rise to a large array of the notation surrounding the energy levels of the NV centre. For an in depth understanding of the notation and its physical origins I would refer you to reference [136].

negatively charged nitrogen vacancy centre NV^-. The charge state of the defect strongly depends on its local lattice environment with the presence of close surrounding impurities acting as electron acceptor or donors [138]. Due to the NV charge states' strong dependence on local lattice effects, NV^- and NV^0 can be found coexisting in the same diamond [139]. Additionally, the same NV defect can undergo photochromic switching between the two charge states [119]†. The two charge states can be clearly identified spectrally due to their different characteristic optical transitions as shown in Figure (4.4b). In practice, the desirable properties of the NV centre rely solely on the properties arising from the NV^- charge state and in most applications, the excitation wavelength is chosen to be from 510 nm to 540 nm in order to maximise the NV^- charge state polarisation [109]. By using a single optimised excitation wavelength the impact of the neutral charge state NV^0 is often neglected despite the optimal charge state polarisation being limited at $\approx 75\%$ [109]. I will show in this chapter that the existence of the NV^0 charge state can no longer be neglected when the NV centres are also irradiated with a second laser wavelength. Before I explore this mechanism we must first understand the photo-physics of both NV^0 and NV^- and their photo-interconversion mechanism.

4.3.1 NV^- Structure

The NV^- charge state consists of a ground triplet state $^3A_2$ and an excited triplet state ^3E, as well as two metastable singlet states $^1E_1$ and $^1A_1$ [122]. Within the spin triplet states the $m_s = 0$ ans $m_s = \pm 1$ spin states are split in energy at zero magnetic field by $D = 2.87\,\text{GHz}$ for the ground triplet and $D = 1.42\,\text{GHz}$ for the excited triplet [122]. The spin transition rate between the ground $m_s = 0$ and $m_s = \pm 1$ spin states is given by the spin-lattice relaxation time T_1 and has been measured to be $\Gamma^{SF} \approx 6\,\text{ms} = 167\,\text{Hz}$ at room temperature and zero magnetic field [140]. This spin mixing rate can be dramatically increased by applying a large magnetic field in the vicinity of the NV centre [134].

The zero-phonon line between the $^3A_2$ and ^3E is centred at 637 nm and can be efficiently excited with spin conservation at most wavelengths below 637 nm [122]. The radiative

†This mechanism will be covered in detail in Figure (4.8).

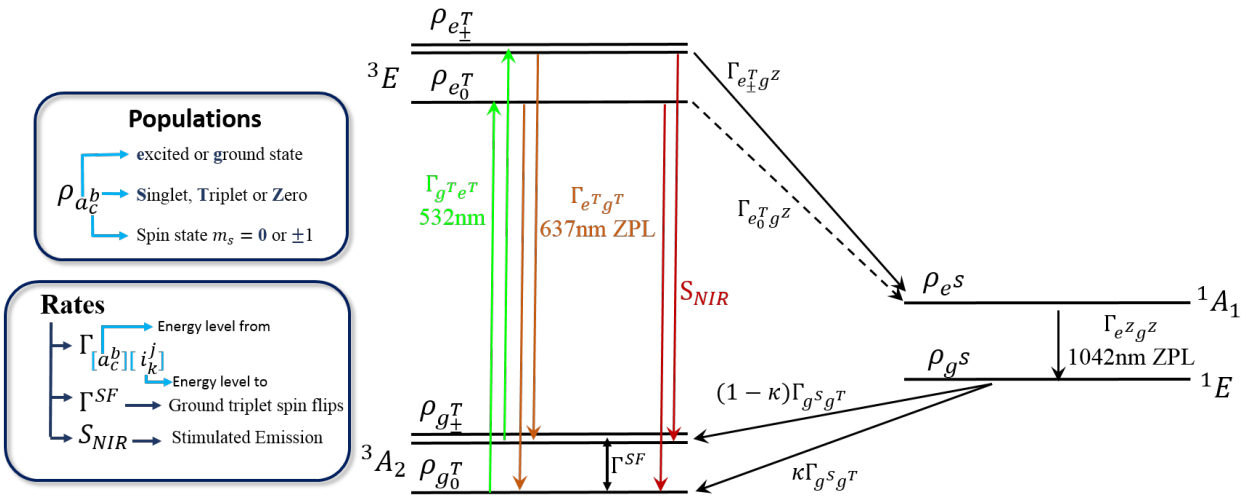

Figure 4.5: Energy level structure of the NV^- centre. The black arrows indicate dominantly non-radiative processes, the orange arrows indicate spontaneous emission processes and the red (NIR Stimulated emission) and green (532 nm excitation) arrows indicate processes that can be accessed by the corresponding laser wavelengths.

lifetime of the excited state is 13 ns for NV centres in bulk diamond and approximately $\Gamma_{e^T g^z T} = 26$ ns for NV centres in nano-diamonds [141, 142]. Only a few percent of the fluorescence is emitted at the ZPL, most fluorescence appears in the phonon side bands between $600 - 800$ nm.

The excited triplet states can also decay to the excited singlet state, the rate from the $m_s = \pm 1$ excited triplet state is $\Gamma_{e^T_{\pm} e^S} = 2\pi \times 9.4\text{MHz} = 16.9$ ns, whereas the rate from the $m_s = 0$ excited triplet state is almost an order of magnitude smaller at $\Gamma_{e^T_0 e^S} = 2\pi \times 1.8\text{MHz} = 88.4$ ns [143, 144]. Whilst it not completely understood why there is a large discrepancy between these decay channels, it is noteworthy that this discrepancy enables many of the interesting optical properties of the NV centre. It leads to the difference in fluorescence intensity between the two excited spin states which in turn leads to a mechanism for an all optical readout of the centres internal spin state. The excited singlet state has a lifetime of $\Gamma_{e^S g^S} \approx 1$ ns [110] populating the longer lived ground singlet state and it has been shown to emit fluorescence at a ZPL of 1042 nm [110, 145]. The longer lived ground metastable state has a lifetime of $\Gamma_{g^S g^T} \approx 150$ ns and decays into the ground the triplet spin state [110]. It was commonly believed that this population decayed only into the $m_s = 0$

spin state, however recently this has been challenged and it has been claimed that the decay into the ground triplet is nano-diamond dependant and only a fraction, between 0.5 and 0.7, of the electrons decay into the $m_s = 0$ ground state [146, 147].

4.3.2 NV^0 Structure

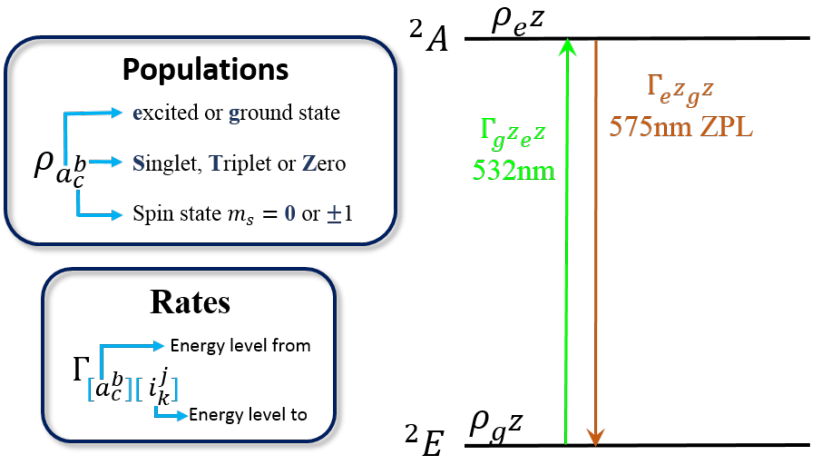

Figure 4.6: Energy levels of the NV^0 centre. The NV^0 centre can be approximated as a two level system with a ZPL at 575 nm.

As opposed to the rigorous study the NV^- charge state has received, the NV^0 charge state has often been neglected. However, I believe in order to study the NV centre as a whole it must be included. I use the established three level model to describe its intrinsic dynamics. The third energy level attributed to the NV^0 is the metastable spin quartet $^4A_2$ which was measured though an electronic parametric signal [148]. However, no ODMR or optical readout of this metastable quartet have been measured and it is expected to have negligible impact on the photo-physics of the NV centre and as such has been neglected[‡]. The NV^0 charge state consists of a ground doublet ^2E and an excited doublet ^2A with a ZPL at 575 nm = 2.156 eV [122]. It can be efficiently excited at most wavelengths below 575 nm

[‡]Between submitting this thesis and subsequent corrections, Manson et.al. [149] identified that it is possible for the conversion of NV from the negative charge state to the neutral charge state to occur by tunneling from the excited NV^- triplet state through to the meta-stable quartet level $^4A_2$. They admit however, that the specific details of the tunneling transitions requires further theoretical consideration. Nevertheless, under high NIR laser fields in nano-diamonds I believe that the dominant process is as described in this chapter.

and in bulk diamonds has a radiative lifetime of 19 ns [150, 151]. In nano-diamonds, the radiative lifetime is altered due to the changed phonon density of states due to the size of the nano-diamonds. Since the wavelength of the emission for NV^0 and NV^- is similar, it is expected that the NV^0 radiative lifetime will increase by approximately the same factor as NV^- in nano-diamonds compared to bulk diamond and as such the radiative lifetime set for the model was $\Gamma_{e^z g^z} = 38$ ns [141, 142]. The exact excitation cross section of the NV^0 centre is unknown, however, the ratio of excitation cross sections between NV^0 and NV^- can be measured by looking at their relative emission intensities. Since the quantum efficiency of both NV^0 and NV^- is ≈ 1 then the ratio of excitation cross sections is given by the ratio of emission cross sections, giving $\Gamma_{g^z e^z} = \frac{1}{3}\Gamma_{g^T e^T}$ [109, 152]. Differing from NV^-, NV^0 does not have detectable magnetic resonances associated with its degenerate spin doublet ground and excited states [148]. Only a few percent of the fluorescence is emitted in the ZPL, whereas most fluorescence appears in the phonon side bands between 550 and 750nm.

4.4 Nano-Diamonds and Surface Effects

The electronic structure in nano-diamonds is different to that from bulk diamond due to the strong surface effects impacting both the band gap of the crystal as well as the charge mobility and charge density. As a consequence, the photoconversion processes of an NV centre in a nano-diamond is more complex than for an isolated NV centre deep inside a high-purity bulk diamond. Our nano-diamonds are highly irradiated, CVD grown nano-diamonds with hydrogen termination. As a result they contain not only NV centres but also a high density of singlet nitrogen acting as charge donors, and hydrogen-carbon surface bonds acting as charge traps.

It has been proposed recently that the NV^- centre should not be considered alone, but rather as an NV^-–N^+ pair [149]. This concept arises as the NV centre needs to have a charge donor providing an additional charge to produce the NV^-charge state. In this picture if there is a singlet nitrogen within 1.2 nm of the NV centre it is energetically favourable for an electron to tunnel from the singlet nitrogen to the NV centre, creating an NV^-–N^+ pair. As a result, the charge state polarisation can be controlled by increasing the singlet nitrogen

concentration. Interestingly, under 532 nm illumination the singlet nitrogen can be ionised providing an increase in the charge carrier density in the diamond converting the majority of the NV centres to the NV^- state.

Competing with the singlet nitrogens providing additional charges to the diamond, surface hydrogen-carbon bonds act as charge acceptors, reducing the availability of electrons to the NV centre. This effect has been shown to create blinking of the NV centres and a reduction of the NV^- charge polarisation [153]. There is also a possibility that with an extremely large charge acceptor density, the NV centres will convert into the NV^+ charge state. This however, has currently only been observed with engineered gate electrodes [120, 121, 154, 155].

As shown in Figure (4.2) our nano-diamonds display a strong fluorescence from both NV^0 and NV^- under 532 nm excitation. This indicates that neither the hydrogen-carbon charge acceptors or the singlet nitrogen charge donors are dominating. I expect that the large density of charge acceptors and charge donors in these nano-diamonds will induce a strong increase in the electron tunneling rates as compared with a bulk diamond and therefore, there are dynamics that may occur in these samples that do not in NV centres contained within bulk diamond [156].

4.5 Quenching Mechanisms

Quenching in NV centres due to NIR emission has been observed previously [123, 130–133]. The underlying quenching mechanism has been attributed to a variety of processes including heating due to pulsed lasers [132], spin depolarisation [130], stimulated emission (STED) [123] and through the addition of a additional fast decaying D state in the NV^- electronic structure [133]. Our data is inconsistent with a number of these mechanisms for a variety of reasons. Firstly, I am collecting the fluorescence in a continuous-wave regime of a few 10s of milliwatts on a coverslip eliminating mechanisms that rely on large thermal changes of the nano-diamond. Secondly, I am observing quenching with a magnet present in the set-up that already depolarises the NV^- centre, removing spin depolarisation as the main quenching mechanism. Finally, I am observing quenching on both the NV^- centre

as well as the NV^0 centre whereas all of the previous papers concentrated on the NV^- in their analysis. In order to understand the dynamics of the whole NV centre, I will cover the main quenching mechanisms that may be occurring and leading to the strong reduction in fluorescence.

4.5.1 Stimulated Emission

Stimulated emission (STED) is one potential quenching mechanism to occur for NV centres. Since the PSB of the NV centre overlaps with the NV centre emission it is possible for the NIR laser to stimulate the excited NV centre, undergoing a transition from the excited state to the ground state. This mechanism will increase the amount of florescence in the NIR laser wavelength channel, which is filtered out of the signal and is therefore observed as a quenching mechanism.

The strength of this mechanism should scale linearly with the overlap between the PSB of the NV centre and the laser wavelength. Whilst a STED mechanism is expected at 785 nm due to the non-zero overlap, the 1064 nm laser is far from the PSB and a STED process is expected to be negligible. It is therefore surprising that both the 785 nm and 1064 nm lasers are quenching the fluorescence in a similar way due to the large wavelength separation [133] [§].

4.5.2 D Band

In order to explain the 1064 nm quenching observed in NV centres without resorting to using a STED mechanism, Gieselmann et.al. [133] introduced a new, fast decay channel to the NV^- centre mediated by the promotion of the excited state to a dark D band shown in Figure (4.7).

The 1064 nm quenching laser is proposed to drive electrons into the fast decaying D band of the NV centre which relax non-radiatively into the ground state of the NV centre. Interestingly, due to the sub-femtosecond fast decay out of the D band, in the continuous

[§]I acquired preliminary data of the 1064 nm laser quenching that displayed the same quenching trends as the 785 nm laser, however more comprehensive systematic measurments were taken of the 785 nm laser quenching as additional model parameters would need to be introduced since it would be possible that the 1064 nm laser would interact with the 1042 nm optical transition of the NV^- centre.

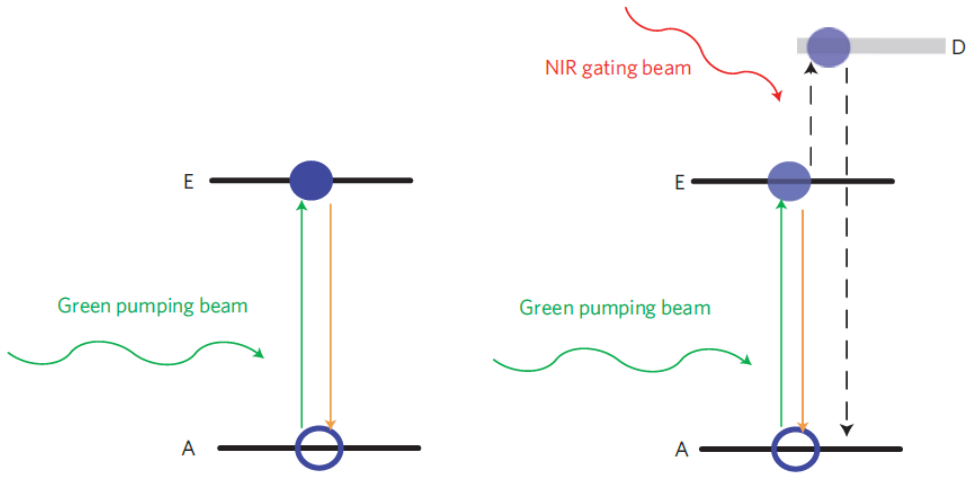

(a) (b)

Figure 4.7: Concept of optical quenching of NV fluorescence through an additional D band. (**a**) In the absence of the NIR laser, the NV can be regarded as a two level system excited by a green pumping beam. (**b**), The NIR laser populates a dark band D, which decays non-radiatively, thus reducing the fluorescence output compared with the emission without NIR laser [133].

wave regime we can assume that there is negligible steady-state population in this D band and the rate equations to describe both mechanisms are equivalent mathematically.

The problem with both of these mechanisms is that they consider only the dynamics of the NV^- centre and not the NV^0 centre which is also quenched considerably. In addition, when the internal spin state is probed, these mechanisms no longer capture the photo-dynamics. As a result, I believed it was essential to understand the interplay between NV^- and NV^0 in order to accurately model the quenching of the NV^- centre.

4.6 Charge State Photo-Interconversion

To convert between the two charge states we need to examine both the ionisation process from NV^- to NV^0 and the recombination process from NV^0 to NV^-[♦]. The desirable effects of the NV centre rely solely on the properties arising from the NV^- charge state and as a result, a standard $\approx 532\,\text{nm}$ excitation laser is chosen to produce the highest charge state

[♦] I have denoted the process from NV^- to NV^0 as ionisation from NV^0 to NV^- as a recombination process. This way of naming the process is centred around the NV^- charge state as it is the charge state with the most interesting optical properties and has been studied in more detail.

polarisation in an effort to optimise these effects and allow any effects due to the NV^0 charge state to be neglected [109]. However, I believe that not only will the excitation laser alter this balance but that any additional laser is going to alter this maximised charge state polarisation under continuous wave excitation.

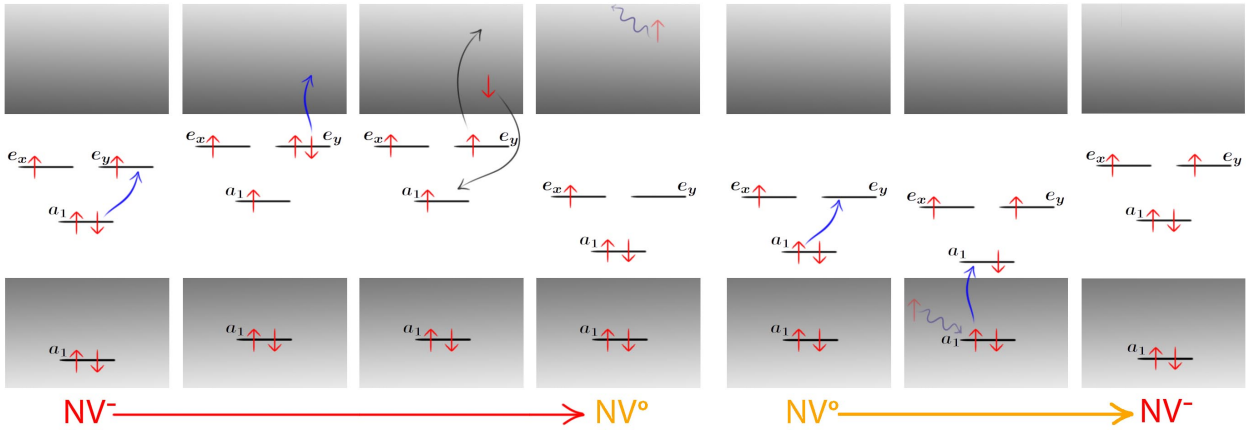

Figure 4.8: Ionisation and recombination processes. Schematic of the internal electron orbital structure for the NV charge conversion process between the negative and neutral charge states of the NV centre. The NV centre is in the NV^0 charge state when there are 5 electrons in the structure and in the NV^- centre when there is an extra sixth electron in the structure. The NV^- to NV^0 conversion involves two photon excitation followed by a process that releases enough energy to ionize an electron from the structure leaving the defect in the ground state of the NV^0. The recombination process from NV^0 to NV^- is also a two step process. First the neutral defect is excited as shown by the movement of an electron from the a_1 orbital to the e orbital. Before decay can occur an additional electron is transferred from the a_1 orbital in the valence band to the vacant place on the a_1 orbital in the band gap. The vacant place in deep lying a_1 orbital is then replaced by a new electron from the valance band leaving the centre in the ground state of the NV^-. The position of orbital levels change with different electron configurations throughout both processes. The energy level labels in this diagram arise from a group theory representation of the internal orbital structure and are different from the typical energy level diagrams that are shown of the NV centre [119].

4.6.1 Ionisation

Ionisation from NV^- to NV^0 occurs in a two photon process described in detail by the internal electron orbital structure as shown in Figure (4.8). The typical energy level structure of the NV centre with the included ionisation and recombination pathways in bulk diamond is given in Figure (4.9). Admittedly, one should be careful using this picture of the NV centre

in nano-diamonds as the surface charge states and electron confinement can alter the Fermi level throughout the crystal [120].

First, a photon must excite an electron into the excited ^3E state of the NV^-, shown in the orbital picture as a transition from the a_1 orbital to the e orbital. The electron can then be excited again into the conduction band leading to an ionisation process which strips an electron from the centre, converting it into the NV^0 charge state in its ground state configuration [119]. This two step process has only been investigated with a single excitation laser, leading to an ionisation rate that is quadratic with excitation power and can no longer occur at wavelengths greater than the ZPL of the transition. However, I observe that this process can be mediated by two lasers: one that strongly excites the transition and one that strongly ionises the electron leading to the ionisation process. One would initially assume that the ionisation mechanism would be spin independent; however, these energy levels already show a spin dependant nature towards the singlet states that leads to the spin polarisation properties of the NV^-. Additionally, the dipole strength of the two excited spin states differ by an order of magnitude which may break the symmetry of the ionisation process leading to different ionisation rates for each excited spin state. As a result, I investigated the possibility that the interaction cross sections of the excited NV^- centre energy levels can be spin dependant.

4.6.2 Recombination

The recombination process from NV^0 to NV^- also occurs in a two step process and is shown in Figure (4.8). First a photon must excite an electron in the NV^0 charge state into the excited ^2A state. A second electron can then be excited from the valence band into the ^2E ground state which provides the extra electron to the centre, converting it into the NV^- charge state in its ground state configuration [119]. Currently, there is no evidence to indicate which spin state the NV^- charge state will now be populated in, however it has recently been observed that the recombination process is a spin depolarising process indicating a non negligible component in the $m_s = \pm 1$ spin state [157]. In my analysis I observe that the rate of recombination from the NV^0 excited state to the NV^- ground state is $180 \pm 90\,\mathrm{MHz/mW}$

at 532 nm and $18 \pm 2\,\mathrm{MHz/mW}$ at 785 nm. Additionally, the model indicates that this process is spin depolarising such that the ratio into the $m_s = 0$ ground state of the NV^0 is $49.0 \pm 6\%$ for both laser wavelengths.

It has been proposed that the conversion from NV^0 to NV^- is mediated by ionisation of single substitutional Nitrogen impurities (N_s) in the nano-diamonds providing free electrons to combine with the NV^0 charge state [148]. Our nano-diamonds contain a high concentration of single substitutional nitrogen N_s which is consistent with high rates of recombination due to the 532 nm laser. However in bulk diamond, singlet nitrogen requires a photon energy of 2.2eV (564 nm) to ionise which would imply that the 785 nm NIR laser should not induce recombination. In our nano-diamonds there are two possible mechanism that could provide this recombination rate. The first is due to the bandgap bending induced by the surface allowing the singlet nitrogen to be ionised with a lower energy. The second and more probable mechanism in my opinion is that the 785 nm NIR laser is ionising the NV^- centres which in turn provides the free electron for a second NV centre to be converted into NV^-.

4.7 Model of the Photo-Dynamics

In order to develop the steady state equations to describe the photo-physics of the system as a whole, I needed to determine the key variables that influence the system. The main question is to determine whether the STED like quenching mechanism itself can explain all of the photo-dynamics of the system or if it necessary to include the ionisation, recombination mechanism. In each of these processes I also need to keep track of the internal spin state of the NV centre. Whilst all the processes between the two triplet states are spin conserving, it is unclear in which spin state the ground spin state will be in when transitioning from either the NV^0 charge state or the singlet state and as such these have been made to be free parameters of the model.

From the known dynamics of the system, I developed an energy level diagram that includes the potential transition mechanisms between each state which is shown in Figure (4.9).

It must be noted that in order to simplify the model I have neglected two mechanisms that I believe will be negligible on the photo-physics of the system. The first is that I have

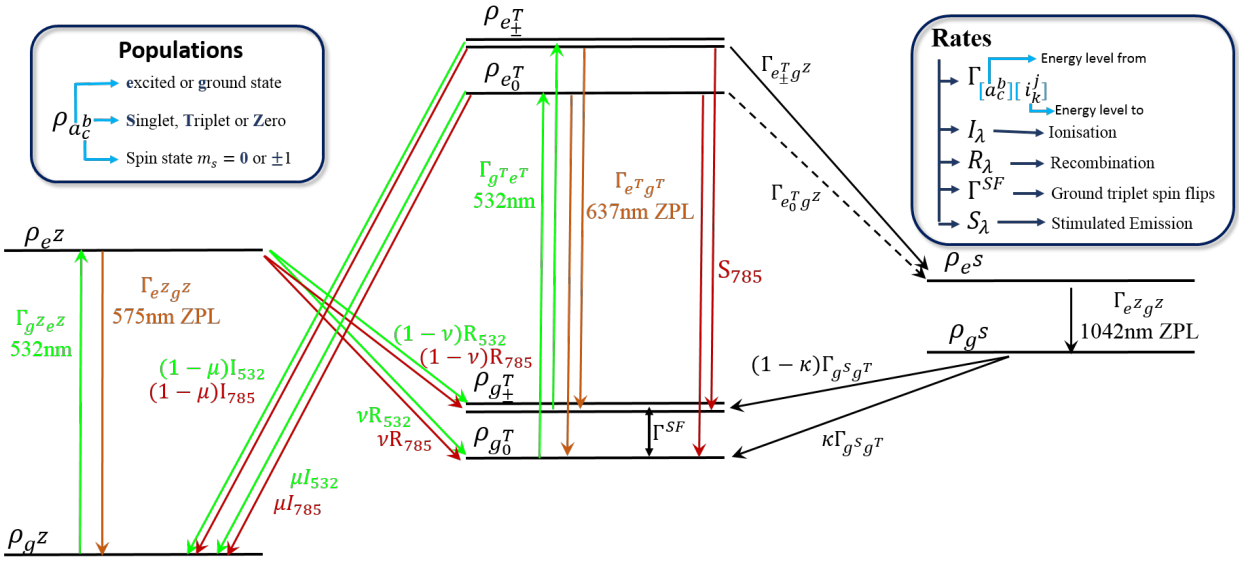

Figure 4.9: Energy levels of the NV centre with both charge states including the ionisation and recombination processes. The black arrows indicate dominantly non-radiative processes, the orange arrows indicate spontaneous emission processes and the red (785 nm) and green (532 nm) arrows indicate processes that can be stimulated by the corresponding laser wavelength.

only placed a spin mixing rate on the ground states of the NV^- centre. Whilst there should also be a spin mixing rate for the excited states of the NV^-, since I am not exciting above saturation of the NV centre the excited states of the NV centre will always have population significantly smaller than the ground state and hence, the spin mixing rate of the excited state will be negligible compared to that of the ground state.

Secondly, whilst it has not been observed, I believe that there will also be an ionisation pathway from the excited singlet state of the NV^- to the ground state of the NV^0. This was neglected in the model for two reasons. The first is that the lifetime of this state is very short and hence there will be no significant population in this state to ionise. Secondly, by including this ionisation pathway, I need to include multiple new free parameters to the model which both increases complexity and risks the possibility of over parametrising the total ionisation pathway leading to non-physical solutions. Over parametrisation of the ionisation pathway is especially true once spin dependent ionisation is considered. Unfortunately, when I illuminate the NV centres with a 1042 nm or 1064 nm laser I can no longer assume the excited singlet state will be unpopulated since these wavelengths may cycle the singlet optical transition.

As a result I focused my attention on the quenching due to the 785 nm laser where this complication can be neglected♣.

From this energy diagram I developed an 8 level rate equation model that incorporates both the ionisation and recombination mechanisms as well as the STED like mechanisms. The population change of each energy level is given by:

$$
\begin{aligned}
\dot{\rho_{e_0^T}} &= -\rho e_0^T \left(\Gamma_{e^T g^T} + \Gamma_{e_0^T e^S} + \mu I_{785} P_{785} + \mu I_{532} P_{532} + S_{785} P_{785} \right) && (4.1)\\
&\quad + \rho_{g_0^T} \left(\Gamma_{g^T e^T} \times P_{532} \right) && (4.2)\\
\dot{\rho_{e_\pm^T}} &= -\rho e_\pm^T \left(\Gamma_{e^T g^T} + \Gamma_{e_\pm^T e^S} + (1-\mu) I_{785} P_{785} + (1-\mu) I_{532} P_{532} + S_{785} P_{785} \right) && (4.3)\\
&\quad + \rho_{g_\pm^T} \left(\Gamma_{g^T e^T} \times P_{532} \right) && (4.4)\\
\dot{\rho_{g_0^T}} &= \rho_{e_0^T} \left(\Gamma_{e^T g^T} \right) + \rho_{g^S} \left(\kappa \Gamma_{g^S} \right) + \Gamma_{SF} \left(\rho_{g_\pm^T} - \rho_{g_0^T} \right) - \rho_{g_0^T} \left(\Gamma_{g^T e^T} \times P_{532} \right) && (4.5)\\
&\quad + \rho_{e^Z} \left(\nu R_{532} + \nu R_{785} \right) + \rho e_0^T \left(S_{785} \times P_{785} \right) && (4.6)\\
\dot{\rho_{g_\pm^T}} &= \rho_{e_\pm^T} \left(\Gamma_{e^T g^T} \right) + \rho_{g^S} \left((1-\kappa) \Gamma_{g^S} \right) + \Gamma_{SF} \left(\rho_{g_0^T} - \rho_{g_\pm^T} \right) - \rho_{g_\pm^T} \left(\Gamma_{g^T e^T} \times P_{532} \right) && (4.7)\\
&\quad + \rho_{e^Z} \left((1-\nu) R_{532} + (1-\nu) R_{785} \right) + \rho e_\pm^T \left(S_{785} \times P_{785} \right) && (4.8)\\
\dot{\rho_{e^S}} &= \rho e_0^T \left(\Gamma_{e_0^T e^S} \right) + \rho e_\pm^T \left(\Gamma_{e_\pm^T e^S} \right) - \rho_{e^S} \left(\Gamma_{e^S g^S} \right) && (4.9)\\
\dot{\rho_{g^S}} &= \rho_{e^S} \left(\Gamma_{e^S g^S} \right) - \rho_{g^S} \left(\Gamma_{g^S g^T} \right) && (4.10)\\
\dot{\rho_{e^Z}} &= \rho_{g^Z} \left(\frac{1}{3} \Gamma_{g^T e^T} \times P_{532} \right) - \rho_{e^Z} \left(\Gamma_{e^Z g^Z} + R_{532} + R_{785} \right) && (4.11)\\
\dot{\rho_{g^Z}} &= -\rho_{g^Z} \left(\frac{1}{3} \Gamma_{g^T e^T} \times P_{532} \right) + \rho e_0^T \left(\mu \left(I_{785} \times P_{785} + I_{532} \times P_{532} \right) \right) && (4.12)\\
&\quad + \rho_{e_\pm^T} \left((1-\mu) \left(I_{785} \times P_{785} + I_{532} \times P_{532} \right) \right), && (4.13)
\end{aligned}
$$

where, the incident power of the 532 nm and 785 nm lasers are P_{532} and P_{785} respectively. The energy level populations can be solved under steady state conditions and the fluorescence intensity F is then given by the populations of each of the excited states and their corresponding fluorescence decay rates,

♣Whilst I can not then confirm that the 1064 nm laser is indeed quenching through the same mechanism as the 785 nm laser, I believe that this is still the case.

$$\mathrm{F} = \left(\rho_{e_{\pm}^T} \times \Gamma_{e_{\pm}^T g_{\pm}^T} + \rho_{e_0^T} \times \Gamma_{e_0^T g_0^T}\right) + \sigma\left(\rho_{e^z} \times \Gamma_{e^z g^z}\right), \tag{4.14}$$

where σ is the ratio between the efficiency of collecting a NV^- photon compared to an NV^0 photon, which depends on the fluorescence spectra and the collection window as well as the spectral response of the detector. This was calculated to be $\sigma = 1.5$ for our APD with a fluorescence window between 550 nm and 750 nm. The fluorescence value is then compared directly against the data for the saturation curves with a single scaling parameter, which is related to the effective number of NV centres and collection efficiency. For the NIR quenching data, the data can be compared directly by normalising to the fluorescence intensity with no NIR laser power,

$$\text{Fluorescence Counts (norm.)} = \frac{F(P_{NIR})}{F(0)}. \tag{4.15}$$

From this complete model, the free parameters were varied in order to determine the most likely dynamics of the system. Five sub-models were investigated and the most likely model was identified by the Akaike information criteria which is covered after fitting the models in Section (4.8).

- Model 1: Stimulated emission only
- Model 2: Spin independent Ionisation and recombination
- Model 3: Spin independent Ionisation and recombination including stimulated emission
- Model 4: Spin dependent Ionisation and recombination
- Model 5: Spin dependent Ionisation and recombination including stimulated emission.

The data was fitted against each model independently and the free parameters for each model are listed in the following tables. The greyed values are parameters that were fixed for that specific model. For reference, the model parameters correspond to the rates shown in Figure (4.9).

Model 1

Table 4.1: Model 1: Stimulated emission only.

	Mean	**Std.Dev.**	**ND1**	**ND2**	**ND3**	**ND4**	**ND5**
$\boldsymbol{\Gamma_{g^T e^T}}$ (MHz/mW)	52.6	7.6	61.2	50.4	45.4	45.7	60.1
$\boldsymbol{\Gamma_{SF}}$ (MHz)	2.5	1.1	4.2	1.4	2.8	1.5	2.7
$\boldsymbol{\kappa}$	0.57	0.13	0.64	0.66	0.38	0.66	0.49
$\boldsymbol{I_{532}}$ (MHz/mW)	0	0	0	0	0	0	0
$\boldsymbol{I_{785}}$ (MHz/mW)	0	0	0	0	0	0	0
$\boldsymbol{\mu}$	0	0	0	0	0	0	0
$\boldsymbol{R_{532}}$ (MHz/mW)	1	1	1	1	1	1	1
$\boldsymbol{R_{785}}$ (MHz/mW)	0	0	0	0	0	0	0
$\boldsymbol{\nu}$	0	0	0	0	0	0	0
$\boldsymbol{S_{785}}$ (MHz/mW)	18.0	0.7	18.9	17.7	17.5	17.3	18.5
Counts Scaling (A.U.)	0.57	0.13	0.64	0.66	0.38	0.66	0.47

Model 2

Table 4.2: Model 2: Spin independent ionisation and recombination.

	Mean	**Std.Dev.**	**ND1**	**ND2**	**ND3**	**ND4**	**ND5**
$\boldsymbol{\Gamma_{g^T e^T}}$ (MHz/mW)	60	21	77	31	59	51	84
$\boldsymbol{\Gamma_{SF}}$ (MHz)	2.5	0.8	3.5	2.3	3.0	1.3	2.5
$\boldsymbol{\kappa}$	1.0	0.0	1.0	1.0	1.0	1.0	1.0
$\boldsymbol{I_{532}}$ (MHz/mW)	9.1	13	0.014	24.6	21.0	0.044	0.0003
$\boldsymbol{I_{785}}$ (MHz/mW)	14	3	14	15	21	12	14
$\boldsymbol{\mu}$	0.5	0	0.5	0.5	0.5	0.5	0.5
$\boldsymbol{R_{532}}$ (MHz/mW)	77	28	96	114	44	58	74
$\boldsymbol{R_{785}}$ (MHz/mW)	58	7	60	54	50	66	62
$\boldsymbol{\nu}$	0.86	0.18	0.93	0.56	0.79	1.0	0.99
$\boldsymbol{S_{785}}$ (MHz/mW)	0	0	0	0	0	0	0
Counts Scaling (A.U.)	0.16	0.15	0.08	0.04	0.36	0.03	0.27

Model 3

Table 4.3: Spin independent ionisation and recombination including stimulated emission.

	Mean	**Std.Dev.**	**ND1**	**ND2**	**ND3**	**ND4**	**ND5**
$\boldsymbol{\Gamma_{g^T e^T}}$ (MHz/mW)	78	42	93	26	139	60	72
$\boldsymbol{\Gamma_{SF}}$ (MHz)	3.7	1.8	5.5	5.3	4.0	1.5	2.0
$\boldsymbol{\kappa}$	0.93	0.10	0.85	0.99	1.0	0.99	0.79
$\boldsymbol{I_{532}}$ (MHz/mW)	8.4	15.7	3.0	36.4	1.7	0.7	0.002
$\boldsymbol{I_{785}}$ (MHz/mW)	6.3	4.5	3.1	7.5	6.3	1.5	13.1
$\boldsymbol{\mu}$	0.5	0	0.5	0.5	0.5	0.5	0.5
$\boldsymbol{R_{532}}$ (MHz/mW)	22	27	3.4	50	0.7	2.6	54
$\boldsymbol{R_{785}}$ (MHz/mW)	2.1	2.6	0.7	2.3	0.3	0.6	6.4
$\boldsymbol{\nu}$	0.40	0.45	0.000	0.002	0.24	0.98	0.76
$\boldsymbol{S_{785}}$ (MHz/mW)	76	101	57	28	254	30	10
Counts Scaling (A.U.)	0.13	0.11	0.08	0.05	0.18	0.03	0.30

Model 4

Table 4.4: Model 4: Spin dependent ionisation and recombination.

	Mean	**Std.Dev.**	**ND1**	**ND2**	**ND3**	**ND4**	**ND5**
$\boldsymbol{\Gamma_{g^T e^T}}$ (MHz/mW)	28	8	39	28	22	19	29
$\boldsymbol{\Gamma_{SF}}$ (MHz)	6.2	3.7	6.1	2.4	9.6	2.6	10.4
$\boldsymbol{\kappa}$	0.70	0.23	0.80	0.32	0.77	0.96	0.65
$\boldsymbol{I_{532}}$ (MHz/mW)	14.3	6.3	12.5	4.4	20.1	15.5	19.4
$\boldsymbol{I_{785}}$ (MHz/mW)	9.40	0.50	9.72	9.59	8.90	8.83	9.95
$\boldsymbol{\mu}$	0.837	0.005	0.835	0.841	0.843	0.836	0.832
$\boldsymbol{R_{532}}$ (MHz/mW)	182	91	116	337	173	135	171
$\boldsymbol{R_{785}}$ (MHz/mW)	18.8	1.8	19.5	17.3	17.7	18.0	21.8
$\boldsymbol{\nu}$	0.49	0.06	0.44	0.59	0.51	0.46	0.45
S_{785} (MHz/mW)	0	0	0	0	0	0	0
Counts Scaling (A.U.)	0.37	0.38	0.16	0.04	0.83	0.08	0.73

Model 5

Table 4.5: Model 5: Spin dependent Ionisation and recombination including stimulated emission.

	Mean	**Std.Dev.**	**ND1**	**ND2**	**ND3**	**ND4**	**ND5**
$\boldsymbol{\Gamma_{g^T e^T}}$ (MHz/mW)	28	8	39	28	23	19	30
$\boldsymbol{\Gamma_{SF}}$ (MHz)	6.1	3.6	5.9	2.4	9.1	2.6	10.2
$\boldsymbol{\kappa}$	0.68	0.23	0.77	0.33	0.74	0.97	0.64
$\boldsymbol{I_{532}}$ (MHz/mW)	14.2	6.2	12.0	4.6	19.7	15.5	19.1
$\boldsymbol{I_{785}}$ (MHz/mW)	9.31	0.51	9.51	9.59	8.74	8.81	9.89
$\boldsymbol{\mu}$	0.842	0.007	0.844	0.840	0.854	0.836	0.836
$\boldsymbol{R_{532}}$ (MHz/mW)	181	93	114	340	167	115	168
$\boldsymbol{R_{785}}$ (MHz/mW)	18.7	1.9	19.3	17.1	17.4	18.1	21.7
$\boldsymbol{\nu}$	0.50	0.06	0.45	0.59	0.53	0.46	0.46
$\boldsymbol{S_{785}}$ (MHz/mW)	0.25	0.24	0.52	0.01	0.48	0.03	0.20
Counts Scaling (A.U.)	0.37	0.38	0.16	0.04	0.82	0.08	0.72

4.8 Comparing Models

The residuals for each model and nano-diamond can be observed in Table (4.6).

Table 4.6: Comparison of models, showing the residuals of each nano-diamond and model, as well as the mean value and standard deviation of each model.

	Mean	**Std.Dev.**	**ND1**	**ND2**	**ND3**	**ND4**	**ND5**	**# of Params.**
Model 1	0.403	0.032	0.386	0.357	0.416	0.441	0.414	5
Model 2	0.189	0.066	0.183	0.091	0.222	0.269	0.181	9
Model 3	0.136	0.051	0.139	0.068	0.106	0.195	0.172	10
Model 4	0.113	0.049	0.129	0.054	0.076	0.178	0.130	10
Model 5	0.113	0.049	0.129	0.054	0.076	0.178	0.130	11

In order to compare models with differing number of free parameters to the model I used the Akaike information criteria.

Akaike Information Criteria

The Akaike information criterion (AIC) estimates the relative quality of a model by measuring the goodness of fit and applying a penalty to models with a higher number of free parameters. The penalty discourages over-fitting because the increasing number of parameters in a model almost always improves the goodness of fit. The model provides a likelihood function for the model that is dependant on the sample size n, the number of parameters k and the residual sum of square of the fit from regression (RSS). I first start with determining the AIC value of each model given by,

$$AIC = n \ln\left(\mathrm{RSS}/n\right) + 2k + \frac{2k\left(k+1\right)}{n-k-1}. \tag{4.16}$$

The best model is determined by examining their relative distances from the model with the lowest AIC value. The relative AIC value Δ_i for the ith model is then given by,

$$\Delta_i = AIC_i - \min\left(AIC\right). \tag{4.17}$$

The relative likelihood $\mathcal{L}$ of the model given the data is then given by,

$$\mathcal{L}_i = \exp\left(-\frac{\Delta_i}{2}\right) \tag{4.18}$$

In order to better interpret this value we can normalise these relative likelihood values across all the models to give the Akaike weights,

$$w_i = \frac{\mathcal{L}_i}{\sum_{j=1}^{5}\mathcal{L}_j}. \tag{4.19}$$

The Akaike weigths can now be interpreted as the probability that the model i is the best model given the data and the set of candidate models.

For the five models the Akaike information criteria analysis is summarised in Table (4.7).

Table 4.7: Model analysis with Akaike information criteria

	k	Mean RSS	Δ_i	w_i
Model 4	10	0.113	0	0.753
Model 5	11	0.113	2.2	0.247
Model 3	10	0.136	40.2	0.000
Model 2	9	0.189	105.0	0.000
Model 1	5	0.403	259.1	0.000

As a result of the Akaike information criteria analysis, I have concluded that Model 4 is 3× more likely than Model 5 and can exclude the remaining models. Interestingly while Model 1, which involves only the NV^- centre, can fit the general quenching trend, it is not capable of fitting the complete set of data as soon as the internal spin state is probed with a magnet. Finally, whilst Model 4 is the most likely model and the one discussed in the following sections, this is true only for continuous wave steady state conditions. The implication is that the stimulated emission pathway has a small impact on the steady steady state populations. Under non-steady state pulsed regimes the stimulated emission pathway may still have a significant impact on the transient populations of the NV centre.

4.9 Discussion of Identified Model

The identified model indicates that the quenching process of the NV centre fluorescence occurs through a continuous spin dependant charge state transfer between NV^0 and NV^- leading to increased non radiative decay through charge state interconversion of the NV centre, without any significant STED-like process. It is important to note that the STED-like mechanism alone could not account for the effects of the internal spin dynamics identified by applying the magnet. Comparing the models using the Akaike information criteria confirms that the steady state photo-physics of the NV centre is not significantly impacted by having an additional STED-like process. I emphasise that this process may be relevant in time resolved measurements. Additionally, while the model is kept quite general and the free

Table 4.8: Final identified model parameters. The units for $\Gamma_{g^T e^T}$, I_{532}, I_{785}, R_{532} and R_{785} are MHz mW^{-1} and for Γ_{SF} is MHz. The spin mixing in the ground state, Γ_{SF}, is noted $\Gamma_{SF}^{\text{NoMag}}$ in the absence of magnet and Γ_{SF}^{Mag} when the magnet is present.

Fixed Parameters				**Free Parameters**				
$\boldsymbol{\Gamma_{e^S g^S}}$	=	1 GHz	[110]	$\boldsymbol{\Gamma_{g^T e^T}}$	=	28	±	0.8
$\boldsymbol{\Gamma_{g^S g^T}}$	=	6.6 MHz	[146]	$\boldsymbol{\Gamma_{SF}^{\text{Mag}}}$	=	6.2	±	3.7
$\boldsymbol{\Gamma_{e_{\pm}^T e^S}}$	=	59 MHz	[143, 144]	$\boldsymbol{\kappa}$	=	0.70	±	0.23
$\boldsymbol{\Gamma_{e_0^T e^S}}$	=	11 MHz	[143, 144]	$\boldsymbol{I_{532}}$	=	14.3	±	6.3
$\boldsymbol{\Gamma_{e^T g^T}}$	=	38 MHz	[142]	$\boldsymbol{I_{785}}$	=	9.40	±	0.50
$\boldsymbol{\Gamma_{e^Z g^Z}}$	=	26 MHz	[151]	$\boldsymbol{\mu}$	=	0.837	±	0.005
$\boldsymbol{\Gamma_{g^Z e^Z}}$	=	$\frac{1}{3}\boldsymbol{\Gamma_{g^T e^T}}$	[109, 152]	$\boldsymbol{R_{532}}$	=	182	±	91
$\boldsymbol{\Gamma_{SF}^{\text{NoMag}}}$	=	1 KHz	[140]	$\boldsymbol{R_{785}}$	=	18.8	±	1.8
				$\boldsymbol{\nu}$	=	0.49	±	0.06

parameters unconstrained, the final values are physically meaningful and comparable with measurements reported in the literature. For the fixed parameters, I used well established values from the literature. In addition, to account for the modification of the lifetime of NV^0 centres in nano-diamonds due to local field effects, I used an average lifetime of 26 ns instead of the usual 13 ns in bulk [141, 142]. The final model parameters including both the fixed and free parameters are given in Table (4.8). I observe two types of model free parameters, those that are dependant on the internal NV structure and those that are influenced by the nano-diamond structure ie. strain or surface effects. When we consider the values that are related to the internal NV structure of the nano-diamond, the results obtained from the model are very consistent across different nano-diamonds.

The model shows that under strong NIR illumination, the continuous charge state interconversion processes provide a non-radiative decay across the different charge states: the ionisation (recombination) provides a path from the excited state of the NV$^-$ (NV^0) to the ground state of the NV^0 (NV$^-$). Under steady state conditions the ionisation and recombination driving rates for the 532 nm laser are consistent with the charge state transfer rates

for single NV centres in nano-diamonds [109]. Such driving between charge states is then dramatically increased by the addition of the 785 nm NIR laser. I note that it is difficult to directly compare the ionisation and recombination rates between the two laser wavelengths as the photo-dynamics are different for each wavelength. The 785 nm laser cannot ionise/recombine the NV centres without the additional excitation of the transition provided by the 532 nm laser. The main result of the model, is that as soon as the incident NIR power exceeds a few mW the ionisation/recombination rate is comparable or larger than the spontaneous decay rates of the NV centre. This process is sufficient to explain the strong fluorescence quenching. Furthermore, by obtaining measurements with a magnet to mix the NV^- ground state spin, we could also study the spin dependence of such ionisation/recombination processes. The exact value of the spin mixing, $\Gamma^{SF}_{\text{Mag}} = (6.2 \pm 3.4)\,\text{MHz}$, depends strongly on the exact number and orientations of the NV centres within the diamond crystal and consequently varies between nano-diamonds. The spin dynamics I obtained for the NV^- through the singlet state closely matches the values reported in the literature where the recombination to NV^- ground state favours the $m_s = 0$ state over the $m_s = \pm 1$ states , but varies significantly between nano-diamonds ($\kappa = 0.70 \pm 0.23$) [146, 147].

Interestingly, the model also indicates that the $NV^- \rightarrow NV^0$ ionisation process is a spin dependant process. On a phenomenological level, this effect is similar to the spin dependent charge dynamics under 1064 nm laser excitation [157] but has important consequence on the spin state of the NV^-. In the work of F. Jelezko and J. Warchtrup [119] it was proposed that this process involves two photons and an Auger ionisation process. These results suggest that this ionisation process is spin dependent, significantly favouring ionisation from the $m_s = 0$ spin state. Using the Akaike information criteria, the Akaike weight for the model without spin dependence is negligible relative to the model with spin dependence, confirming that this effect needs to be taken into account to properly describe the experimental data. Remarkably, the spin selectivity of the ionisation process is the same between nano-diamonds with a very small variation of the μ coefficient for the different nano-diamonds measured ($\mu = 0.837 \pm 0.005$). This is consistent with a process related to the photo-physical properties of the NV^- centre with little to no effect from any of the neighbouring impurities in the crystal or strain. One important consequence of this spin selectivity is the impact of the

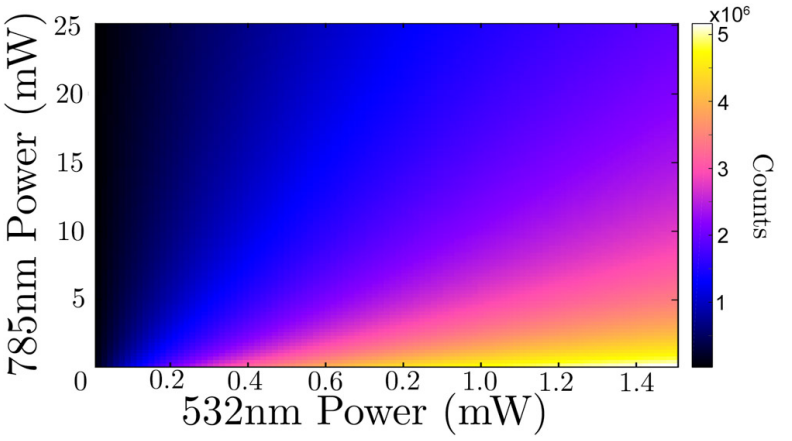

(a)

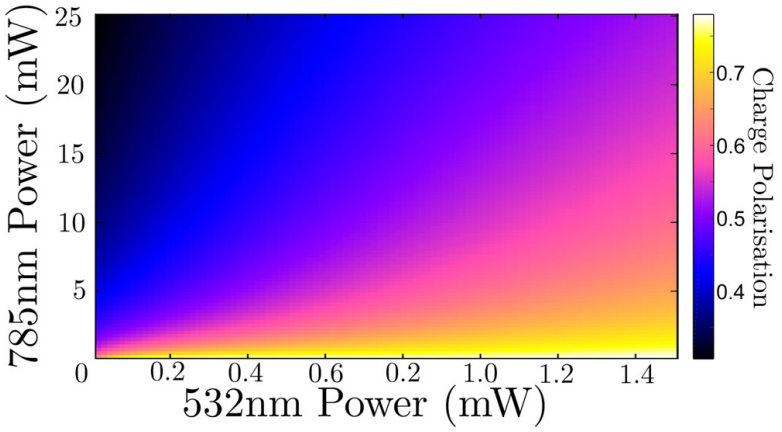

(b)

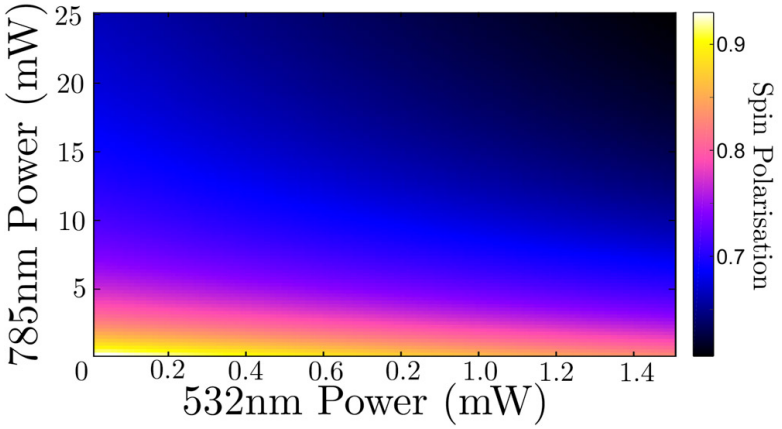

(c)

Figure 4.10: Predicted fluorescence, charge and spin polarisation of NV centres under 532 nm excitation and 785 nm quenching. (**a**) Fluorescence count, (**b**) charge polarisation (1 is completely in the NV^- state) and (**c**) spin polartisation (1 is completely in the $m_s = 0$ state) obtained using the model with the average parameters obtained from fitting the experimental measurements from 5 distinct nano-diamonds.

785 nm laser on the spin polarisation of the NV^-. For example, when operating above saturation (532 nm power of $\sim$ 1 mW), moderate powers of 785 nm does not appreciably change the charge state since the 532 nm will efficiently polarise the NV into NV^-. On the other hand, the spin polarisation is significantly modified as can be seen in Figure (4.10). In most quantum applications of NV centres, the control of the spin plays a central role. In particular, the spin initialisation is typically realised using 532 nm pumping to efficiently prepare the NV^- in the $m_s = 0$ spin state. The results show that even a moderate amount of 785 nm is sufficient to significantly reduce the spin polarisation. As a result under NIR illumination the charge state interconversion process must be taken into account in order to prepare the charge state of the NV but also for preparation of the spin state of the NV^- for quantum manipulation protocols.

For high resolution microscopy in which this process is used, maximising the quenching efficiency would increase the resolution of the imaging. In order to maximise the STED-like effect, the quenching laser would ideally be one that maximises the ionisation and recombination rates. The ionisation and recombination quenching process could be dramatically increased by first exciting each charge state at the ZPL and further driving the ionisation and recombination process with an additional quenching laser. Identifying the optimal driving laser wavelength can be determined by observing the quenching of a nano-diamond as a function of quenching laser wavelength. This result is consistent with the work of F.W. Sun *et al.* [158]. Finally in comparison to traditional STED microscopy, this charge state interconversion microscopy uses more laser wavelengths for imaging but reduces total laser power incident on the sample reducing the heating and photodamage of the sample.

These results show that the 785 nm NIR illumination plays a critical role on the photodynamics of the NV centre which could have a detrimental effect on manipulation protocols of the quantum state of the NV^- centre. A logical next step towards understanding and controlling the charge state interconversion processes is to investigate the wavelength dependence and the effect of the local environment on these processes. For example, the strain on the crystal and density of nitrogen in the crystal could significantly impact the ionisation and recombination rates. In addition, by capitalising on the various time scales of the processes at play I believe it will be possible to achieve a better control on either the charge state or

the spin state of the NV centres by pulse sequencing the different lasers wavelengths.

Whilst I have the ability to experimentally study the quenching dynamics of a 1064 nm laser, the current model is not suitable for the analysis. It is expected that the mechanism is indeed similar and that the quenching is due to the charge state interconversion process, however in this case there will be a stronger ionisation pathway from the singlet state of the NV^- centre to the NV^0 ground state. A wavelength close to the optically active 1042 nm transition will drive the singlet transition providing a potentially significant population in the excited singlet state resulting in this ionisation pathway to no longer be negligible. As mentioned previously, this additional pathway is beyond the scope of this model since accounting for it introduces a number of extra free parameters, risking over-fitting.

Unfortunately, for optically levitated NV centres there does not appear to be an easily accessible wavelength that does not depopulate the excited state of the NV centres. Even at 1550 nm the fluorescence of NV centre has been observed to be quenched [56]. Potentially working in the deep IR will be possible since these photons may not have enough energy to efficiently ionise and recombine the defects charge state, however this will require a complete replacement of all of the optical elements and detectors. As a result, observing resonant optical dipole forces on NV centres in optical levitation does not appear to be feasible.

The reason that resonant optical forces were indeed possible to be observed in liquid trapping was that the trapping laser powers needed to hold the nano-diamonds are approximately 50 to 100 times weaker than for levitation. Thus in the aqueous regime, the 2-photon charge interconversion processes were minimal and the optically resonant forces were observable. Due to the power constraints in optical levitation, the quenching is unavoidable and eliminates the possibility of observing the additional atomic dipole forces from levitated NV centres. Our attention must now change to other defects in diamond in which a quenching mechanism has not been observed, namely, the Silicon Vacancy and the Germanium Vacancy centres. However, there is much less research on the Silicon Vacancy and Germanium Vacancy centres since they do not possess the same room temperature optically initialisable spin state that make the NV so interesting. Whilst recently there has been more interest in these defects, it is still possible that quenching and charge state interconversion processes

still occur in these defects under intense NIR illumination but has yet to be observed. Unfortunately, we do not have samples of Germanium Vacancies in nano-diamonds, however we have two samples of Silicon Vacancies in nano-diamonds that I was able to investigate. Chapter 5 covers the details of investigating the high power NIR trapping lasers effects on Silicon Vacancy centres with, the aim of observing resonantly enhanced optical forces.

> 'I've been making a list of the things they don't teach you at school. They don't teach you how to love somebody. They don't teach you how to be famous. They don't teach you how to be rich or how to be poor. They don't teach you how to walk away from someone you don't love any longer. They don't teach you how to know what's going on in someone else's mind. They don't teach you what to say to someone who's dying. They don't teach you anything worth knowing.'
>
> –Neil Gaiman, The Kindly Ones

'The rock still has something to teach me.'

– Chris Sharma

5

Silicon Vacancy Centres in Nano-Diamonds

Optically levitating Silicon Vacancy (SiV) centres is the clear next choice after Nitrogen Vacancy (NV) centres due to both the availability of samples and their strong dipole transition at optically available wavelengths. Additionally, the SiV emits over 80% of its fluorescence into the zero phonon line (ZPL) [159], whereas the NV centre typically emits only 4% of the fluorescence into the ZPL. To form the SiV defect in the diamond matrix, two neighbouring carbon atoms along the $\langle 111 \rangle$ direction are replaced by a single silicon atom [160–162]. Unlike the NV centre, where the Nitrogen atom occupies the place of a carbon atom, the silicon atom in the SiV centre sits between the two vacancies of the diamond matrix. This provides additional symmetries to the centre which give the atomic structure additional spin degeneracies as well partially reducing the strength of the phonon side band (PSB).

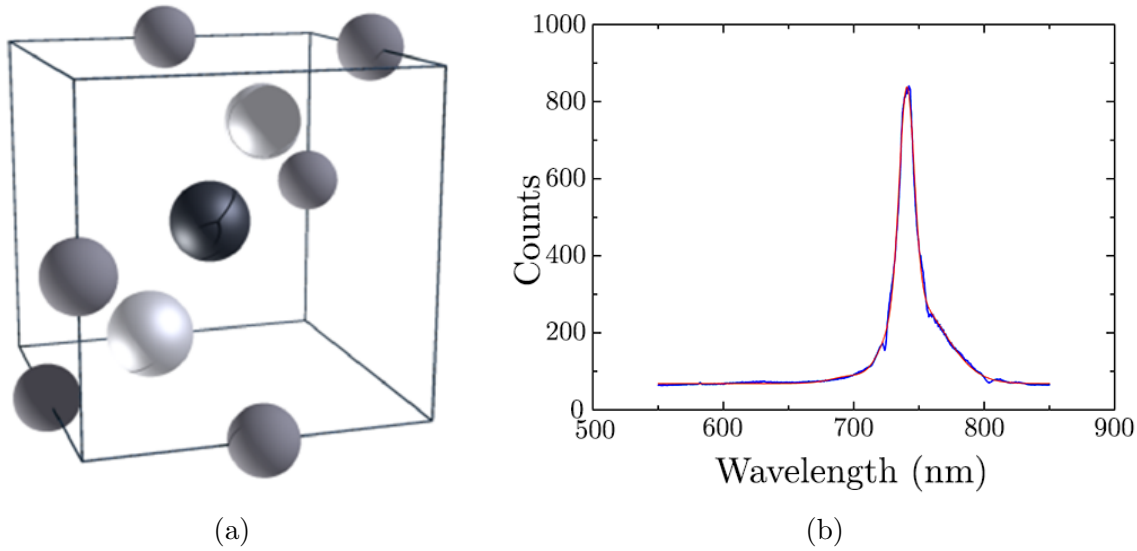

(a) (b)

Figure 5.1: SiV structure in the diamond lattice and photo-luminescence structure. (**a**) The SiV centre has a principal axis of symmetry in the crystallographic ⟨111⟩ direction. The silicon atom is shown in black sitting in the centre of the unit cell, between the two vacancies shown in white. (**b**) Fluorescence emission spectra of a nano-diamond containing many SiV centres showing a strong ZPL emission centred at 739 nm.

Similar to the NV, the SiV can exist in either a neutral charge state SiV^0, or a negatively charged state, SiV^-. The negatively charged state shows a strong ZPL at 739 nm that can be off resonantly excited, typically using a 532 nm laser. The excited state lifetime is ≈1 ns [163–166], an order of magnitude faster than for the NV centre.

The combination of a shorter fluorescence lifetime and weaker PSB, makes the SiV^- centre appear as a better candidate for observing atomic dipole forces in levitated nano-diamonds. However, there are still unknown parameters and detrimental effects that may limit the possibility of observing atomic dipole forces on an ensemble of SiV centres. The quantum efficiency, for example, is only on the order of 10% which reduces the effective dipole strength and dramatically increases the heating rate of the nano-diamond since 90% of the absorbed photons are being converted into heat in diamond lattice. This important heating necessitates extra care because the SiV thermal dephasing rates broaden the spectral properties of the transition as the temperature increases. Furthermore, the increased heating rate can potentially vaporise the nano-diamonds within the trap if they get too hot.

Observation of dipole forces on NV centres in water relied on the appearance of cooperative effects which have not been investigated in SiV centres. We foresee that if we obtain sufficiently large concentrations of SiV centres in nano-diamonds there would indeed be cooperative effects increasing the decay rate, beneficial for two reasons. Firstly, the increased decay rate and therefore decreased transition linewidth (Γ), directly increases the dipole force as observed in Chapter 2, Equation (2.60). Secondly, I anticipate that an increased decay rate would increase the quantum efficiency of the fluorescence emission further increasing the force and reducing the heating rate. Here, I am assuming that the channels for non-radiative decay do not act cooperatively. In this case, an increase in the fluorescence rate with no increase in the non-radiative decay rate would lead an to increased likelihood of a fluorescence photon being emitted over being absorbed in the crystal lattice. This is directly related to an increase in the quantum efficiency. I must note that the effects of superradiance and its effects on the non-radiative pathways in solid state are unknown and that it may indeed be possible for non-radiative transitions to behave cooperatively.

The other concern for the SiV centre is that the neutral charge state is often neglected and may strongly interact with the trapping lasers as we observed for the NV centre. The neutral charge state of the SiV centre has a lower energy ZPL at 946 nm [167]. I speculate that unlike the NV centre, since the neutral charge state of the SiV centre is at a lower energy, the excitation laser that excites the negatively charged state can also excite the neutral charge state allowing for an efficient recombination process to occur. Unfortunately, at this stage the charge state interconversion photo-dynamics of the SiV complex is unknown.

As a result, I found it imperative to investigate the SiV centres from two angles. The first is to ensure that we can optically levitate the available samples of nano-diamonds containing SiV centres. However, before attempting to observe the fluorescence of the SiV centres in levitation, the second and more fundamental experiment is to investigate in detail the photo-physics of SiV centres and assess the potential effects that the various high intensity trapping lasers could have on the SiV centres.

5.1 Silicon Vacancy Samples

> 'You will not believe me even when I tell you, so it is fairly safe to tell you. And it will be a comfort to tell someone. I really have a big business in hand, a very big business. But there are troubles just now. The fact is...I make diamonds.'
>
> – H. G. Wells, The Diamond Maker

Synthesis and growth of diamond and nano-diamond samples is still an ongoing scientific field of research. Due to the immense research interest on NV centres and their room temperature quantum properties, many research groups have refined the process of growing nano-diamonds with the desired number of NV centres with low strain and low amorphous/graphitic carbon impurities. In comparison, whilst they are the second most available defects, Silicon Vacancy samples are much harder to obtain especially with high concentrations, exhibiting low strain and low amorphous and graphitic carbon.

High concentration samples are desirable for two reasons. Firstly, the higher the number of SiV centres the stronger the atomic dipole forces are on the nano-diamond as a whole. More excitingly, a higher concentration of SiV centres provides an increase in the likelihood of collective effects*.

Obtaining nano-diamonds with lower strain reduces the overall spectral broadening of the SIV centres. This allows for the ensemble SiV spectral response within the one nano-diamond to be sharper, providing a stronger resonance and therefore combined atomic dipole force. This will also provide enhanced indistinguishability, a necessary condition to observe collective effects.

Finally, the presence of amorphous and graphitic carbon on the surface of the nano-diamonds is detrimental as it is absorbing in the visible and near infrared spectrum, drastically increasing the absorption of the nano-diamond. The increased absorption leads to both heating of the nano-diamonds as well as increasing the absorptive scattering force pushing the diamonds out of the optical trap.

We have obtained two nano-diamond samples containing Silicon Vacancy centres. The

*Admittedly, if the SiV concentration is too high the defects themselves will create strain in the crystal causing an increase in indistinguishability between centres, however we are far for reaching these concentrations and can therefore ignore this effect.

first sample was obtained from Fedor Jelezko's group in Ulm University, Germany. This sample is a high temperature, high pressure (HPHT) grown sample. The HPHT process is a low cost process for growing diamonds but does not allow a great deal of control during the synthesis process. These diamonds are low strain showing a width of the ZPL on the order of 2 nm and are very clean, containing little to no surface amorphous and graphitic carbon. Unfortunately, whilst these and other HPHT grown diamonds exhibit excellent SiV properties, the HPHT growth process is unsuitable for obtaining high concentrations of SiV required for observing either cooperativity or atomic dipole forces [168]. We must therefore look for alternative growth methods.

The second sample we have available was grown using the chemical vapour deposition method, abbreviated CVD, in house at Macquarie University. The CVD process allows for a high level of control and customisation over the growth process of the artificial diamonds. The inclusion of colour centres via the CVD growth method is undertaken by introducing the desired dopant as the diamond is grown. This can be achieved by either choosing the appropriate substrate or by introducing the dopant near the substrate in the reaction chamber. We aimed to create a high concentration of silicon impurities in the diamonds by growing the diamond films on a seeded silicon substrate wafer. Coating the silicon wafer with 4 nm detonation diamonds provides a foundation for the material growth, called seeding, which can easily be seen on the final silicon wafer as shown in Figure (5.2). Once the samples are removed from the CVD reactor the silicon atoms are dispersed within the diamond films, however typically, they have not combined with vacancies to produce Silicon Vacancy centres. In order to produce the Silicon Vacancies the diamond matrix needs to be air oxidised.

Air oxidisation is the process of heating a diamond sample in an oxygen environment, resulting in the mobilisation of vacancies within the diamond lattice. Above $\approx 850°C$ the vacancies within the diamonds lattice move through the matrix where they can combine with an adjacent silicon atom, producing a stable Silicon Vacancy defect [170]. In addition, this process reduces imperfections and strain in the crystal lattice and removes amorphous and graphic carbon from the surface of the diamonds, converting it into carbon dioxide (CO_2).

Once the diamond films are air oxidised, to turn the diamond films into nano-diamonds,

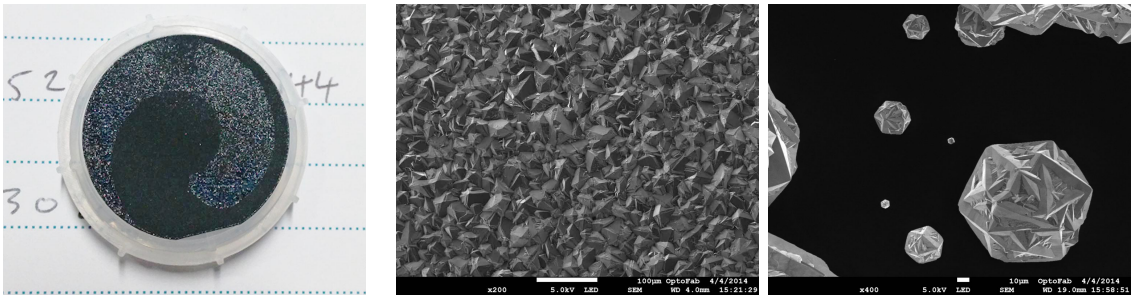

(a) (b) (c)

Figure 5.2: (**a**) Seeded silicon substrate after nano-diamond growth. We can observe that the region where the substrate was seeded has resulted in a greater diamond growth when compared to that of the unseeded region. (**b**) SEM image of the seeded region of the substrate showing a polycrystalline diamond film. (**c**) SEM image of isolated diamond crystals of various sizes on the unseeded region of the silicon substrate. These diamonds were grown in house at Macquarie University and contain a high concentration of Silicon Vacancy centres due to the silicon substrate [169].

the films needs to be milled to the desired size range using a planetary ball mill. The planetary ball mill uses tungsten carbide milling balls in order to ground the diamond by impact, shearing and frictional forces. The nano-diamond is then separated from the tungsten balls through a sonication and centrifugation process producing a concentrated water solution containing many nano-diamonds [169].

Unfortunately, due to the violent nature of the process, ball milling introduces large inhomogeneous strain in the nano-diamond crystals. The inhomogeneous strain across the crystal shifts the ZPL of each SiV centre creating a broad ensemble emission spectrum for the nano-diamond as a whole. Typically, the nano-diamonds can be placed on a coverslip and air oxidised for a second time, reducing the inhomogeneous strain, further improving the ensemble spectral emission. For optical levitation however, this process is unavailable to us since the nano-diamonds are unrecoverable once they are adhered to the coverslip surface. I speculate that it may be possible to enhance the ensemble spectrum of the SiV centres by air oxidising the nano-diamonds in levitation by heating the nano-diamonds above $\approx 850°$ in an air environment. This approach however would require significant research since thermometry of levitated nano-particles is still a nascent field.

The solution of high density Silicon Vacancy centres made at Macquarie University was characterised without the second air oxidation step using a combined confocal and high

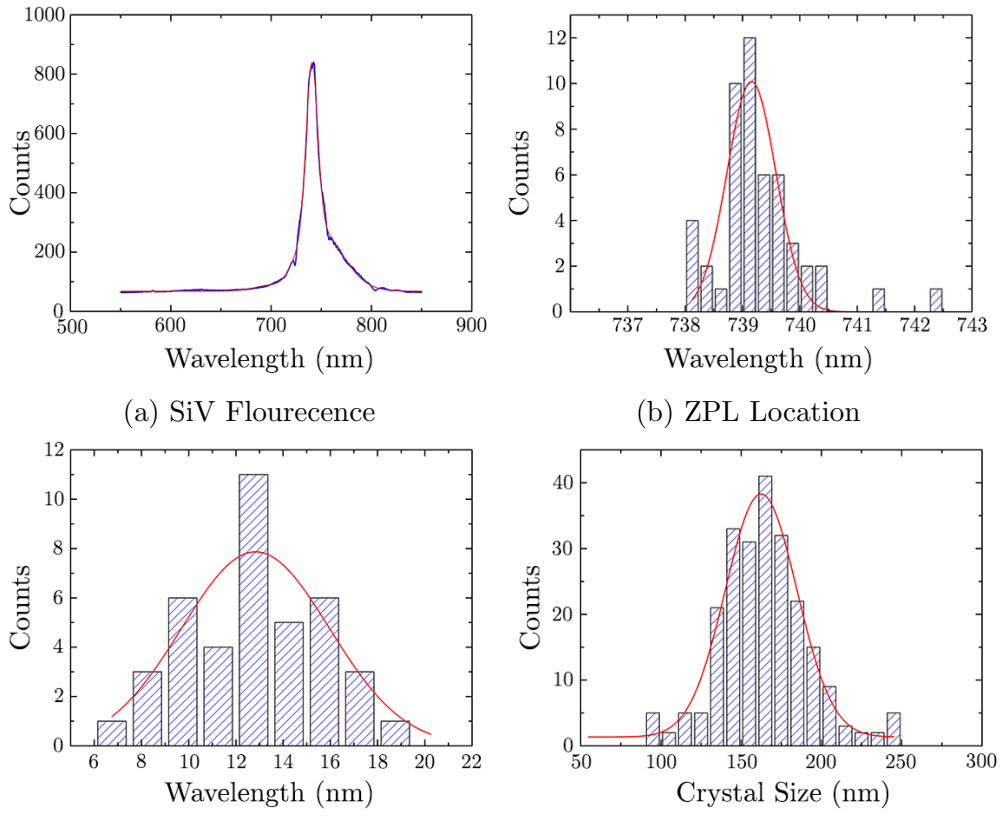

(a) SiV Flourecence (b) ZPL Location

(c) ZPL Width (d) Nano-Diamond Size

Figure 5.3: Optical properties of nano-diamonds containing a high density of SiV centres. (**a**) Photo-luminescence spectrum of the grown nano-diamond sample containing SiV centres. A fit comprising of a Lorentzian and three Gaussians was applied to extract the ZPL location and FWHM data. (**b**) Location of the SiV centre ZPL. The peak of the fitted Gaussian is located at 739.1 nm. (**c**) Full width at half maximum of the nano-diamond fluorescence. The peak of the fitted Gaussian corresponds to 12.8 nm. (**d**) Distribution of nano-diamond crystal sizes, the peak of the fitted Gaussian corresponds to a crystal size of 162±22 nm [169].

resolution atomic force microscope scan [169]. A typical fluorescence spectrum of a nano-diamond is shown in Figure (5.3a). Statistics of the sample show the average location of the ZPL to be 739.8 nm± 0.8 nm with a FWHM of 12.8±3.1 nm as shown in Figure (5.3b) and Figure (5.3c) respectively. Finally, the average crystal size was determined to be 162.5± 22.3 nm as shown in Figure (5.3d). These results show the significant strain that has been induced in the nano-diamond crystals. Without the second stage air oxidation process these nano-diamonds exhibit an ensemble spectrum six times wider than for the low strain low SiV concentration sample. Whilst this strain should not limit the ability to create an induced dipole in the nano-diamonds and levitate them using the bulk dielectric polarisability, it will

drastically reduce the atomic dipole forces and indistinugishability between centres needed for cooperativity.

5.2 Optical Levitation of SiV Centres in Vacuum

In parallel to the spectroscopy measurements of the Silicon Vacancy centres, I attempted to optically levitate the nano-diamonds containing SiV centres in a vacuum environment using only the dielectric polarisability of the diamond. The two SiV samples in ethanol can be observed in Figure (5.4). The low density SiV sample is observed to be a milky white colour indicating low absorption, however the high SiV concentration sample is dark and opaque. This indicates that the nano-diamonds are likely coated in a significant amount of amorphous and graphitic carbon. In the following section I outline the new optical trapping arrangement as well as the preliminary attempts of optically levitating the nano-diamond samples.

This vacuum levitation platform was built specifically for observing and manipulating the atomic optical dipole forces with further potential of applying optical cooling strategies. To apply optical cooling strategies on an optically levitated nano-particle, the oscillation of the particle must be in the under-damped regime. In order to reach the under-damped regime the Brownian motion arising from the collision of gas molecules with the nano-particle must be removed. In the new platform as shown in Figure (5.5) I implemented an optical levitation set-up contained within a vacuum chamber in order to levitate nano-particles in the under-damped regime.

The vacuum chamber contains a microscope objective and an aspheric condenser lens to collect the laser and scattered fields for position detection as shown in Figure (5.6). The trapping laser was fed in through one of the windows of the vacuum chamber and was collected from two different ports. The first, collimated by the aspheric lens for position detection and the second for observing particles within the chamber using a CCD camera. Particles are nebulized into the chamber at standard atmospheric pressure. Many particles are observed to pass through the CCD camera's field of view and some particles may appear as bright spots as they pass near the focus of the trapping laser. After a certain point in

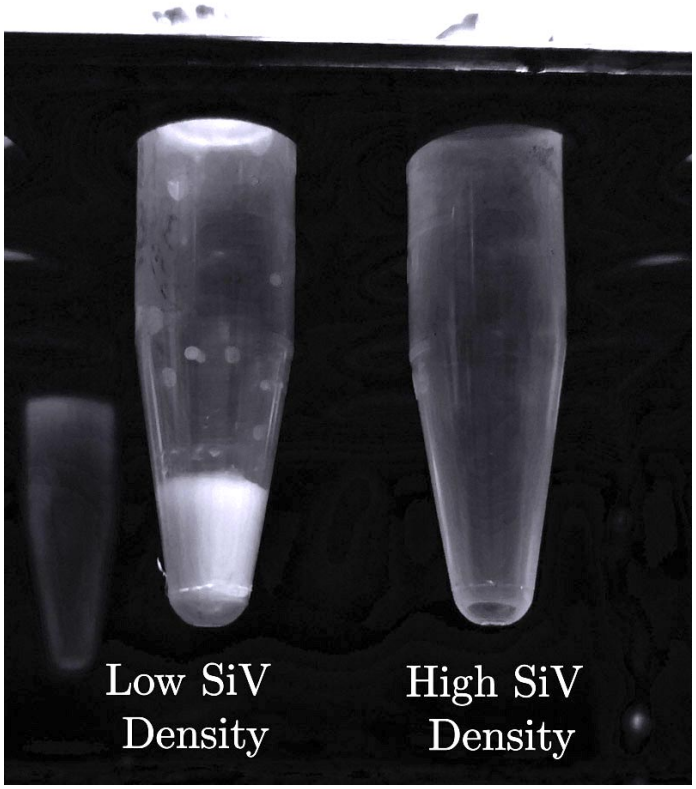

Figure 5.4: Photo of the SiV samples after settling for a long period of time. Without sonicating the samples, the nano-diamonds will sediment at the bottom of the water solutions. The sample containing a low density of SiV centres within each nano-diamonds is a milky white colour. The sample containing a high density of SiV centres within each nano-diamonds however, when settled, is dark and opaque suggesting that the nano-diamonds are coated in graphitic and amorphous carbon.

time a low speed particle will pass through the focal point of the laser and would be trapped, appearing as a stable bright spot on the CCD camera as shown in Figure (5.7).

At this point the vacuum pump is enabled, purging the chamber of both the remaining nano-particles and surrounding air. The vacuum chamber is capable of obtaining a minimum pressure of 10^{-6} mBar using the Turbopump; however currently, we can only maintain trapping of a nano-particle down to appropriately 1 mBar at which point they are lost from the optical trap. The loss of nano-particles at this pressure has been observed previously by other research groups and the exact mechanism for particle loss is still disputed [171–174]. It has been repeatedly shown however, that providing a particle cooling mechanism will allow

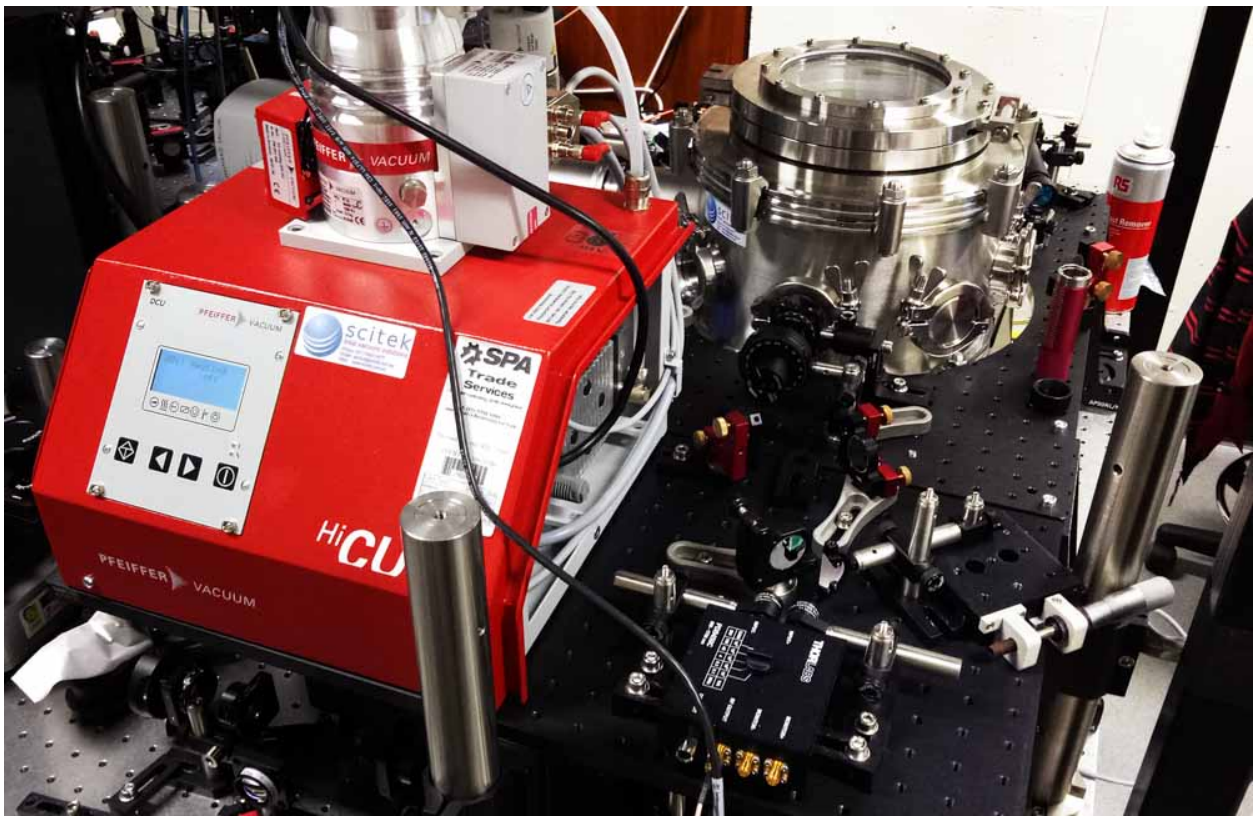

Figure 5.5: Pan image of the full vacuum levitation set-up. The red roughing pump can be seen on the left which can reduce the pressure of the chamber down to mBar pressures. On top of the roughing pump is the second stage Turbopump which can get to a minimum pressure of 10^{-6}mBar. Next to it on the right lies the balanced photodetector and its associated optics, a detail of which was shown in the previous section. Further away, theres the setting for the vacuum chamber with its optical ports visible. Underneath the vacuum pump and vacuum chamber is all of the lasers and associated optics preparing the beams for optical trapping and detection.

the particle trap to be maintained through this pressure transition towards a high vacuum regime. At this stage I have not implemented a cooling or feedback system and cannot go to lower pressures. An additional advantage provided by this system is the ability to trap nano-diamonds at lower trapping intensities due to the reduced Brownian motion kicking the particles out of the trap. Typically nano-diamonds are lost at trapping intensities below 20 mW at 10 mBar as opposed to 50 mW for trapping at atmospheric pressure.

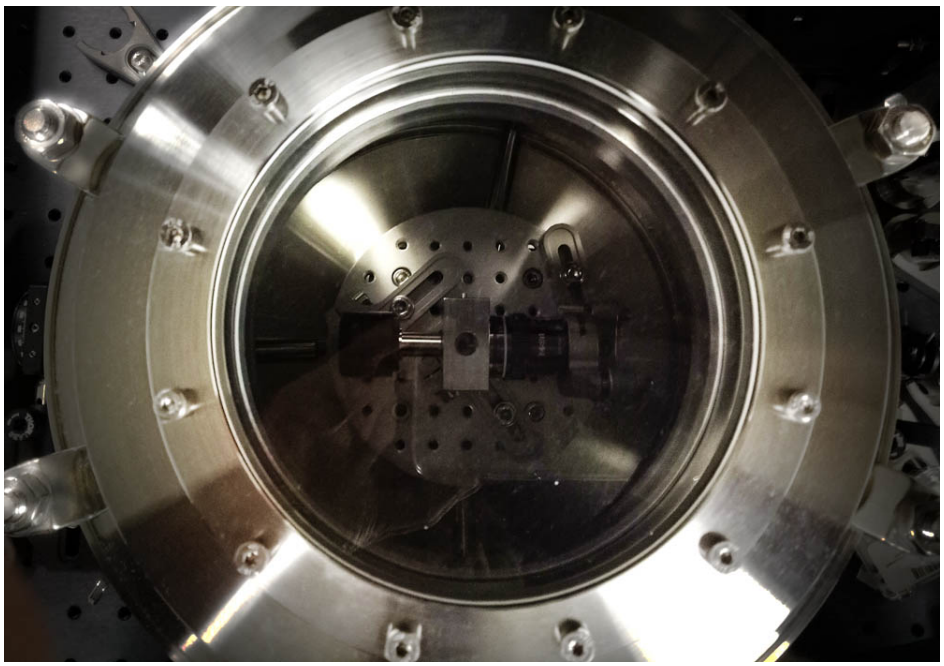

(a)

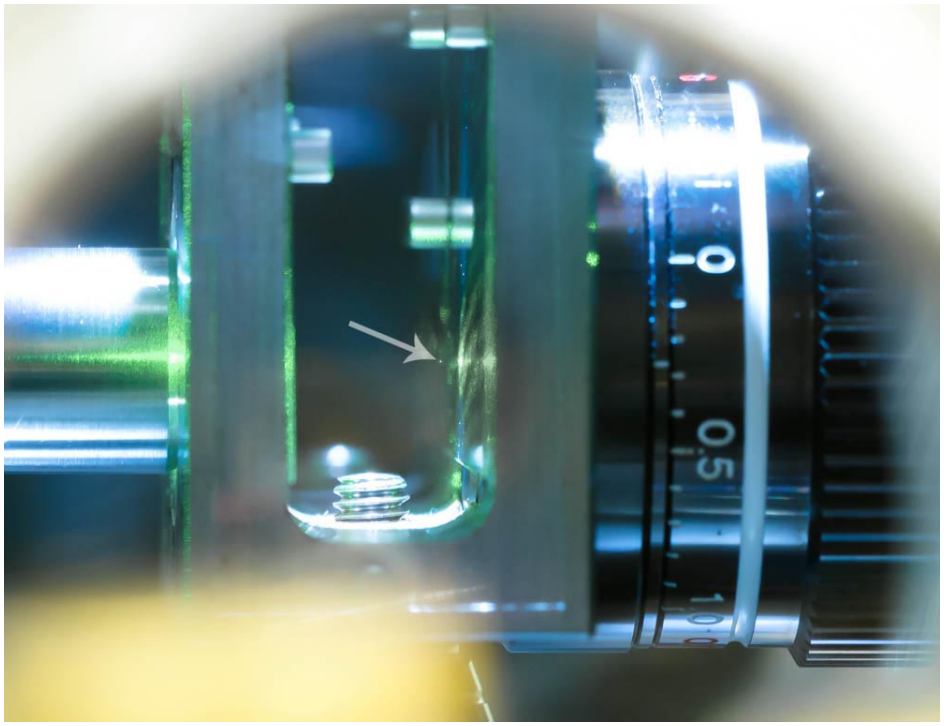

(b)

Figure 5.6: **(a)** Image of the vacuum chamber from outside and **(b)**, a levitated nano-diamond inside the vacuum chamber. Glass coverslips are held in place protecting the optical surfaces by the cylindrical magnets. The nano-particles are nebulized inside the vacuum chamber with the laser on. The chamber is then closed and the particles float freely until one is trapped in the laser beam. The vacuum pump is then engaged to evacuate the chamber and any remaining nano-particles.

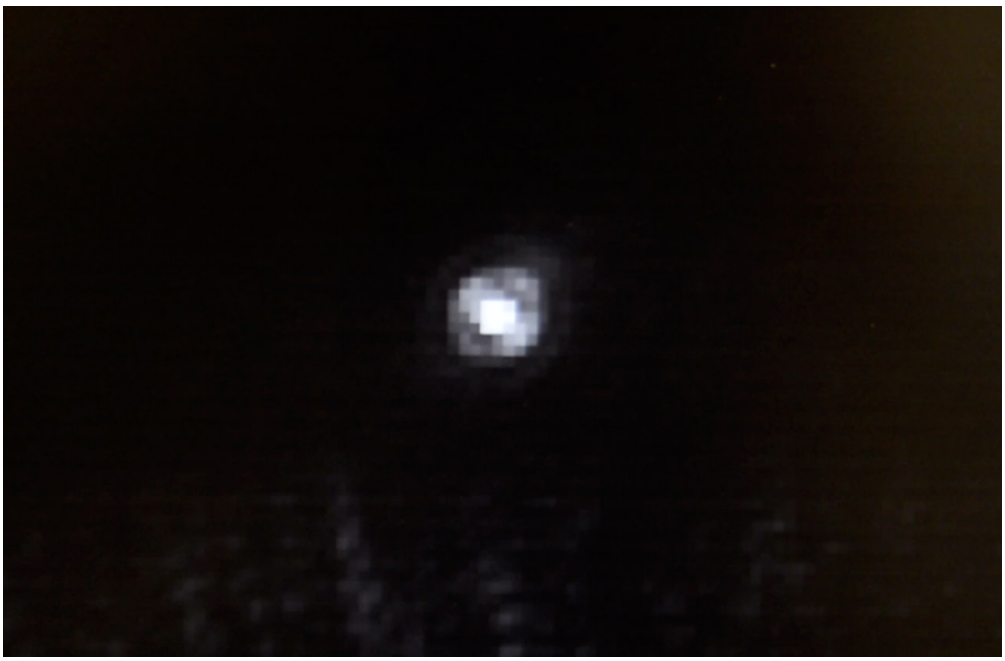

Figure 5.7: CCD image of a stably trapped nano-particle appearing as a bright diffraction limited spot.

In this platform, trapping of nano-diamonds containing low concentrations of Silicon Vacancies is possible, however the concentration is so low, on the order of single sites per nano-diamond, that observation of atomic optical dipole forces is infeasible. The high concentration sample however after repeated attempts can not be optically trapped within this platform. We attribute the inability to trap due to the high absorption and scattering from the optically opaque amorphous and graphitic carbon that covers the nano-diamonds. In order to provide ourselves with a better SiV sample I investigated the potential of chemically treating the nano-diamonds to both reduce the strain as well as the amorphous and graphitic carbon surface impurities. This process was designed to replace the second air oxidisation process that can not be implemented on our aqueous samples.

5.2.1 Nano-Diamond-Acid Treatment

I performed an acid cleaning treatment to the nano-diamonds consisting of boiling the solution in a 1:1:1 Sulfuric Acid, Perchloric Acid and Nitric acid as shown in Figure (5.8). The acid-nano-diamond mix was boiled at 150° C for 6 hours to remove the amorphous and

graphitic carbon. Raising the temperature of the three acid mix does increase the reaction speed, and should make it faster to clean the nano-diamonds as well as begin to remove strain. However, this effect is non-linear and difficult to predict. When the strong acids are boiled at too high a temperature they can produce highly toxic gases such as NOx. In short, I could not perform an acid treatment that would reduce strain as well as reducing the amorphous and graphic carbon. After boiling, the acid-nano-diamond mix was repeatedly centrifuged, decanted, diluted in water and sonicated until the cleaned nano-diamonds were suspended in a neutral pH water solution. The complete acid cleaning treatment is given in the appendix, Section (A.1).

This acid treatment removed part of the amorphous and graphic carbon from the nano-diamonds, however there was still too much absorbing material to successfully levitate them[†]. To further remove more of the surface impurities, a more rigorous cleaning treatment is needed [175]. I believe that there is potential in this space to also include boiling of the acid solution at temperatures high enough to allow morphology changes in the crystal structure as is the case in high temperature air oxidation. A process of this type will allow the strain of the nano-diamonds to be reduced in an aqueous environment allowing for improved ensemble optical transitions. This experimental approach was not followed as I continued to investigate the spectral properties of the nano-diamonds containing SiV centres.

Whilst the levitation platform is ideally built to manipulate and take advantage of the resonant forces from the internal defects, at this stage I have been unable to observe these forces and as a result no publishable measurements have been obtainable from this system. For NV centres the internal dynamics of the defects and the charge state interconversion processes do not allow for observable dipole forces for the trapping lasers I have available. For the SiV centres, the inability to levitate the high concentration sample has prevented further exploration of the dipole forces for this centre. In the future levitation of Germanium Vacancy centres, which I believe will be the most promising optical defect to date, will require further engineering and research in order to have samples with the desired high concentration, low strain and low surface impurities.

[†]I also attempted to trap the nano-diamonds in a water solution, however the scattering force was still too large and the particles were pushed out of the trap.

Figure 5.8: Image of the acid boiling treatment process on the nano-diamonds containing many SiV centres to remove the unwanted surface impurities coating the nano-diamond. The solution sits in a round bottom flask in a heated sand bath. A thermometer is placed in the solution to measure the temperature of the acid nano-diamond mix. Above the solution is the water cooled glass condensor to ensure that no nano-diamond material is lost.

5.3 Silicon Vacancy Photo-Physics

The following section shows the preliminary results probing the interaction between the trapping laser wavelengths and the photo-physics of the Silicon Vacancy centre. This preliminary investigation shows a strong up-conversion mechanism in the SiV centre providing the possibility to optically cool both the nano-diamond itself and its CoM motion with a single trapping laser.

5.3.1 SiV Preliminary Data

Using the set-up described in Chapter 4, Figure (4.1) to probe the quenching of fluorescence of NV centres, I placed our bright CVD grown sample of Silicon Vacancy centres at the focal plane of the confocal microscope. Under 532 nm green excitation, the 739 nm Silicon Vacancy florescence could be observed and increased with excitation power as shown in Figure (5.9). The off resonant excitation mechanism of the SiV from the ground ^2E state to the excited ^2E state occurs through a third ^2A level sitting above the excited state that quickly and non-radiatively decays to the excited ^2E state [176]. The slight non-linearity in excitation is attributed to the saturation dynamics of the two level transition.

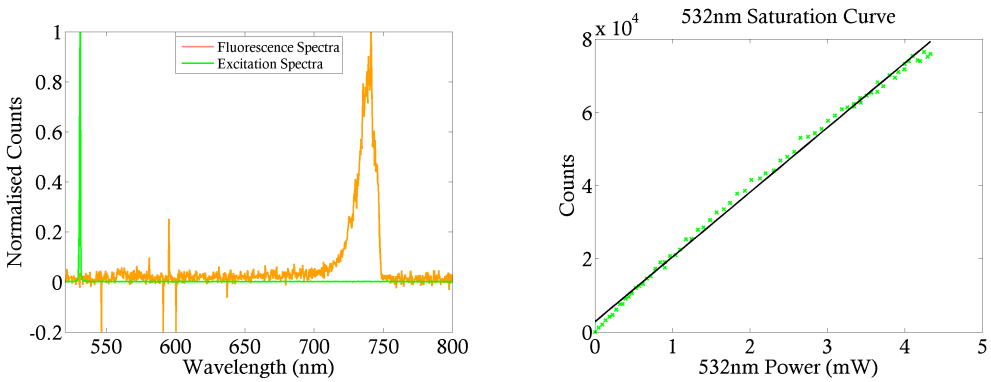

(a) (b)

Figure 5.9: Preliminary SiV measurements, exciting with a 532 nm laser. (**a**) excitation and fluorescence spectra of the nano-diamonds showing SiV emission. The fluorescence spectra was filtered with the 550 nm to 750 nm filter stack as shown in Figure (3.20). (**b**) Saturation curve of the SiV centres under 532 nm excitation with a linear fit.

Probing the nano-diamonds with 1064 nm laser light showed no change in the fluorescence

signal of the SiV centres. This preliminary measurement is a promising sign that the SiV centres contained within levitated nano-diamonds will not directly interact with the intense additional laser field destroying the strong optical dipole. It is true however that heating due to the additional laser field will still effect the optical transitions and can not be investigated on our current platform.

The 785 nm laser on the other hand, contrary to any expected effect, increased the SiV fluorescence signal. Interestingly, the nano-diamonds probed with only 785 nm and no green 532 nm laser, exhibited fluorescence from the Silicon Vacancy centres that increased linearly with input power as shown in Figure (5.10).

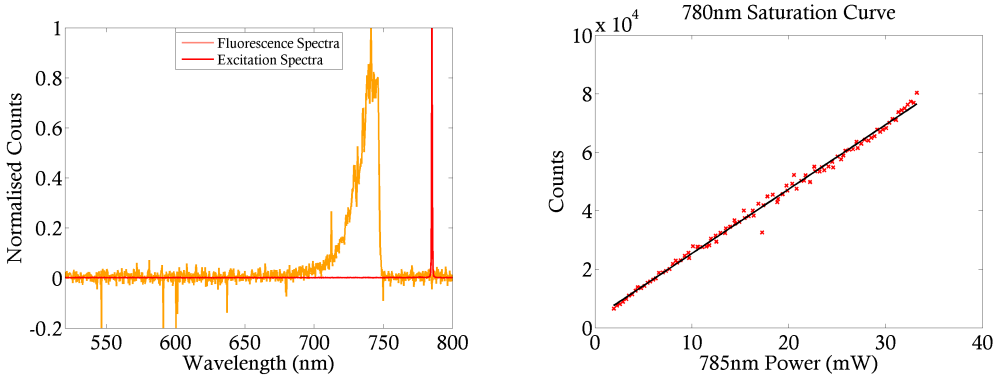

(a) (b)

Figure 5.10: Preliminary SiV measurements, exciting with a 785 nm laser. (**a**) Excitation and fluorescence spectra of the nano-diamonds showing SiV emission. The fluorescence spectra was filtered with the 550 nm to 750 nm filter stack as shown in Figure (3.20). (**b**) Saturation curve of the SiV centres under 785 nm excitation showing a linear excitation.

The linear increase with excitation power indicates that this effect is not due to a two photon process but by a single photon up-conversion or anti-stokes shift process. With this data we thought of two possible theories that could explain the SiV fluorescence from the 785 nm excitation.

The first possibility is that the phonon side band of the Silicon Vacancy centres could be thermally occupied and the laser is exciting from a thermally occupied state into the excited state, absorbing a lattice phonon in the process as shown in Figure (5.11a). If this were the case tuning the excitation wavelength above 739 nm and observing the excitation efficiency as a function of wavelength should be approximately a Botlzmann distribution as shown

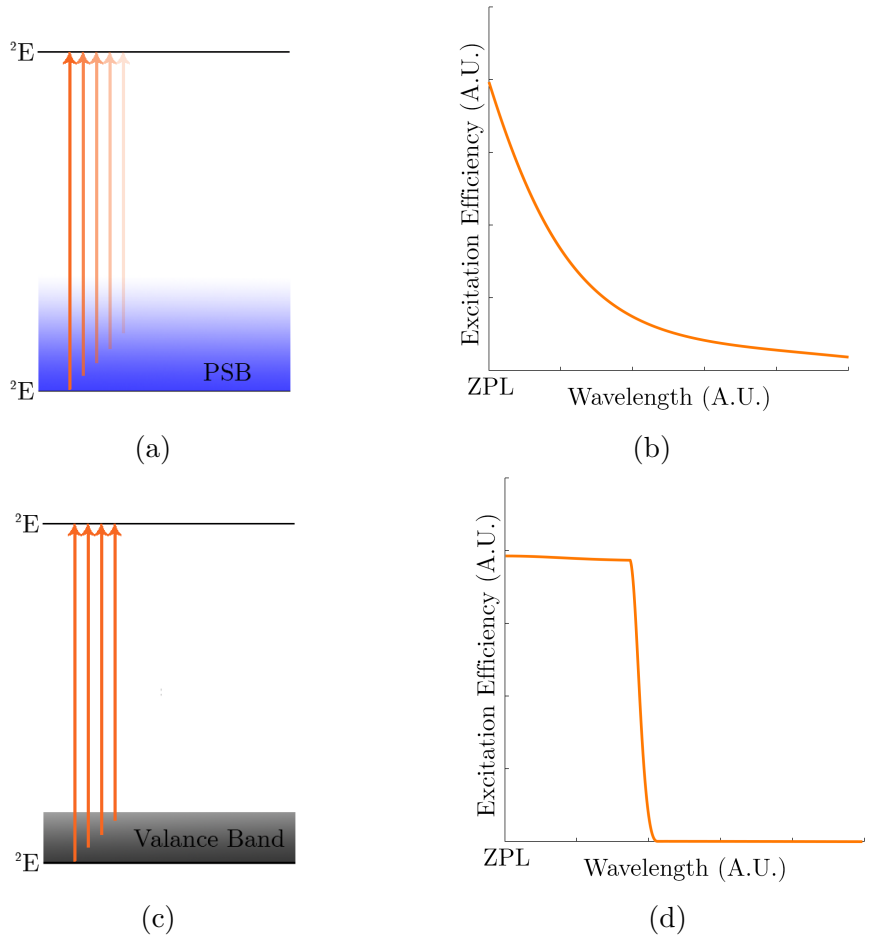

Figure 5.11: **(a)** The first mechanism is an anti-stokes mechanism through excitation from a populated phonon side band mode of the ground state. **(b)** This mechanism will appear to have an excitation efficiency curve as a function of wavelength that can be approximated as a Boltzmann distribution. **(c)** The second mechanism arises if the ground state of the SiV centre is beneath the valence band of the diamond matrix. **(d)** For this mechanism, when the excitation laser energy is higher than the energy difference from the valence band to the excited state there will be a strong excitation efficiency. For wavelengths larger than this the excitation efficiency will drastically reduce.

in Figure (5.11b). The second possibility of up-conversion arose during a literature review on the SiV centre where I found that *ab-initio* calculations of the silicon energy structure have placed the ground state of the Silicon Vacancy below the valence band of the diamond crystal [177]. Whilst *ab-initio* are known to have large errors and this in not a typical energy structure consistent with a sharp ZPL and weak PSB, if this were indeed the case, then the phonon side band would be strongly occupied up to a specific energy difference between the ground state of the SiV and the valence band energy as shown in Figure (5.11c). Again

tuning the excitation wavelength above 739 nm and observing the excitation efficiency will give some insight into the mechanism at play. In this regime, the excitation efficiency should be slowly changing above 739 nm and drop off quickly once the excitation energy is too small and doesn't span from the valence band to the excited state as shown in Figure (5.11d).

It became apparent that to further understand this mechanism we would need to build a spectroscopy set-up to investigate the wavelength dependence of the SiV excitation.

5.3.2 Experimental Platform

To observe the photo-luminescence properties of the SiV centres I built a new purpose built microscopy experiment with an M Squared 700 nm to 1000 nm CW Ti:Sapphire laser. This experiment was built for examining the SiV fluorescence. However, we anticipate that the future directions of this project will require a customisable spectroscopy experiment for analysis of a number of different fluorescent transitions and particles. We therefore designed the experiment for systematic and repeatable measurements of the spectral properties of any fluorescent particle, with easy control of the input and output spectral windows. The entire experiment was integrated with a python program to efficiently and systematically probe the SiV centres for a wide range of wavelengths and powers. The tunable M^2 laser can be tuned from 700 nm to 1000 nm in order to probe the excitation efficiency of the Silicon Vacancy centres. The schematic of the new confocal microscopy set-up can be observed in Figure (5.12).

The tunable M^2 laser was fibre coupled into a single mode fibre, power controlled by a half wave plate and polariser. The half wave plate was mounted on a Thorlabs rotation mount (KDC101/PRM1Z8). The output of the fibre was collimated through a 750 nm long pass filter and set incident through a 90:10 pellicle beam splitter. A highly reflecting pellicle was used to maximise the detection signal since we had sufficient laser intensity. The reflected light from the pellicle was set incident on a Thorlabs power meter for continuous power measurement. The power meter was calibrated using a second power meter since the reflection coefficent from the pellicle beam splitter is highly dependent on wavelength. The transmitted laser power through the pellicle beam splitter was focused by a 40× 0.95 NA

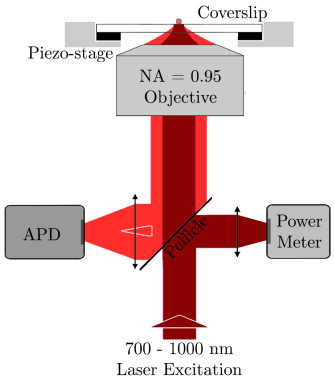

Figure 5.12: Schematic representation of the confocal microscopy set-up for systematic measurements of SiV centre fluorescence. The nano-diamonds, deposited on a coverslip, are positioned using a piezo-stage. The incident tunable 700 nm to 1000 nm Ti:Sapphire laser is transmitted through a pellicle beam splitter and focused by the 40× 0.95 NA Olympus objective onto the nano-diamond sample. The reflected power from the pellicle beam splitter is used to monitor the incident power. The emission from the nano-diamond is collected by the same objective and reflected off the pellicle beam splitter and collected by an avalanche photo-diode.

Olympus objective. At the focus of the objective, a nano-diamond sample was placed on a 3 axis piezo-nano-positioning stage (P-563.3CD PIMars) so that a number of nano-diamonds can be moved to the focus and investigated. The fluorescence of the nano-diamonds was back collected by the objective lens and partially reflected by the pellicle beam splitter and then fibre coupled into a 50 µm multimode fibre before being set incident on the APD. The input and output filter stacks can easily be modified to collect the fluorescence of any particle, using their respective excitation and fluorescence wavelengths.

Ideally, I wanted to collect only the ZPL fluorescence of the SiV centre and excite as close to and above the ZPL as possible, however a number of sharp, long and shortpass filters are needed to achieve this result, which are not typically available at these wavelengths. Ideally, the excitation M^2 Ti:Sapphire laser is used in continuous wave laser regime with extremely narrow line-widths tunable over a wide range. Whilst it indeed generates a strong beam with narrow linewidth at the desired range, it also leaks a collinear beam of low background, broadband light as shown in Figure (5.13a). Any of this broadband light that is not filtered out of the beam is transmitted efficiently through the set-up and can be clearly observed on the APD. Thus, we need a longpass filter to block out this broadband light and allow the

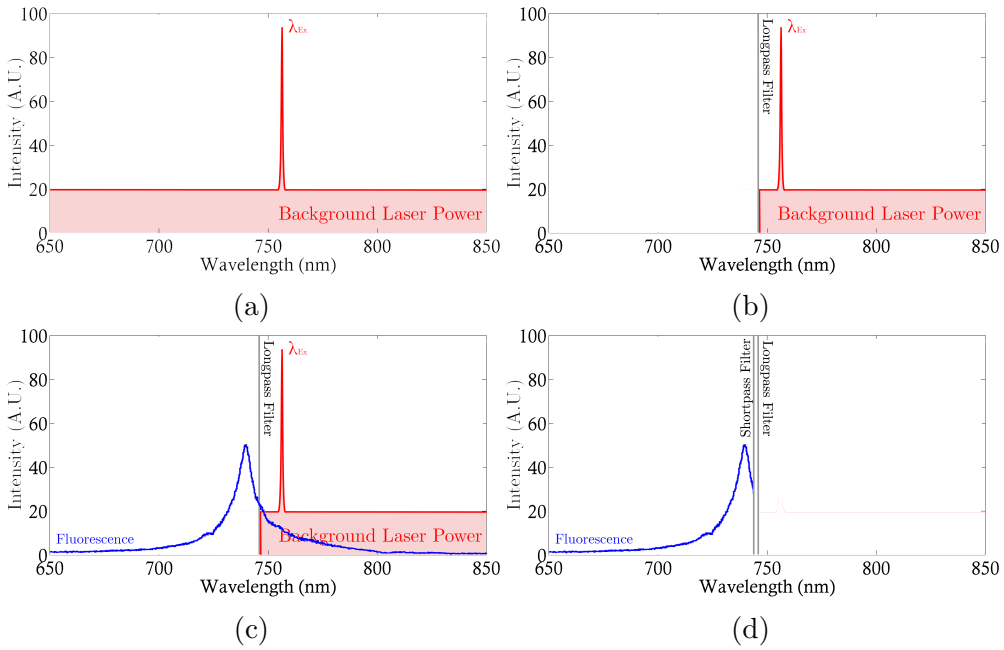

Figure 5.13: Filtering scheme for the SiV fluorescence measurement. Since the laser emits a broadband background field on top of the intense excitaion wavelength **(a)**, we need a spectrally sharp longpass filter **(b)**. After exciting the SiV centres **(c)**, we need to block out the remaining broadband field as well as the excitation laser **(d)**. The result is that we require two spectrally sharp long and shortpass overlapping filters, close to the ZPL.

desired narrow linewidth through the experiment as shown in Figure (5.13b). Now this laser spectrum excites the nano-diamonds and emits fluorescence from the SiV centres as shown in Figure (5.13c). Once the nano-diamonds have been excited, we need to efficiently block out the intense laser wavelength and transmit the desired 739 nm fluorescence as shown in Figure (5.13d). Thus, to perform this measurement we require spectrally sharp overlapping long and shortpass filters at a wavelength as close to but above 739 nm.

We found and obtained three filters specifically for this experiment. For blocking out the background of the M^2 laser I used a Thorlabs hardcoated 750 nm longpass filter (FELH0750). For blocking the input excitation laser I used two shortpass filters, a Thorlabs hardcoated 750 nm shortpass filter (FESH0750) and a Semrock 758 nm blocking edge BrightLine shortpass filter (FF01-758/SP). The transmission profiles obtained from the manufacturer of each filter and the expected optical density (OD) of the complete filter set is given in Figure (5.15). From these profiles we can determine that we have an OD greater than 5 for all wavelengths, sufficient to block out the broadband background of the M^2 laser. For wavelengths above

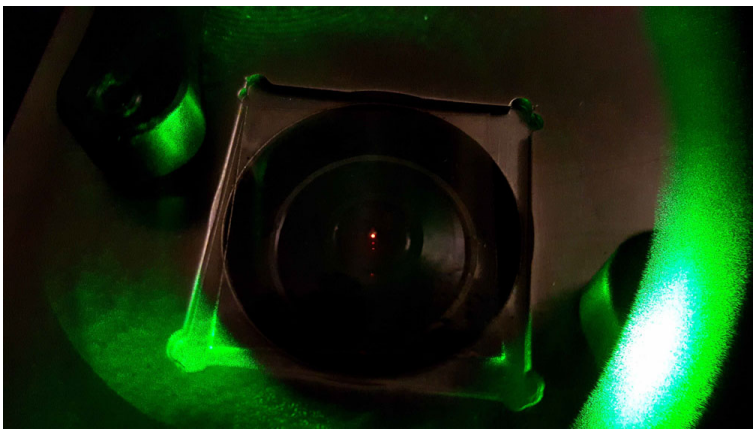

Figure 5.14: SiV emission from a nano-diamond sample at the focus of the confocal microscope photographed through a 532nm notch filter. 532nm excitation can be transmitted and observed through the filter for sufficiently large k vectors.

760 nm, the combined filtering from the two short pass filters provides an OD of over 17 which should be sufficient for completely eliminating the intense excitation beam. Using these filters we expect that we can observe the fluorescence from the SiV centres centred around 739 nm with excitation wavelengths above 760 nm and obtain no background counts from the input laser.

5.3.3 Data Collection

This confocal platform is designed to efficiently and systematically analyse any fluorescent sample under various conditions. To systematically control and collect the data from the set-up we integrated all of the hardware components with Qudi [178]. The Qudi program is a general, modular, multi-operating system suite, written in Python 3 for controlling laboratory experiments. Currently the program contains experimental modules for performing quantum optics experiments, however the open source nature of Qudi and its framework allows for anyone to use and modify the software to fit their research needs. We are developing on top of the confocal microscope module which is written to control an experiment of this type. For each module the Qudi program is abstracted into a three layer design; hardware, logic and graphical user interface (GUI) which are connected together using interfuse files as shown in Figure (5.16).

A given experimental module expects particular devices that are necessary to perform

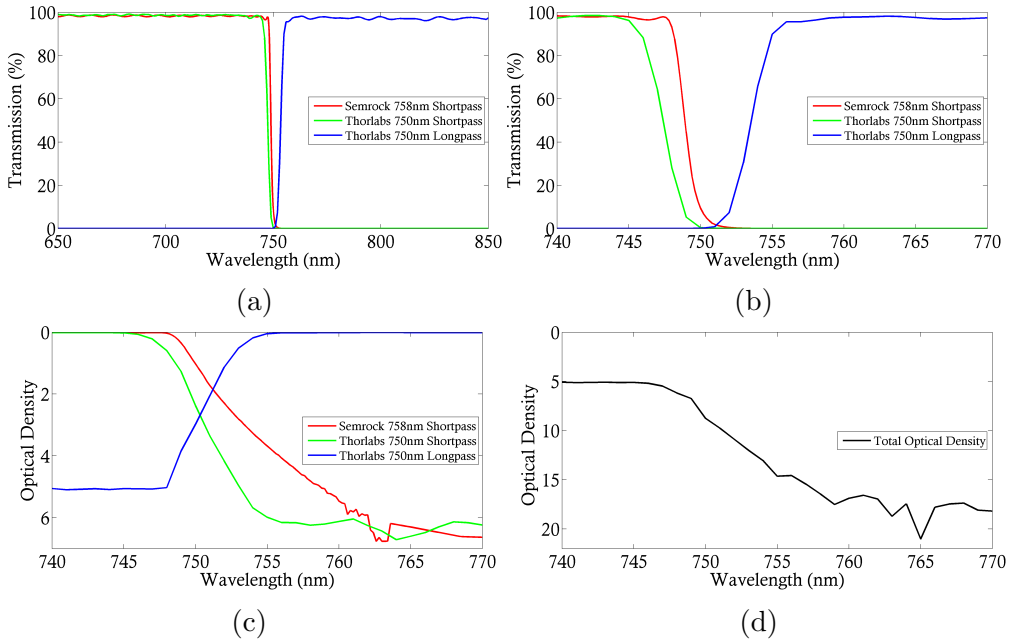

Figure 5.15: Analysis of the three filters using manufacturers transmission profiles. Individual transmission profiles of the filters in broadband **(a)** and around the 750 nm cut off wavelength **(b)**. **(c)** Individual OD profiles of the filters around the 750 nm cut off wavelength. **(D)** total OD throughout all three filters showing that the incident laser field is reduced by 5 orders of magnitude for $\lambda < 750\,\text{nm}$ and by more than 15 orders of magnitude for $\lambda > 760\,\text{nm}$.

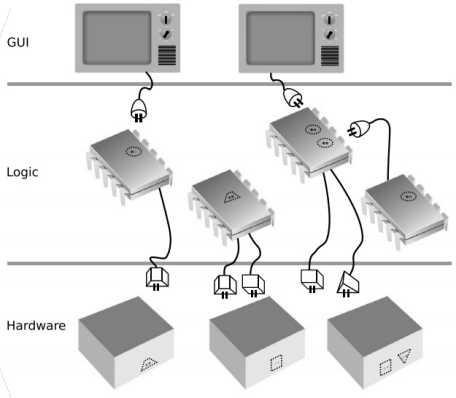

Figure 5.16: Qudi structural design. There is a strongly-enforced three-layer design for all Qudi experiment modules. Specific measurements are written as logic modules, including the required tasks and data analysis. These logic modules connect down to hardware modules by writing the appropriate interfuse file, meaning that the experiment itself is hardware agnostic as long as the hardware can fulfil the minimum requirements. GUI modules connect to the logic and provide a way for a user to operate the experiment, as well as a means to display data and calculated results [178].

measurements. The confocal logic module requires communication with at a minimum, a scanning stage and a fluorescence detection signal. Controlling experimental hardware remotely is usually possible with today's devices, unfortunately, the communication techniques and protocols vary widely between them. It is thus the task of the hardware modules to overcome these problems by translating the typical commands given by the logic files into the language of the specific hardware. This abstraction allows the logic of the experiment to operate without caring about the specific details of the device.

The hardware elements that were integrated into the Qudi program to run the experiment were:

- Thorlabs rotation mount (KDC101/PRM1Z8) for controlling input laser power.
- M Squared SolsTiS 2000 700 nm to 1000 nm laser for controlling input laser wavelength.
- Physik Instrumente 3 axis piezo-nano-positioning stage (P-563.3CD PIMars) for moving the sample plane.
- Thorlabs power meter (PM100) for collecting input power readings.
- ID Quantique APD (ID100) for collecting fluorescence counts.

The logic files then control and synchronise the hardware devices for a given experiment. They pass input parameters from the user interface to the respective hardware modules, processing the measurement data in the desired way. The logic files are ultimately the core of the program, performing all of the steps from the start of a measurement to its end, including data evaluation and storage.

The graphical user interface (GUI) modules create windows on the screen that a user can interact with, allowing for experiment control and data visualisation. However, Qudi is fully functional without the GUI modules as the logic can be controlled by the integrated IPython console or from a Jupyter notebook. The interactive GUI is useful for probing the experiment and testing experimental approaches. Once the experimental approach is designed, integrating the logic into an executable script allows for systematic measurements for a variety of input parameters over a number of hours or days[‡]. The Qudi manager screen displaying the Ipython console and providing the initial GUI for loading further GUI's, logic modules and hardware is shown in Figure (5.17).

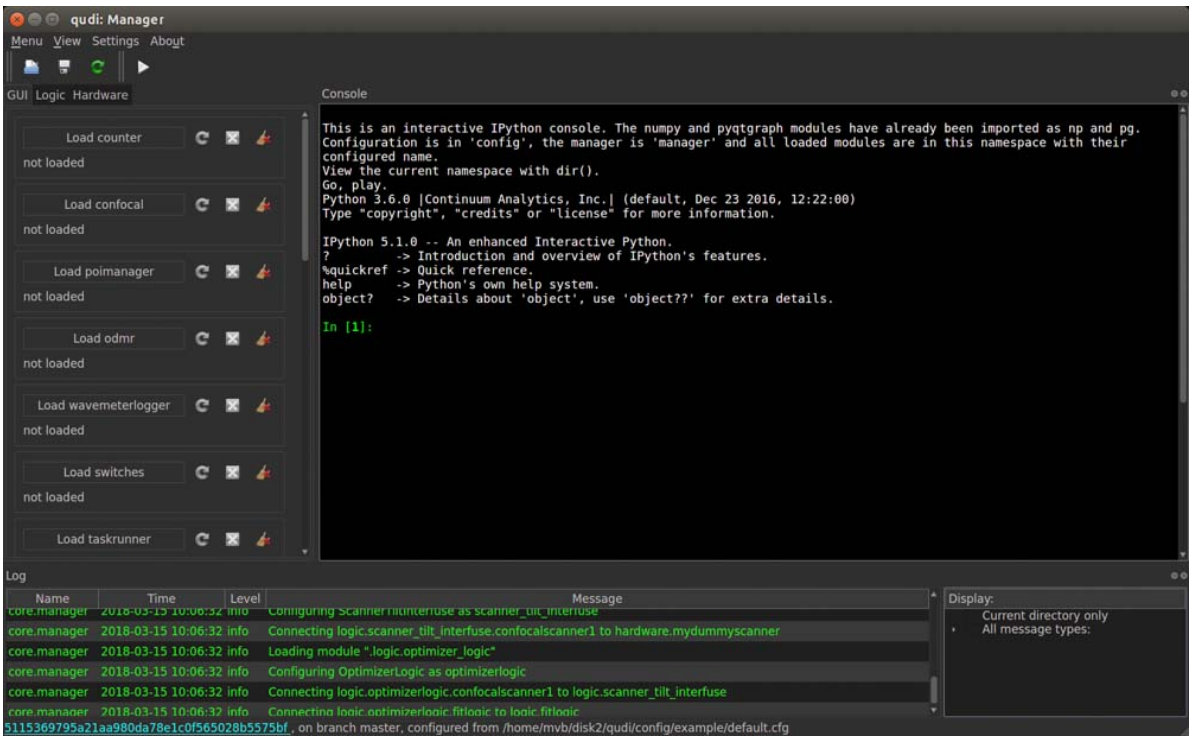

Figure 5.17: Qudi manager GUI for loading the appropriate hardware, logic and GUI files. The manager also includes an IPython console for debugging and control of the experiment through python commands.

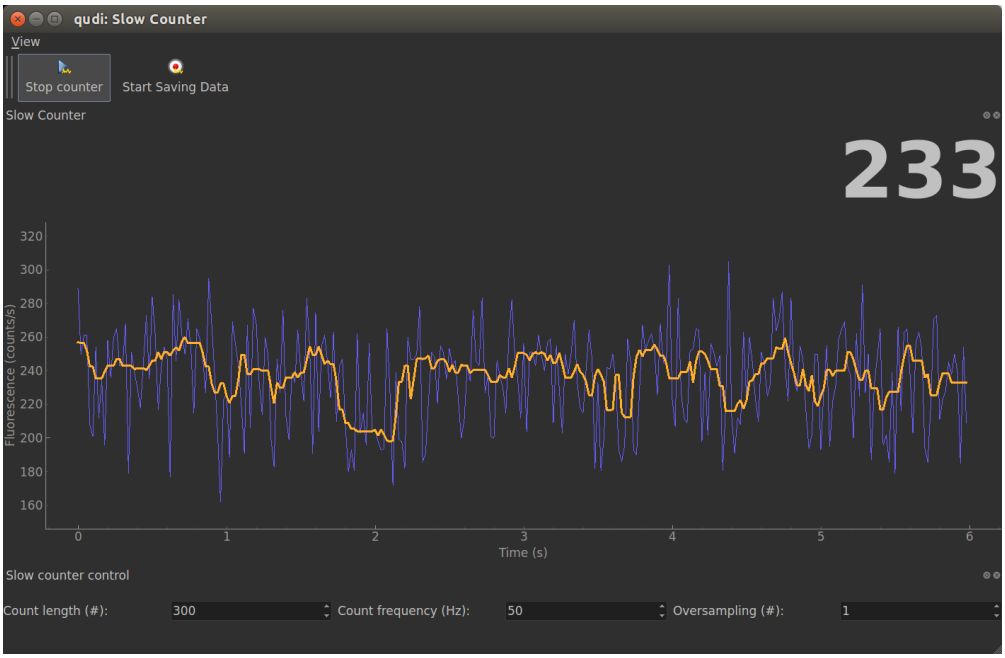

Figure 5.18: Qudi counter GUI for observing the fluorescence signal. The blue curve is the raw data signal as a function of time with a customisable moving average in yellow.

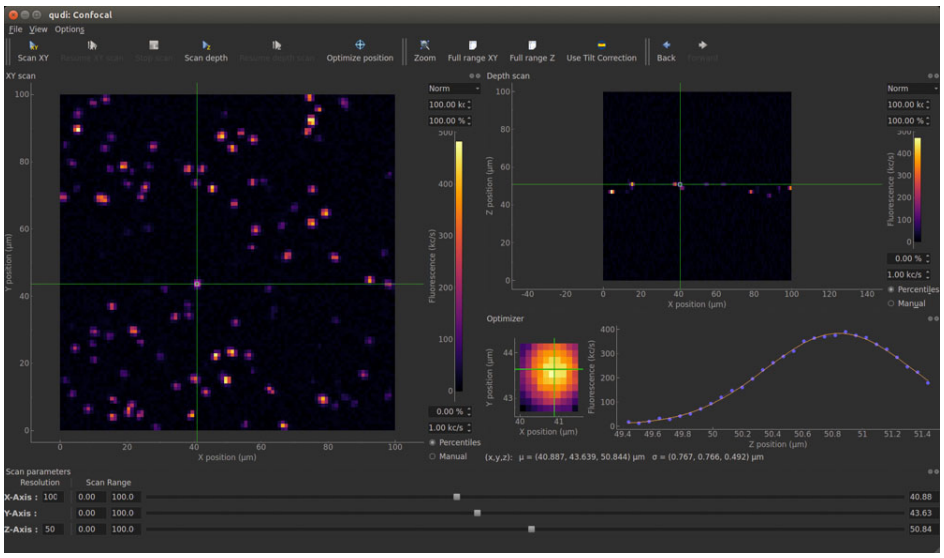

Figure 5.19: Qudi confocal experiment GUI. This is the main window for controlling the confocal microscopy experiment. An XY and XZ scan of the sample plane shows the location of a number of fluorescent particles. The optimizer function in the lower right side performs an XY and Z scan around a single fluorescent particle in order to place the particle at the optimal position in the confocal set-up.

Our complete Qudi program consists of many logic files that operate the core confocal set-up as well as a number of additional useful features. The core confocal program tracks the APD counts, as shown in Figure (5.18), and performs 3 dimensional scans of the sample plane to find and investigate fluorescent particles as shown in Figure (5.19). The program includes an additional optimisation algorithm that scans a specified region around the fluorescent particle in x, y and z in order to find the centre of a fluorescent particle and its maximum signal. The position optimiser logic in conjunction with a point of interest (POI) manager allows the program to not only systematically re-find fluorescent particles but also keep track of any slow drift or changes in position, as shown in Figure (5.20). For example, position changes in the confocal experiment can arise from chromatic aberrations as the incident wavelength changes. We developed additional logic and hardware files for monitoring and controlling the laser's excitation wavelength and power. The result is a complete externally controllable experiment that can easily be controlled with the GUI or run over extended periods of time with no additional interaction by executing a script containing the required functions.

[‡]Even longer if that accuracy and quantity of data is required

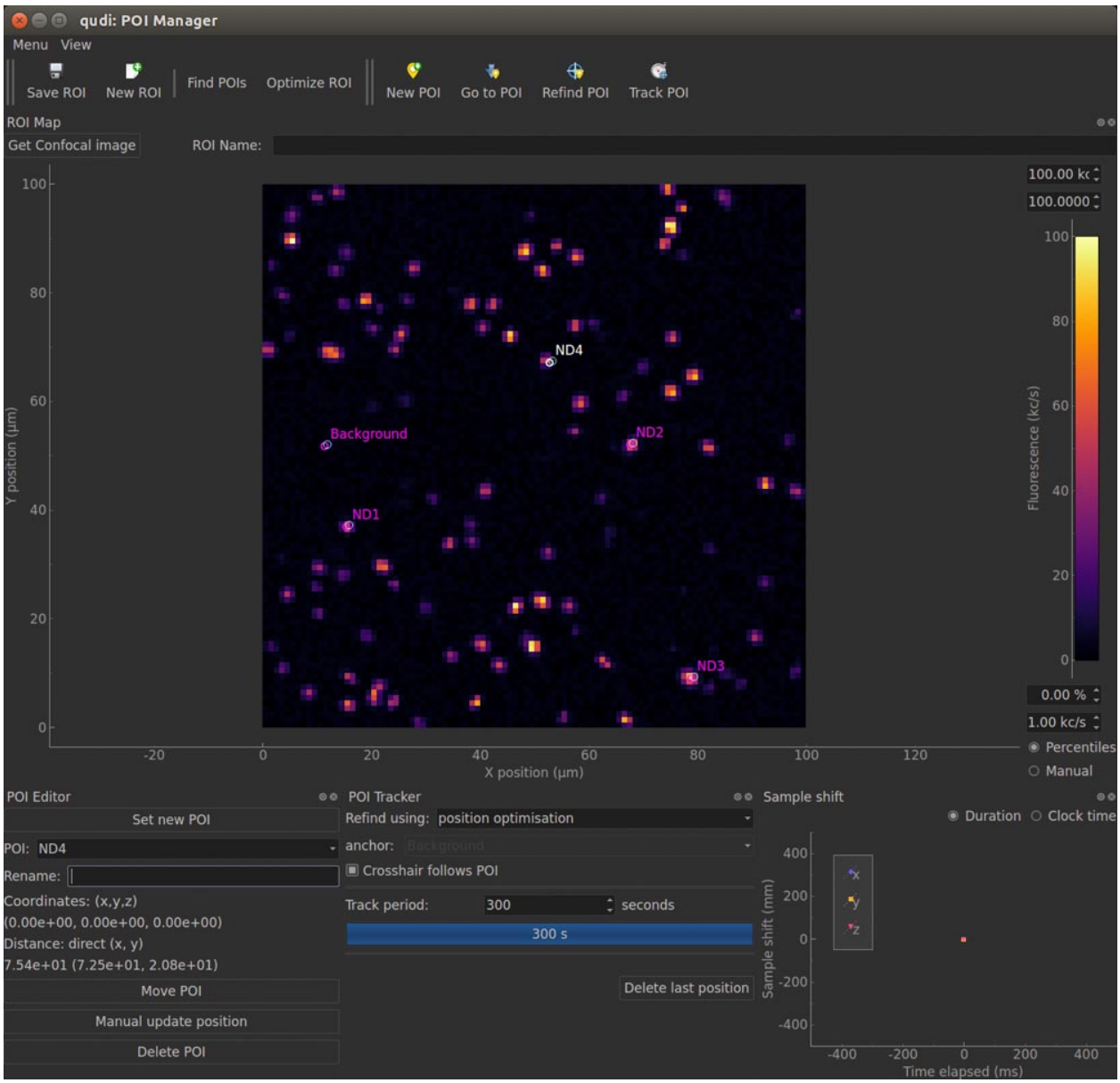

Figure 5.20: Qudi position of interest (POI) GUI. Each POI can be given a name and in combination with the optimizer logic, the sample plane as a function of time can be tracked (Bottom right), ensuring that the particle are always in the same relative position. This function is essential for continuous systematic measurements.

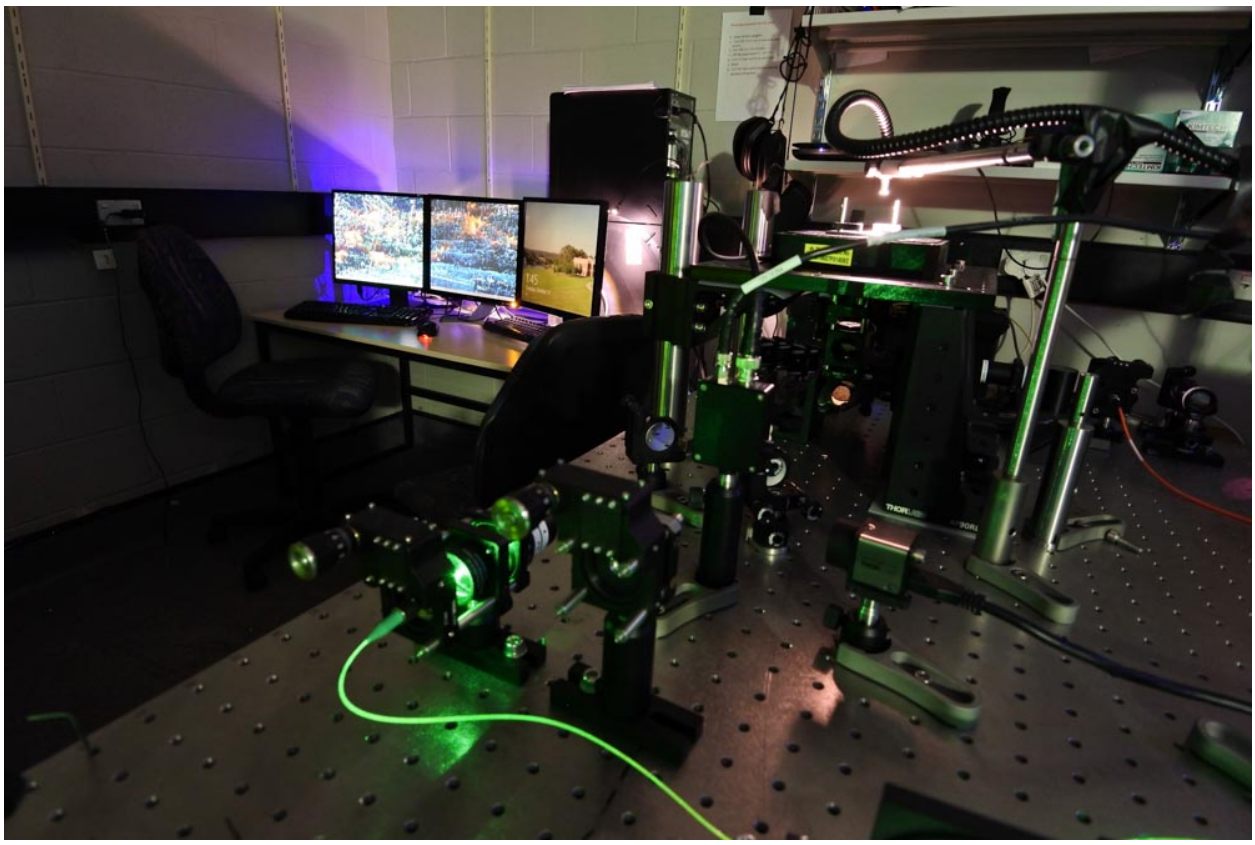

Figure 5.21: Photograph of SiV Lab and confocal microscopy set-up. Here, a 532 nm laser was coupled for excitation of SiV centres and alignment of the set-up before being replaced by the M^2 laser for up-conversion measurements. In the background the computer used to systematically control the experiment can be seen. Multiple screens are useful for monitoring all of the Qudi modules.

5.3.4 Silicon Vacancy Excitation with Tunable Laser

In order to determine the excitation efficiency of the Silicon Vacancy centres for each wavelength the Qudi program was used to systematically investigate each POI on our confocal scan. The executable jupyter notebook script produces a saturation curve and a point spread function (PSF) of the nano-diamond for each wavelength from 765 nm to 815 nm, which was then repeated over each of the nine identified nano-diamonds. The complete array of saturation curves and point spread functions on a single nano-diamond is shown in Figure (5.22) and Figure (5.23).

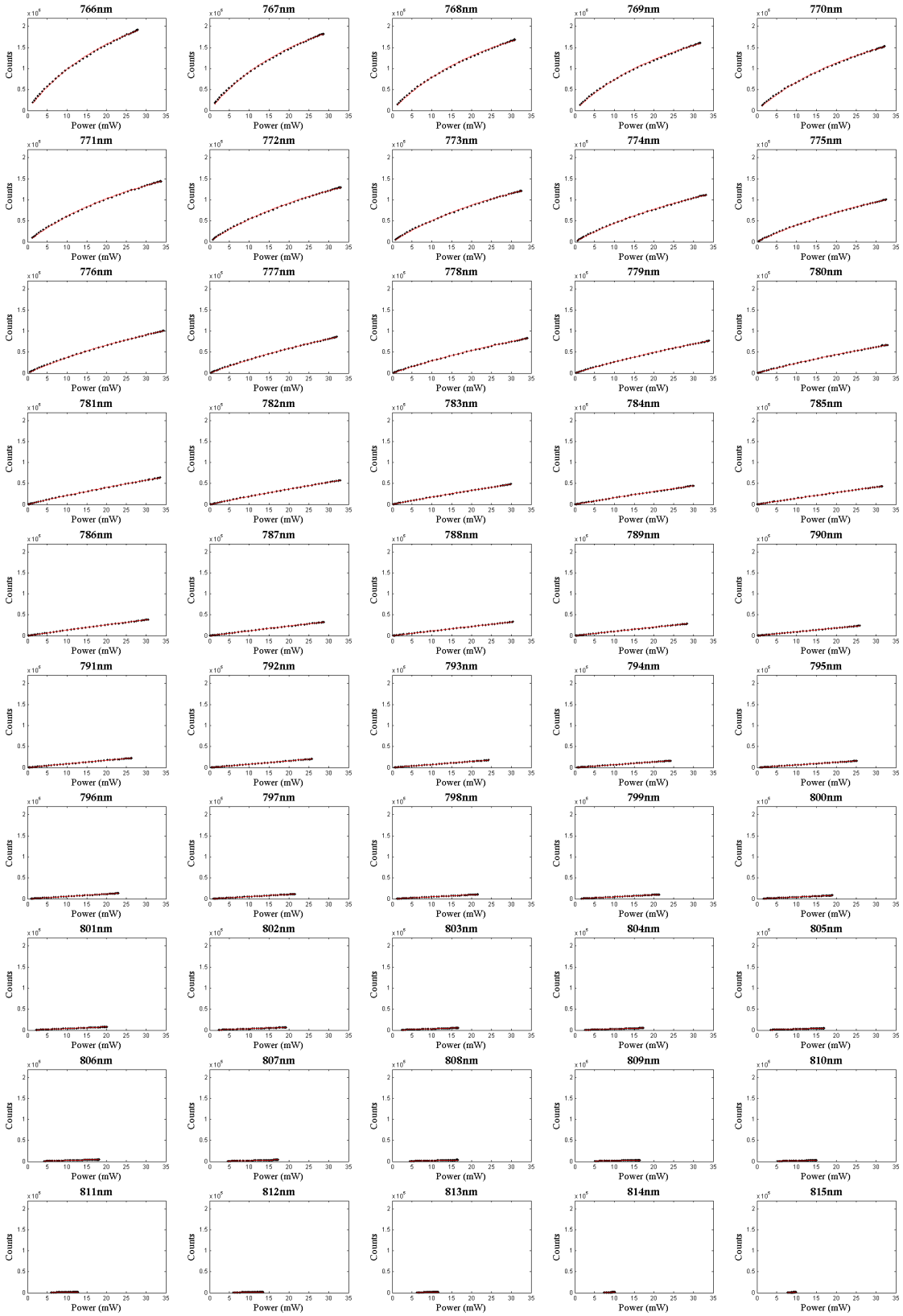

Figure 5.22: Systematically collected saturation curves from a nano-diamond containing many SiV centres from 766 nm to 815 nm. Each curve is fitted in red with a saturation curve described by Equation (5.1) in order to extract the excitation efficiency.

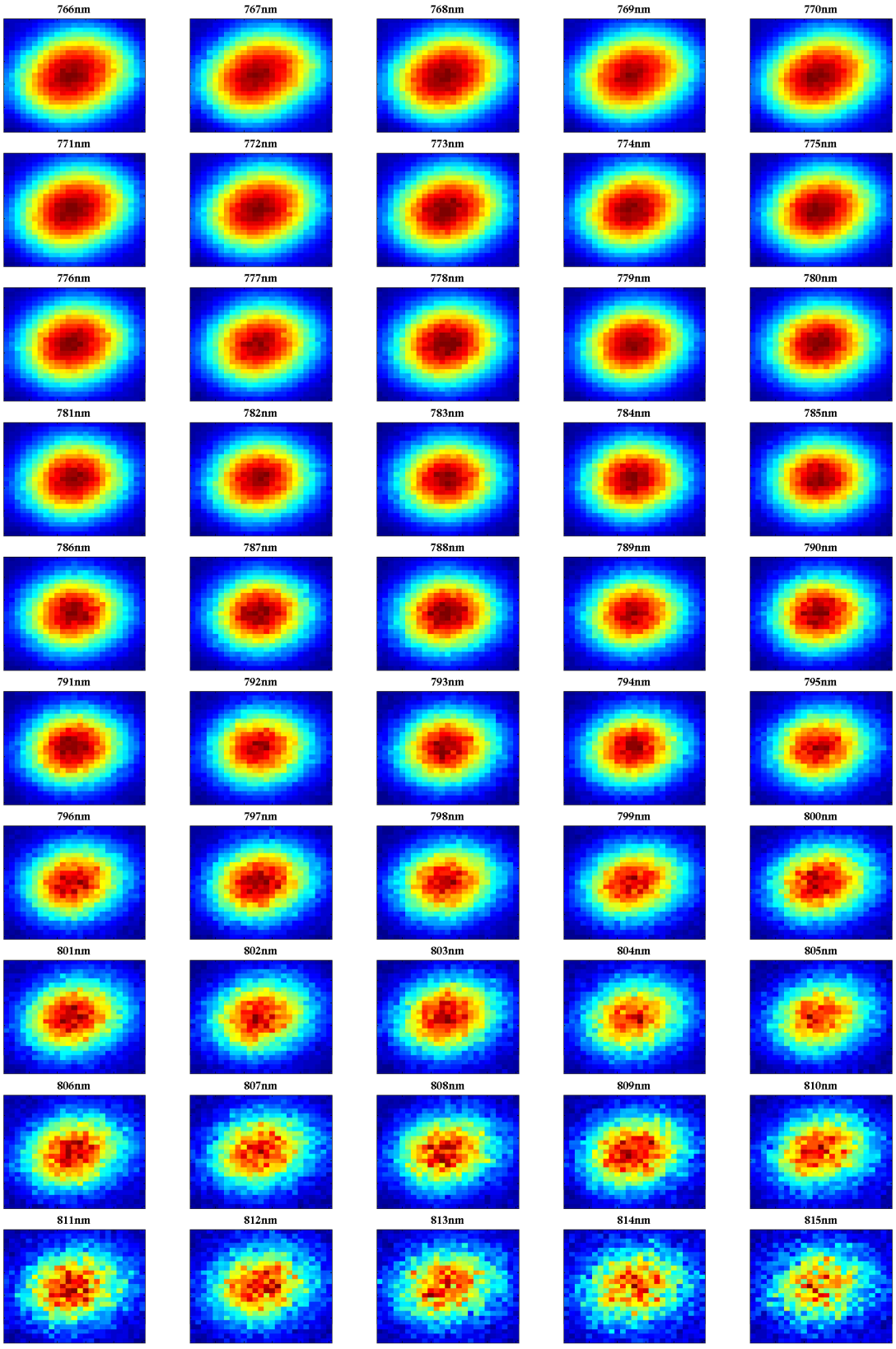

Figure 5.23: Systematically collected point spread functions (PSF) from a nano-diamond containing many SiV centres from 766 nm to 815 nm. Each PSF is a 1.6 nm by 1.6 nm scan taken far from saturation.

The PSF's were used to normalise the excitation efficiency to account for changes in local intensity for each wavelength. Ideally, an additional POI on a region without a nano-diamond would be used to determine the background counts arising from the excitation laser in the wavelength range where the filters were not optimal. Unfortunately, due to changes in the scattering field induced by the presence of the nano-diamond, the background laser counts varied rapidly with both position and wavelength over the coverslip surface. In addition, contrary to the expected filtering, significant counts from the incident laser were observed with wavelengths up to 773 nm. In fact, the short pass filters were tilted in order to shift their response to shorter wavelengths and optimise the available wavelengths with negligible laser background counts[§]. As a result only wavelengths above 774 nm are valid for analysis since the background counts from the excitation laser were insignificant. Obtaining sharper filters in this region will improve the filtering and enable us to scan a larger wavelength range closer to the 739 nm ZPL of the SiV transition.

From the saturation curves at each wavelength we can obtain the excitation efficiency of the SiV centres as a function of wavelength in order to gain insight into the up-conversion mechanism, as described in Figure (5.11). The excitation efficiency here is a measure of how strongly a particular wavelength can excite the optical transition and is defined as the ratio of counts per watt far from saturation. For a linear saturation curve the excitation efficiency is simply the gradient of a linear fit. For curves that show a saturation trend, it is possible to obtain the excitation efficiency from fitting only the low power linear part of the saturation curve. A more optimal way to obtain the excitation efficiency for all curves with a single function is to fit a saturation function to the data given by,

$$C(I) = \frac{C_{sat}}{I + I_{sat}}, \tag{5.1}$$

where, C is the number of counts, C_{sat} is the saturation counts, I is the excitation intensity and I_{sat} is the saturation intensity as shown by the red fits in Figure (5.22). The excitation

[§]Whilst naively one may expect tilting a dielectric filter to shift the filter features to longer wavelengths caused by the increased distance between each dielectric layer, the opposite is true. The explanation for this counter-intuitive effect is due to the fact that the resonance condition depends on the k-vector component perpendicular to the filter surface and not the k-vector components parallel to the surface.

efficiency (η) is then the tangent of the curve at low excitation intensities ($I \ll I_{sat}$) given by,

$$\eta = \frac{C_{sat}}{I_{sat}}. \tag{5.2}$$

For linear saturation curves the saturation fit does not provide a meaningful value for either fitting parameter C_{sat} or I_{sat} however the ratio $\frac{C_{sat}}{I_{sat}}$ is fitted accurately and corresponds to the gradient of the linear data and hence the excitation efficiency.

For each nano-diamond the excitation efficiency is then plotted as a function of wavelength as shown in Figure (5.24). These curves resemble the Boltzmann distribution which describes the probability of an electron to occupy a particular energy level given by,

$$\eta(\lambda) = A \exp\left(-\frac{\Delta E}{k_B T}\right), \tag{5.3}$$

where $\eta(\lambda)$ is the excitation efficiency as a function of wavelength, A is the normalisation constant, ΔE is the energy difference between the excitation energy and the ZPL energy, k_B is the Boltzmann constant and T is the temperature in Kelvin. As shown in Figure (5.24), this model provides a good fit to the data and indicates strongly that the excitation mechanism is an anti-Stokes shift process, absorbing phonons from the phonon side band of the ground state. This simple model uses only the Boltzmann distribution leaving the normalisation constant (A) and temperature (T) as free parameters as shown in Table (5.1).

Table 5.1: Simple Boltzmann fit

	Temperature (°K)	**A ($\frac{\textbf{Counts}\times 10^6}{\textbf{Watt}}$)**
ND1	240	70
ND2	246	206
ND3	243	190
ND4	248	45
ND5	274	58
ND6	266	73
ND7	254	27
ND8	253	116
ND9	260	19
Mean	253	89
Std.Dev.	10	68

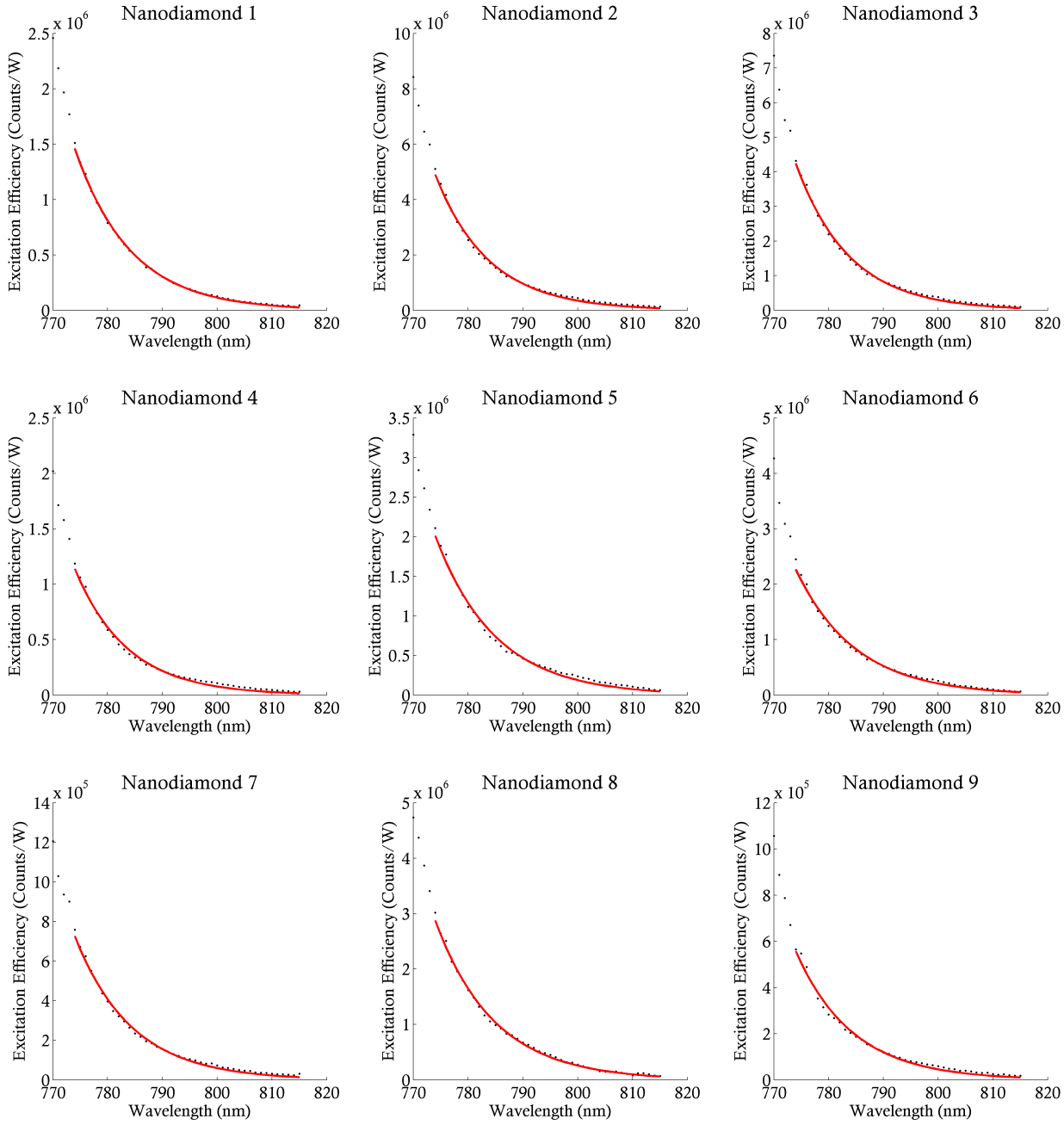

Figure 5.24: Excitation efficiency of the SiV centres as a function of wavelength. The trend of the plots indicate that the up-conversion mechanism for excitation is through an anti-Stokes shift by absorbing a phonon from the phonon side band. The red fit to the data points is a least squares fit of a simple Boltzmann distribution given in Equation (5.3).

Whilst the fitted temperature is expected to be 300 K, this simple Boltzmann distribution gives an average value of 253 ± 10 K. The simple Boltzmann distribution however disregards a number of properties that complicate the true physics of this system.

Firstly, in our nano-diamonds, we have an ensemble of emitters with a distribution of ZPL's smearing out the fluorescence structure as compared to a single emitter with a single ZPL. As shown in Figure (5.26) the ensemble spectra of the SiV emission varies from nano-diamond to nano-diamond and is much broader than a single emitter, which should be less than 10 nm at room temperature [179]. This highlights the large stress variations in the crystal lattices that changes the absolute position of the ZPL of each emitter [179, 180].

More impactful to our analysis is that we are assuming that there is an equal optical coupling between each phonon mode and the excited state. Instead, this excitation process will not only depend on the Boltzmann distribution but also the density of optically coupled states (ρ_g) of the ground state modifying the availability of particular phonon modes as shown in Figure (5.25). To measure the shape of the optically coupled density of states, without any effects of thermal occupation, one must measure the number of photons decaying from the excited state into each phonon mode at or close to absolute zero [181]. This measurement can be obtained from the photo-luminescence spectra of the phonon side band of the SiV centres at low temperature.

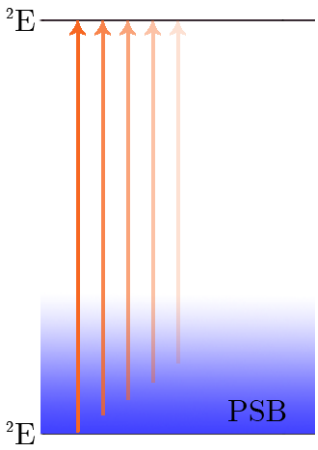

Figure 5.25: SiV fluorescence model including the modification due to the effective SiV density of optically coupled states. At excitation energies lower than the ZPL we can excite the transition by absorbing a phonon. The probability of a phonon being absorbed is dependent on the Boltzmann distribution and the effective phonon density of optically coupled states.

Rather than obtain the exact density of optically coupled states, requiring a cryogenic setup, I model the effective density of optically coupled states at room temperature as the normalised intensity of the phonon side band measured from the photo-luminescence spectra of the defects at room temperature as shown in Figure (5.26c). Interestingly, since we are measuring the up-conversion process only at room temperature and far from the ZPL ($> 35\,\text{nm}$) we can wrap up a number of the more complicated defect processes into the room temperature fluorescence approximation of the optically coupled density of states. Firstly, both the Huang-Rhys factor and n-phonon processes can be neglected as we do not need to calculate each n-phonon transition probability or their normalisations, since the room temperature fluorescence approximation measures all of these effective couplings at once. The temperature dependence of the SiV ZPL can neglected as not only do we only measure at room temperature, but we also measure at much larger wavelength shifts ($35\,\text{nm}$ to $76\,\text{nm}$) than arise from the shift in ZPL position from absolute zero to room temperature ($\sim 1\,\text{nm}$). Admittedly, to get a better picture of the exact density of phonon states, Huang-Rhys factor, temperature dependence of the ZPL width and position as well as detemining the relevence and strength of any Jahn-Teller interactions in the SiV centre, one should take careful measurments of the SiV fluorescence from room temperature through to cryogenic temperatures [181, 182]. However, for these nano-diamonds where stress and strain drastically broadens the ensemble emission of the SiV centres, these measurements are gratuitous.

Unfortunately, in this experimental platform we could not also measure the SiV flores-cence spectrum for each nano-diamond which would have been ideal for the following data analysis. We do however have a number of fluorescence signals from the same sample of nano-diamonds containing SiV centres. As shown in Figure (5.26), the fluorescence signal of three different nano-diamonds containing SiV centres have similar features, however, varying strain in the diamond matrix shifts and broadens the features of the spectra. For our analysis the shape of the effective optically coupled density of states was calculated directly from the normalised spectrum of SiV#1 (red) in Figure (5.26), which was chosen since it is the SiV centre which showed the strongest fluorescence signal and appeared to be representative of a typical SiV centre.

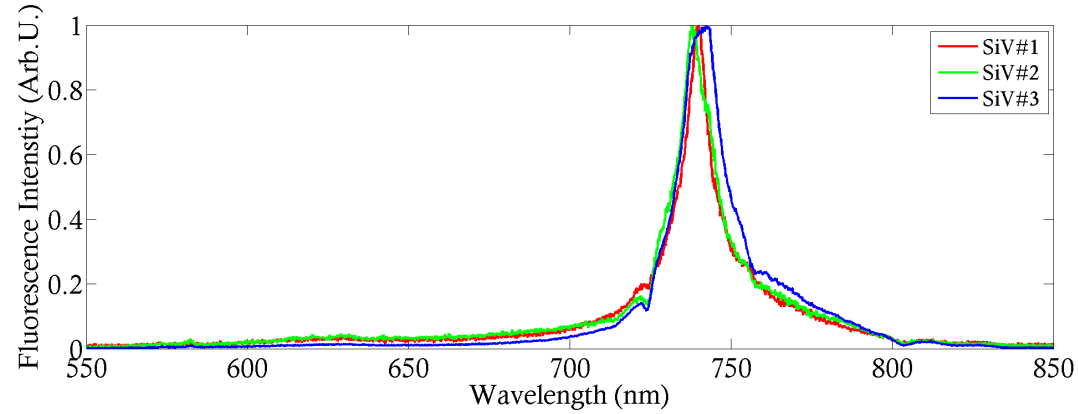

(a)

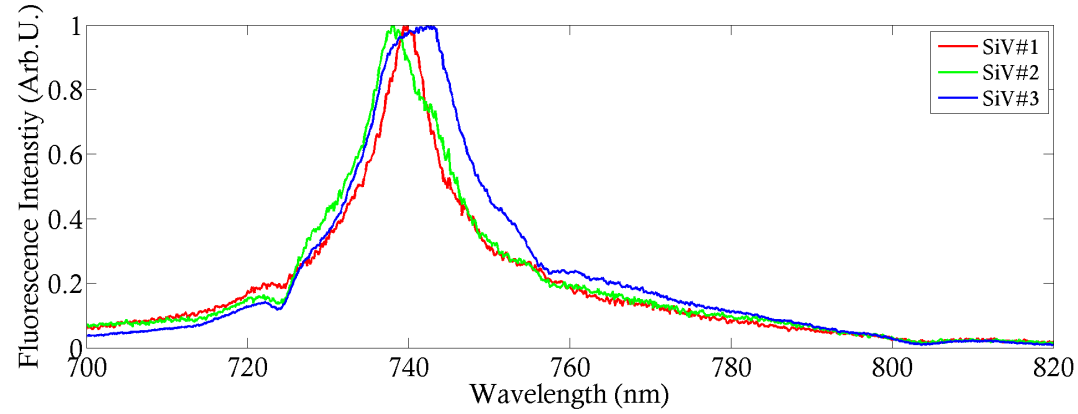

(b)

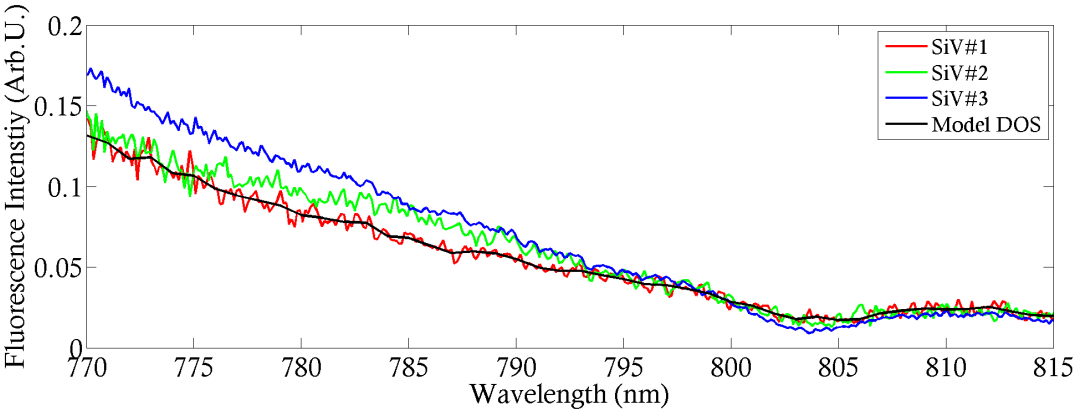

(c)

Figure 5.26: Three representative normalised fluorescence spectra of the nano-diamonds containing many SiV centres. **(a)** The full spectral region acquired from 550 nm to 850 nm. **(b)** Spectral region from 700 nm to 820 nm highlighting the shift in ZPL position between each nano-diamond. **(c)** Spectral region investigated using our confocal microscopy experiment and model from 770 nm to 815 nm. The effective optically coupled density of states (DOS) used in our model is shown in black and was approximated by the moving average of the normalised fluorescence signal of SiV#1.

The second model to fit the nano-diamonds is again the Boltzmann distribution, but now it includes a modulation due to the PSB given by,

$$C = A \exp\left(-\frac{\Delta E}{k_B T}\right) \rho_g(E), \tag{5.4}$$

where $\rho_g(E)$ is the effective density of optically coupled states of the ground state at energy E, measured directly from the photo-luminescence intensity. The fitting parameters of this model are given in Table (5.2) providing an average temperature of 260 $\pm$ 13 K for the 9 nano-diamonds.

Table 5.2: Boltzmann fit modified by the effective density of optically coupled states.

	Temperature (°K)	**A ($\frac{\text{Counts}\times 10^6}{\text{Watt}}$)**
SiV1	256	61
SiV2	247	233
SiV3	246	205
SiV4	243	58
SiV5	278	63
SiV6	276	73
SiV7	260	28
SiV8	272	97
SiV9	261	21
Mean	260	93
Std.Dev.	13	75

The temperature indicated by this model is closer to the expected result, however it still does not accurately fit the expected temperature of the nano-diamonds. The final model that further captures the underlying physics of the Silicon Vacancy centre emission includes the ability of the excitation laser to off resonantly excite the transition. In this final model we assume that the excitation laser can not only excite directly from the PSB of the ground state to the excited state, but also into phonon modes of the excited state as shown in Figure (5.27). Since there can be phonon occupation in both the ground and excited states then it should indeed be possible for the NIR laser to excite from higher phonon modes of the ground state to phonon modes of the excited state which then decay non radiatively

into the excited state of the SiV centre[♦]. This model now requires not only the calculation of the Boltzmann distribution and the effective density of optically coupled states at one excitation wavelength, but the sum of this distribution for all wavelengths of lower energy than the excitation wavelength.

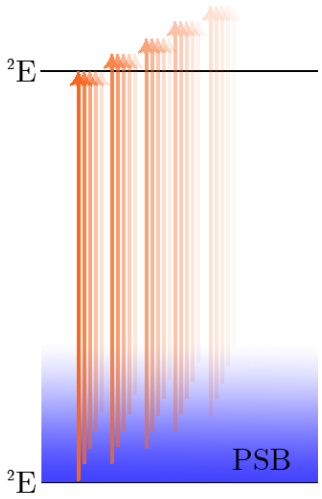

Figure 5.27: Off resonant excitation; SiV fluorescence model including the modification due to the effective SiV density of optically coupled states. At excitation energies lower than the ZPL we can excite the transition by absorbing a phonon. The probability of a phonon being absorbed is dependent on the Boltzmann distribution and the effective density of optically coupled states. In addition, we can not only excite directly to the excited state but also to excited phonon modes of the excited state. Thus, we can excite from all phonon modes where the transition energy to the excited state is lower than the excitation laser energy.

The final off resonant excitation model is then given by,

$$C = A \sum_{E<E_0} \exp\left(-\frac{\Delta E}{k_B T}\right) \rho_g(E), \tag{5.5}$$

where we sum the point wise multiplication of the Boltzmann distribution with the effective density of optically coupled states of the ground state $\rho_g(E)$ for all energies E below the incident photon energy E_0. The fitting parameters of this model are given in Table (5.3).

[♦]Whilst one may initially assume that since the typical green laser can off resonantly excite the transition then of course the 785 nm laser can off resonantly excite the transition into excited state phonon modes. This line of reasoning however is flawed since the mechanism of excitation using a 532 nm laser is through an additional orbital state that has not been introduced in this thesis. In particular that orbital transition occurs from an a-orbital to an e-orbital which results in a large PSB providing the broad range of available wavelengths available for exciting the SiV centre.

Table 5.3: Boltzmann fit modified by the effective density of optically coupled states including off resonant excitation.

	Temperature (°K)	**A** ($\frac{\textbf{Counts}\times 10^6}{\textbf{Watt}}$)
SiV1	276	11
SiV2	273	36
SiV3	268	34
SiV4	269	9
SiV5	319	8
SiV6	327	8
SiV7	285	4
SiV8	306	13
SiV9	314	2
Mean	293	13
Std.Dev.	23	12

The off resonant model provides an average temperature of 293 $\pm$ 23 K for the 9 nano-diamonds, which is more realistic and provides a good indication of the underlying physics behind the up conversion mechanism. Unfortunately, the spectrum used for this model is only from a single nano-diamond measured using a separate confocal arrangement, whereas each nano-diamond in this sample has a varied ZPL and FWHM arising from the strain in each crystal. Since the PSB of the centres differ dramatically between nano-diamonds our model will not accurately represent the expected excitation efficiency spectra and attributes considerable errors in these models. Confirming this result for nano-diamonds and further differentiating between these models requires improving our measurement set-up. We would need to obtain the fluorescence spectra of each individual nano-diamond and use that spectra in our fitting model. In combination with utilizing better filters, allowing us to span a larger spectral region, we will have an increased ability to investigate and analyse the effective density of optically coupled states' effect on the anti-Stokes up-conversion mechanism.

Ideally a clean sample of identical emitters can be used in conjunction with a thermally controlled confocal setup that can reach cryogenic temperatures should be used. By taking systematic measurements of both the emission and absorption spectra as function of temperature and follwing Davies et. al. [181] will allow us to get a much better value of the exact phonon density of states as well as access to the Huang-Rhys factor and a determination of

the impact and strength of the Jahn-Teller coupling.

Currently, there is no evidence to suggest under intense 785 nm or 1064 nm illumination that the SiV centre is being ionised to it's neutral charged state. There are many unknown properties that would affect the ionisation and recombination rates and processes of the SiV centre, such as the energy gaps to the valence or conduction bands. This makes it difficult to speculate on these processes impact on the photo-physics of the centre. The consequence of this lack of ionisation in combination with the upconversion mechanism is that each fluorescence photon is drawing a phonon away from the nano-diamond lattice. As a result, if we can optically levitate the nano-diamonds with a 785 nm laser we can not only excite the SiV centres but also draw phonons out of the diamond lattice, thereby cooling its internal temperature. However, since the Quantum efficiency of the SiV centre is only 10%, then most photons are absorbed by the crystal lattice and decay non-radiatively, heating the crystal lattice. Whilst internal cooling may not be immediately possible with SiV centres at 785 nm, this mechanism highlights the possibility that a precisely tuned laser acting on an optical defect with a high quantum efficiency will be able to optically cool both the internal temperature and CoM motional temperature of a levitated nano-diamond simultaneously.

In conjunction with collective effects this mechanism becomes even more interesting. Optically levitating a nano-diamond exhibiting collective effects between its ensemble emitters will not only dramatically enhance the optical forces, it may also dramatically increase the quantum efficiency due to the increased rate of spontaneous emission. This increase in quantum efficiency will thereby increase the effectiveness of the optical cooling effect leading to cooler nano-diamonds and sharper transition lines. If the strain in the crystal is still present and the SiV centres are not spectrally identical, this cooling can actually reduce the spectral indistinguishably that the thermal dephasing provides. If the strain in the nano-diamonds is indeed well controlled and the SiV centres are centred at the same frequencies, then cooling the diamond matrix and creating spectrally sharper emitters would indeed create a feedback loop of increasingly degenerate collective effects and enhanced cooling. At this point, collective effects will be limited by dephasing caused by dipole-dipole interactions. Nevertheless, collective effects improves the cooling of the nano-diamonds and may even lead to optical cooling in defects where it is not possible with single emitters alone. The final result of

levitating a defect of this type is that we have an optically levitated nano-diamond where cooling of both the CoM motion and the internal temperature could be done efficiently with the same trapping laser.

It is clear that this system is extremely intricate, depending strongly on the physical properties of each individual nano-diamond and optical transition. The goal now is to find the optimal transition and engineer nano-diamonds with high concentrations of these defects, exhibiting low strain and amorphous carbon to optimise these effects and create a massive mechanical oscillator in its quantum ground state.

'The beautiful thing about learning
is nobody can take it away from you.'

– B. B. King

'When you read, don't just consider what the author thinks, consider what you think.'

– John Keating, Dead Poets Society

6

Conclusion and Future Work

Recent developments in optical levitation of dielectric particles have shown the potential of levitated systems for macroscopic quantum experiments and high precision sensing [57–59]. These schemes however require for the CoM temperature of the levitated dielectric particle to be cooled down towards the quantum ground state. Exciting experimental progress has been made on the implementation of cooling through both feedback [28–30] and cavity cooling techniques [24, 31, 32].

In this thesis I focused on the development of a new optical levitation scheme that brings together opto-mechanics of levitated nano-particles with cold atom physics and diamond material science. The aim was to observe and use an atom trapping like resonant force arising from embedded optical defects within the levitated nano-diamonds. In the case where this resonant force from the optical defects dominates, the nano-diamond will behave similarly to a giant atom, allowing us to apply a number of well developed techniques from

atom physics directly to the levitated nano-diamond.

This goal is an ambitious one requiring intimate knowledge of a variety of separate fields: optical forces, opto-mechanics, material science, artificial atoms and some elements of atomic physics. I initially wanted to simply use the well understood properties of the NV centre and focus primarily on the physics of optical levitation. Instead, I found that they exhibited complex mechanisms that required a deeper understanding of their photo-physical properties.

My initial investigation into observing optical forces on levitated NV centres within nano-diamonds, detailed in Chapter 3, found that the intense trapping laser strongly interfered with the ideal two level structure needed for observing resonant optical dipole forces. Ultimately, in Chapter 4, I found that the infrared laser induces a strong charge state interconversion process that continuously and non-radiatively, depopulated the excited state of both charge states. Whilst I identified a number of possible applications of this mechanism, unfortunately the charge state interconversion mechanism prevents us from observing resonant optical forces on NV centres in levitation, which typically requires higher laser intensities.

The second candidate for observing resonant optical dipole forces in nano-diamonds was the Silicon Vacancy (SiV) centre, due to its stronger dipole transition and smaller phonon side band. In Chapter 5, I showed that unfortunately, we were unable to optically trap the sample of nano-diamonds that contains a dense number of SiV centres. We attribute the inability to trap them due to the large quantity of amorphous and graphitic carbon impurities on the surface of the diamonds. We did observe however, that a strong 1064 nm trapping laser did not alter the photo-physics of the SiV centre, indicating that levitating them with this wavelength will not be detrimental, as it is the case with NV centres. More interestingly, I observed an anti-Stokes shift process in the SiV centres that could potentially be used to draw phonons out, optically refrigerating the nano-diamond crystal. However, since the quantum efficiency of the SiV defect is only 10%, most of the photons are absorbed, negating the cooling effects of the anti-Stokes process. In this context, superradiance offers an exciting opportunity. By harnessing cooperative effects between SiV centres within the nano-diamond, their emission rate could be significantly increased. This would in turn increase the quantum efficiency, enabling optical refrigeration.

The analysis of the Silicon Vacancy centre provided insight into the ideal optical defect for observing cooperatively enhanced dipole forces in optical levitation and ultimately provided a number of questions and research goals that must be achieved in order to create a levitated nano-diamond that behaves like a giant atom.

Whilst I have not yet reached my goal of experimentally levitating and manipulation a giant atom, I have undertaken a number of steps providing both the experimental and theoretical ground work for ultimately observing and using these forces. I have established an important theoretical understanding of the photo-physics of colour centres and the potential they have for generating cooperatively enhanced resonant optical dipole forces. In addition, I have designed and built an optical levitation system specifically prepared for observing and manipulating these forces on an appropriate nano-particle sample.

6.0.1 Future Work

The relevance of this research is ultimately concentrated on the interesting physics of a dielectric nano-particles containing many optically addressable emitters. These objects establish two novel research directions one of optical trapping and the other in the material science of collective effects. In optical levitation, these nano-particles offer a mechanism for resonantly enhanced dipole forces on a massive mechanical oscillator. If these forces are large enough this kind of system enables a number of well developed cooling mechanisms, developed for atom trapping, to be applied to a more massive nano-particle. This constitutes an ideal system for macroscopic quantum experiments and high precision sensing. However, in addition to optical levitation, these nano-particles offer a platform for studying and controlling collective effects such as superradiance in solid-state systems. Controlling superradiance in a solid-state system would be particularly exciting as one could control and enhance the emission properties of the nano-particles. In addition, since superradiance is strongly dependent on environmental dipole-dipole interactions these nano-particles could be used for high sensitivity measurements of dipole-dipole interactions.

Fundamentally, for these nano-particles to show either strong resonant dipole forces or cooperativity it is essential to engineer the growth and preparation of these nano-particles to

exhibit low strain and surface impurities, whilst containing a high concentrations of emitters.

Surface impurities, such as amorphous and graphitic carbon, dramatically increase the absorption of the nano-particle, preventing the dielectric gradient force from overcoming the scattering force. In addition, the increase in absorption directly relates to an increase of the bulk temperature of the crystal, broadening the emission of each emitter and ultimately leading to the destruction of the sample.

Strain on the other hand alters the local environment around each individual optical defect modifying the spectral properties of each individual SiV centre. Engineering nano-particles with low inhomogeneous strain not only sharpens the ensemble spectra but also dramatically improves the spectral indistinguishability between each of the emitters within the nano-diamond. This increased indisingushability improves the strength of the superradiance of the collective emission drastically increasing the resonant dipole force by modifying both the spontaneous decay rate and the steady-state population. It was shown in Chapter 3, that for the water trapping experiment, without superradiance, the resonant optical dipole force would not have been observed. I expect that without supperadiance in a nano-diamond sample the resonant dipole forces will not be strong enough to overcome the dipole force on the dielectric material. Whilst superradiance has been observed for NV centres it has yet to be observed for other closely packed emitters in diamond. It is therefore necessary to confirm that this is not somehow specific for NV centres, but also true for optical defects in general.

As a result, engineering higher quality samples is an important step. It is currently a technological challenge to create nano-diamonds with high defect concentrations with low strain and amorphous carbon impurities that are ideal for both cooperativity and enhanced dipole forces*. Typically, high concentrations of defects in nano-diamonds are formed by milling larger CVD grown diamonds down to the appropriate size. Due to the violent nature of the process, ball milling introduces large inhomogeneous strain in the nano-diamond crystals. Engineering a process to mitigate the additional strain in the crystal will greatly

*Whilst low strain Silicon Vacancy samples have been made, they are made using the HPHT process which does not produce the densities of optical defects that would be ideal for cooperatively enhanced dipole forces [168]. In addition most research in colour centres in diamond has been driven by quantum technologies where high quality and control of only a few or single defects is required.

benefit both cooperative effects and the strength of the resonantly enhanced dipole forces. I anticipate that a better acid treatment than the one I implemented in Section (5.2.1) can be devised to dramatically reduce the strain and surface impurities of the nano-diamonds. This treatment is beyond the scope of this thesis as it involves boiling strongly reactive acids at high temperatures, producing highly toxic gasses and as a result must be carefully designed and conducted by a specialised chemist.

In regards to optical trapping these nano-particles, it is currently hard to establish the intrinsic limitation of the strength of the resonant optical dipole forces. This is because the resonant optical dipole forces will depend strongly on the specific spectral properties of the emitters as well as their collective effect, dependent on the crystal matrix. As shown in Chapter 2, to obtain the strongest resonant dipole forces we want an optical transition with a short spontaneous lifetime, a small phonon-side band and a good quantum efficiency (small non-radiative decay rate). We also require that the two level structure of the transition to be insensitive to an off resonant high power trapping laser so that we can optically trap the dielectric particle without affecting the internal photo-dynamics.

Having a high quantum efficiency is beneficial for two reasons. Firstly, by having a high quantum efficiency the heating rate of the crystal is reduced since the number of photons absorbed by the crystal is minimal. Secondly, the high quantum efficiency allows the possibility of optical refrigeration using an anti-Stokes process drawing thermal phonons out of the crystal. Reducing the temperature in this way helps by both reducing the thermal broadening of the optical transition as well as mitigating any thermal heating that has been observed to vaporise diamonds at low atmospheric pressures. One particular defect that deserves special mention is the Germanium Vacancy centre, which shows many of the same properties as the Silicon Vacancy centre such as a strong dipole transition and small phonon side band, but also exhibits a much larger quantum efficiency [183]. In addition these defects don't appear to suffer large thermal dephasing at room temperature like the SiV centre since the optical transition has a higher energy (ZPL $= 602\,\mathrm{nm}$).

In regards to maximising collective effects in solid-state emitters, the focus is on maximising the spatial and spectral indistinguishability of emitters. Engineering nano-particles

of this type provides a very promising way to systematically study and control the collective effects at room temperature. Controlling collective effects is particularly exciting as one could control the emission properties of the crystal as a whole, tailoring the emission characteristics of the ensemble emitter. Additionally, since the nano-particles' superradiant behaviour depends strongly on the environment (dephasing), these nano-particles can be used as sensors to study classical and quantum systems through their dipole-dipole interactions. Further applications of superradiant nano-particles include efficient photon counting, efficient energy harvesting, quantum sensing and importantly for this thesis, a mechanism for drastically increasing resonantly enhanced optical dipole forces [103, 184].

Ultimately, this work naturally leads towards generating cooperatively enhanced resonant dipole forces on a massive mechanical oscillator. By dominating the forces on a levitated object with resonant forces of this type, we obtain a massive dielectric particle that behaves like a giant atom. This type of force opens up an array of atom trapping techniques, including many resonant cooling mechanisms and quantum manipulation protocols, optimal for performing quantum opto-mechanical applications and protocols with novel superposition sizes. Commercially, this is exciting for its applications on high precision force and vibration sensing. More fundamentally however, we can use this system for generating non-classical quantum states of the mechanical oscillator modes, providing a promising platform for fundamental tests of quantum mechanics such as, probing quantum gravity and experimentally placing stricter bounds on collapse theories. Finally, by including additional optical defects we can encode information into the vibrations and spin structure of defects and create new, unprecedented hybrid quantum systems, linking incompatible quantum systems together and preserving their quantum coherence.

‘On the summit, part of me wished that someone, anyone, had noticed that I’d just done something noteworthy – though maybe it was better that I didn’t have to talk to anybody. How could I have expressed what my last few hours had been like? It was enough that I knew. I didn’t make a sound. I took off my shoes and started hiking down the Cable route. It was only then that someone noticed. “Oh, my God,” this dude blurted out. “You’re hiking barefoot! You’re so tough!”’

– Alex Honnold, On free soloing El Capitan

A

Appendix

A.1 Nano-Diamond Acid Treatment

Nano-diamonds made in a CVD reactor are coated on Tungsten Carbide milling balls and need to be cleaned of impurities including amorphous Carbon. The nano-diamonds need to be removed from the milling balls, cleaned using a heated three acid treatment and subsequently rinsed with deionised water.

Chemicals

- H2S04, Sulfuric Acid ($\sim 90\%$)
- HClO4, Perchloric Acid ($\sim 70 - 72\%$)
- HNO3, Nitric Acid ($\sim 65\%$)

Temperature Concerns

Raising the temperature for the three acid mix does increase the reaction speed, and should make it faster to clean the nano-diamonds. However, this effect is non-linear and difficult to predict. When the strong acids are boiled at too high a temperature they can produce highly toxic gases such as NOx. In short, do not set the temperature above 130 degrees celsius for the heat block and 170 degrees celsius for the sand bath.

Overview of the Steps

The procedure can be divided into three main steps,

1. Removing nano-diamonds from the Tungsten Carbide milling balls. Concluding with a solution of nano-diamonds in the three acid mix.
2. Heating and cleaning the nano-diamonds with the three acid mix.
3. Rinsing the nano-diamonds to arrive at a solution of cleaned nano-diamonds in deionised water.

Step 1

All of the following steps should be undertaken in the acid fume hood with safety equipment for strong acids. List of required PPE at bottom.

- Prepare the three acids, a beaker with wash water, pipette, four pipette tips, the Tungsten Carbide milling balls, small glass flask, small round bottom flask and sonicator.
- Place Tungsten Carbide milling balls into small glass flask.
- Pipette 1 ml of sulfuric acid into the small glass flask, rinse the pipette tip in the beaker of water and remove tip.
- Pipette 1 ml of perchloric acid into the small glass flask, rinse the pipette tip in the beaker of water and remove tip.
- Pipette 1 ml of nitric acid into the small glass flask, rinse the pipette tip in the beaker of water and remove tip.

- Place the small glass flask in the sonicator for 15 minutes, holding with a boss head and clamp.
- Place acid bottles back into appropriate places.
- Once sonicated the small glass flask is removed from the sonicator. The nanodiamnonds should then be suspended in solution with the tungsten carbide balls at the bottom of the small glass flask.
- Pipette all of the three acid mix solution containing nano-diamonds from the small glass flask and transfer it to the small round bottom flask for heating. Rinse the pipette tip in the beaker of water and remove tip.
- Clear acid waste including the Tungsten Carbide balls coated in the three acid mix.

The nano-diamonds are now suspended in a three acid mix within the heating flask.

Step 2

All of the following steps should be undertaken in the acid fume hood with PPE.

- Mount condenser and connect water tubings.
- Prepare sand bath ontop of a heating plate with a temperature sensor to monitor the temperature.
- Mount the flask containing the sample onto the condenser, ensuring good contact between the flask and the sand bath.
- After ensuring tight water seal, turn on the water, ensuring water is flowing from the bottom of the condenser.
- Turn on the heating plate and monitor so that the sand bath is held at **150 degrees** for **6 hours**.
- Switch off the heating plate after the necessary cleaning time and wait until the the three acid mixture has reached room temperature.
- Turn off the water and to the condenser and disassemble. Clean it with water and place in the appropriate place.

The nano-diamonds should now be cleaned and still suspended in the concentrated three acid mix.

Step 3

We now need to rinse the nano-diamonds so that the are suspended in a water solution rather than the three acid mix solution.

- Prepare **6** eppindorfs and pipette **1 ml** of millipore water into each.
- Prepare a beaker of wash water
- Prepare pipette with spare pipette tips.
- Place 500 µl of three acid solution into each of the eppindorfs.
- Close eppindorfs and centrifuge to sediment the nano-diamonds.
- Clean acid flask.
- Pipette off the top layer of liquid from the eppindorfs and place in small beaker.
- Refill each eppindorf with millipore water using pipette and sonicate.
- Test pH of solution in the beaker and treat the solution as acid waste.
- Repeat the centrifuge process until the solution removed from the eppindorfs reaches a pH of ~ 7, ensuring to clean the beaker between each centrifugation.
- If need be on the last centrifugation after the pH was tested to be ~ 7, enthanol can be used instead of millipore water to produce a nano-diamond sample suspended in ethanol.
- Deal with all of the remaining acid waste, clean the items used and place back in the correct places.

The solution of nano-diamonds should now be clean from impurities, amorphous carbon and now suspended in a water or ethanol solution.

Needed Items

- 1ml of each acid
- Large Beaker for washing of acid equipment
- Small glass flask for sonication

- Pipette
- Four pipette tips
- Small round bottom flask
- Heating Plate
- Sand and convection container
- Temperature sensor that can handle up to 170 Degrees and sit in the 3 acid mix
- Condenser
- Water Tubing
- pH meter or pH strips
- Six eppindorfs

PPE

Eye/face protection

Tightly fitting safety goggles.
Faceshield (8-inch minimum).
Use equipment for eye protection tested and approved under appropriate government standards such as NIOSH (US) or EN 166(EU).

Skin protection

Handle with gloves double layer of Nitrile and Latex gloves.
Gloves must be inspected prior to use. Use proper glove removal technique (without touching glove's outer surface) to avoid skin contact with this product. Dispose of contaminated gloves after use in accordance with applicable laws and good laboratory practices. Wash and dry hands. The selected protective gloves have to satisfy the specifications of EU Directive 89/686/EEC and the standard EN 374 derived from it.

A.2 Fluorescence Detection Calculation

From a similar confocal microscopy set-up, with 1 mW of 532 nm we typically observe more than 10^6 Counts/s using the same filter stack arrangement and objective for the collection of fluorescence.

To calculate the expected fluorescence in the levitation experiment, we must calculate the ratio of excitation intensities between the two set-ups, as this is the only optical difference between the two arrangements.

As opposed to the 0.85 NA objective the levitation experiment is focusing on the nanodiamonds using a 30 mm lens with a 5 mm diameter beam, resulting in a Numerical Aperture of the lens of 0.15.

The intensity of the beam at the focus is proportional to, NA^2. Thus the reduction in excitation intensity is,

$$\frac{I_{lens}}{I_{obj}} = \frac{\mathrm{NA}_{lens}^2}{\mathrm{NA_{obj}}^2} = \frac{0.15^2}{0.85^2} \approx 0.03. \tag{A.1}$$

The excitation intensity ratio is therefore 3% and the expected counts in the levitation experiment is the roughly greater than 10^6 Counts/s $\times$ 3% $\approx$ 3×10^4 Counts/s with no quenching.

The result of this calculation is that even with 99% quenching the expected counts are greater than 300 Counts/s. Since our dark count is $\approx$ 200 Counts/s, even with 99% quenching a signal should be observed.

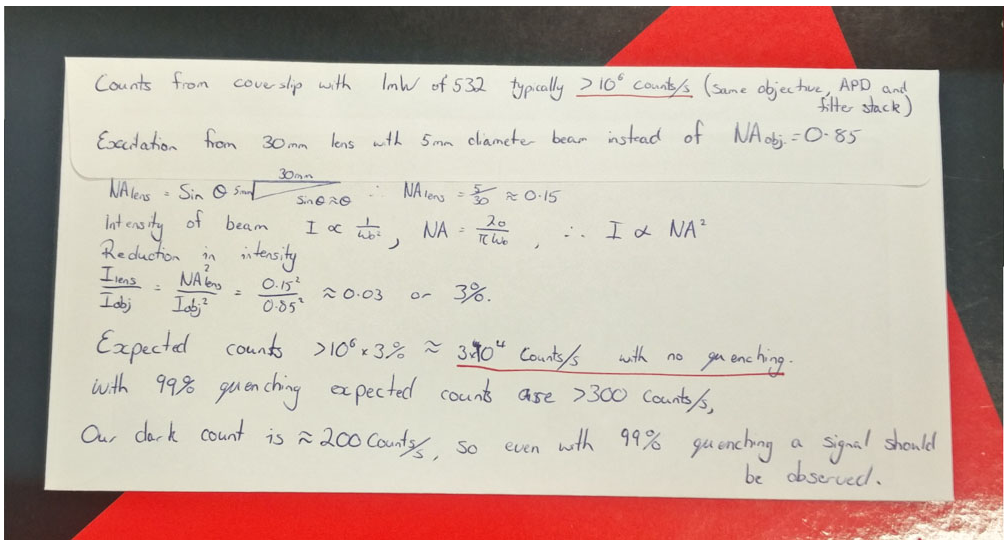

Figure A.1: Back of envelope calculation for detection of NV centre fluorescence. By comparing our levitation experiment to a confocal experiment on a glass coverslip even with 99% quenching we should still observe a flurescence signal above the noise.

List of Symbols

The following list is neither exhaustive nor exclusive, but may be helpful.

a . . . . . Particle radius

a_1 . . . . . Aperture radius at the lens plane

a_2 . . . . . Aperture radius at the axicon plane

$A(\rho)$ . . . . . Electric field profile

AFM . . . . . Atomic force microscope

AIC . . . . . Akaike information criteria

APD . . . . . Avalanche photo-diode

BD . . . . . Balance detector

c . . . . . Speed of light

$c.c$ . . . . . Complex Conjugate

CCD . . . . . Charge coupled device

CoM . . . . . Centre of Mass

CW . . . . . Continuous wave

d . . . . . Lens-axicon displacement

d . . . . . Dipole moment

D . . . . . Spectral domain size

$\langle \hat{\boldsymbol{D}}_\epsilon \rangle$ . . . . . Expectation value of the dipole moment

$\boldsymbol{E}$ ..... Electric field

E_0 ..... Electric field strength

$\mathcal{E}$ ..... Electric field vector

f ..... Focal length

f_c ..... Corner frequency

FFT ..... Fast Fourier transform

FPGA ..... Field programmable gate array

GeV ..... Germanium Vacancy

GUI ..... Graphical user interface

$\mathbf{H}$ ..... Magnetic field vector

I ..... Beam intensity

J_0 ..... Zeroth order Bessel function

k ..... Extinction coefficient

k ..... Wave number

k ..... Number of model parameters

K-F ..... Kirchoff-Fresnel

$\mathcal{L}_i$ ..... Relative likelihood of the model

m ..... Ratio of the refractive indexes $m = n_p/n_m$

n ..... Refractive Index

n_m ..... Refractive index of the medium

n_p ..... Refractive index of the particle

NA ..... Numerical Aperture

NV ..... Nitrogen Vacancy

NV^0 ..... Neutral charge state of the Nitrogen Vacancy

NV^0 ..... Negatively charge state of the Nitrogen Vacancy

P ..... Beam power

PBS ..... Polarisation beam splitter

PSB ..... Phonon side band

PZT ..... Piezoelectric transducer

QPD ..... Quadrant photo-diode

q ..... Charge

$\boldsymbol{r}$ ..... Position vector

R ..... Radius of curvature

RSS ..... Residual sum of squares

s ..... Saturation parameter

$\mathbf{S}$ ..... Poynting vector

SiV ..... Silicon Vacancy

STED ..... Stimulated emission

$u(r, z)$ ..... Electric field as a function of radius (r) and axial position (z)

$\boldsymbol{v}$ ..... Velocity

w_i ..... Akaike weights

W ..... Beam diameter

W_0 ..... Beam waist

$\hat{\boldsymbol{x}}, \hat{\boldsymbol{x}}, \hat{\boldsymbol{x}}$ ..... Unit vectors

$\tilde{x}, \tilde{y}, \tilde{z}$ ..... Normalised spatial coordinates

Z_0 ..... Intrinsic impedance of the medium

Z_R ..... Rayleigh range

ZPL ..... Zero phonon line

α ..... Axicon angle

α ..... Polarisability

α' ..... Real part of the polarisability

α'' ..... Complex part of the polarisability

β ..... Drag coefficient

Γ ..... Transition linewidth

δ ..... Laser detuning $(\omega - \omega_0)$

Δ_i ..... Relative AIC value

ϵ_0 ..... Permittivity of free space

η ..... Excitation efficiency

Θ ..... Gaussian beam angular divergence

κ ..... Trap stiffness

λ ..... Wavelength

μ_0 ..... Permeability of free space

ρ ..... Momentum

ρ_1 ..... Radial coordinate in the lens plane

ρ_2 ..... Radial coordinate in the axicon plane

ρ_g ..... Density of optically coupled states

σ ..... Scattering cross section

τ ..... Spontaneous decay rate

ϕ ..... Phase of the electric field

$\phi(\rho)$ ..... Phase retardation

ω ..... Electric field frequency

ω_0 ..... Transition frequency

Ω_1 ..... Rabi angular frequency

References

[1] Arthur Ashkin. Optical trapping and manipulation of neutral particles using lasers. *Proceedings of the National Academy of Sciences*, 94(10):4853–4860, May 1997.

[2] A. Ashkin. Atomic-Beam Deflection by Resonance-Radiation Pressure. *Physical Review Letters*, 25(19):1321–1324, November 1970.

[3] A. Ashkin. Acceleration and Trapping of Particles by Radiation Pressure. *Physical Review Letters*, 24(4):156–159, January 1970.

[4] H. Felgner, R. Frank, and M. Schliwa. Flexural rigidity of microtubules measured with the use of optical tweezers. *Journal of Cell Science*, 109(2):509–516, February 1996.

[5] M D Wang, H Yin, R Landick, J Gelles, and S M Block. Stretching DNA with optical tweezers. *Biophysical Journal*, 72(3):1335–1346, March 1997.

[6] L. Tskhovrebova, J. Trinick, J. A. Sleep, and R. M. Simmons. Elasticity and unfolding of single molecules of the giant muscle protein titin. *Nature*, 387(6630):308–312, May 1997.

[7] Michelle D. Wang, Mark J. Schnitzer, Hong Yin, Robert Landick, Jeff Gelles, and Steven M. Block. Force and Velocity Measured for Single Molecules of RNA Polymerase. *Science*, 282(5390):902–907, October 1998.

[8] S. C. Grover, A. G. Skirtach, R. C. Gauthier, and C. P. Grover. Automated single-cell sorting system based on optical trapping. *Journal of Biomedical Optics*, 6(1):14–22, January 2001.

[9] L. P. McGuinness, Y. Yan, A. Stacey, D. A. Simpson, L. T. Hall, D. Maclaurin, S. Prawer, P. Mulvaney, J. Wrachtrup, F. Caruso, R. E. Scholten, and L. C. L. Hollenberg. Quantum measurement and orientation tracking of fluorescent nanodiamonds inside living cells. *Nature Nanotechnology*, 6(6):358–363, June 2011.

[10] A. Ashkin and J. M. Dziedzic. Optical Levitation by Radiation Pressure. *Applied Physics Letters*, 19(8):283–285, October 2003.

[11] Steven Chu, J. Bjorkholm, A. Ashkin, and A. Cable. Experimental Observation of Optically Trapped Atoms. *Physical Review Letters*, 57(3):314–317, July 1986.

[12] F. Diedrich, J. C. Bergquist, Wayne M. Itano, and D. J. Wineland. Laser Cooling to the Zero-Point Energy of Motion. *Physical Review Letters*, 62(4):403–406, January 1989.

[13] Steven Chu, L. Hollberg, J. E. Bjorkholm, Alex Cable, and A. Ashkin. Three-dimensional viscous confinement and cooling of atoms by resonance radiation pressure. *Physical Review Letters*, 55(1):48–51, July 1985.

[14] A. Aspect, E. Arimondo, R. Kaiser, N. Vansteenkiste, and C. Cohen-Tannoudji. Laser Cooling below the One-Photon Recoil Energy by Velocity-Selective Coherent Population Trapping. *Physical Review Letters*, 61(7):826–829, August 1988.

[15] J. Dalibard and C. Cohen-Tannoudji. Laser cooling below the Doppler limit by polarization gradients: simple theoretical models. *Journal of the Optical Society of America B*, 6(11):2023–2045, November 1989.

[16] W. M. Itano, J. J. Bollinger, J. N. Tan, B. Jelenkovi, X.-P. Huang, and D. J. Wineland. Bragg Diffraction from Crystallized Ion Plasmas. *Science*, 279(5351):686–689, January 1998.

[17] M. H. Anderson, J. R. Ensher, M. R. Matthews, C. E. Wieman, and E. A. Cornell. Observation of Bose-Einstein Condensation in a Dilute Atomic Vapor. *Science*, 269(5221):198–201, July 1995.

[18] R. Blatt and P. Zoller. Quantum jumps in atomic systems. *European Journal of Physics*, 9(4):250, October 1988.

[19] Peter T. H. Fisk. Trapped-ion and trapped-atom microwave frequency standards. *Reports on Progress in Physics*, 60(8):761, August 1997.

[20] Oriol Romero-Isart, Anika C. Pflanzer, Mathieu L. Juan, Romain Quidant, Nikolai Kiesel, Markus Aspelmeyer, and J. Ignacio Cirac. Optically Levitating Dielectrics in the Quantum Regime: Theory and Protocols. *Physical Review A*, 83(1), January 2011.

[21] D. E. Chang, C. A. Regal, S. B. Papp, D. J. Wilson, J. Ye, O. Painter, H. J. Kimble, and P. Zoller. Cavity opto-mechanics using an optically levitated nanosphere. *Proceedings of the National Academy of Sciences*, 107(3):1005–1010, January 2010.

[22] Tongcang Li, Simon Kheifets, and Mark G. Raizen. Millikelvin cooling of an optically trapped microsphere in vacuum. *Nature Physics*, 7(7):527–530, July 2011.

[23] Igor Pikovski, Michael R. Vanner, Markus Aspelmeyer, M. S. Kim, and Caslav Brukner. Probing Planck-scale physics with quantum optics. *Nature Physics*, 8(5):393–397, May 2012.

[24] Nikolai Kiesel, Florian Blaser, Uro Deli, David Grass, Rainer Kaltenbaek, and Markus Aspelmeyer. Cavity cooling of an optically levitated submicron particle. *Proceedings of the National Academy of Sciences*, 110(35):14180–14185, August 2013.

[25] O. Romero-Isart, A. C. Pflanzer, F. Blaser, R. Kaltenbaek, N. Kiesel, M. Aspelmeyer, and J. I. Cirac. Large Quantum Superpositions and Interference of Massive Nanometer-Sized Objects. *Physical Review Letters*, 107(2), July 2011.

[26] Andrew A. Geraci, Scott B. Papp, and John Kitching. Short-range force detection using optically-cooled levitated microspheres. *arXiv:1006.0261 [hep-ph, physics:quant-ph]*, June 2010.

[27] Asimina Arvanitaki and Andrew A. Geraci. Detecting High-Frequency Gravitational Waves with Optically Levitated Sensors. *Physical Review Letters*, 110(7):071105, February 2013.

[28] Jamie Vovrosh, Muddassar Rashid, David Hempston, James Bateman, Mauro Paternostro, and Hendrik Ulbricht. Parametric feedback cooling of levitated optomechanics in a parabolic mirror trap. *JOSA B*, 34(7):1421–1428, July 2017.

[29] Jan Gieseler, Bradley Deutsch, Romain Quidant, and Lukas Novotny. Sub-Kelvin Parametric Feedback Cooling of a Laser-Trapped Nanoparticle. *Physical Review Letters*, 109(10), September 2012.

[30] Pau Mestres, Johann Berthelot, Marko Spasenovi, Jan Gieseler, Lukas Novotny, and Romain Quidant. Cooling and manipulation of a levitated nanoparticle with an optical fiber trap. *Applied Physics Letters*, 107(15):151102, October 2015.

[31] J. Millen, P.Z.G. Fonseca, T. Mavrogordatos, T.S. Monteiro, and P.F. Barker. Cavity Cooling a Single Charged Levitated Nanosphere. *Physical Review Letters*, 114(12):123602, March 2015.

[32] P.Z.G. Fonseca, E.B. Aranas, J. Millen, T.S. Monteiro, and P.F. Barker. Nonlinear Dynamics and Strong Cavity Cooling of Levitated Nanoparticles. *Physical Review Letters*, 117(17):173602, October 2016.

[33] A. J. Neves and Maria Helena Nazar. *Properties, Growth and Applications of Diamond*. IET, 2001.

[34] H. R. Phillip and E. A. Taft. Kramers-Kronig Analysis of Reflectance Data for Diamond. *Physical Review*, 136(5A):A1445–A1448, November 1964.

[35] Carlo Bradac. *The properties of nitrogen-vacancy centres in nanodiamond*. Thesis, Macquarie University, North Ryde, N.S.W., 2012.

[36] A M Zaitsev. *Optical Properties of Diamond - A Data Handbook*. Springer, 2001.

[37] J. Walker. Optical absorption and luminescence in diamond. *Reports on Progress in Physics*, 42(10):1605, October 1979.

[38] A T Collins. The detection of colour-enhanced and synthetic gem diamonds by optical spectroscopy. *DIAMOND AND RELATED MATERIALS*, 12(10-11):1976 – 1983, 2003.

[39] M. S. Grinolds, S. Hong, P. Maletinsky, L. Luan, M. D. Lukin, R. L. Walsworth, and A. Yacoby. Nanoscale magnetic imaging of a single electron spin under ambient conditions. *Nature Physics*, 9(4):215–219, February 2013.

[40] P. London, J. Scheuer, J.-M. Cai, I. Schwarz, A. Retzker, M. B. Plenio, M. Katagiri, T. Teraji, S. Koizumi, J. Isoya, R. Fischer, L. P. McGuinness, B. Naydenov, and F. Jelezko. Detecting and Polarizing Nuclear Spins with Double Resonance on a Single Electron Spin. *Physical Review Letters*, 111(6):067601, August 2013.

[41] M. V. Gurudev Dutt, L. Childress, L. Jiang, E. Togan, J. Maze, F. Jelezko, A. S. Zibrov, P. R. Hemmer, and M. D. Lukin. Quantum Register Based on Individual Electronic and Nuclear Spin Qubits in Diamond. *Science*, 316(5829):1312–1316, June 2007.

[42] Gopalakrishnan Balasubramanian, I. Y. Chan, Roman Kolesov, Mohannad Al-Hmoud, Julia Tisler, Chang Shin, Changdong Kim, Aleksander Wojcik, Philip R. Hemmer, Anke Krueger, Tobias Hanke, Alfred Leitenstorfer, Rudolf Bratschitsch, Fedor Jelezko, and Jrg Wrachtrup. Nanoscale imaging magnetometry with diamond spins under ambient conditions. *Nature*, 455(7213):648–651, October 2008.

[43] J. R. Maze, P. L. Stanwix, J. S. Hodges, S. Hong, J. M. Taylor, P. Cappellaro, L. Jiang, M. V. Gurudev Dutt, E. Togan, A. S. Zibrov, A. Yacoby, R. L. Walsworth, and M. D. Lukin. Nanoscale magnetic sensing with an individual electronic spin in diamond. *Nature*, 455(7213):644–647, October 2008.

[44] H. J. Mamin, M. Kim, M. H. Sherwood, C. T. Rettner, K. Ohno, D. D. Awschalom, and D. Rugar. Nanoscale Nuclear Magnetic Resonance with a Nitrogen-Vacancy Spin Sensor. *Science*, 339(6119):557–560, February 2013.

[45] Jui-I. Chao, Elena Perevedentseva, Pei-Hua Chung, Kuang-Kai Liu, Chih-Yuan Cheng, Chia-Ching Chang, and Chia-Liang Cheng. Nanometer-sized diamond particle as a probe for biolabeling. *Biophysical Journal*, 93(6):2199–2208, September 2007.

[46] F. Treussart, V. Jacques, E. Wu, T. Gacoin, P. Grangier, and J.-F. Roch. Photoluminescence of single colour defects in 50 nm diamond nanocrystals. *Physica B: Condensed Matter*, 376-377:926–929, April 2006.

[47] Amanda S. Barnard. Diamond standard in diagnostics: nanodiamond biolabels make their mark. *The Analyst*, 134(9):1751–1764, September 2009.

[48] Yi-Ren Chang, Hsu-Yang Lee, Kowa Chen, Chun-Chieh Chang, Dung-Sheng Tsai, Chi-Cheng Fu, Tsong-Shin Lim, Yan-Kai Tzeng, Chia-Yi Fang, Chau-Chung Han, Huan-Cheng Chang, and Wunshain Fann. Mass production and dynamic imaging of fluorescent nanodiamonds. *Nature Nanotechnology*, 3(5):284–288, May 2008.

[49] David P DiVincenzo. Quantum computation. *Science*, 270(5234):255–261, 1995.

[50] Jrg Wrachtrup and Fedor Jelezko. Processing quantum information in diamond. *Journal of Physics: Condensed Matter*, 18(21):S807, May 2006.

[51] F. Jelezko and J. Wrachtrup. Single defect centres in diamond: A review. *physica status solidi (a)*, 203(13):3207–3225, October 2006.

[52] F. Jelezko and J. Wrachtrup. Read-out of single spins by optical spectroscopy. *Journal of Physics: Condensed Matter*, 16(30):R1089, August 2004.

[53] Torsten Gaebel, Michael Domhan, Iulian Popa, Christoffer Wittmann, Philipp Neumann, Fedor Jelezko, James R. Rabeau, Nikolas Stavrias, Andrew D. Greentree, Steven Prawer, Jan Meijer, Jason Twamley, Philip R. Hemmer, and Jrg Wrachtrup. Room-temperature coherent coupling of single spins in diamond. *Nature Physics*, 2(6):408–413, June 2006.

[54] Levi P. Neukirch, Jan Gieseler, Romain Quidant, Lukas Novotny, and A. Nick Vamivakas. Observation of nitrogen vacancy photoluminescence from an optically levitated nanodiamond. *Optics Letters*, 38(16):2976–2979, August 2013.

[55] Robert M. Pettit, Levi P. Neukirch, Yi Zhang, and A. Nick Vamivakas. Coherent control of a single nitrogen-vacancy center spin in optically levitated nanodiamond. *JOSA B*, 34(6):C31–C35, June 2017.

[56] Thai M. Hoang, Jonghoon Ahn, Jaehoon Bang, and Tongcang Li. Electron spin control of optically levitated nanodiamonds in vacuum. *Nature Communications*, 7:12250, July 2016.

[57] A. D. O'Connell, M. Hofheinz, M. Ansmann, Radoslaw C. Bialczak, M. Lenander, Erik Lucero, M. Neeley, D. Sank, H. Wang, M. Weides, J. Wenner, John M. Martinis, and A. N. Cleland. Quantum ground state and single-phonon control of a mechanical resonator. *Nature*, 464(7289):697–703, April 2010.

[58] J. D. Teufel, T. Donner, Dale Li, J. W. Harlow, M. S. Allman, K. Cicak, A. J. Sirois, J. D. Whittaker, K. W. Lehnert, and R. W. Simmonds. Sideband cooling of micromechanical motion to the quantum ground state. *Nature*, 475(7356):359–363, July 2011.

[59] Jasper Chan, T. P. Mayer Alegre, Amir H. Safavi-Naeini, Jeff T. Hill, Alex Krause, Simon Grblacher, Markus Aspelmeyer, and Oskar Painter. Laser cooling of a nanomechanical oscillator into its quantum ground state. *Nature*, 478(7367):89–92, October 2011.

[60] T. A. Palomaki, J. D. Teufel, R. W. Simmonds, and K. W. Lehnert. Entangling mechanical motion with microwave fields. *Science (New York, N.Y.)*, 342(6159):710–713, November 2013.

[61] Ralf Riedinger, Sungkun Hong, Richard A. Norte, Joshua A. Slater, Juying Shang, Alexander G. Krause, Vikas Anant, Markus Aspelmeyer, and Simon Grblacher. Non-classical correlations between single photons and phonons from a mechanical oscillator. *Nature*, 530(7590):313, February 2016.

[62] Thomas Corbitt, Yanbei Chen, Edith Innerhofer, Helge Mller-Ebhardt, David Ottaway, Henning Rehbein, Daniel Sigg, Stanley Whitcomb, Christopher Wipf, and Nergis Mavalvala. An All-Optical Trap for a Gram-Scale Mirror. *Physical Review Letters*, 98(15):150802, April 2007.

[63] B. M. Zwickl, W. E. Shanks, A. M. Jayich, C. Yang, A. C. Bleszynski Jayich, J. D. Thompson, and J. G. E. Harris. High quality mechanical and optical properties of commercial silicon nitride membranes. *Applied Physics Letters*, 92(10):103125, March 2008.

[64] Dustin Kleckner and Dirk Bouwmeester. Sub-kelvin optical cooling of a micromechanical resonator. *Nature*, 444(7115):75–78, November 2006.

[65] Clemens Schfermeier, Hugo Kerdoncuff, Ulrich B. Hoff, Hao Fu, Alexander Huck, Jan Bilek, Glen I. Harris, Warwick P. Bowen, Tobias Gehring, and Ulrik L. Andersen. Quantum enhanced feedback cooling of a mechanical oscillator using nonclassical light. *Nature Communications*, 7:13628, November 2016.

[66] T. P. Purdy, D. W. C. Brooks, T. Botter, N. Brahms, Z.-Y. Ma, and D. M. Stamper-Kurn. Tunable Cavity Optomechanics with Ultracold Atoms. *Physical Review Letters*, 105(13):133602, September 2010.

[67] W. H. P. Pernice, Mo Li, and Hong X. Tang. Optomechanical coupling in photonic crystal supported nanomechanical waveguides. *Optics Express*, 17(15):12424–12432, July 2009.

[68] Levi P. Neukirch and A. Nick Vamivakas. Nano-optomechanics with optically levitated nanoparticles. *Contemporary Physics*, 56(1):48–62, January 2015.

[69] Vijay Jain, Jan Gieseler, Clemens Moritz, Christoph Dellago, Romain Quidant, and Lukas Novotny. Direct Measurement of Photon Recoil from a Levitated Nanoparticle. *Physical Review Letters*, 116(24):243601, June 2016.

[70] Jeffrey R. Moffitt, Yann R. Chemla, Steven B. Smith, and Carlos Bustamante. Recent Advances in Optical Tweezers. *Annual Review of Biochemistry*, 77(1):205–228, 2008.

[71] M. Padgett and L. Allen. Optical Tweezers And Spanners. *Physics World*, 10(9):35–38, 1997.

[72] Gilbert Grynberg, Alain Aspect, and Claude Fabre. *Introduction to Quantum Optics From the Semi classical Approach to Quantized Light | Optics, optoelectronics and photonics | Cambridge University Press*. Cambridge University Press, 2010.

[73] Yasuhiro Harada and Toshimitsu Asakura. Radiation forces on a dielectric sphere in the Rayleigh scattering regime. *Optics Communications*, 124(56):529–541, March 1996.

[74] L. W. Davis. Theory of electromagnetic beams. *Physical Review A*, 19(3):1177–1179, March 1979.

[75] J. P. Barton and D. R. Alexander. Fifthorder corrected electromagnetic field components for a fundamental Gaussian beam. *Journal of Applied Physics*, 66(7):2800–2802, October 1989.

[76] Jun Chen, Jack Ng, Shiyang Liu, and Zhifang Lin. Analytical calculation of axial optical force on a Rayleigh particle illuminated by Gaussian beams beyond the paraxial approximation. *Physical Review E*, 80(2):026607, August 2009.

[77] C. A. McQueen, J. Arlt, and K. Dholakia. An experiment to study a nondiffracting light beam. *American Journal of Physics*, 67(10):912–915, September 1999.

[78] J. Arlt and K. Dholakia. Generation of high-order Bessel beams by use of an axicon. *Optics Communications*, 177(1):297–301, April 2000.

[79] S Monk, J Arlt, D. A Robertson, J Courtial, and M. J Padgett. The generation of Bessel beams at millimetre-wave frequencies by use of an axicon. *Optics Communications*, 170(4):213–215, November 1999.

[80] Igor A. Litvina, Melanie G. Mclarena, and Andrew Forbesa. *Propagation of obstructed Bessel and BesselGauss beams*.

[81] Vladimir N. Belyi, Larisa I. Kramoreva, Muhanna K. Al-Muhanna, and Nikolai A. Khilo. Focusing Bessel Beams by a Lens with Strong Spherical Aberrations, 2012.

[82] Christian Parigger, Y. Tang, D. H. Plemmons, and J. W. L. Lewis. Spherical aberration effects in lensaxicon doublets: theoretical study. *Applied Optics*, 36(31):8214–8221, November 1997.

[83] Max Born, Emil Wolf, A. B. Bhatia, P. C. Clemmow, D. Gabor, A. R. Stokes, A. M. Taylor, P. A. Wayman, and W. L. Wilcock. Principles of Optics: Electromagnetic Theory of Propagation, Interference and Diffraction of Light, October 1999.

[84] A. E. Siegman. *Lasers*. University Science Books, 1986. Google-Books-ID: 1BZVwUZLTkAC.

[85] Allen Nussbaum and Richard A. Phillips. *Contemporary Optics for Scientists and Engineers*. 1976.

[86] Iftekher Chowdhury. *Application of Bessel-Gaussian Beam in Optical Trapping of Nanoparticles for Sensitive Gravimetry*. 2017.

[87] Craig F. Bohren and Donald R. Huffman. Particles Small Compared with the Wavelength. In *Absorption and Scattering of Light by Small Particles*, pages 130–157. Wiley-VCH Verlag GmbH, 1998.

[88] Karel Svoboda and Steven M. Block. Optical trapping of metallic Rayleigh particles. *Optics Letters*, 19(13):930–932, July 1994.

[89] Milton Kerker. *The scattering of light, and other electromagnetic radiation*. Academic Press, 1969.

[90] C. CohenTannoudji. Theory of atomic motion in laser light. *AIP Conference Proceedings*, 160(1):318–318, September 1987.

[91] Daniel Adam Steck. *Quantum and Atom Optics*. 2007. Google-Books-ID: bc9TMwEACAAJ.

[92] P. J. Ungar, D. S. Weiss, E. Riis, and Steven Chu. Optical molasses and multilevel atoms: theory. *JOSA B*, 6(11):2058–2071, November 1989.

[93] David S. Weiss, Erling Riis, Yaakov Shevy, P. Jeffrey Ungar, and Steven Chu. Optical molasses and multilevel atoms: experiment. *JOSA B*, 6(11):2072–2083, November 1989.

[94] William D. Phillips. Nobel Lecture: Laser cooling and trapping of neutral atoms. *Reviews of Modern Physics*, 70(3):721–741, July 1998.

[95] H. J. Metcalf and P. van der Straten. Laser cooling and trapping of atoms. *JOSA B*, 20(5):887–908, May 2003.

[96] A. C. Frangeskou, A. T. M. A. Rahman, L. Gines, S. Mandal, O. A. Williams, P. F. Barker, and G. W. Morley. Pure nanodiamonds for levitated optomechanics in vacuum. *New Journal of Physics*, 20(4):043016, 2018.

[97] A. T. M. Anishur Rahman and P. F. Barker. Laser refrigeration, alignment and rotation of levitated Yb 3+ :YLF nanocrystals. *Nature Photonics*, 11(10):634–638, October 2017.

[98] Levi P. Neukirch, Eva von Haartman, Jessica M. Rosenholm, and A. Nick Vamivakas. Multi-dimensional single-spin nano-optomechanics with a levitated nanodiamond. *Nature Photonics*, 9(10):653–657, October 2015.

[99] Maria Dienerowitz, Michael Mazilu, and Kishan Dholakia. Optical manipulation of nanoparticles: a review. *Journal of Nanophotonics*, 2(1):021875, September 2008.

[100] Yangcheng Li, Oleksiy V. Svitelskiy, Alexey V. Maslov, David Carnegie, Edik Rafailov, and Vasily N. Astratov. Giant resonant light forces in microspherical photonics. *Light: Science & Applications*, 2(4):e64, April 2013.

[101] Xavier Zambrana-Puyalto, Xavier Vidal, and Gabriel Molina-Terriza. Excitation of single multipolar modes with engineered cylindrically symmetric fields. *Optics Express*, 20(22):24536–24544, October 2012.

[102] P. F. Barker. Doppler Cooling a Microsphere. *Physical Review Letters*, 105(7):073002, August 2010.

[103] Benjamin Besga, Carlo Bradac, Gabriel Molina-Terriza, Gavin Brennen, Mathieu L. Juan, Mattias Johnsson, and Thomas Volz. Cooperatively enhanced dipole forces from artificial atoms in trapped nanodiamonds. *Nature Physics*, 13(3):241, March 2017.

[104] Carlo Bradac, Torsten Gaebel, Nishen Naidoo, James R. Rabeau, and Amanda. S. Barnard. Prediction and Measurement of the Size-Dependent Stability of Fluorescence in Diamond over the Entire Nanoscale. *Nano Letters*, 9(10):3555–3564, October 2009.

[105] Chi-Cheng Fu, Hsu-Yang Lee, Kowa Chen, Tsong-Shin Lim, Hsiao-Yun Wu, Po-Keng Lin, Pei-Kuen Wei, Pei-Hsi Tsao, Huan-Cheng Chang, and Wunshain Fann. Characterization and application of single fluorescent nanodiamonds as cellular biomarkers. *Proceedings of the National Academy of Sciences*, 104(3):727–732, January 2007.

[106] R. H. Dicke. Coherence in Spontaneous Radiation Processes. *Physical Review*, 93(1):99–110, January 1954.

[107] Carlo Bradac, Mattias T. Johnsson, Matthew van Breugel, Ben Q. Baragiola, Rochelle Martin, Mathieu L. Juan, Gavin K. Brennen, and Thomas Volz. Room-temperature

spontaneous superradiance from single diamond nanocrystals. *Nature Communications*, 8(1):1205, October 2017.

[108] Stefan Huler, Gerg Thiering, Andreas Dietrich, Niklas Waasem, Tokuyuki Teraji, Junichi Isoya, Takayuki Iwasaki, Mutsuko Hatano, Fedor Jelezko, Adam Gali, and Alexander Kubanek. Photoluminescence excitation spectroscopy of SiV and GeV color center in diamond. *New Journal of Physics*, 19(6):063036, 2017.

[109] N. Aslam, G. Waldherr, P. Neumann, F. Jelezko, and J. Wrachtrup. Photo-induced ionization dynamics of the nitrogen vacancy defect in diamond investigated by single-shot charge state detection. *New Journal of Physics*, 15(1):013064, 2013.

[110] V. M. Acosta, A. Jarmola, E. Bauch, and D. Budker. Optical properties of the nitrogen-vacancy singlet levels in diamond. *Physical Review B*, 82(20):201202, November 2010.

[111] Lukas Novotny and Bert Hecht. Principles of Nano-Optics by Lukas Novotny, June 2006.

[112] M K Cheezum, W F Walker, and W H Guilford. Quantitative comparison of algorithms for tracking single fluorescent particles. *Biophysical Journal*, 81(4):2378–2388, October 2001.

[113] Russell E. Thompson, Daniel R. Larson, and Watt W. Webb. Precise nanometer localization analysis for individual fluorescent probes. *Biophysical Journal*, 82(5):2775–2783, May 2002.

[114] John C. Crocker and David G. Grier. Methods of Digital Video Microscopy for Colloidal Studies. *Journal of Colloid and Interface Science*, 179(1):298–310, April 1996.

[115] Charlie Gosse and Vincent Croquette. Magnetic tweezers: micromanipulation and force measurement at the molecular level. *Biophysical Journal*, 82(6):3314–3329, June 2002.

[116] M. Keller, J. Schilling, and E. Sackmann. Oscillatory magnetic bead rheometer for complex fluid microrheometry. *Review of Scientific Instruments*, 72(9):3626–3634, September 2001.

[117] Poul Martin Hansen, Iva Marija Toli-Nrrelykke, Henrik Flyvbjerg, and Kirstine Berg-Srensen. tweezercalib 2.0: Faster version of MatLab package for precise calibration of optical tweezers. *Computer Physics Communications*, 174(6):518–520, March 2006.

[118] G. Davies and M. F. Hamer. Optical Studies of the 1.945 eV Vibronic Band in Diamond. *Proceedings of the Royal Society of London A: Mathematical, Physical and Engineering Sciences*, 348(1653):285–298, February 1976.

[119] P. Siyushev, H. Pinto, M. Vrs, A. Gali, F. Jelezko, and J. Wrachtrup. Optically Controlled Switching of the Charge State of a Single Nitrogen-Vacancy Center in Diamond at Cryogenic Temperatures. *Physical Review Letters*, 110(16):167402, April 2013.

[120] Sinan Karaveli, Ophir Gaathon, Abraham Wolcott, Reyu Sakakibara, Or A. Shemesh, Darcy S. Peterka, Edward S. Boyden, Jonathan S. Owen, Rafael Yuste, and Dirk Englund. Modulation of nitrogen vacancy charge state and fluorescence in nanodiamonds using electrochemical potential. *Proceedings of the National Academy of Sciences*, 113(15):3938–3943, April 2016.

[121] M. V. Hauf, B. Grotz, B. Naydenov, M. Dankerl, S. Pezzagna, J. Meijer, F. Jelezko, J. Wrachtrup, M. Stutzmann, F. Reinhard, and J. A. Garrido. Chemical control of the charge state of nitrogen-vacancy centers in diamond. *Physical Review B*, 83(8):081304, February 2011.

[122] Marcus W. Doherty, Neil B. Manson, Paul Delaney, Fedor Jelezko, Joerg Wrachtrup, and Lloyd C. L. Hollenberg. The nitrogen-vacancy colour centre in diamond. *Physics Reports*, 528(1):1–45, July 2013.

[123] Silvia Arroyo-Camejo, Marie-Pierre Adam, Mondher Besbes, Jean-Paul Hugonin, Vincent Jacques, Jean-Jacques Greffet, Jean-Franois Roch, Stefan W. Hell, and Franois Treussart. Stimulated Emission Depletion Microscopy Resolves Individual Nitrogen Vacancy Centers in Diamond Nanocrystals. *ACS Nano*, 7(12):10912–10919, December 2013.

[124] P. Neumann, N. Mizuochi, F. Rempp, P. Hemmer, H. Watanabe, S. Yamasaki, V. Jacques, T. Gaebel, F. Jelezko, and J. Wrachtrup. Multipartite entanglement among single spins in diamond. *Science (New York, N.Y.)*, 320(5881):1326–1329, June 2008.

[125] E. Togan, Y. Chu, A. S. Trifonov, L. Jiang, J. Maze, L. Childress, M. V. G. Dutt, A. S. Srensen, P. R. Hemmer, A. S. Zibrov, and M. D. Lukin. Quantum entanglement between an optical photon and a solid-state spin qubit. *Nature*, 466(7307):730–734, August 2010.

[126] P. Neumann, R. Kolesov, B. Naydenov, J. Beck, F. Rempp, M. Steiner, V. Jacques, G. Balasubramanian, M. L. Markham, D. J. Twitchen, S. Pezzagna, J. Meijer,

J. Twamley, F. Jelezko, and J. Wrachtrup. Quantum register based on coupled electron spins in a room-temperature solid. *Nature Physics*, 6(4):249–253, April 2010.

[127] C. L. Degen. Scanning magnetic field microscope with a diamond single-spin sensor. *Applied Physics Letters*, 92(24):243111, June 2008.

[128] J. M. Taylor, P. Cappellaro, L. Childress, L. Jiang, D. Budker, P. R. Hemmer, A. Yacoby, R. Walsworth, and M. D. Lukin. High-sensitivity diamond magnetometer with nanoscale resolution. *Nature Physics*, 4(10):810–816, October 2008.

[129] Romana Schirhagl, Kevin Chang, Michael Loretz, and Christian L. Degen. Nitrogen-vacancy centers in diamond: nanoscale sensors for physics and biology. *Annual Review of Physical Chemistry*, 65:83–105, 2014.

[130] Taras Plakhotnik and Robert Chapman. Nitrogen-vacancy centers in nano-diamond reversibly decrease the luminescence quantum yield under strong pulsed-laser irradiation. *New Journal of Physics*, 13(4):045001, 2011.

[131] Robert Chapman and Taras Plakhotnik. Anomalous saturation effects due to optical spin depolarization in nitrogen-vacancy centers in diamond nanocrystals. *Physical Review B*, 86(4):045204, July 2012.

[132] N. D. Lai, O. Faklaris, D. Zheng, V. Jacques, H.-C. Chang, J.-F. Roch, and F. Treussart. Quenching nitrogenvacancy center photoluminescence with an infrared pulsed laser. *New Journal of Physics*, 15(3):033030, 2013.

[133] Michael Geiselmann, Renaud Marty, F. Javier Garca de Abajo, and Romain Quidant. Fast optical modulation of the fluorescence from a single nitrogen-vacancy centre. *Nature Physics*, 9(12):785–789, December 2013.

[134] Roger Mc Murtrie, Lachlan J. Rogers, and Neil B. Manson. Effects of magnetic field on the low temperature emission of nitrogen vacancy centres in diamond. *Physics Procedia*, 3(4):1583–1589, February 2010.

[135] Xusan Yang, Yan-Kai Tzeng, Zhouyang Zhu, Zhihong Huang, Xuanze Chen, Yujia Liu, Huan-Cheng Chang, Lei Huang, Wen-Di Li, and Peng Xi. Sub-diffraction imaging of nitrogen-vacancy centers in diamond by stimulated emission depletion and structured illumination. *RSC Advances*, 4(22):11305–11310, February 2014.

[136] A. Lenef and S. C. Rand. Electronic structure of the N-V center in diamond: Theory. *Physical Review B*, 53(20):13441–13455, May 1996.

[137] Adam Gali, Maria Fyta, and Efthimios Kaxiras. Ab initio supercell calculations on nitrogen-vacancy center in diamond: its electronic structure and hyperfine tensors. *Physical Review B*, 77(15), April 2008.

[138] Yoshimi Mita. Change of absorption spectra in type-Ib diamond with heavy neutron irradiation. *Physical Review B*, 53(17):11360–11364, May 1996.

[139] Alan T. Collins. The Fermi level in diamond. *Journal of Physics: Condensed Matter*, 14(14):3743, April 2002.

[140] A. Jarmola, V. M. Acosta, K. Jensen, S. Chemerisov, and D. Budker. Temperature- and Magnetic-Field-Dependent Longitudinal Spin Relaxation in Nitrogen-Vacancy Ensembles in Diamond. *Physical Review Letters*, 108(19):197601, May 2012.

[141] Faraz A. Inam, Torsten Gaebel, Carlo Bradac, Luke Stewart, Michael J. Withford, Judith M. Dawes, James R. Rabeau, and Michael J. Steel. Enhanced spontaneous emission from nanodiamond colour centres on opal photonic crystal. *New Journal of Physics*, 13(7):073012, July 2011. arXiv: 1102.0051.

[142] Jelle Storteboom, Philip Dolan, Stefania Castelletto, Xiangping Li, and Min Gu. Lifetime investigation of single nitrogen vacancy centres in nanodiamonds. *Optics Express*, 23(9):11327–11333, May 2015.

[143] M.L. Goldman, A. Sipahigil, M.W. Doherty, N.Y. Yao, S.D. Bennett, M. Markham, D.J. Twitchen, N.B. Manson, A. Kubanek, and M.D. Lukin. Phonon-Induced Population Dynamics and Intersystem Crossing in Nitrogen-Vacancy Centers. *Physical Review Letters*, 114(14):145502, April 2015.

[144] M. L. Goldman, M. W. Doherty, A. Sipahigil, N. Y. Yao, S. D. Bennett, N. B. Manson, A. Kubanek, and M. D. Lukin. State-selective intersystem crossing in nitrogen-vacancy centers. *Physical Review B*, 91(16):165201, April 2015.

[145] L. J. Rogers, S. Armstrong, M. J. Sellars, and N. B. Manson. Infrared emission of the NV centre in diamond: Zeeman and uniaxial stress studies. *New Journal of Physics*, 10(10):103024, October 2008.

[146] Lucio Robledo, Hannes Bernien, Toeno van der Sar, and Ronald Hanson. Spin dynamics in the optical cycle of single nitrogen-vacancy centres in diamond. *New Journal of Physics*, 13(2):025013, 2011.

[147] J.-P. Tetienne, L. Rondin, P. Spinicelli, M. Chipaux, T. Debuisschert, J.-F. Roch, and V. Jacques. Magnetic-field-dependent photodynamics of single NV defects in diamond: an application to qualitative all-optical magnetic imaging. *New Journal of Physics*, 14(10):103033, 2012.

[148] S. Felton, A. M. Edmonds, M. E. Newton, P. M. Martineau, D. Fisher, and D. J. Twitchen. Electron paramagnetic resonance studies of the neutral nitrogen vacancy in diamond. *Physical Review B*, 77(8):081201, February 2008.

[149] Neil B Manson, Morgan Hedges, Michael S J Barson, Rose Ahlefeldt, Marcus W Doherty, Hiroshi Abe, Takeshi Ohshima, and Matthew J Sellars. NV N^+ pair centre in 1b diamond. *New Journal of Physics*, 20(11):113037, November 2018.

[150] N. B. Manson and J. P. Harrison. Photo-ionization of the nitrogen-vacancy center in diamond. *Diamond and Related Materials*, 14(10):1705–1710, October 2005.

[151] G. Liaugaudas, G. Davies, K. Suhling, R. U. A. Khan, and D. J. F. Evans. Luminescence lifetimes of neutral nitrogen-vacancy centres in synthetic diamond containing nitrogen. *Journal of Physics: Condensed Matter*, 24(43):435503, 2012.

[152] Martin Berthel, Oriane Mollet, Graldine Dantelle, Thierry Gacoin, Serge Huant, and Aurlien Drezet. Photophysics of single nitrogen-vacancy centers in diamond nanocrystals. *Physical Review B*, 91(3):035308, January 2015.

[153] C. Bradac, T. Gaebel, N. Naidoo, M. J. Sellars, J. Twamley, L. J. Brown, A. S. Barnard, T. Plakhotnik, A. V. Zvyagin, and J. R. Rabeau. Observation and control of blinking nitrogen-vacancy centres in discrete nanodiamonds. *Nature Nanotechnology*, 5(5):345–349, May 2010.

[154] Matthias Pfender, Nabeel Aslam, Patrick Simon, Denis Antonov, Gerg Thiering, Sina Burk, Felipe Fvaro de Oliveira, Andrej Denisenko, Helmut Fedder, Jan Meijer, Jose A. Garrido, Adam Gali, Tokuyuki Teraji, Junichi Isoya, Marcus William Doherty, Audrius Alkauskas, Alejandro Gallo, Andreas Grneis, Philipp Neumann, and Jrg Wrachtrup. Protecting a Diamond Quantum Memory by Charge State Control. *Nano Letters*, 17(10):5931–5937, October 2017.

[155] Moritz V. Hauf, Patrick Simon, Nabeel Aslam, Matthias Pfender, Philipp Neumann, Sbastien Pezzagna, Jan Meijer, Jrg Wrachtrup, Martin Stutzmann, Friedemann Reinhard, and Jos A. Garrido. Addressing Single Nitrogen-Vacancy Centers in Diamond with Transparent in-Plane Gate Structures. *Nano Letters*, 14(5):2359–2364, May 2014.

[156] Jan Jeske, Desmond W. M. Lau, Xavier Vidal, Liam P. McGuinness, Philipp Reineck, Brett C. Johnson, Marcus W. Doherty, Jeffrey C. McCallum, Shinobu Onoda, Fedor Jelezko, Takeshi Ohshima, Thomas Volz, Jared H. Cole, Brant C. Gibson, and Andrew D. Greentree. Stimulated emission from nitrogen-vacancy centres in diamond. *Nature Communications*, 8(1):1–8, January 2017.

[157] Peng Ji and M. V. Gurudev Dutt. Charge state dynamics of the nitrogen vacancy center in diamond under 1064 nm laser excitation. *Physical Review B*, 94(2), July 2016. arXiv: 1603.08066.

[158] Xiang-Dong Chen, Shen Li, Ao Shen, Yang Dong, Chun-Hua Dong, Guang-Can Guo, and Fang-Wen Sun. Near-Infrared-Enhanced Charge-State Conversion for Low-Power Optical Nanoscopy with Nitrogen-Vacancy Centers in Diamond. *Physical Review Applied*, 7(1):014008, January 2017.

[159] Elke Neu, David Steinmetz, Janine Riedrich-Mller, Stefan Gsell, Martin Fischer, Matthias Schreck, and Christoph Becher. Single photon emission from silicon-vacancy colour centres in chemical vapour deposition nano-diamonds on iridium. *New Journal of Physics*, 13(2):025012, 2011.

[160] J. P. Goss, R. Jones, S. J. Breuer, P. R. Briddon, and S. berg. The Twelve-Line 1.682 eV Luminescence Center in Diamond and the Vacancy-Silicon Complex. *Physical Review Letters*, 77(14):3041–3044, September 1996.

[161] S. S. Moliver. Electronic structure of neutral silicon-vacancy complex in diamond. *Technical Physics*, 48(11):1449–1453, November 2003.

[162] J. P. Goss, P. R. Briddon, and M. J. Shaw. Density functional simulations of silicon-containing point defects in diamond. *Physical Review B*, 76(7):075204, August 2007.

[163] I. Aharonovich, S. Castelletto, D. A. Simpson, C.-H. Su, A. D. Greentree, and S. Prawer. Diamond-based single-photon emitters. *Reports on Progress in Physics*, 74(7):076501, July 2011.

[164] Chunlang Wang, Christian Kurtsiefer, Harald Weinfurter, and Bernd Burchard. Single photon emission from SiV centres in diamond produced by ion implantation. *Journal of Physics B: Atomic, Molecular and Optical Physics*, 39(1):37, 2006.

[165] null Sternschulte, null Thonke, null Sauer, null Mnzinger, and null Michler. 1.681-eV luminescence center in chemical-vapor-deposited homoepitaxial diamond films. *Physical Review. B, Condensed Matter*, 50(19):14554–14560, November 1994.

[166] A. V. Turukhin, C.-H. Liu, A. A. Gorokhovsky, R. R. Alfano, and W. Phillips. Picosecond photoluminescence decay of Si-doped chemical-vapor-deposited diamond films. *Physical Review B*, 54(23):16448–16451, December 1996.

[167] U. F. S. D'Haenens-Johansson, A. M. Edmonds, B. L. Green, M. E. Newton, G. Davies, P. M. Martineau, R. U. A. Khan, and D. J. Twitchen. Optical properties of the neutral silicon split-vacancy center in diamond. *Physical Review B*, 84:245208, December 2011.

[168] Uwe Jantzen, Andrea B. Kurz, Daniel S. Rudnicki, Clemens Schfermeier, Kay D. Jahnke, Ulrik L. Andersen, Valery A. Davydov, Viatcheslav N. Agafonov, Alexander Kubanek, Lachlan J. Rogers, and Fedor Jelezko. Nanodiamonds carrying silicon-vacancy quantum emitters with almost lifetime-limited linewidths. *New Journal of Physics*, 18(7):073036, 2016.

[169] Matthew van Breugel. *Exploring the Silicon Vacancy Centre in CVD Grown Nanodiamond for Near-resonant Optical Trapping*. 2014. Google-Books-ID: MnnfjgEACAAJ.

[170] J. Meijer, T. Vogel, B. Burchard, I. W. Rangelow, L. Bischoff, J. Wrachtrup, M. Domhan, F. Jelezko, W. Schnitzler, S. A. Schulz, K. Singer, and F. Schmidt-Kaler. Concept of deterministic single ion doping with sub-nm spatial resolution. *Applied Physics A*, 83(2):321–327, May 2006.

[171] F. Ricci, R. A. Rica, M. Spasenovi, J. Gieseler, L. Rondin, L. Novotny, and R. Quidant. Optically levitated nanoparticle as a model system for stochastic bistable dynamics. *Nature Communications*, 8:15141, May 2017.

[172] Gambhir Ranjit, Mark Cunningham, Kirsten Casey, and Andrew A. Geraci. Zeptonewton force sensing with nanospheres in an optical lattice. *Physical Review A*, 93(5):053801, May 2016.

[173] Jan Gieseler and James Millen. Levitated Nanoparticles for Microscopic Thermodynamics—A Review. *Entropy*, 20(5):326, April 2018.

[174] Erik Hebestreit, Ren Reimann, Martin Frimmer, and Lukas Novotny. Measuring the internal temperature of a levitated nanoparticle in high vacuum. *Physical Review A*, 97(4):043803, April 2018.

[175] Ishan Rastogi, Macquarie University Department of Chemistry, biomolecural sciences institution.), and Louise Brown. *Luminescent nanodiamonds as biolabels*. Thesis, 2016.

[176] Lachlan J. Rogers, Kay D. Jahnke, Marcus W. Doherty, Andreas Dietrich, Liam P. McGuinness, Christoph Mller, Tokuyuki Teraji, Hitoshi Sumiya, Junichi Isoya, Neil B. Manson, and Fedor Jelezko. Electronic structure of the negatively charged silicon-vacancy center in diamond. *Physical Review B*, 89(23):235101, June 2014.

[177] Gerg Thiering and Adam Gali. Complexes of silicon, vacancy, and hydrogen in diamond: A density functional study. *Physical Review B*, 92(16):165203, October 2015.

[178] Jan M. Binder, Alexander Stark, Nikolas Tomek, Jochen Scheuer, Florian Frank, Kay D. Jahnke, Christoph Mller, Simon Schmitt, Mathias H. Metsch, Thomas Unden, Tobias Gehring, Alexander Huck, Ulrik L. Andersen, Lachlan J. Rogers, and Fedor Jelezko. Qudi: A modular python suite for experiment control and data processing. *SoftwareX*, 6:85–90, January 2017.

[179] Elke Neu, Christian Hepp, Michael Hauschild, Stefan Gsell, Martin Fischer, Hadwig Sternschulte, Doris Steinmller-Nethl, Matthias Schreck, and Christoph Becher. Low-temperature investigations of single silicon vacancy colour centres in diamond. *New Journal of Physics*, 15(4):043005, April 2013.

[180] Fabio Grazioso, Brian R. Patton, Paul Delaney, Matthew L. Markham, Daniel J. Twitchen, and Jason M. Smith. Measurement of the full stress tensor in a crystal using photoluminescence from point defects: The example of nitrogen vacancy centers in diamond. *Applied Physics Letters*, 103(10):101905, September 2013.

[181] G. Davies. Vibronic spectra in diamond. *Journal of Physics C: Solid State Physics*, 7(20):3797–3809, October 1974.

[182] G Davies. The Jahn-Teller effect and vibronic coupling at deep levels in diamond. *Reports on Progress in Physics*, 44(7):787–830, July 1981.

[183] M.K. Bhaskar, D.D. Sukachev, A. Sipahigil, R.E. Evans, M.J. Burek, C.T. Nguyen, L.J. Rogers, P. Siyushev, M.H. Metsch, H. Park, F. Jelezko, M. Lonar, and M.D. Lukin. Quantum Nonlinear Optics with a Germanium-Vacancy Color Center in a Nanoscale Diamond Waveguide. *Physical Review Letters*, 118(22):223603, May 2017.

[184] K. D. B. Higgins, S. C. Benjamin, T. M. Stace, G. J. Milburn, B. W. Lovett, and E. M. Gauger. Superabsorption of light via quantum engineering. *Nature Communications*, 5:4705, August 2014.